

Imaging Dilute Contrast Materials in Small Animals Using Synchrotron Light

A Dissertation Submitted to
the College of Graduate Studies and Research
in Partial Fulfillment of the Requirements
for the Degree of Doctor of Philosophy
in the Division of Biomedical Engineering
University of Saskatchewan
Saskatoon

By

Honglin Zhang

Permission to Use

In presenting this dissertation in partial fulfillment of the requirements for a Degree of Doctor of Philosophy from the University of Saskatchewan, I agree that the Libraries of this University may make it freely available for inspection. I further agree that permission for copying of this dissertation in any manner, in whole or in part, for scholarly purposes may be granted by the professors who supervised this thesis work or, in their absence, by the Head of the Division or the Dean of the College in which this thesis work was done. It is understood that any copying or publication or use of this thesis or parts thereof for financial gain shall not be allowed without the author's written permission. It is also understood that due recognition shall be given to me and to the University of Saskatchewan in any scholarly use which may be made of any material in this dissertation.

Requests for permission to copy or to make other use of material in this dissertation in whole or part should be addressed to:

Head of the Division of Biomedical Engineering
University of Saskatchewan
Saskatoon, Saskatchewan,
Canada, S7N 5A9

Abstract

The development of a non-invasive method of visualizing gene expression in larger animals could revolutionize some aspects of gene research by opening up a wider variety of animal systems to explore; some of which may be better models of human systems. Presently, most gene expression studies employ *Green Fluorescent Protein (GFP)* transfected into the genome of the animal system. For larger animals, an “x-ray” equivalent of GFP would be desirable due to the high penetrating power of x-rays. A model gene modification system is to use the *Sodium (Na) Iodide Symporter (NIS)* which will cause the accumulation of iodine in cells which express the NIS. To non-invasively observe the dilute iodine accumulated by the cancer cells transfected with NIS in the head of small animals, such as a rat, two synchrotron-based imaging methods were studied: *K-Edge Subtraction (KES)* imaging and *Fluorescence Subtraction Imaging (FSI)*.

KES needs wide monochromatic x-ray beams at two energies bracketing the K-edge of the contrast agent existing or injected in the tissues. The monochromatic beam in the synchrotron facility normally is prepared by a double crystal monochromator. The appearance of the azimuthal angle (tilt error) in the double crystal monochromator creates intensity variations across the imaging field. This misalignment was studied through another two synchrotron-based imaging methods, *Diffraction Enhanced Imaging (DEI)* and *Multi-Image Radiography (MIR)*, which show this problem clearly in their processed images. The detailed analysis of the effect of the tilt error, how it affects the resulting images, and how to quantify such an error were presented in the thesis. A post processing method was implemented and the artifacts caused by the improper experimental settings were discussed.

With the wide monochromatic beam prepared by the double crystal monochromator, a sequence of KES experiments were done and the detection limit of KES was quantified at a projected amount of 17.5mM-cm iodine in a physical model of a rat head with a radiation dose of 2.65mGy. With the raster scan of the object relative to the monochromatic pencil beam, FSI was studied to obtain higher *Signal to Noise Ratio (SNR)* for local area and better detection limit compared to KES. The detection limit of FSI was

measured as a projected amount of 2.5mM-cm iodine in the same physical rat head with a tolerable radiation dose of 24mGy. According to the comparison of these two imaging techniques with references to imaging time and area, radiation dose, spatial resolution, and SNR, it was concluded that these two imaging techniques can be used complementarily in imaging dilute contrast material. Due to the short imaging time and large imaging area, KES is used first to provide a global view of the object, locate the area of interest, do the preliminary diagnosis, and decide whether the further FSI is necessary. Due to its high SNR for the dilute sample, FSI can be used when the area of interest is known. The combination of these two imaging techniques will be very promising and powerful. To facilitate the comparison of KES and FSI, a quality factor was developed to evaluate the performance of the imaging system.

The measured detection limits in our experiments are far beyond the thyroidal iodine concentration of a rat (around 1mM). To further improve the performance of KES, a bent Laue crystal monochromator was designed to do the simultaneous iodine KES imaging which overcomes the artifacts in the iodine image caused by the temporal difference for a single set of images. The designed monochromator can provide two separated x-ray beams bracketing the K-edge of iodine at the same time with a very high spatial resolution which is only depends on the source size, a very high energy resolution which can almost compete with that of the double crystal monochromator, and an acceptable photon flux.

Acknowledgements

I would like to express my sincere appreciations to Dr. Dean Chapman, one of my major professors, for leading me to this interesting area, passing me his passion, and guiding me all the way to my degree. He taught me not only how to do research but also how to be a person. His attitude to research and to people will no doubt affect the rest of my life. The financial support he provided also made my study and research possible. The support and care from his wife, Liz Chapman, is also highly appreciated.

I also would like to give my high appreciations to Dr. Madan Gupta, the other major professor of mine, for his consistent support and guidance. My gratitude would also go to his wife, Suman Gupta, for her encouragement.

I would like to thank Dr. Zhong Zhong and Dr. Dean Chapman for the experiments they did at National Synchrotron Light Source on tilt error. Also the gratitude should be given to my labmates, Brian Bewer, for the experimental setup and data collection of K-Edge Subtraction imaging and Fluorescence Subtraction Imaging, and Ying Zhu, for the first set of animal restraint and flattener.

Special thanks should be conveyed to my husband, Yajun Yang, for his patience and support. My daughter, Qinmeng Yang, and my son, Qinjia Yang made the period of my study more enjoyable and challenging.

The gratitude is also owned to my parents, Deqing Zhang and Enyan Wang. They made their contributions to the thesis by love.

To my parents,

Deqing Zhang & Enyan Wang

Contents

Permission to Use	i
Abstract	ii
Acknowledgements	iv
List of Figures	ix
List of Tables	xvi
List of Abbreviations	xvii
Chapter 1 Synchrotron Based Biomedical Imaging Techniques: Some Basics.....	1
1.1 Properties of the Synchrotron Light	1
1.2 Synchrotron Based Biomedical Imaging Techniques	3
1.2.1 Diffraction Enhanced Imaging and Multiple-Image Radiography	3
1.2.2 K-edge Subtraction Imaging	4
1.2.3 X-Ray Fluorescence Imaging	5
1.3 Motivation and Outline of the Thesis	6
Chapter 2 Crystal Tilt Error and its Correction	9
2.1 Introduction	9
2.2 Tilt Error	18
2.3 Experiments	26
2.3.1 Tilt of the Analyzer	27
2.3.2 Tilt of the 2 nd Crystal of the Monochromator	32
2.4 Corrections of the Tilt Error in DEI/MIR Images	35
2.5 Conclusions.....	38
Chapter 3 KES and Fluorescence Subtraction Imaging (FSI).....	40
3.1 Motivation	40
3.2 K-Edge Subtraction Imaging and Fluorescence Subtraction Imaging	41
3.2.1 K-Edge Subtraction Imaging	42
3.2.2 Fluorescence Subtraction Imaging	47

3.2.2.1	X-Ray Fluorescence Imaging	47
3.2.2.2	Fluorescence Subtraction Imaging	48
3.2.2.3	Fluorescence Detector	52
3.2.3	Quality Factor	58
3.2.4	Harmonics Analysis	59
3.3	Experiments and Results	62
3.3.1	The 1 st Experiments and Results	62
3.3.2	The 2 nd Experiments and Results	63
3.3.3	The 3 rd Experiments and Results	64
3.3.3.1	Rat Head Restraint	65
3.3.3.2	Field Flattener	67
3.3.3.3	K-Edge Subtraction Imaging Experiments and the Results	68
3.3.3.3.1	K-Edge Subtraction Imaging Experiments with the First Test Object	68
3.3.3.3.2	K-Edge Subtraction Imaging Experiments with the Second Test Object	77
3.3.3.4	Fluorescence Subtraction Imaging Experiments and the Results...	82
3.3.4	The 4th Experiments and Results	83
3.3.4.1	Smoothing of the Flatteners	83
3.3.4.2	Smoothing of the Restraint	85
3.3.4.3	The Sample used in the Experiments	88
3.3.4.4	Experimental Setup	88
3.3.4.5	K-Edge Subtraction Imaging Experiments and Results	90
3.3.4.6	Fluorescence Subtraction Imaging Experiments and Results	95
3.4	Comparison of K-Edge Subtraction Imaging and Fluorescence Subtraction Imaging.....	97
3.5	Conclusions.....	100
Chapter 4 A Design Study of a Bent Laue Monochromator for Simultaneous K- Edge Subtraction Imaging.....		105
4.1	Introduction	105

4.2 Cylindrically Bent Laue Crystal Optics	106
4.2.1 Some Definitions	107
4.2.2 Geometrical Focusing	109
4.2.3 Polychromatic Focusing	110
4.2.4 Focus Size	118
4.2.5 Reflectivity	121
4.3 Conceptual Design	122
4.3.1 Selection of the Crystal	123
4.3.2 Design of the Bending Radius and the Focus Size	125
4.3.3 Requirement of the Beam Vertical Size of the Design	127
4.3.4 Reflectivity of the Design	128
4.3.5 Energy Resolution of the Design	129
4.4 Conclusions.....	132
Chapter 5 Conclusions and Further Research.....	134
5.1 Summary and Achievements.....	134
5.1 Challenges for Further research.....	136
Appendix A Basic Physics Concepts	138
A.1 Miller Indices and D-spacing	138
A.2 Reciprocal Lattice	139
A.3 Dynamical Diffraction Theory, Crystal Reflectivity and Darwin width	141
A.4 Stereographic Projection	143
Appendix B Analysis of Tilt Errors	146
References	156

List of Figures

Figure 1.1	Structure of a synchrotron facility	2
Figure 2.1	Synchrotron DEI/MIR experimental setup	10
Figure 2.2	Calculation of the reflectivity of the monochromator for Si(3,3,3) at 40keV	11
Figure 2.3	Calculation of the intrinsic rocking curve of the analyzer for Si(3,3,3) at 40keV	12
Figure 2.4	Rocking curve dependence on the energy of the incident beam and the lattice plane of the crystal	13
Figure 2.5	Rocking curve of Si(3, 3, 3) at 40keV and DEI images taken at analyzer settings of $-0.78\mu r$ and $0.78\mu r$	14
Figure 2.6	The absorption and refraction image of the Lucite sphere from DEI method, MIR method and the real absorption and refraction properties of the object	15
Figure 2.7	Rocking curve (solid line) of Si(3, 3, 3) at 40keV, its Lorentzian fit (dashed line) and MIR images taken at analyzer settings of $-3\mu r$, $-2\mu r$, $-$ $1\mu r$, $-0.5\mu r$, $0\mu r$, $0.5\mu r$, $1\mu r$, $2\mu r$, and $3\mu r$ from left to right	16
Figure 2.8	Distillation of MIR parametric images, absorption image, refraction image, extinction image, and scatter width image	17
Figure 2.9	Definitions of the Bragg angle θ_B , the tilt angle χ , and the diffraction plane of the crystal	19
Figure 2.10	Illustration of a fan beam incident on the crystal with a tilt error χ	20
Figure 2.11	Energy selection across the fan beam of the first crystal of the monochromator in the cases of $-500\mu r$, $0\mu r$, and $500\mu r$ tilt	21
Figure 2.12	Reflectivity as a function of energy of the first crystal for the ray with a fan angle (β) of $500\mu r$, with crystal tilts of $-500\mu r$, $0\mu r$, and $500\mu r$, respectively	22
Figure 2.13	The effects of the tilt error of the second crystal of the monochromator	

on the reflectivity as a function of x-ray energy	23
Figure 2.14 Effect of a mis-aligned analyzer with an aligned monochromator for the ray with an opening angle of 500 μ r	25
Figure 2.15 Beamline setup for tilt experiments	27
Figure 2.16 A sample image of the beam	29
Figure 2.17 Image of the beam at different analyzer settings and the accordingly calculated refraction angle as a function of the beam width and its linear fitting when the tilt of the analyzer was set as 6.06mr	29
Figure 2.18 Some DEI mammography images and the estimated intrinsic rocking curves at different locations in the images	31
Figure 2.19 Estimated refraction image of the top of the original images and its averaged profile	32
Figure 2.20 k as a function of the tilt of the analyzer	33
Figure 2.21 k as a function of the tilt of the analyzer	34
Figure 2.22 Comparison of the estimated parametric images using different methods	36
Figure 2.23 Imaging object and the distilled parametric images with artifacts	37
Figure 2.24 Weakened artifacts with the decrease of the increment of the analyzer angular settings	38
Figure 3.1 Mass attenuation coefficients as a function of the energy of the incident beam	42
Figure 3.2 Illustration of fluorescent x-ray emission	48
Figure 3.3 Mass attenuation coefficient and its components of 100mM iodine solution as a function of x-ray energy	49
Figure 3.4 Fluorescence spectra obtained from a 5mm \times 5mm filter paper absorbed with dilute iodine solution at two different incident beam energies: 33.25keV and 33.10keV	51
Figure 3.5 The arrangement of the channels of the fluorescence detector	52
Figure 3.6 Scattering geometry	54
Figure 3.7 Differential cross section of Compton scattering as a function of the scatter angle θ	54

Figure 3.8	Spectrum collected by different elements of the detector with the filter paper absorbed with 100mM iodine solution	55
Figure 3.9	Weighted and un-weighted spectrum and their corresponding fluorescence signal	56
Figure 3.10	Characteristics of the collected spectrum as functions of the relative locations of the sample and the channels of the detector	57
Figure 3.11	Estimated sample position	57
Figure 3.12	Spectrum of the beam delivered by the HXMA wiggler	59
Figure 3.13	Reflectivity of the fundamentals and its 2 nd and 3 rd order harmonics by [2, 2, 0] monochromator	61
Figure 3.14	Illustration of the test object in the 1 st experiment and the incident beam	63
Figure 3.15	Result images of the test object in the 1 st experiments	63
Figure 3.16	Test object in 2 nd experiment	64
Figure 3.17	Result images of the test object in the 2 nd experiments	64
Figure 3.18	Rat head restraint fabricated by a rapid prototyper	65
Figure 3.19	Experimental results on the restraint	66
Figure 3.20	A dorsal-ventral view flattener and the rat head in its restraint in the experiment	67
Figure 3.21	Test object in the 3 rd experiments	69
Figure 3.22	Experimental setup in the 3 rd experiments	70
Figure 3.23	Resulting images of the test object	71
Figure 3.24	Logarithmic plots of the theoretical and measured projected iodine amounts and a linear fitting of the measured values	74
Figure 3.25	The theoretical and measured SNRs for 100mM projected iodine amount as a function of the number of the image sets used to obtain the iodine image	77
Figure 3.26	The micropipette used in the experiments	78
Figure 3.27	KES resulting images of the lateral view of the demised rat head	78
Figure 3.28	KES resulting images of the dorsal ventral view of the demised rat head	79

Figure 3.29	Local iodine images obtained from different image sets	80
Figure 3.30	The measured SNRs as a function of the number of the image sets used to obtain the iodine images	80
Figure 3.31	The Resulting images from 8 image sets with flatteners	81
Figure 3.32	FSI experimental resulting images of the interested area from the lateral view	83
Figure 3.33	The original projected curve of a slice with the teeth and the teeth-cut curve	84
Figure 3.34	The original and the smoothed projection images	85
Figure 3.35	Conversion of a 2-D contour to 1-D curve with the polar coordinates of each point as its Cartesian coordinates	86
Figure 3.36	The original converted image and the smoothed one	87
Figure 3.37	Conversion of a 1-D smoothed curve to 2-D contour	87
Figure 3.38	Sample in the 4 th experiment	88
Figure 3.39	Experimental setup for the 4th experiment	89
Figure 3.40	Experimental result of KES with one image set	91
Figure 3.41	Iodine images obtained from 1-8 image sets in KES	92
Figure 3.42	SNR as a function of the projected amount of the contrast agent and the number of image sets	95
Figure 3.43	Resulting images of the fluorescence experiment	96
Figure 3.44	Linear dependence of SNR on the projected amount of the contrast agent and the square root of the incident photon count	97
Figure 3.45	Recast iodine image of KES	98
Figure 3.46	Comparison of SNR in recast KES iodine image and the FSI iodine image	99
Figure 4.1	Typical simultaneous KES imaging experimental setup	106
Figure 4.2	Optics of Bragg type and Laue type crystals	108
Figure 4.3	Definition of upper and lower incident conditions	108
Figure 4.4	Definition of divergent and convergent geometry	109
Figure 4.5	Geometrical focusing of the bent Laue crystal	110
Figure 4.6	Single ray broadening by Laue crystal	111

Figure 4.7	Real and virtual polychromatic foci after the broadening of the single ray by the bent Laue crystal	113
Figure 4.8	Lamellar model for calculation of the single ray focus	114
Figure 4.9	Relationship between the number of lamellar plane used in the calculation and the calculated angular change along one lattice plane by bending	116
Figure 4.10	Angular change of the lattice planes and the single ray focus distance as functions of energy	117
Figure 4.11	Three relative locations of the geometric focus and the polychromatic focus	118
Figure 4.12	The distance from the crystal to the polychromatic focus as a function of crystal thickness	119
Figure 4.13	Effects of bending radius and asymmetry angle on focus size	121
Figure 4.14	Stereographic projection of silicon wafer Si(4, 0, 0), Si(2, 1, 1), Si(1, 1, 1), Si(2, 2, 0), and Si(5, 1, 1)	124
Figure 4.15	Focus size as a function of bending radius and asymmetry angle of the crystal	126
Figure 4.16	The dependence of polychromatic focus, geometric focus, and focus size on the bending radius	127
Figure 4.17	Vertical beam size as a function of bending radius	128
Figure 4.18	Reflectivity of the design and a comparison to the design of the coronary angiography project in the NSLS	129
Figure 4.19	Phase space and energy space of the beam of our design compared to the phase space and energy space of the beam transmission in NSLS design	130
Figure 4.20	Energy resolution of the center ray that the NSLS design can achieved as a function of the distance from the detector to the crystal	131
Figure 4.21	Energy resolution as a function of the distance from the detector to the crystal	132
Figure A.1	Miller indices and d-spacing of crystal lattice plane.....	139
Figure A.2	Crystal lattice and the reciprocal lattice of a cubic crystal	141

Figure A.3	Reflectivity of Si(3,3,3) at 40keV and the definition of Darwin width.....	143
Figure A.4	The stereographic projection	145
Figure B.1	Image of the beam at different analyzer settings and the accordingly calculated refraction angle as a function of the beam width and its linear fitting when the tilt of the analyzer was set at 3.03mr	146
Figure B.2	Image of the beam at different analyzer settings and the accordingly calculated refraction angle as a function of the beam width and its linear fitting when there was no tilt of the analyzer	147
Figure B.3	Image of the beam at different analyzer settings and the accordingly calculated refraction angle as a function of the beam width and its linear fitting when the tilt of the analyzer was set at -3.03mr	147
Figure B.4	Image of the beam at different analyzer settings and the accordingly calculated refraction angle as a function of the beam width and its linear fitting when the tilt of the analyzer was set at -6.06mr	148
Figure B.5	Image of the beam at different analyzer settings and the accordingly calculated refraction angle as a function of the beam width and its linear fitting when the tilt of the analyzer was set at 0.606mr and the tilt of the 2 nd crystal of the monochromator was set at the 1 st tilt value	149
Figure B.6	Image of the beam at different analyzer settings and the accordingly calculated refraction angle as a function of the beam width and its linear fitting when the tilt of the analyzer was set at 0mr and the tilt of the 2 nd crystal of the monochromator was set at the 1 st tilt value	149
Figure B.7	Image of the beam at different analyzer settings and the accordingly calculated refraction angle as a function of the beam width and its linear fitting when the tilt of the analyzer was set at -0.606mr and the tilt of the 2 nd crystal of the monochromator was set at the 1 st tilt value	150
Figure B.8	Image of the beam at different analyzer settings and the accordingly calculated refraction angle as a function of the beam width and its linear fitting when the tilt of the analyzer was set at -1.212mr and the tilt of the 2 nd crystal of the monochromator was set at the 1 st tilt value	150
Figure B.9	Image of the beam at different analyzer settings and the accordingly	

	calculated refraction angle as a function of the beam width and its linear fitting when the tilt of the analyzer was set at -1.818mr and the tilt of the 2 nd crystal of the monochromator was set at the 1 st tilt value	151
Figure B.10	Image of the beam at different analyzer settings and the accordingly calculated refraction angle as a function of the beam width and its linear fitting when the tilt of the analyzer was set at -1.818mr and the tilt of the 2 nd crystal of the monochromator was set at the 2 nd tilt value	152
Figure B.11	Image of the beam at different analyzer settings and the accordingly calculated refraction angle as a function of the beam width and its linear fitting when the tilt of the analyzer was set at -0.606mr and the tilt of the 2 nd crystal of the monochromator was set at the 2 nd tilt value	152
Figure B.12	Image of the beam at different analyzer settings and the accordingly calculated refraction angle as a function of the beam width and its linear fitting when the tilt of the analyzer was set at 0mr and the tilt of the 2 nd crystal of the monochromator was set at the 2 nd tilt value	153
Figure B.13	Image of the beam at different analyzer settings and the accordingly calculated refraction angle as a function of the beam width and its linear fitting when the tilt of the analyzer was set at 0.606mr and the tilt of the 2 nd crystal of the monochromator was set at the 2 nd tilt value	153
Figure B.14	Image of the beam at different analyzer settings and the accordingly calculated refraction angle as a function of the beam width and its linear fitting when the tilt of the analyzer was set at 1.212mr and the tilt of the 2 nd crystal of the monochromator was set at the 2 nd tilt value	154
Figure B.15	Image of the beam at different analyzer settings and the accordingly calculated refraction angle as a function of the beam width and its linear fitting when the tilt of the analyzer was set at 1.818mr and the tilt of the 2 nd crystal of the monochromator was set at the 2 nd tilt value	154
Figure B.16	Image of the beam at different analyzer settings and the accordingly calculated refraction angle as a function of the beam width and its linear fitting when the tilt of the analyzer was set at 2.424mr and the tilt of the 2 nd crystal of the monochromator was set at the 2 nd tilt value	155

List of Tables

Table 2.1	Verification of the linear relationship between the angular shift of the rocking curve and the tilt error of the analyzer	30
Table 3.1	Iodine images obtained with different image sets and different projected iodine amount	72
Table 3.2	Theoretical and measured value of the projected iodine amount in mM-cm	73
Table 3.3	Measured signals from 8 image sets and their corresponding errors	73
Table 3.4	Measured SNRs of the projected iodine amount of the iodine image obtained with different number of image sets for 1 st object in the 3 rd experiment	75
Table 3.5	Theoretical SNRs with different projected iodine amount and the number of image sets for the 1 st object in the 3 rd experiment	76
Table 3.6	Measured SNRs of each projected iodine amount of each iodine image for the simulated rat head with iodine step wedge	93
Table 3.7	Theoretical SNRs of each projected iodine amount of each iodine image for the simulated rat head with iodine step wedge	94
Table 3.8	Measured SNRs of each projected iodine amount of the iodine image obtained with different number of channels of the fluorescence detector for the simulated rat head with iodine step wedge	97
Table 3.9	Comparison of KES and FSI	100
Table 4.1	Minimum asymmetry angles achieved in widely available silicon wafers and their corresponding lattice plane directions	125

List of Abbreviations

ABI	Analyzer based Imaging
BL	BeamLine
BM	Bending Magnet
BMIT-BM	BioMedical Imaging and Therapy Bending Magnet beamline
CCD	Charge-Coupled Device
CLS	Canadian Light Source
DEI	Diffraction Enhanced Imaging
DNA	DeoxyriboNucleic Acid
DXAS	energy Dispersive X-ray Absorption Spectroscopy
EBCT	Electron Beam Computed Tomography
EH	Experimental Hutch
FSI	Fluorescence Subtraction Imaging
FWHM	Full Width Half Maximum
GEMS	Gene Expression Mapping using Synchrotron light
GFP	Green Fluorescent Protein
HXMA	Hard X-ray Micro-Analysis beamline
IC	Ion Chamber
KES	K-Edge Subtraction imaging
MIR	Multi-Image Radiography
MRI	Magnetic Resonance Imaging
MSCT	Multi-Slice Computed Tomography
NIS	Sodium Iodide Symporter
NSLS	National Synchrotron Light Source
RF	Radio Frequency
SNR	Signal to Noise Ratio
STL	Standard Tessellation Language
XRF	X-Ray Fluorescence imaging

Chapter 1

Synchrotron Based Biomedical Imaging Techniques: Some Basics

Over the past two decades, biomedical imaging techniques based on synchrotron light have developed rapidly. Some of them were created because of synchrotron light, such as *Diffraction Enhanced Imaging (DEI)*. And now DEI is in its trial to be used clinically [1]. Some of them were developed using x-ray source and now benefit from the properties of the synchrotron light, such as *K-Edge Subtraction (KES)* imaging. In this chapter, the properties of the synchrotron light are introduced and three main synchrotron based biomedical imaging techniques are reviewed. Also, the outline of the thesis is given in the last section.

1.1 Properties of the Synchrotron Light

The synchrotron radiation was first produced in 1947 by General Electric and now there are over 50 synchrotron radiation sources world wide because of its significant properties over the conventional x-ray sources.

Generally speaking, synchrotron radiation is the electromagnetic radiation emitted as charged particles (electron or positrons) change direction while passing through electromagnets. As shown in Fig. 1.1, a synchrotron facility is typically composed of injector, storage ring, *Bending Magnets (BM)*, insertion devices (undulators and wigglers), *Radio Frequency (RF)* cavity, *BeamLines (BL)*, and *Experimental Hutches (EH)*. The storage ring is composed of many straight sections which are connected by the bending magnets. Undulators and wigglers may be inserted into the straight sections of the storage ring. The electrons are sent into the storage ring by the injector and circulate there for many hours at very high speed (near the speed of light). The bending magnets keep electrons circulating within the storage ring. When the circulated electrons pass through the bending magnets and insertion devices, electromagnetic waves are emitted, which is also called synchrotron light. RF cavities compensate the energy of the

electrons which is lost during the radiation emission. The emitted synchrotron light is collected and channeled into experimental hutches by beamlines.

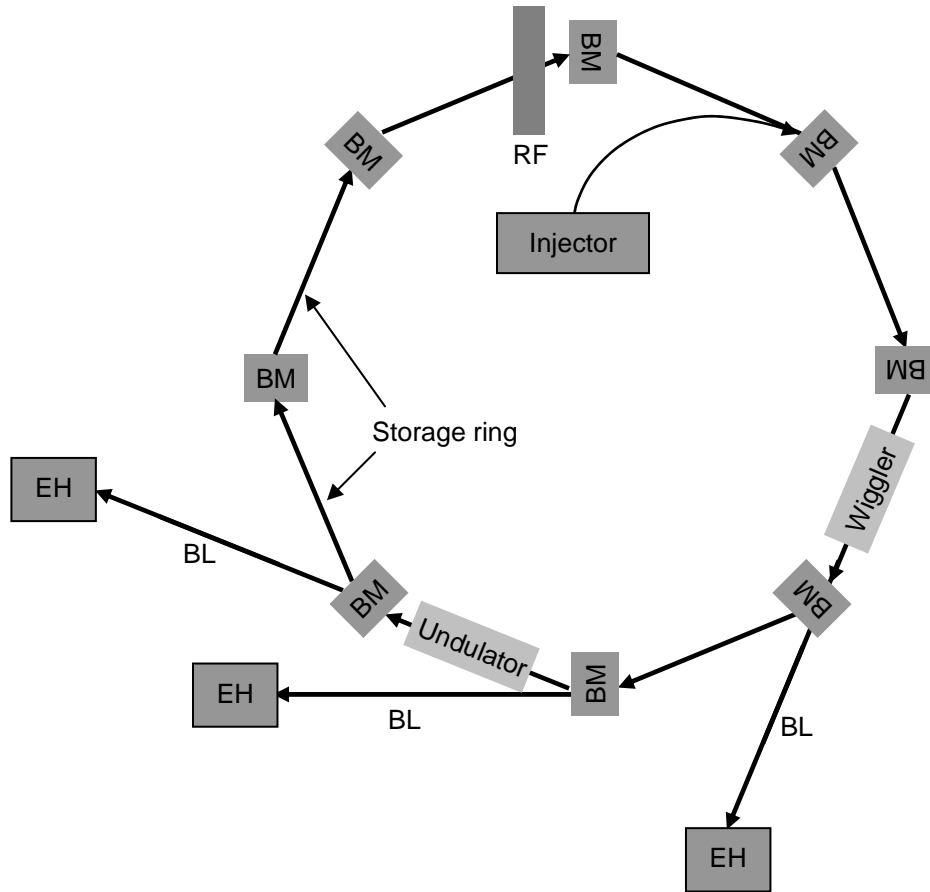


Figure 1.1 Structure of a synchrotron facility. A synchrotron facility is typically composed of injector, storage ring, bending magnets (BM), insertion devices (undulators and wigglers), radio frequency (RF) cavity, beamlines (BL), and experimental hutches (EH).

Since the traveling electrons are at or near the speed of light, the radiation produced has broad and continuous energy (wavelength) spectrum which extends from infrared to hard x-ray region. So the energy of the radiation is tunable according to the application. The intensity of the radiation is very high, 5 to 6 orders of magnitude higher than that of a laboratory source. The source of the radiation is very small, a few microns, and the emitted radiation is extremely collimated. The radiation is plane (linearly) polarized in the plane of the storage ring and elliptically polarized out of this plane. The radiation has

a pulsed structure with a pulse duration in the nanosecond range or less and a dead time in the RF range (microsecond).

The combinations of these properties make synchrotron radiation a unique and powerful tool for a wide range of scientific and technical applications.

1.2 Synchrotron Based Biomedical Imaging Techniques

Three main biomedical imaging techniques are introduced in this part of the chapter. They are DEI and *Multi-Image Radiography (MIR)*, KES, and *X-Ray Fluorescence (XRF)* imaging.

1.2.1 Diffraction Enhanced Imaging and Multi-Image Radiography

DEI [2] is a phase sensitive x-ray imaging method to measure an object's x-ray transmission based on a highly collimated imaging beam which is prepared by a perfect crystal monochromator at the synchrotron facility. DEI employs a crystal as analyzer which is positioned between the object and the detector. Normally, the analyzer is the same type crystal as the double-crystal monochromator and positioned at the same orientation. The transmitted beam of the object is reflected more or less by the analyzer according to the beam's incident angle. The scatter with big angular change in the direction of the transmitted beam is rejected by the analyzer because the angular width of the accepted beam normally is within several micro-radians or tens of micro-radians. The small angular change (several micro-radians) in the beam, which carries the refractive information of the object, is converted into huge intensity change (several percent of the beam intensity per micro-radian) which can be recorded by the detector. With DEI, both absorption and refraction properties of the object can be revealed with the rejection of the scattering.

MIR [3,4], as an extension of DEI, takes several images along the crystal rocking curve instead of 2 images on the waist of the rocking curve in DEI so that the subtle features of the actual rocking curve can be used to distill parametric images.

With the implementation of DEI and MIR in the 3rd generation synchrotron facilities [5-8], they have shown great potential in conveying information about subtle density and structural differences in soft tissues. Many morphological features in soft tissues that are

difficult or impossible to see in clinical radiography can be detected using DEI and MIR [9-11]. DEI and MIR have been applied successfully to image breast tissue [11-14], articular cartilage [15-19], vertebral column [20], eye [21], soft tissue of the foot and ankle [22], etc.

1.2.2 K-Edge Subtraction Imaging

KES, which is also called dichromography or dual energy subtraction imaging, is a non-invasive imaging technique to detect dilute contrast agent in the object. It utilizes the discontinuity in the x-ray absorption across the absorption edge, especially K-edge, of the selected contrast agent. Normally two images are acquired at energies bracketing the K-edge of the element; one is taken at the energy just above the absorption edge and the other one is taken just below the edge. The logarithmic subtraction of these two images creates an image of the projected density of a contrast agent or trace element with enhanced element contrast and free of the structural or anatomical information.

This imaging idea was first proposed by Jacobson in 1953 [23]. However, the intensity of the monochromatic x-ray beam produced by filtering the spectrum of the conventional x-ray source was not sufficient to make this technique work. So this technique was not useful until the advent of synchrotron radiation which makes it possible to create very intense monochromatic x-ray beams [24]. Work on intravenous coronary angiography with synchrotron radiation can be traced back to 1979 at the *Stanford Synchrotron Radiation Laboratory (SSRL)*, Stanford, USA. Since then KES has been proved powerful in coronary angiography [25-27], cerebral angiography [28], neurovascular intravenous angiography [29], bronchography [30], lung imaging [31,32], mammography [33], lymphatic imaging [34], and brain tumor imaging [35]. Dix has demonstrated that synchrotron KES method has satisfactory sensitivity and very high specificity for severe stenoses and it is over *Magnetic Resonance Imaging (MRI)*, *Electron Beam Computed Tomography (EBCT)*, and *Multi-Slice Computed Tomography (MSCT)* [36]. The computed tomography mode of KES has been developed since 1984 [37].

In biomedical imaging, to keep the surface dose within an acceptable range, the beam energy has to be higher than 30keV, so does the k-edge of the contrast agent. The

atomic number of the elements has to be above 50 to be suitable for this technique [38]. The normally used contrast agents for KES experiments are iodine (atomic number 53) for angiography, mammography, and lymphatic imaging, xenon (atomic number 54) for bronchography and lung imaging, and colloidal gold (atomic number 79) for brain tumor imaging.

The energy of the x-ray beam can be tuned by a monochromator at a synchrotron facility. A monochromator is composed of two crystals either in Bragg geometry or in Laue geometry and has a single unfocused energy beam as its output. In this case, the high and low energy images are acquired separately by switching energies of the beam with an area detector. Some monochromators can produce two monochromatic and focused beams with energy bracketing the K-edge of the selected contrast element. In this case, the high and low energy images are acquired simultaneously with a two-line detector. Also there are some other modes to acquire KES images. If an energy sensitive photon counting detector is used, simultaneous acquisition of KES images is allowed by setting an electronic threshold near the middle of the x-ray spectrum discriminates between high- and low-energy photons [33]. If a contrast agent filter is used, a mixed-energy x-ray image (both high and low energy) is taken without the filter and a low energy image is obtained with the filter blocking the high energy component of the x-ray. The high energy image is obtained by subtracting the low energy image from the mixed-energy image [39].

The sensitivity of KES is directly related to the beam intensity. As low as $1\text{mg}/\text{cm}^2$ ($7.87\text{mM}\cdot\text{cm}$, $1\text{mM}=0.127\text{mg}/\text{cm}^3$) projected iodine amount is reported visible with sufficient beam intensity (up to 3×10^{11} photons $\text{mm}^{-2} \text{s}^{-1}$) [26].

1.2.3 X-Ray Fluorescence Imaging

The use of the fluorescence radiation excited by a primary x-ray beam from the sample to perform elemental analysis was first proposed by Glocker and Schreiber in 1928 [40]. With x-ray microprobe, the role of the trace elements in the living matter would be revealed since the distribution and the identification of the trace elements indicates the function of the detected elements [41]. Due to the advent of synchrotron radiation and its rapid development, as well as the increasing availability of the micro-

focusing optical elements and sophisticated x-ray detectors, the scan can be conducted in two and three dimensions and the beam size can be in a nanometer range [42-44]. The fluorescent x-rays that escape the sample are detected by an energy-sensitive solid-state detector. The detection limit of the XRF can be as low as $3 \times 10^{-3} \mu\text{g}/\text{cm}^2$ for the K-edge emission line with thin samples which corresponds to absolute detect ability of $3 \times 10^{-12} \text{ g}$ [45].

XRF analyses can be done non-invasively on a wide range of sample types, rock fragments, powders, soils, and biological materials; samples can be in solution, liquids, amorphous solids, aggregates, plant roots, and surfaces [46]. XRF has become extremely powerful tools for in vivo measurement of the element's concentration and distribution in biological sample, such as iodine in the thyroid gland [47,48], uranium[49], strontium [50,51], and lead [52,53] in bone, cadmium [54,55] and mercury [56] in kidneys. It is also widely used to measure iron, zinc, copper, nickel, and arsenic [57,58].

1.3 Motivation and Outline of the Thesis

The development of a non-invasive method of visualizing gene expression in larger animals could revolutionize some aspects of gene research by opening up a wider variety of animal systems to explore; some of which may be better models of human systems. Presently, most gene expression studies employ *Green Fluorescent Protein (GFP)* transfected into the genome of the animal system. For larger animals, an “x-ray” equivalent of GFP would be desirable due to the high penetrating power of x-rays. A model gene modification system is to use the *Sodium (Na) Iodide Symporter (NIS)* which will cause the accumulation of iodine in cells which express the NIS. To non-invasively observe the dilute iodine accumulated by the cancer cells transfected with NIS in the head of small animals, such as a rat, two synchrotron-based imaging methods were studied, *K-Edge Subtraction (KES)* imaging and *Fluorescence Subtraction Imaging (FSI)*, as a main line of the thesis.

KES needs wide monochromatic x-ray beams at two energies bracketing the K-edge of the contrast agent existing or injected in the tissues. The monochromatic beam in the synchrotron facility normally is prepared by a double crystal monochromator. The appearance of the azimuthal angle (tilt error) in the double crystal monochromator creates

intensity variations across the imaging field. Chapter 2 addresses this tilt error, discusses the origin and appearance of the error and gives methods to correct for the error if present in DEI and MIR imaging. Meanwhile, the relationship among the tilt errors of different crystals in the imaging system is presented and verified by the experiments. Also some recommendations are given on the settings of the experimental parameters so that the images taken with this error can be corrected. The work described in Chapter 2 has been published:

H. Zhang, D. Chapman, Z. Zhong, C. Parham, M. Gupta, Crystal tilt error and its correction in diffraction enhanced imaging system, *Nuclear Instruments and Methods in Physics Research A* 572 (2007) 961–970

In Chapter 3, KES is compared to *Fluorescence Subtraction Imaging (FSI)*, an extension imaging method of XRF, by a series of experiments with gradual improvements of the imaging systems. A new parameter, quality factor, is developed to facilitate the comparison. These two imaging techniques can be used complementarily. KES can be used first to locate the area of interest due to its short imaging time and large imaging area. FSI can be used to focus only on the area of interest due to its high *Signal to Noise Ratio (SNR)* for the dilute sample. The work described in Chapter 3 has been published:

H. Zhang, Y. Zhu, B. Bewer, L. Zhang, G. Korbas, I. Pickering, G. George, M. Gupta, and D. Chapman, Comparison of iodine K-edge subtraction and fluorescence subtraction imaging in an animal system, *Nuclear Instruments and Methods in Physics Research A* 594 (2008) 283-291

Chapter 4 designs a bent Laue monochromator to do simultaneous KES to further improve the performance of the KES imaging for small animals, such as a rat. The conceptual design of the monochromator shows that a very small (several microns) focal spot can be achieved by small (several degree) asymmetry cut of the crystal which make it possible to have the geometrical focus and monochromatic focus of the beam positioned at the same point. Good energy resolution (several eV) is also achieved in the design. The conceptual design has been presented on the Fifteenth Pan-American Synchrotron Radiation Instrumentation in 2008. This work will be published when experimental results have been obtained.

Chapter 5 summarizes the main contributions of the thesis and discusses the possible research in the future.

Chapter 2

Crystal Tilt Error and its Correction

To prepare beam with consistent intensity along the beam width by double crystal monochromator for KES imaging, a misalignment of the crystals is studied through *Diffraction Enhanced Imaging (DEI)* and *Multi-Image Radiography (MIR)* imaging techniques. DEI and MIR employ a third crystal, analyzer, to transfer the small angular change (several micro-radians) in the transmitted beam into the huge intensity change (several percent of the beam intensity per micro-radian). The intensity change, including that caused by system errors, recorded by the detector is interpreted into object properties. So the errors in the system alignment will lead to some misunderstanding of the image and so the object. In this chapter, this misalignment of the crystals is investigated in detail, from its definition to its correction, and the restoration of the images taken with this misalignment. Although practical techniques exist to align crystals, no analytic expressions have been previously developed to describe the effects of this misalignment to the images, to the interpretation from original images to the object properties. And the recommendation is also firstly given to guide the experimental settings to avoid the artifacts shown in the resulting parametric images in DEI and MIR caused by this misalignment.

2.1 Introduction

Different from the conventional x-ray imaging, which records the attenuation property of the object, DEI and MIR detect the absorption, refraction, and even scatter properties of the object through an analyzer. The experimental setup of DEI and MIR is shown in Fig. 2.1. A fan shaped, synchrotron-generated x-ray beam is firstly incident on the monochromator, and then the monochromatic beam goes through the object. The transmitted beam is selectively reflected by the crystal analyzer and finally reaches the detector. In the experiment, the object and the detector are in line scan mode to have an area image. This experimental setup is also commonly referred to as *Analyzer Based Imaging (ABI)* [59]. In the following description, the imaging system is referred to as a

DEI system. In the commonly used DEI system, there are three crystals that have the same type of diffraction plane and all of them are set at their Bragg angle; the first two as a monochromator, the third one as an analyzer. The crystal analyzer is positioned between the object and the detector. The angle of the analyzer can be changed relative to the monochromator crystals. The angular yield function of the analyzer is described by rocking curve which is calculated by the convolution of the reflectivity of the monochromator and the reflectivity of the analyzer (Appendix A.3).

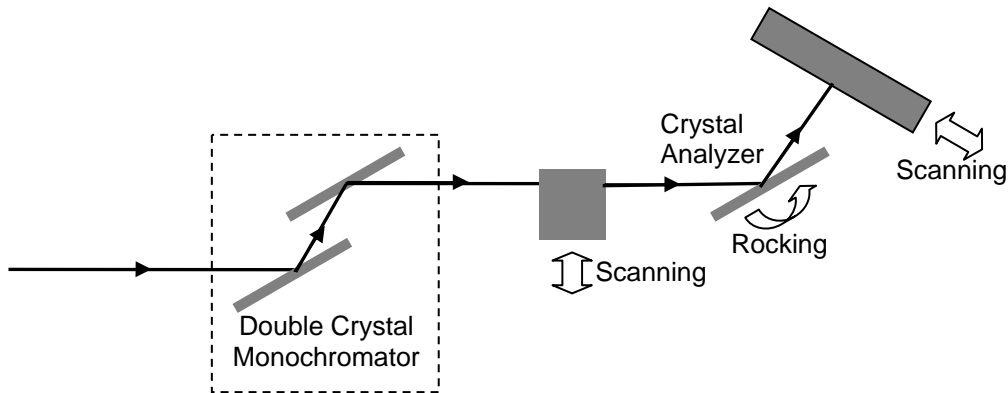


Figure 2.1 Synchrotron DEI/MIR experimental setup. A fan shaped, synchrotron-generated x-ray beam is firstly incident on the monochromator, and then the monochromatic beam goes through the object. The transmitted beam is selectively reflected by the crystal analyzer and finally reaches the detector.

Figure 2.2 shows the calculation of the reflectivity of the monochromator for Si(3, 3, 3) (Appendix A.1) at 40keV. Figure 2.3 shows the calculation of the rocking curve of the analyzer which is also Si(3, 3, 3) with the same monochromator at 40keV. As shown in Fig. 2.3, the rocking curve describes how the reflectivity of the analyzer responds to small variations, of the order of micro-radians (μr), in the directionality of the transmitted beam through an object. It transfers these small variations in the directionality of the transmitted beam into large intensity changes which results in image contrast. For example, a direction change of $0.1 \mu\text{r}$ at 40 keV using a Si(3,3,3) crystal set results in an approximate intensity change of 7%. This contrast conveys the refraction and extinction or ultra small angle x-ray scattering information of the object.

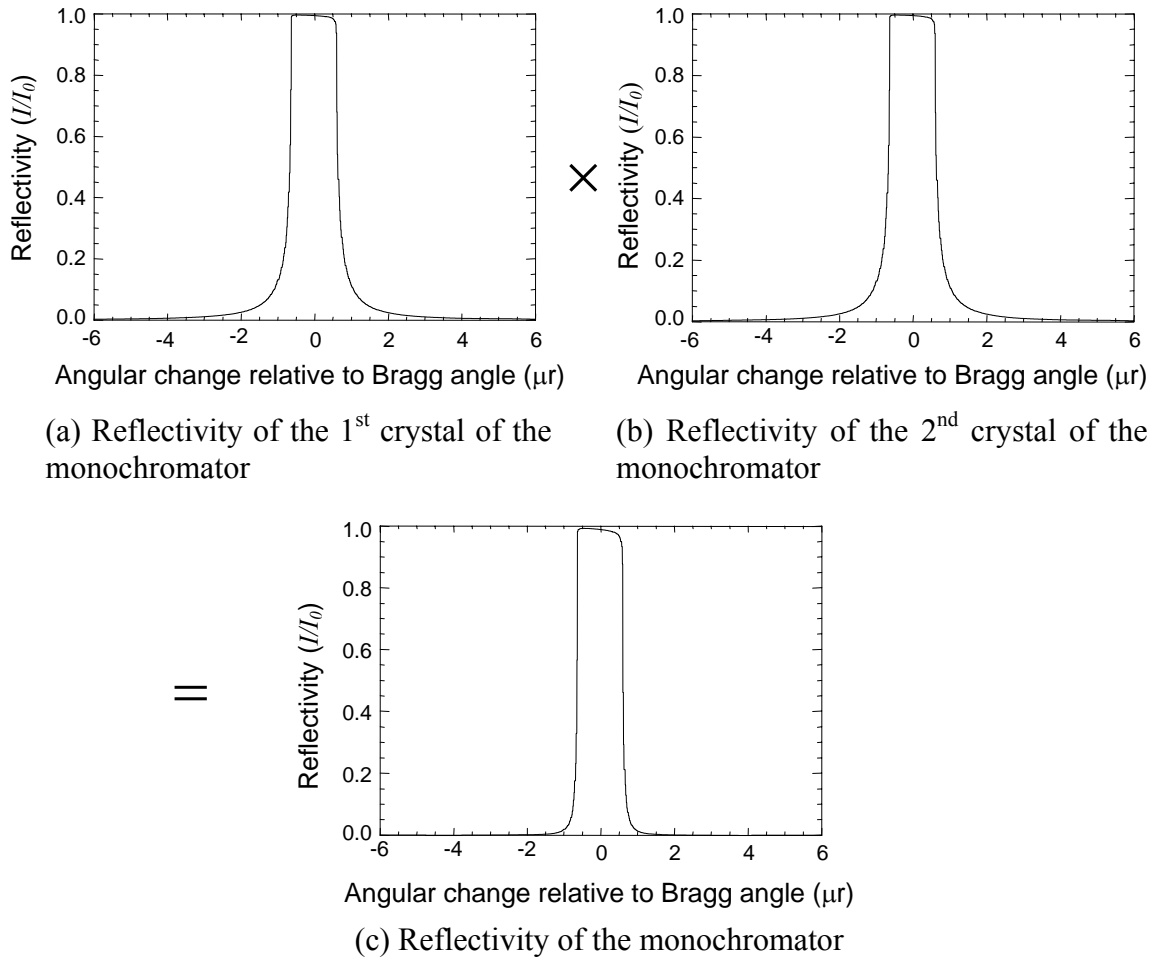


Figure 2.2 Calculation of the reflectivity of the monochromator for Si(3,3,3) at 40keV

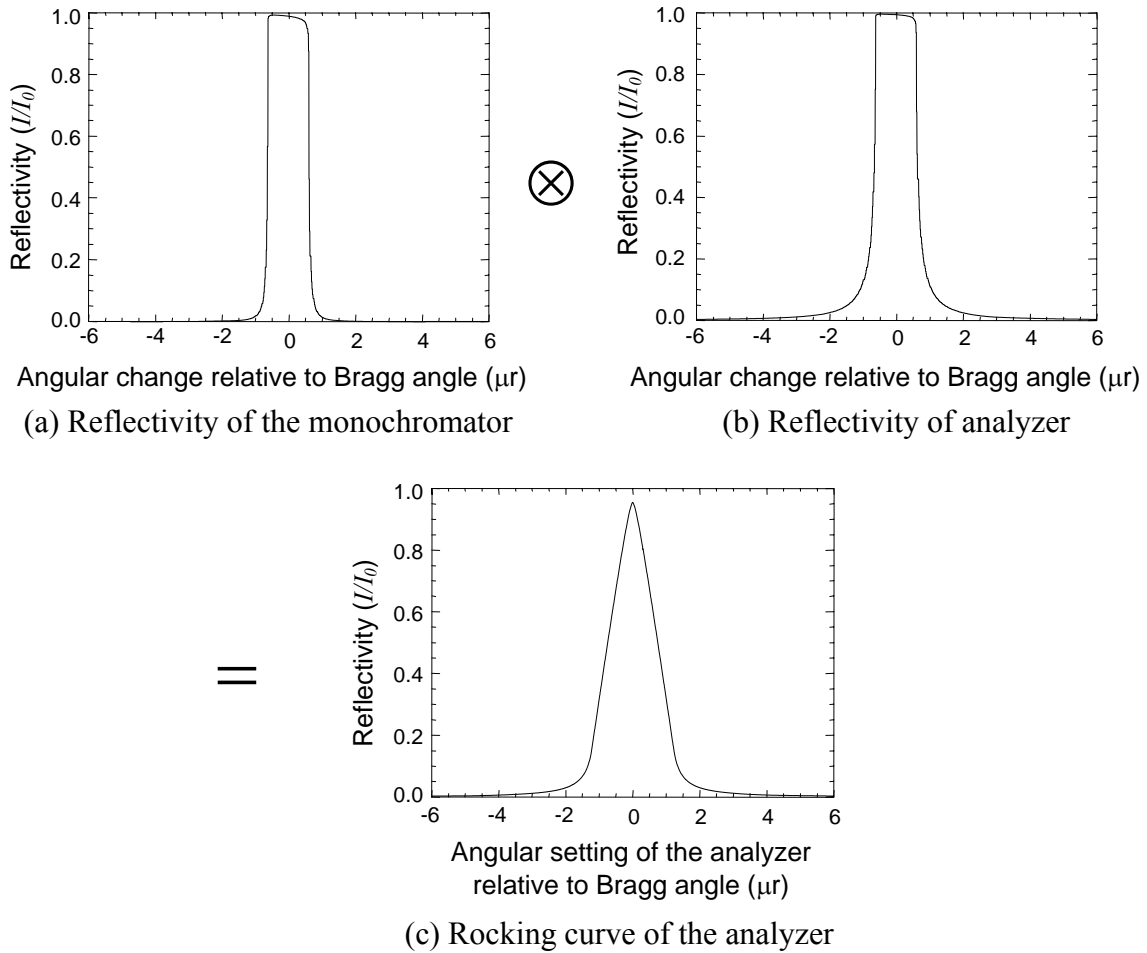


Figure 2.3 Calculation of the intrinsic rocking curve of the analyzer for Si(3,3,3) at 40keV

Obviously, the angular sensitivity of the DEI system depends on the local slope of the rocking curve which is determined by the angular width of the analyzer's rocking curve and the position on the rocking curve to which the analyzer is tuned. The angular width of the rocking curve further depends on the beam energy and the type of the diffraction plane of the crystal. Figure 2.4(a) shows the energy dependence of the rocking curve. The higher the energies of the incident beam, the narrower the rocking curves. Figure 2.4(b) shows the d-spacing dependence of the rocking curve. The concept of d-spacing can be referred to Appendix A.1. The width of the rocking curve decreases when the d-spacing of the crystal increases. Since the presence of the object will change the shape of the rocking curve, the measured rocking curve when no object presents is called intrinsic rocking curve.

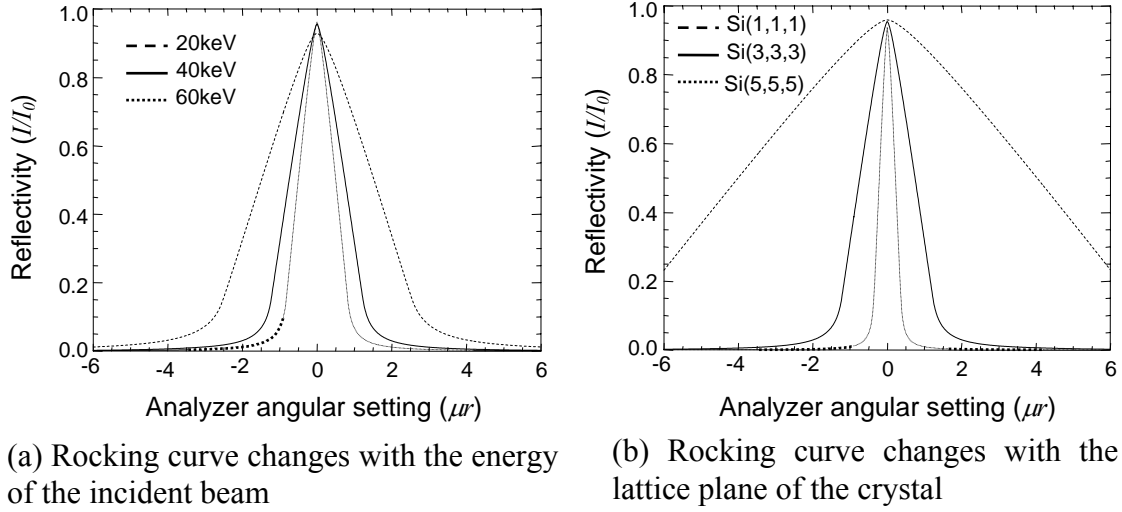


Figure 2.4 Rocking curve dependence on the energy of the incident beam and the lattice plane of the crystal

In DEI, two images of the object are acquired at the waist of the rocking curve as shown in Fig. 2.5; one is taken on the low angle side of the rocking curve (θ_L) and the other is taken on the high angle side (θ_H). The object in the images is a Lucite sphere. In these two images, the same angular change in the transmitted beam caused by the refraction of the object shows two reversed intensity changes because the sign of the slope of the rocking curve changes. These two images can be described as low angular setting image (I_L) and high angular setting image (I_H).

$$\begin{cases} I_L = I_R \left(R(\theta_L) + \left. \frac{dR}{d\theta} \right|_{\theta=\theta_L} \Delta\theta_Z \right) \\ I_H = I_R \left(R(\theta_H) + \left. \frac{dR}{d\theta} \right|_{\theta=\theta_H} \Delta\theta_Z \right) \end{cases} \quad (2.1)$$

where I_R is the apparent absorption property of the object (including scattering), R is the rocking curve of the analyzer which describes the reflectivity of the analyzer as a function of the analyzer angular settings, $R(\theta_L)$ and $R(\theta_H)$ are the reflectivity of the analyzer when the analyzer is set at the low angle side and at the high angle side respectively, and $\Delta\theta_Z$ is the deflected angle of the transmitted ray in the plane of the diffraction which carries the refraction property of the object.

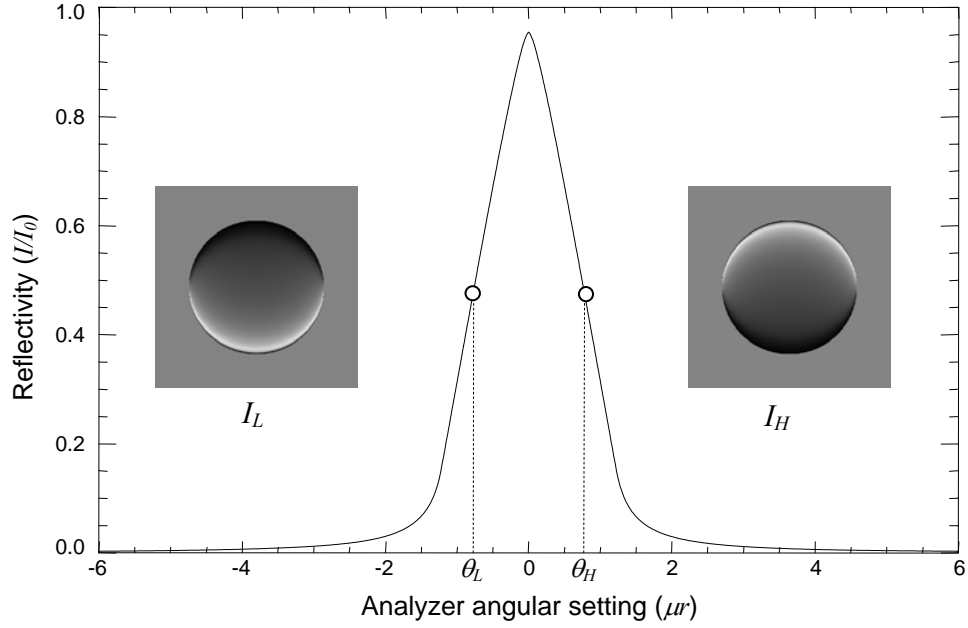


Figure 2.5 Rocking curve of Si(3, 3, 3) at 40keV and DEI images of a Lucite sphere taken at analyzer settings of $-0.78\mu r$ and $0.78\mu r$ relative to its Bragg angle

From these two images and a linear approximation of the rocking curve, the apparent absorption I_R and refraction $\Delta\theta_Z$ information of the object can be obtained by Eq. 2.2 from Eq. 2.1.

$$\begin{cases} I_R = \frac{I_L \left. \frac{dR}{d\theta} \right|_{\theta=\theta_H} - I_H \left. \frac{dR}{d\theta} \right|_{\theta=\theta_L}}{R(\theta_L) \left. \frac{dR}{d\theta} \right|_{\theta=\theta_H} - R(\theta_H) \left. \frac{dR}{d\theta} \right|_{\theta=\theta_L}} \\ \Delta\theta_Z = \frac{I_H R(\theta_L) - I_L R(\theta_H)}{I_L \left. \frac{dR}{d\theta} \right|_{\theta=\theta_H} - I_H \left. \frac{dR}{d\theta} \right|_{\theta=\theta_L}} \end{cases} \quad (2.2)$$

The linear approximation of the rocking curve limits the application of DEI method. If the refraction angle of the ray is big enough to be out of the linear range of the rocking curve, DEI method delivers wrong information of the object which can be observed in the apparent absorption image from DEI in Fig. 2.6. The upper and lower edges of the sphere shown in the image had high absorption because of the big refraction angle in the beam. The parametric images from DEI method in Fig. 2.6, apparent absorption image and refraction image, are obtained by Eq. 2.2.

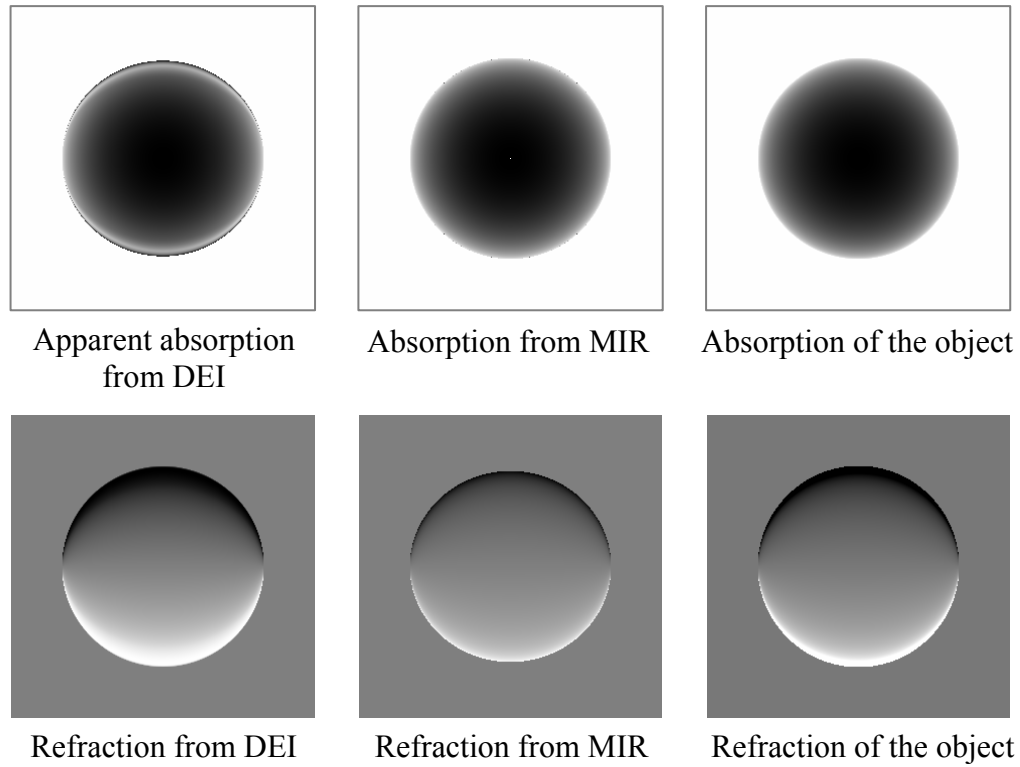


Figure 2.6 The absorption and refraction images of the Lucite sphere from the DEI method, MIR method and the real absorption and refraction properties of the object

To overcome this limitation, MIR [4] was developed. MIR takes multiple images with different analyzer settings along the rocking curve. Figure 2.7 shows 9 images taken at analyzer angular settings of -3mr , -2mr , -1mr , -0.5mr , 0mr , 0.5mr , 1mr , 2mr , 3mr respectively. Normally, the measured rocking curve at the specific point is fitted by Gaussian or Lorentzian function. Figure 2.7 also shows the fitted rocking curve (dashed curve) by Lorentzian function (Eq. 2.3) compared to the original rocking curve (solid curve).

$$f(x; a_1, a_2, a_3, a_4) = a_1 + \frac{a_2}{\left\{1 + \left[\frac{(x - a_3)}{a_4}\right]^2\right\}^3} \quad (2.3)$$

where x is the analyzer angular settings relative to its Bragg angle, a_1 , a_2 , a_3 , a_4 are four parameters to be determined by some optimal estimation method, such as linear least squares.

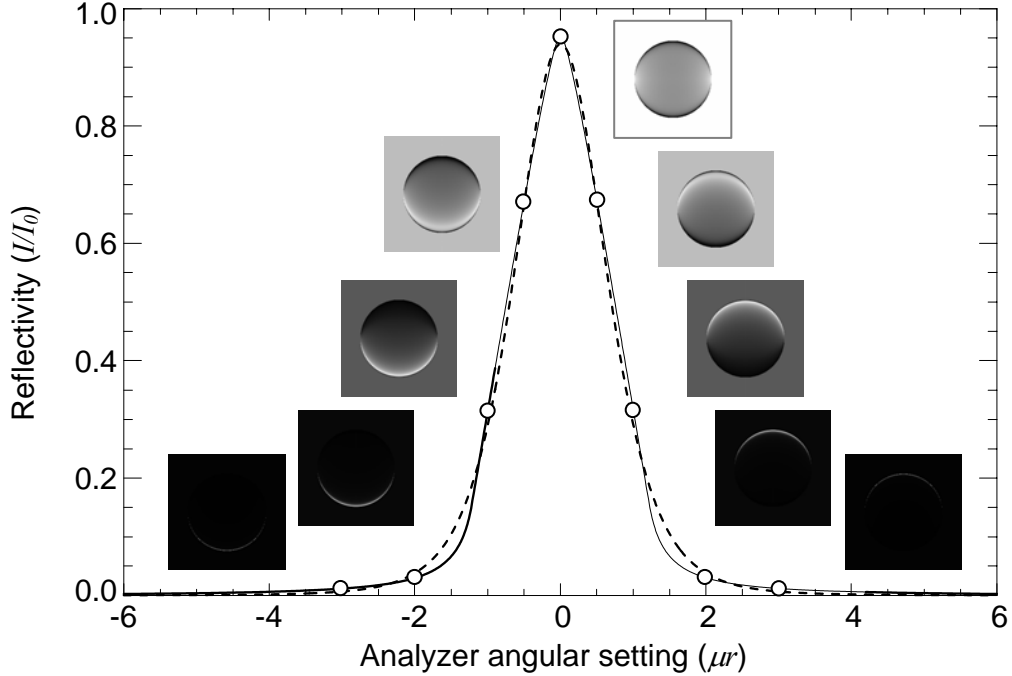


Figure 2.7 Rocking curve (solid line) of Si(3, 3, 3) at 40keV, its Lorentzian fit (dashed line) and MIR images taken at analyzer settings of $-3\mu r$, $-2\mu r$, $-1\mu r$, $-0.5\mu r$, $0\mu r$, $0.5\mu r$, $1\mu r$, $2\mu r$, and $3\mu r$ from left to right

The parametric images of MIR, absorption image, refraction image, extinction image, and scatter width image, are derived by the comparison of the intrinsic rocking curve and the rocking curve measured at the specific point of the object (pixel) as shown in Fig. 2.8 [60]. Since integrating the rocking curve over all settings of the analyzer yields a quantity related only to the total absorption, the absorption image is obtained by the area under the intrinsic rocking curve (A_I) and the area under the measured curve of the pixel (A_M) as shown in Fig. 2.8(a). The angular shift of the beam centroid is only due to the refraction phenomena when the beam passes through the object, so the mapping of the angular shift as an image is the refraction image (Fig. 2.8(b)). As shown in Fig. 2.8(c), the extinction parameter is determined by using the absorption parameter because the intensity at the measured peak (P_M) can be approximated by the intensity loss to the absorption and the extinction ($P_M = P_I e^{-\mu t} e^{-\chi t}$) (At the right Bragg angle setting of the analyzer, the measured intensity of the transmitted x-ray is almost free of scattering). The amount of angular broadening of the beam that represents the scattering is found by determining the difference between the *Full Width Half Maximum (FWHM)* of the curves as shown in Fig. 2.8(d) which defines the scatter width parameter.

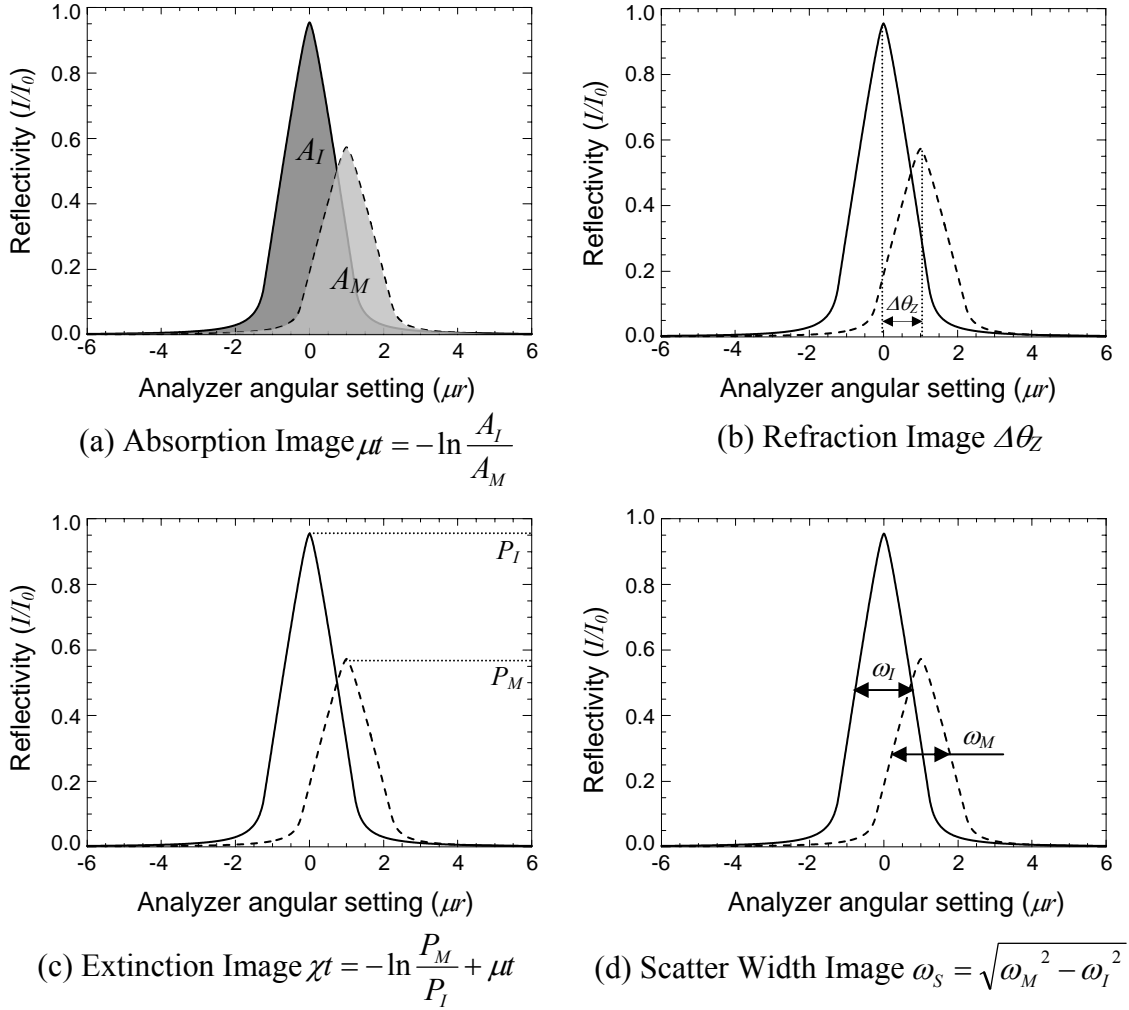


Figure 2.8 Distillation of MIR parametric images, absorption image, refraction image, extinction image, and scatter width image

The absorption image and refraction image distilled from original MIR images in Fig. 2.7 are also shown in Fig. 2.6 to compare to the parametric images from DEI method and the real absorption and refraction properties of the object.

In conclusion, the interpretation of DEI and MIR images is made by a comparison between the rocking curves measured with the object and the intrinsic rocking curve, which is acquired in an area where no structured object is present.

2.2 Tilt Error

The high sensitivity of the DEI and MIR methods requires accurate alignment of the crystals in their experimental setup. To understand the impact of a crystal misalignment, the Bragg's law and some geometry definitions of the crystal are introduced first.

Figure 2.9 shows the definitions of the Bragg angle θ_B , the tilt angle χ and the diffraction plane of the crystal for the incident x-ray beam. A coordinate system for the Bragg crystal is defined in Fig. 2.9(a). The incident x-ray is transmitted in XOY plane and X-axis is in the plane of the surface of the crystal. XOY plane is called the diffraction plane and the Bragg angle θ_B is defined in this plane as shown in Fig. 2.9(b). Z-axis is perpendicular to the diffraction plane and the azimuthal tilt angle χ is defined in YOZ plane as shown in Fig. 2.9(c). When the wavelength of the incident ray λ satisfies the Bragg's law in the diffraction plane of the crystal which is shown as Eq. 2.4, the ray is diffracted by the crystal.

$$\lambda = 2d_{hkl} \sin \theta_B \quad (2.4)$$

where d_{hkl} is the d-spacing of the crystal.

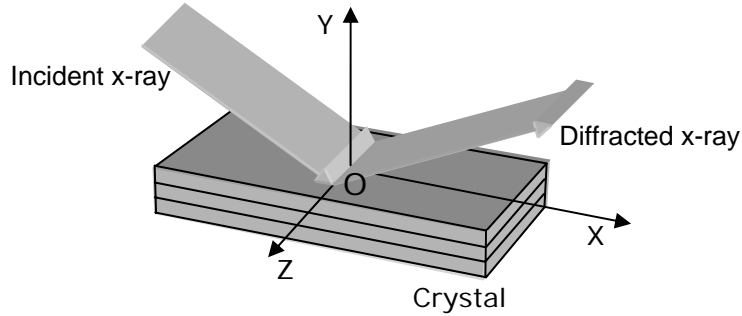
The Bragg angle θ_B can also be obtained by the inner product of the reciprocal lattice vector \vec{G} of the crystal (Appendix A.2) and the incident wave vector \vec{k} , $|\vec{k}| = 1/\lambda$.

$$\sin \theta_B = -\frac{\vec{k} \cdot \vec{G}}{|\vec{k}| |\vec{G}|} \quad (2.5)$$

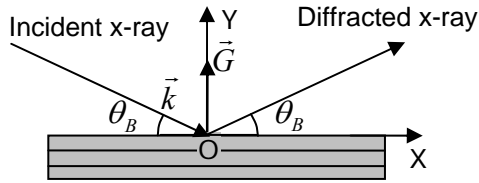
As shown in Fig. 2.9(b), the reciprocal lattice vector \vec{G} is perpendicular to the lattice plane of the crystal and its amplitude is defined by $|\vec{G}| = 1/d_{hkl}$.

The rocking curve calculation introduced before is based on the exact alignment of the Bragg angle of the monochromator crystals and the analyzer crystal. Any misalignment will cause a change in the reflectivity of the crystal. So in the experimental setup of DEI, it is essential to have the monochromator and analyzer crystals aligned at their Bragg angle around Z-axis (as shown in Fig. 2.9(b)). Also the crystal should be aligned around a perpendicular axis (X-axis as shown in Fig. 2.9(c) which is along the beam direction) in the plane of scattering (azimuthal tilt angle). Ideally, there should be no azimuthal tilt angle. However, it is difficult to be achieved and this angle will appear

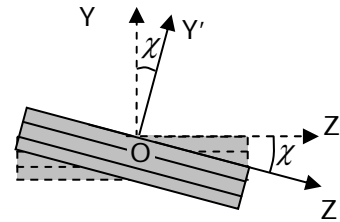
with time even in an accurate alignment due to thermal or mechanical drift. Thus the azimuthal tilt angle is referred to as tilt error.



(a) 3-D crystal and its lattice plane, incident and diffracted x-ray



(b) Diffraction plane XOY and the Bragg angle θ_B of the crystal and its incident and diffracted x-ray



(c) Tilt angle χ of the crystal defined in YOZ plane

Figure 2.9 Definitions of the Bragg angle θ_B , the azimuthal tilt angle χ , and the diffraction plane of the crystal.

Figure 2.10 shows how a fan beam from a point source is reflected by the crystal with a tilt error χ as would be the case in the DEI experimental setup in a synchrotron facility. A fan beam is used to cover the object in one dimension perpendicular to the median ray; the object is scanned in the other perpendicular direction to form a two dimensional projection image. The crystals are aligned at their Bragg angle θ_B corresponding to the median ray of the incident beam. This angle must be aligned with sub-microradian accuracy corresponding to the high angular sensitivity of DEI system. The diffraction plane is perpendicular to the crystal lattice plane XOZ and contains the source point, S. The presence of azimuthal tilt angle χ causes intensity variations in the image field, although it is somewhat less sensitive (in 10's of microradians). The following analysis is for a ray, SA, in the fan beam which has an opening angle β with the

median ray. $\Delta\beta$ is defined as the maximum angular range of the beam, $\Delta\beta = 2\beta_{\max}$, where β_{\max} is the maximum opening angle of the ray with respect to the median ray.

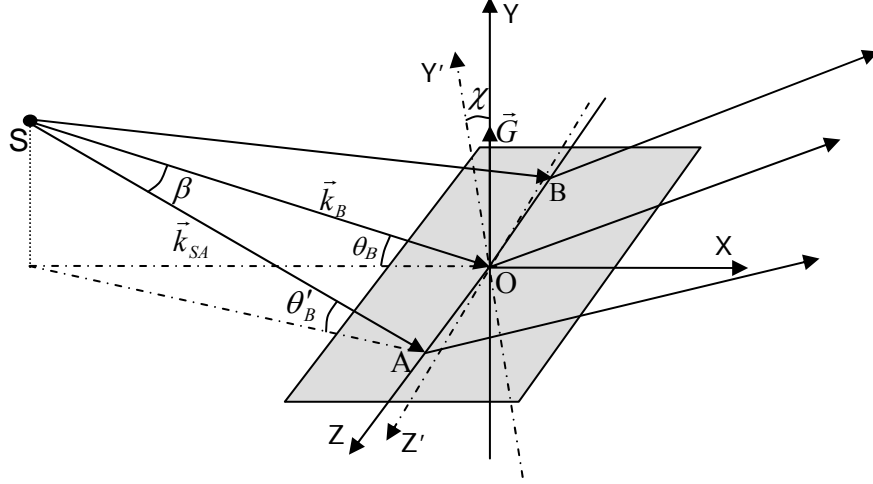


Figure 2.10 Illustration of a fan beam incident on the crystal with a tilt error χ . The coordinate system in this figure is the same as that in Fig. 2.9.

If there is a tilt χ_{m1} for the first crystal of the monochromator, the reciprocal lattice vector of this crystal \vec{G}_{m1} represented in the X, Y, and Z system of Fig. 2.10 is:

$$\vec{G}_{m1} = \frac{1}{d_{hkl}} \begin{bmatrix} 0 \\ \cos \chi_{m1} \\ \sin \chi_{m1} \end{bmatrix} \quad (2.6)$$

The wave vector \vec{k}_{SA} of the incident ray SA in the crystal coordinate system also as shown in Fig. 2.10 is:

$$\vec{k}_{SA} = \frac{1}{\lambda_{SA}} \begin{bmatrix} \cos \theta_B \cos \beta \\ -\sin \theta_B \cos \beta \\ \sin \beta \end{bmatrix} \quad (2.7)$$

Since the incident ray is polychromatic, the wavelength λ_{SA} is selected by the first crystal of the monochromator according to the incident angle on the crystal lattice plane of this ray. This incident angle will be referred to as $\theta_{\chi B}^\beta$. The wavelength, λ_{SA} , of this ray can be evaluated by the sine of this incident angle according to the Bragg's law.

$$\lambda_{SA} = 2d_{hkl} \sin \theta_{\chi B}^\beta \quad (2.8)$$

$$\sin \theta_{\chi_B}^\beta = -\frac{\vec{k}_{SA} \cdot \vec{G}_{m1}}{|\vec{k}_{SA}| |\vec{G}_{m1}|} = \sin \theta_B \cos \beta \cos \chi_{m1} - \sin \beta \sin \chi_{m1} \quad (2.9)$$

The 1st crystal of the monochromator selects the energy for the ray SA. The energy selection along Z' axis (from Fig. 2.10) is shown in Fig. 2.11 as a function of the opening angle β for tilt angles of 0 and $\pm 500 \mu r$ (0.0286°). In the calculation, the crystal is selected as a Si(3,3,3), and is aligned at its Bragg angle for 40keV.

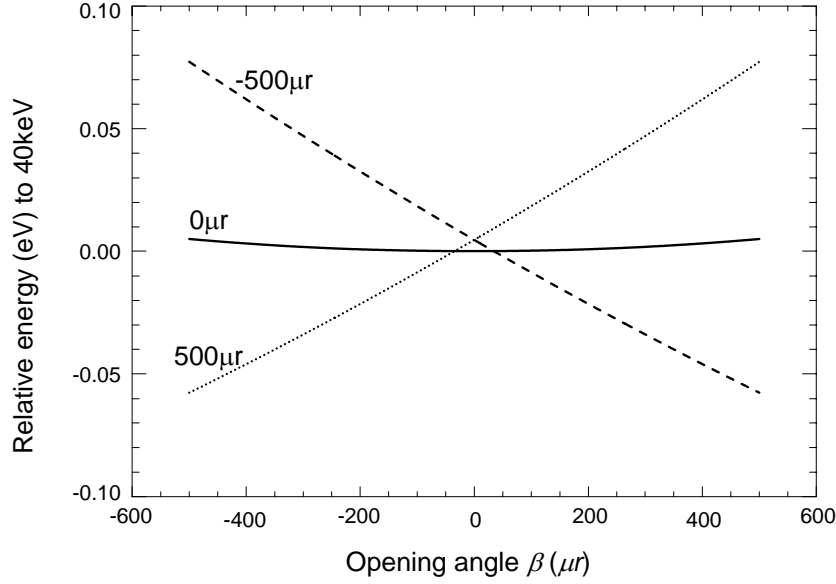


Figure 2.11 Energy selections across the fan beam of the first crystal of the monochromator in the cases of $-500 \mu r$, $0 \mu r$, and $500 \mu r$ tilt.

Figure 2.12 shows the reflectivity of the 1st crystal of the monochromator as a function of x-ray energy for the ray with an opening angle $500 \mu r$ at different tilt errors of 0 and $\pm 500 \mu r$.

The ray is reflected by the 1st crystal of the monochromator in its diffraction plane. So the wave vector of the reflected ray \vec{k}'_{SA} is:

$$\vec{k}'_{SA} = \frac{1}{\lambda_{SA}} \begin{bmatrix} \cos \theta_B \cos \beta \\ \cos 2\chi_{m1} \sin \theta_B \cos \beta - \sin 2\chi_{m1} \sin \beta \\ \sin 2\chi_{m1} \sin \theta_B \cos \beta + \cos 2\chi_{m1} \sin \beta \end{bmatrix} = \frac{1}{\lambda_{SA}} \begin{bmatrix} \cos \theta_B \cos \beta \\ Y_1 \\ Z_1 \end{bmatrix} \quad (2.10)$$

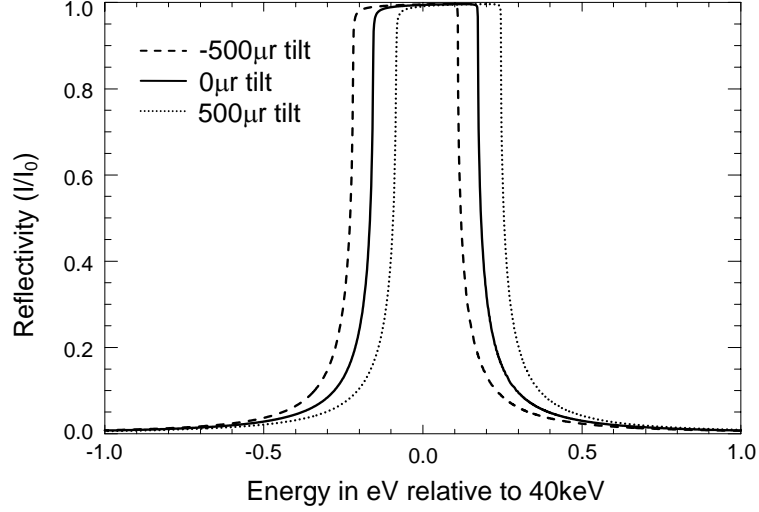


Figure 2.12 Reflectivity as a function of energy of the first crystal for the ray with a fan angle (b) of $500\mu r$, with crystal tilts of $-500\mu r$, $0\mu r$, and $500\mu r$, respectively

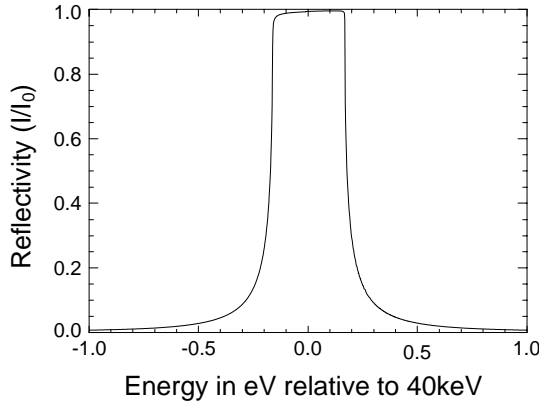
This ray is incident on the second crystal of the monochromator and reflected by this crystal in its diffraction plane. When there is a tilt error χ_{m2} in the 2nd crystal of the monochromator, the reciprocal lattice vector of this crystal, \vec{G}_{m2} , is:

$$\vec{G}_{m2} = \frac{1}{d_{hkl}} \begin{bmatrix} 0 \\ -\cos \chi_{m2} \\ -\sin \chi_{m2} \end{bmatrix} \quad (2.11)$$

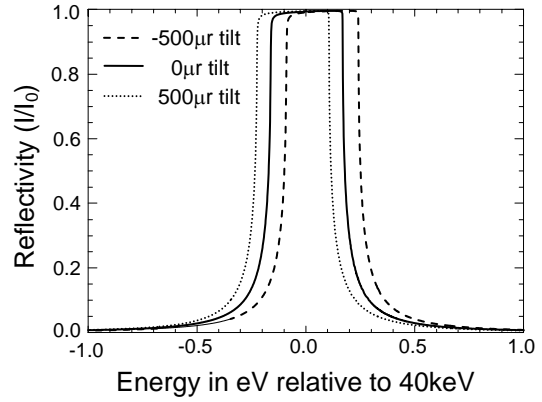
So the incident angle of the ray on the 2nd crystal of the monochromator θ_{m2} is:

$$\sin \theta_{m2} = -\frac{\vec{k}'_{SA} \cdot \vec{G}_{m2}}{|\vec{k}'_{SA}| |\vec{G}_{m2}|} = Y_1 \cos \chi_{m2} + Z_1 \sin \chi_{m2} \quad (2.12)$$

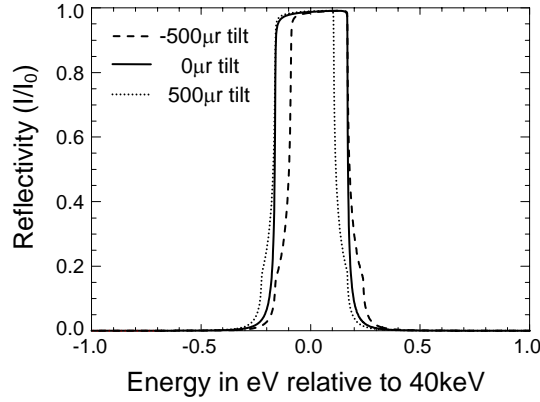
The incident angle on the crystal will deviate from the Bragg angle which is determined by the first crystal. This angular deviation will cause an energy shift of the reflectivity of the 2nd crystal which narrows down the energy width of the double crystal monochromator reflectivity. This effect is shown in Fig. 2.13 again for the case of two Si(3,3,3) crystals at 40keV for the ray with $\beta = 500\mu r$. The cases of the 2nd crystal tilt with values of $0, \pm 500\mu r$ are shown.



(a) The reflectivity of the first crystal which does not have a tilt error for the ray with the fan angle (β) of $500\mu\text{r}$



(b) The reflectivity of the 2nd crystal when it has a tilt of $-500\mu\text{r}$, $0\mu\text{r}$, and $500\mu\text{r}$ respectively for the same ray with a fan angle (β) of $500\mu\text{r}$



(c) The combined reflectivity of the double crystal monochromator for this ray with three different second crystal tilts obtained by a point by point multiplication of the curve in (a) with the one in (b).

Figure 2.13 The effects of the tilt error of the second crystal of the monochromator on the reflectivity as a function of x-ray energy.

The ray then is reflected by the 2nd crystal of the monochromator in its diffraction plane. The wave vector of the reflected ray \vec{k}_{SA}'' is:

$$\vec{k}_{SA}'' = \frac{1}{\lambda_{SA}} \begin{bmatrix} \cos\theta_B \cos\beta \\ -\cos 2\chi_{m2} Y_1 - \sin 2\chi_{m2} Z_1 \\ -\sin 2\chi_{m2} Y_1 + \cos 2\chi_{m2} Z_1 \end{bmatrix} \quad (2.13)$$

The reflected ray potentially passes through the object being imaged prior to arriving at the analyzer. To evaluate the effects of the tilt errors of the crystals, it is supposed that no object is in the way, so that the ray is directly incident on the analyzer.

If there is a tilt error χ_a in the analyzer crystal, the reciprocal lattice vector of the analyzer \vec{G}_a is:

$$\vec{G}_a = \frac{1}{d_{hkl}} \begin{bmatrix} 0 \\ \cos \chi_a \\ \sin \chi_a \end{bmatrix} \quad (2.14)$$

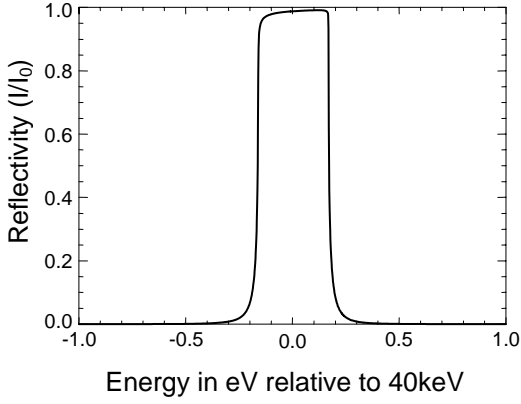
So the sine of the incident angle of the ray on the analyzer θ_χ^β is:

$$\begin{aligned} \sin \theta_\chi^\beta &= \cos(\chi_a - 2\chi_{m2})Y_1 - \sin(\chi_a - 2\chi_{m2})Z_1 \\ &= \cos(\chi_a - 2\chi_{m2} + 2\chi_{m1})\sin \theta_B \cos \beta - \sin(\chi_a - 2\chi_{m2} + 2\chi_{m1})\sin \beta \end{aligned} \quad (2.15)$$

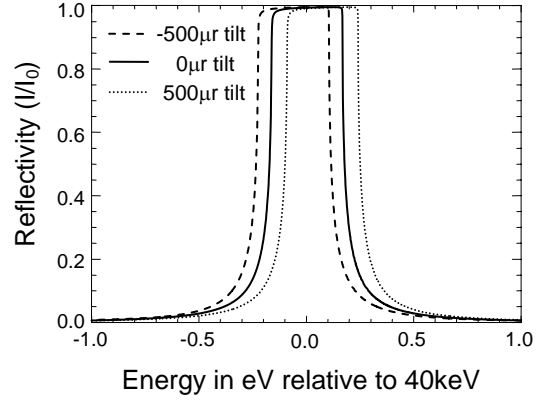
A tilt of the analyzer will cause the energy shift of its reflectivity and then lead to the angular shift of the rocking curve as shown in Fig. 2.14. The reflectivity of the aligned monochromator is shown in Fig. 2.14(a) and the reflectivity of the analyzer crystal with tilts $0\mu r$ and $\pm 500\mu r$ is shown in Fig. 2.14(b) for the ray with an opening angle of $500\mu r$. The rocking curve in Fig. 2.14(c) as a function of the relative energy is obtained by the convolution of the reflectivity of the monochromator (Fig. 2.14(a)) and the reflectivity of the analyzer (Fig. 2.14(b)). The rocking curve as a function of the analyzer angular settings is shown in Fig. 2.14(d).

From the calculation of the rocking curve, we may know that the tilts of any crystal in the DEI and MIR experimental setup will, at last, lead to the angular shift of the rocking curve and then change the intensity distribution of the resulting images. This angular shift directly affects the refraction information of the object according to the distillation of the refraction image of the object. The amount of the angular shift $\Delta\theta$ caused by the tilts of the crystals can be estimated by the difference between the incident angle of the ray on the analyzer θ_χ^β and the incident angle of the ray on the 1st crystal of the monochromator $\theta_{\chi B}^\beta$, the Bragg angle of this ray. Thus,

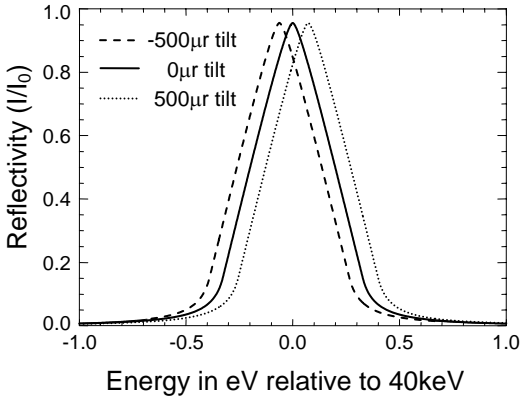
$$\Delta\theta = \theta_\chi^\beta - \theta_{\chi B}^\beta \quad (2.16)$$



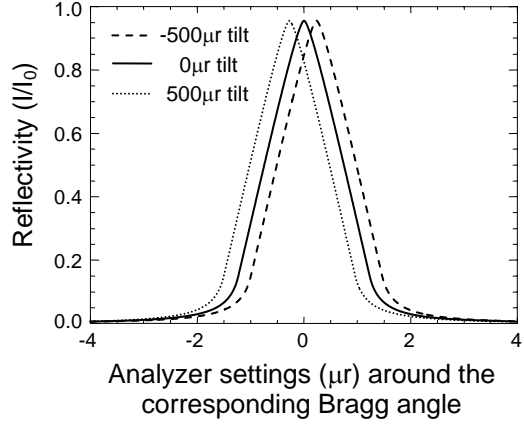
(a) Reflectivity of the aligned monochromator



(b) Reflectivity of the analyzer with tilts of $-500\mu\text{m}$, $0\mu\text{m}$, and $500\mu\text{m}$ for the ray with an opening angle of $500\mu\text{m}$



(c) Rocking curves for $-500\mu\text{m}$, $0\mu\text{m}$ and $500\mu\text{m}$ analyzer tilts as a function of the energy relative to 40keV



(d) Rocking curves for $-500\mu\text{m}$, $0\mu\text{m}$ and $500\mu\text{m}$ analyzer tilts as a function of the analyzer settings

Figure 2.14 Effect of a mis-aligned analyzer with an aligned monochromator for the ray with an opening angle of $500\mu\text{m}$.

Employing a Taylor expansion knowing that this will be a small angle practically, we may get

$$\Delta\theta = \{[\cos(\chi_a - 2\chi_{m2} + 2\chi_{m1}) - \cos\chi_{m1}]\sin\theta_B \cos\beta - [\sin(\chi_a - 2\chi_{m2} + 2\chi_{m1}) - \sin\chi_{m1}]\sin\beta\} / \cos\theta_{\chi B}^{\beta} \quad (2.17)$$

Since the angular shift $\Delta\theta$, the opening angle of the ray β , and all the tilt angles, χ_{m1} , χ_{m2} , and χ_a , are very small angles, the following approximate relationship is obtained.

$$\Delta\theta = (2\chi_{m2} - \chi_{m1} - \chi_a)\beta / \cos\theta_B \quad (2.18)$$

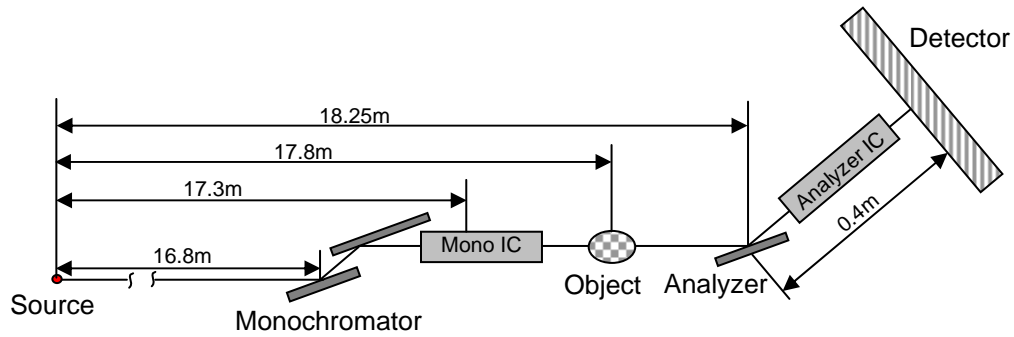
This angular change from the Bragg angle will modulate the intensity of the reflected beam in the imaging field according to the rocking curve of the analyzer. The occurrence of the tilt angles will introduce a systematic shift in the rocking curve center and will appear as a linear refraction angle across the field of view (the “ β ” axis). The tilts from the crystals can not be separated from each other if only the angular shift of the analyzer rocking curve as a function of β is known. However, by monitoring the rocking curve of the second monochromator crystal one can separate the combined tilt errors of the monochromator crystals from that of the analyzer. It is also seen from Eq. 2.18 that if the two crystals of the monochromator are tilted in the same direction then the effects of the tilts can cancel each other, resulting in no net effect as seen by the analyzer. This agrees with intuitive observation that the absolute alignment of the crystals is less important than that of relative alignment between them.

2.3 Experiments

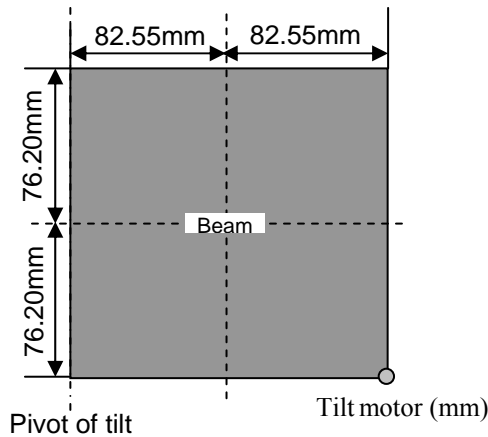
The experiments to verify the relationship between the angular shift of the rocking curve and the tilt errors has been done on the X15A beamline [5] at the *National Synchrotron Light Source (NSLS)* in Upton, New York.

Figure 2.15(a) shows the experimental setup at the beamline and its geometric parameters. The distance from the source to the double crystal monochromator is 16.8m and the distance from the source to the analyzer is 18.25m. The detector is mounted 40cm from the analyzer and its pixel size is $9\mu\text{m}$ square. In the experiment, the beam energy is set at 33.22keV. The three crystals in the system are Si(3,3,3). Figure 2.15(b) shows the mechanism of the realization of the tilt of the crystals. The tilt pivot (in the paper plane) is at one side of the plate (in the paper plane) at the center of which the crystal is mounted and the beam center goes through the same center. There is a tilt motor to heave the other side of the plate up in the out-of-paper direction which makes the plate rotate around the tilt pivot so that the tilt angle can be adjusted by the precession of the tilt motor. Note that this mechanism of tilt will create a displacement of the center of the crystal while rotating it. Figure 2.15(c) shows the alignment of the *Ion Chambers (ICs)* of the beamline. In our experiments, IC0 and IC2 were used to measure the

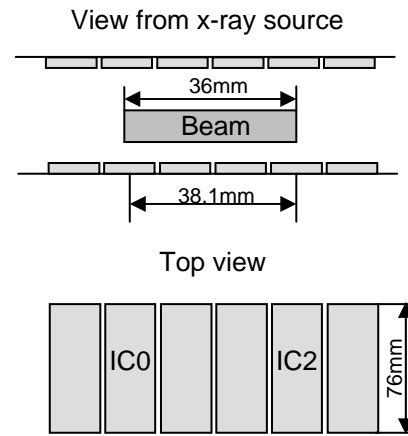
intensity of the beam. The distance between them is 38.1mm, which is just bigger than the beam width 36mm.



(a) Experimental DEI system setup at X15A beamline, NSLS



(b) Crystal mount and the realization of tilt



(c) Alignment of ion chambers, IC0 for out board and IC2 for in board

Figure 2.15 Beamline setup for tilt experiments

2.3.1 Tilt of the Analyzer

If there are no tilts between the two crystals of the monochromator, the systematic refraction angle across the fan beam (as a function of β) can be linearly determined by the tilt of the analyzer. From Eq. 2.18, we have

$$\Delta\theta = -\chi_a\beta/\cos\theta_B \quad (2.19)$$

Since DEI is designed to detect changes in refraction angle, the tilt error of the analyzer can be estimated by the systematic refraction angle derived from the resulting images.

$$\chi_a = -\frac{\Delta\theta}{\beta} \cos\theta_B \quad (2.20)$$

The opening angle β can be approximated by the beam width w_B divided by the distance from the x-ray source to the detector d_D which is 18.65m at X15A beamline at the NSLS. So Eq. 2.20 can be re-written as

$$\chi_a = -\frac{\Delta\theta}{w_B} d_D \cos\theta_B = -k_{\Delta\theta} d_D \cos\theta_B \quad (2.21)$$

where $k_{\Delta\theta}$ is the changing rate of the refraction angle $\Delta\theta$ along the beam width w_B .

In the experiments, the tilt of the analyzer has been deliberately set much larger than what we expect in practice to verify the trigonometric approximations we made in the derivation of Eq. 2.18. The sequence of the precession of the tilt motor was as 1mm, 0.5mm, 0.0mm, -0.5mm, -1.0mm which correspond to tilt angles of 6.06mr, 3.03mr, 0.0mr, -3.03mr, and -6.06mr. IC0 and IC2 were used to find the angular settings of the analyzer at which rocking curve peaks could be found in both IC0 and IC2. The averaged angular position of these two rocking curve peaks can be considered as the Bragg angle with the set tilt. For each analyzer tilt setting, 101 beam images were taken with 0.2 μ r angular step of the analyzer around the Bragg angle with the set tilt. In each image, a bright spot showed when the incident angle of the monochromatic beam matched the Bragg angle of the tilted analyzer as shown in Fig. 2.16. 11 lines of the center of the bright spot were extracted from each original image. The center of the bright spot was determined as the center of the beam (slit). As the beam image shown in Fig. 2.16, the slit was not positioned exactly parallel to the edge of the image which can be discerned by the edge of the bright spot and the image edge. In the extraction, the slope and the intercept of the beam (slit) edge was estimated so that the line parallel to the beam (slit) edge was extracted instead of the simple line in the image. If the extracted lines from 101 images were vertically laid one by one according to the analyzer angular settings, an image was created to show the moving of the bright spot which corresponds to the rocking curve peak, as shown in Fig. 2.17(a) for an analyzer tilt of 6.06mr. Also, the calculated refracted angles by MIR method along the beam width, together with their

linear fitting, are plotted in Fig. 2.17(b). The listed slope of the fitted line corresponds to $-k_{\Delta\theta}$.

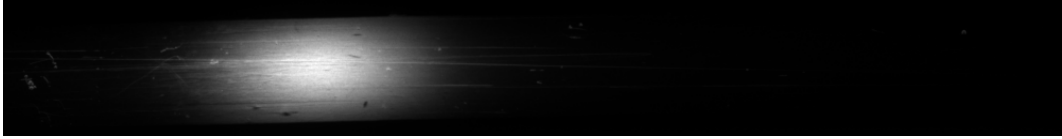
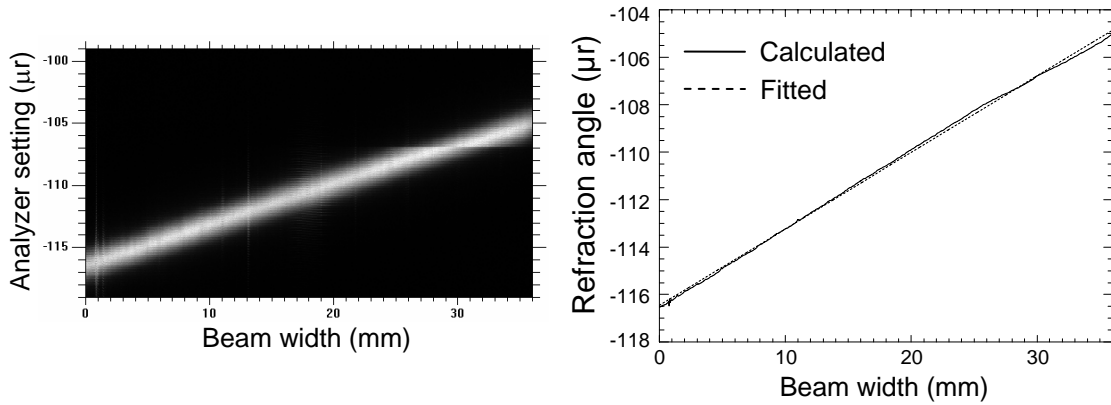


Figure 2.16 A sample image of the beam. The tilt of the analyzer was 6.06mr and the angular setting of the analyzer was $-113\mu\text{r}$.



(a) Image of the beam at different analyzer settings

(b) Refraction angle as a function of the beam width and its linear fitting. The slope of the fitted line is $0.323\mu\text{r}/\text{mm}$

Figure 2.17 Image of the beam at different analyzer settings and the accordingly calculated refraction angle as a function of the beam width and its linear fitting when the tilt of the analyzer was set as 6.06mr.

In the same way, the data collected with analyzer tilt errors of 3.03mr, 0.0mr, -3.03mr, and -6.06mr can be analyzed and the results can be refer to Appendix B.

The induced tilt and the measured values using Eq. 2.21 are listed in Table 2.1. Good agreement was obtained. So the tilt error of the analyzer can be estimated according to the systematic refraction angle found in the images using Eq. 2.20 or Eq. 2.21.

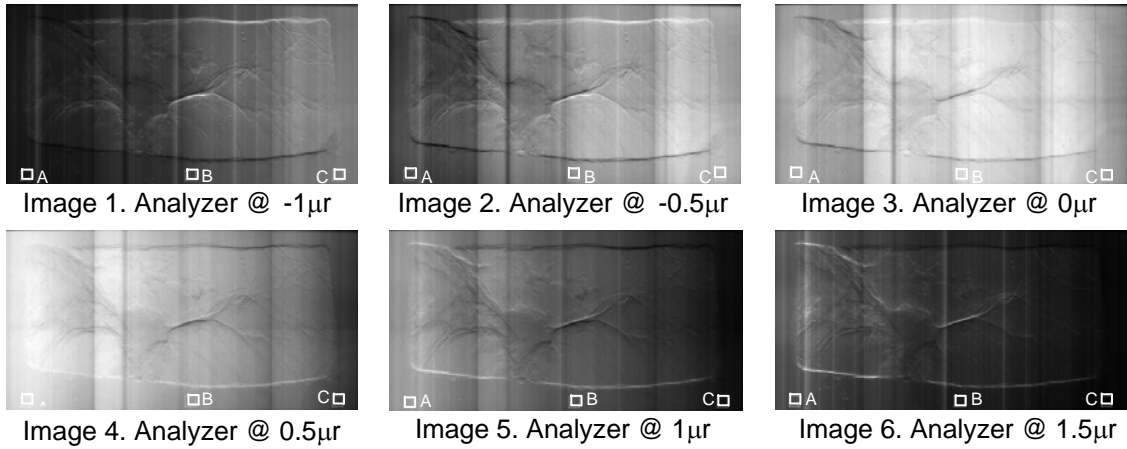
Table 2.1 Verification of the linear relationship between the angular shift of the rocking curve and the tilt error of the analyzer

Set tilt error (mr)	6.06	3.03	0.0	-3.03	-6.06
Estimated tilt error (mr)	5.92	3.06	0.026	-3.01	-6.17
Error in the estimation (%)	-2.32	0.98	-	0.54	1.82

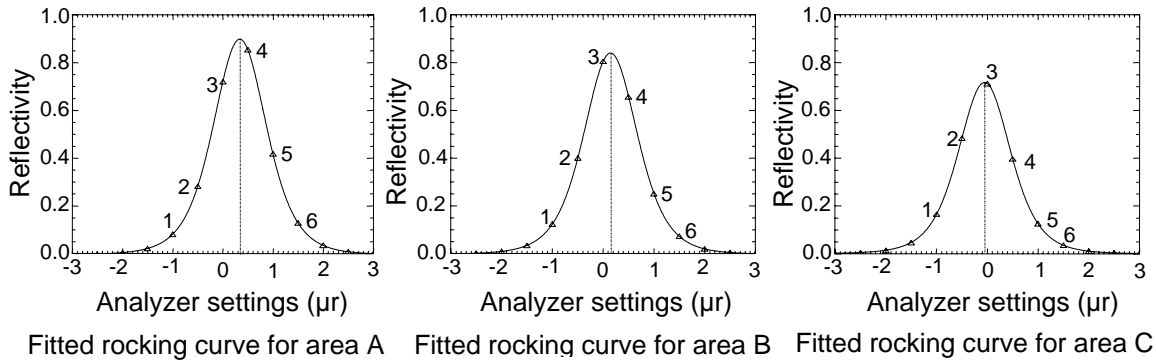
To demonstrate how the above understanding can be applied to practical DEI imaging, images of a set of DEI mammography images taken at different rocking curve points are shown in Fig. 2.18(a). They were taken at 40keV on the X15A beamline at the NSLS. The three rocking curves shown in Fig. 2.18(b) are from three different areas in the bottom of the images where no structured object was present. These three different areas are shown in Fig. 2.18(a), from left to right marked in squares as A, B, and C. The triangle points on the fitted rocking curves correspond to the analyzer settings ($0.5\mu\text{r}$ increments from $-3\mu\text{r}$ to $3\mu\text{r}$). To be clear, the analyzer positions where the shown images in Fig. 2.18(a) were taken were marked from 1 to 6 corresponding to image 1 to image 6.

It is obvious that the three fitted rocking curves have different angular shifts. Thus there is a “refraction angle” which is not expected across the image field from left to right. And the effects of this angle can be clearly found in the images. The left region of images taken on the low angle side of the rocking curve is darker than the right region, and vice versa, the right region of images taken on the high angle side of the rocking curve is darker than the left region.

The refraction image, $\Delta\theta$, of the top region of the images where no structured object was present was estimated and is shown in Fig. 2.19(a) as a gray scale image. The averaged profile of the refraction image is shown in Fig. 2.19(b). The profile can be fitted by a straight line which is also shown in Fig. 2.19(b). The slope of this line is $-0.00426\mu\text{r}/\text{mm}$. So a tilt error of $\chi = 78.58\mu\text{r}$ is found using Eq. 2.21.



(a) Six unprocessed DEI mammography images obtained at different analyzer positions from $-1\mu\text{m}$ to $1.5\mu\text{m}$ with increment of $0.5\mu\text{m}$ corresponding to images 1 to 6. The 3 square areas in the original images show locations where the estimation of the intrinsic rocking curves was performed.

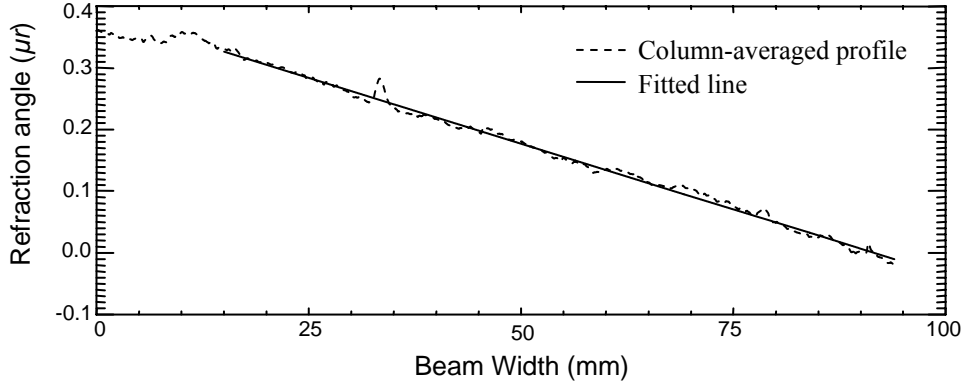


(b) Three rocking curves estimated from 3 different areas A, B, and C in (a). The numbers noted on the curves correspond to the images shown in Fig. (a). Note the systematic shift in peak location to smaller angle between regions A, B, and C.

Figure 2.18 Some DEI mammography images and the estimated intrinsic rocking curves at different locations in the images



(a) Estimated refraction image



(b) Column-averaged profile of the refraction image and a fitted line of the profile

Figure 2.19 Estimated refraction image of the top of the original images and its averaged profile

2.3.2 Tilt of the 2nd Crystal of the Monochromator

At the X15A beamline of the NSLS, there is no way to tilt the 1st crystal of the monochromator due to the mechanical design of the monochromator. So only the following equation can be verified in the experiments.

$$\Delta\theta = (2\chi_{m2} - \chi_a)\beta / \cos\theta_B \quad (2.22)$$

Similar as Eq. 2.21, Eq. 2.22 can be re-written as:

$$2\chi_{m2} - \chi_a = k_{\Delta\theta} d_D \cos\theta_B \quad (2.23)$$

It is also difficult to determine the amount of the tilt of the 2nd crystal of the monochromator due to the mechanical system which is used to control the tilt angles. In the experiments, two tilts of the 2nd crystal of the monochromator were set (the 1st tilt and the 2nd tilt set) approximately the same value but in the opposite direction. At each tilt set of the 2nd crystal of the monochromator, a sequence of analyzer tilts were applied. With each set tilt of the analyzer, the Bragg angle of the tilted analyzer was approximately estimated by the measured rocking curves of IC0 and IC2. Then the tilted analyzer rocked around its Bragg angle in a range of $\pm 10\mu r$ with a step of $0.2\mu r$. At each

analyzer setting, a beam image was taken. 11 lines at the bright spot center were extracted. A new image was formed by laying all the extracted lines from 101 images vertically together.

Analyzer tilts of 0.606mr, 0mr, -0.606mr, -1.212mr, -1.818mr were applied when the 2nd crystal of the monochromator was set at the 1st tilt. Also, it can be found in Appendix B for the new formed images to show the track of the bright spot of the beam for different analyzer tilts and the refraction angles along the beam width, together with their slopes corresponding to $-k_{\Delta\theta}$.

If the right side of Eq. 2.23 is denoted as k ($k = k_{\Delta\theta} d_D \cos\theta_B$), Fig. 2.20 shows the measured k in the experiments as a function of the tilt of the analyzer χ_a . The measured value can be fitted by a line which is shown in solid line in the figure. The slope of the fitted line is -0.968 and the intercept of the line is -1.478mr, which indicates the tilt value of the 2nd crystal of the monochromator was 0.739mr if the coefficient 2 is considered correct. Eq. 2.23 has been verified in the experiments except the coefficient 2.

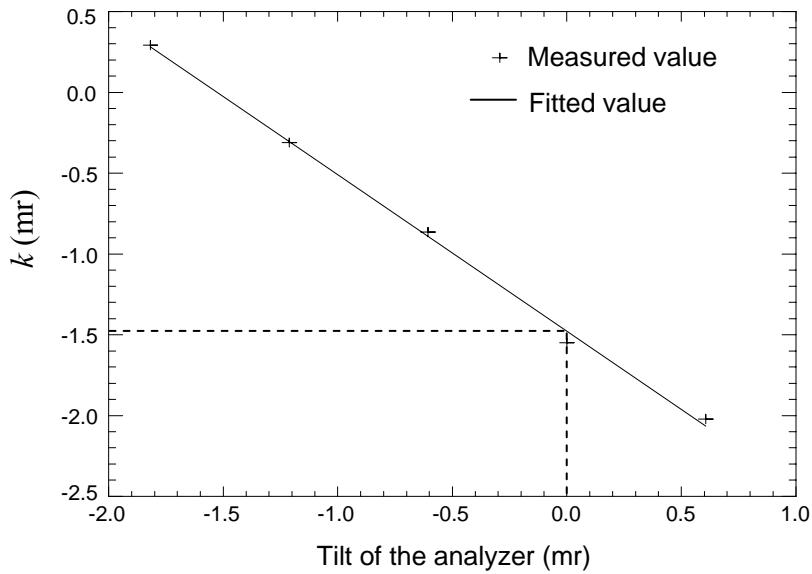


Figure 2.20 k as a function of the tilt of the analyzer

When the 2nd crystal of the monochromator was set at its 2nd tilt value (approximately the same value as the 1st tilt value but with opposite sign), analyzer tilts of -1.818mr, -0.606mr, 0mr, 0.606mr, 1.212mr, 1.828mr, 2.424mr were applied. Similarly,

the position of the bright spot of the beam at different analyzer settings and the calculated refraction angle as a function of the beam width can be referred to Appendix B.

Similarly, Fig. 2.21 shows the measured k in the experiments as a function of the tilt of the analyzer χ_a . The measured value was fitted by the solid line in the figure. The slope of the fitted line is -1.018 and the intercept of the line is 1.498mr which indicates the 2nd tilt value of the 2nd crystal of the monochromator was 0.749mr if the coefficient 2 is considered correct. Since the relationship of the 1st tilt value and the 2nd tilt value of the 2nd crystal of the monochromator was almost symmetric around 0, the coefficient 2 in Eq. 2.23 has not been verified.

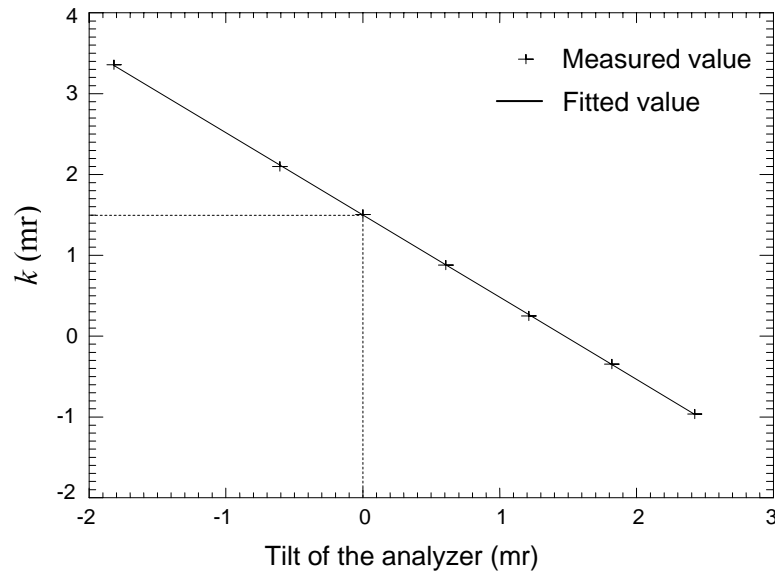


Figure 2.21 k as a function of the tilt of the analyzer

In the above experiments, the compensation of an induced tilt of the 2nd crystal of the monochromator by the tilt of the analyzer was verified. This compensation is possible as shown in Eq. 2.18 and occurs when the terms in parentheses sum to zero.

It is also seen from Fig. 2.28(a) and Fig. 2.34(a) that even though the angular effect of a monochromator tilt can be compensated perfectly by tilting the analyzer crystal, the intensity variation as a result of a tilted monochromator crystal can not be compensated. Thus it is still desirable to align the monochromator crystals independently of the analyzer.

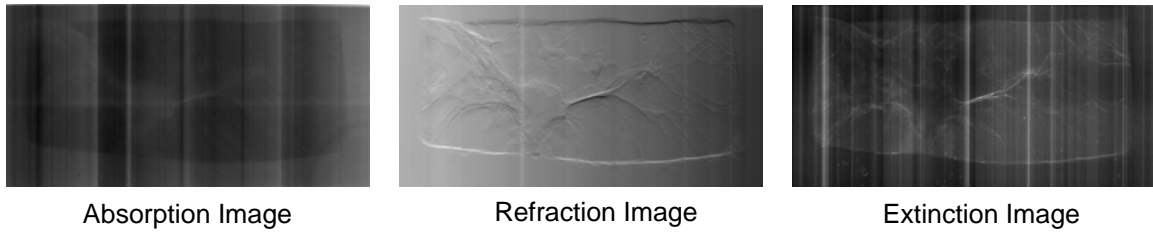
2.4 Corrections of the Tilt Error in DEI/MIR Images

In DEI/MIR image processing, an intrinsic rocking curve of the analyzer is usually estimated from parts of images where no object is present. The parametric images which convey the properties of the object are derived by the comparison between rocking curves from all pixels in the images and this intrinsic rocking curve as introduced in 2.1. Obviously, the tilt error complicates the interpretation of the DEI/MIR images by changing the intrinsic rocking curve's angular location across the image field (" β " axis).

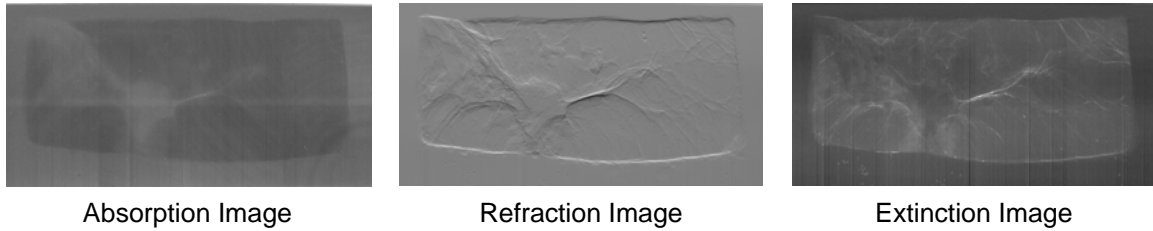
To remove the tilt error, either careful alignment of the crystals is required prior to imaging, or an algorithm will be necessary to remove the effects after imaging. Before imaging two ion chambers are used to measure the flux emitted from the monochromator and the analyzer respectively, which are both segmented into two regions about the median ray as shown in Fig. 2.15. The fluxes of these two regions are sampled to make sure that the rocking curve peaks are aligned; if not, the tilt angle is adjusted [61]. However, even if the crystals are exactly aligned at its Bragg angle before imaging, it may drift away during imaging. So it is important to remove the effects of tilt error from the DEI/MIR images by a robust algorithm.

A method employing multiple reference rocking curves instead of a single intrinsic rocking curve is proposed. The requirement of this method is that there are areas along the beam width where no object is present or reference rocking curves are acquired prior to imaging with the object. These areas can be used to create one reference rocking curve for each column of images by interpolation. In the distillation of parametric images, the current rocking curve is compared to its corresponding column reference rocking curve instead of one single intrinsic rocking curve. The parametric images of the previous MIR mammography images were estimated by the proposed multiple reference rocking curves method. Compared to the parametric images distilled using only one intrinsic rocking curve as shown in Fig. 2.22(a), the tilt error was successfully removed as shown in Fig. 2.22(b).

In addition, when there is no tilt, the increment and the range of the analyzer angular settings are determined by the rocking curve, the physical properties of the object, and the sensitivity required in the experiment. When there is a tilt error, the effect of the tilt error has to be considered when the settings in the experiment are determined.



(a) Parametric images distilled using only one intrinsic rocking curve



(b) Parametric images obtained by the proposed multiple reference rocking curves

Figure 2.22 Comparison of the estimated parametric images using different methods

Figure 2.23 shows an imaging object and its absorption, refraction, and extinction images distilled from an image set which is acquired when the analyzer had a tilt error 6.06mr. The angular settings of the analyzer were from $-15\mu\text{r}$ to $15\mu\text{r}$ about the peak with $3\mu\text{r}$ increments. The object was composed of paper sheets, a horizontal Lucite rod, and a vertical Lucite rod, overlapping from the front to the back as shown in Fig. 2.23(a). The artifacts in the parametric images are obvious on the horizontal Lucite rod. This phenomenon is reproduced in the simulation assuming 6mr analyzer tilt shown in Fig. 2.24(a) when the object is selected as a vertical rod followed by a horizontal rod. These artifacts are caused by the analyzer steps being significantly larger than half of the Darwin width ω_D (Appendix A.3). In this situation there are regions in the image where there is insufficient information to determine the reference rocking curve. The ‘S’ shaped artifacts indicate these regions. When the increment of the analyzer angular settings is decreased to $1\mu\text{r}$, the artifacts are weakened as shown in Fig. 2.24(b); and when the increment of the analyzer angular settings is further decreased to $0.3\mu\text{r}$, the artifacts can not be detected any more as shown in Fig. 2.24(c).

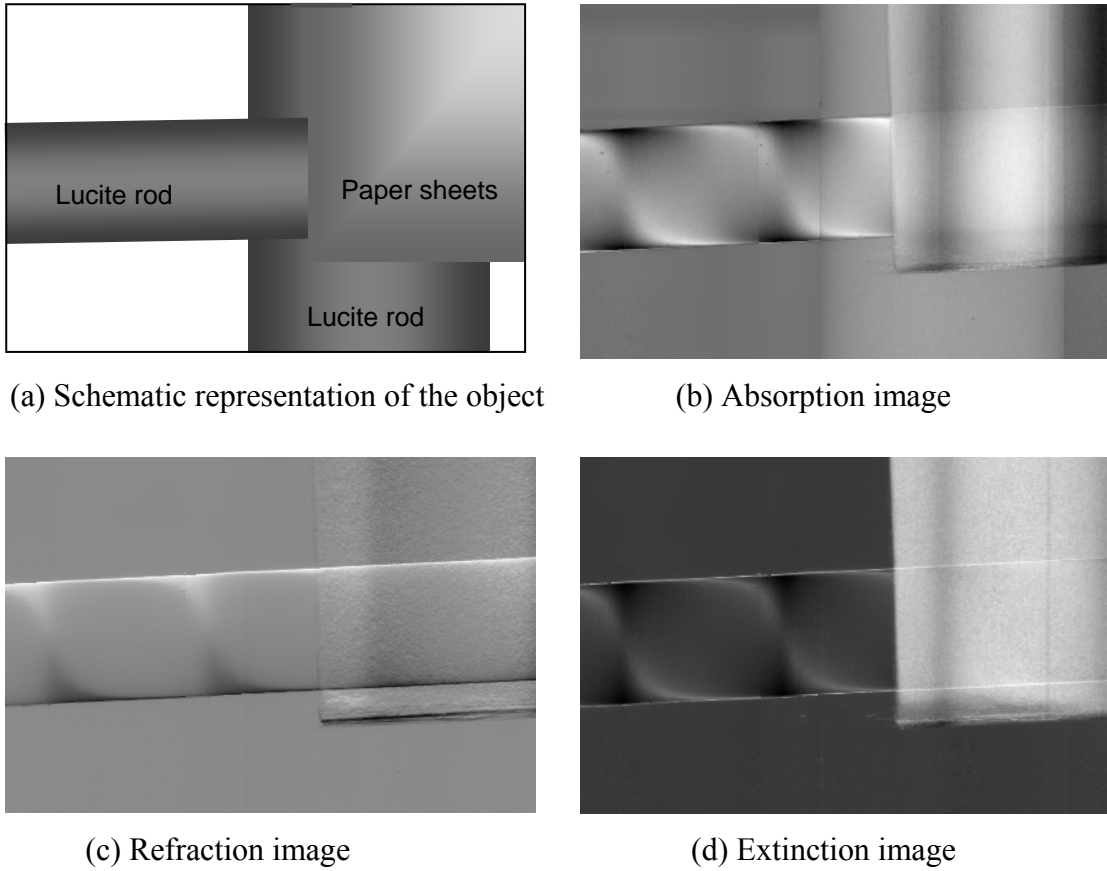
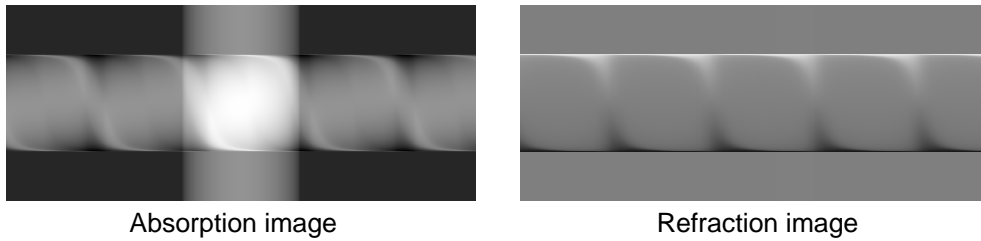


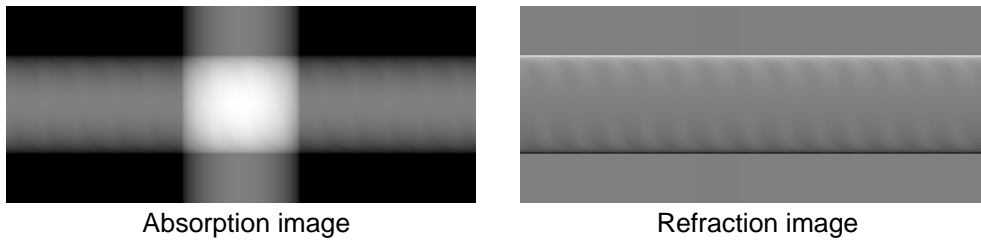
Figure 2.23 Imaging object and the distilled parametric images with artifacts.

The tilted analyzer creates an imaging situation where the reference rocking curve changes in angular location across the image field of view. Thus, if the tilt is large $\left(\chi_a \geq \frac{\omega_D}{\Delta\beta} \cos\theta_B\right)$ then the DEI analysis method is no longer possible, and the MIR analysis is required to correct the image. The MIR method requires sufficiently dense analyzer settings to be able to determine the object scattering, refraction, and absorption properties. These settings are typically less than $\omega_D/2$ in step size. The case of a tilted analyzer then requires that the scan range be extended so that a sufficient angular range is covered across the field of view. The extension of range should be approximately,

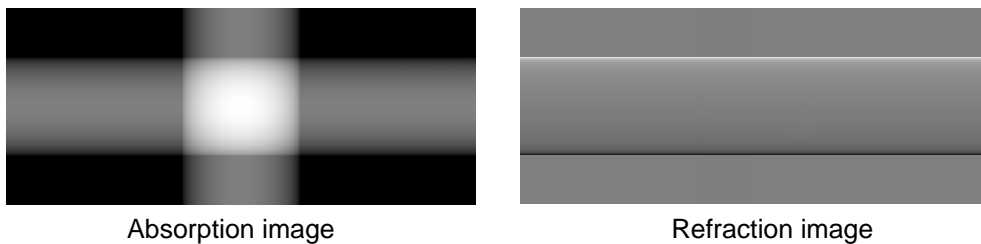
$$\Delta\theta_{ext} \approx \frac{\chi_a \Delta\beta}{\cos\theta_B} \quad (2.24)$$



(a) Simulation result when the analyzer settings are from -15μ to 15μ with 3μ increments with an obvious artifact.



(b) Simulation result when the analyzer settings are from -15μ to 15μ with 1μ increments. The artifact is weakened.



(c) Simulation result when the analyzer settings are from -15μ to 15μ with 0.3μ increment. The artifact can not be detected.

Figure 2.24 Weakened artifacts with the decrease of the increment of the analyzer angular settings.

2.5 Conclusions

DEI/MIR requires high precision alignment of crystals in both the Bragg angle and the azimuthal tilt angle. In this chapter a detailed analysis was presented on the effect of a tilt angle, how it affects the resulting images, and how to determine such a tilt exists. The evaluation of the tilt of the analyzer was given and verified by the experiments. The compensation of an induced tilt of the 2nd crystal of the monochromator by the tilt of the analyzer was also verified by the experiments. However, the intensity variation as a result of a tilted monochromator crystal can not be compensated. It is still desirable to

align the monochromator crystals independently of the analyzer. A post processing method employing multiple reference rocking curves instead of one intrinsic rocking curve for distilling the parametric images was implemented and the artifacts caused by the improper angular increment of the analyzer settings is discussed. The result shows that the tilt error can be successfully removed. Estimates have been made for the tilt alignment requirements to achieve the DEI and MIR analysis methods. This information is essential if such systems are to be properly engineered or duplicated. The analysis also applies to multiple crystal systems such as monochromators on synchrotron beamlines, especially for wide horizontal acceptance situations such as bend magnet or wiggler monochromators, which is the right case for the monochromator for KES imaging.

Chapter 3

K-Edge Subtraction Imaging and Fluorescence Subtraction Imaging

With the well prepared beam delivered by the double crystal monochromator, two non-destructive imaging techniques, *K-Edge Subtraction (KES) Imaging* and *Fluorescence Subtraction Imaging (FSI)*, were implemented to locate the iodine accumulation in the rat head. The imaging techniques were improved in a sequence of experiments. The detection limits were measured and the SNR were analyzed. Based on the experimental results, two imaging techniques were compared with reference to radiation dose, image acquisition time, resolution, SNR, and a newly developed quality factor. This quality factor makes the imaging systems evaluable and comparable. Since it is based on Poisson statistics in the detector, it sets an upper achievable limit for the imaging system and can be used as a guide to improve the imaging systems. Also to smooth the restraint of the rat head, an algorithm is developed firstly to convert this 3D problem into a 2D one. An imaging plan of using KES and FSI complementarily is proposed.

3.1 Motivation and Objectives

The *Sodium Iodide Symporter (NIS)* is a membrane glycoprotein that mediates active iodide uptake in the thyroid gland and several extra-thyroidal tissues [62]. The gene responsible for the expression of the NIS can be inserted (transfected) into the *deoxyribonucleic acid (DNA)* in all kinds of living cells, including cancer cells. Living cancer cells transfected and expressing NIS accumulate iodine with the proliferation of the cancer cells and the accumulation is only in cells in which the NIS is expressed. *Gene Expression Mapping using Synchrotron Light (GEMS)* employs the advantages of the synchrotron light to observe the accumulated iodine so that the growth of the cancer cells can be seen *in vivo*.

The concentration of iodine in human thyroid is around $0.6\text{mg}/\text{cm}^3$ (4.7mM) [47]. If the projected thickness of the thyroid is assumed as 1cm (normally the dimension of a

human thyroid is $(4-4.8) \times (1.0-1.8) \times (0.8-1.6 \text{cm})$), the projected iodine amount of 4.7mM-cm is expected to be detected. The iodine concentration value for a small animal thyroid such as a rat is approximately 1mM [63]. If we assume the thyroid thickness is 1mm then we would expect a projected contrast density of 0.1mM-cm. To assess if this concentration is detectable with x-rays we need to have an estimation of exposure for a small animal. According to the review paper of Badea [64] on in vivo small animal imaging, a range of 17mGy – 0.78Gy whole body radiation dose was applied to small animals in literature.

Therefore, our objective is to determine both theoretically and experimentally if a 0.1mM-cm projected iodine concentration can be observed with a moderate x-ray exposure that will allow multiple imaging to follow progression of gene expression in a live animal system. Our intent is to stay well below 1Gy exposure and to have several pixels per millimeter spatial resolution.

Two non-destructive x-ray imaging techniques are available to detect dilute elements and reveal their distributions in the living matter; KES and XRF. The projected amount of iodine in human thyroid is at the detection limit of the KES at moderate radiation dose. KES is expected to provide a global view of the distribution and the projected amount of the accumulated iodine within tolerable imaging time. Although the iodine concentration in human thyroid is much more than the detection limit of XRF, there are also several other issues to be addressed. Our sample is the head of a living rat, which is quite different from a well-prepared thin flat tissue sample which was used in the detection of the limit of the method (See also Chapter 1). In our condition, the fluorescence is less likely to arrive at the detector and more Compton scattered x-rays contribute to noise.

3.2 K-Edge Subtraction Imaging and Fluorescence Subtraction Imaging

The theory and basic equations of KES imaging are introduced. FSI which was inspired by KES and developed from XRF is also discussed. To make the two imaging methods comparable in spite of all the geometric dependent factors in the experiments, a quality factor is developed by integrating the influence of SNR, radiation dose, and

spatial resolution together. Harmonics which will affect the quality of the image is also analyzed.

3.2.1 K-Edge Subtraction Imaging

In an x-ray transmission image, the number of photons in each image impinging on the detector is given by

$$N(E) = N_0(E) \exp\left(-\sum_i \left(\frac{\mu(E)}{\rho}\right)_i \rho_i t_i\right) \quad (3.1)$$

where $N(E)$ is the photon count transmitted through the object at an energy of E , $N_0(E)$ is the photon number of the incident beam at the same energy E , $\left(\frac{\mu(E)}{\rho}\right)_i$ is the mass attenuation coefficient of the object at this energy, ρ_i is the mass density of the material, and t_i is the transmitted path length in the object. The subscript i denotes different tissues and materials: bone, soft tissue, and contrast agent, such as iodine.

In KES, two transmission images, $N(E_L)$ and $N(E_H)$, are obtained with monochromatic x-rays just below (E_L) and above (E_H) the absorption edge of the contrast agent. Figure 3.1 illustrates the mass attenuation coefficients of iodine, bone, and water (to approximate soft tissue) as a function of the energy of the incident beam, (a) for large range of the energy (10keV-100keV) and (b) for small range of the energy just around the K-edge of iodine.

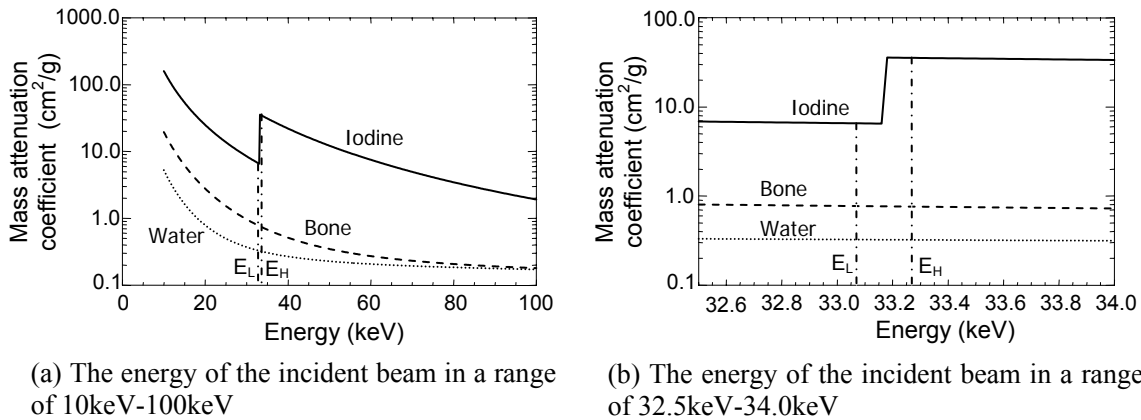


Figure 3.1 Mass attenuation coefficients as a function of the energy of the incident beam

If the logarithmic subtraction is conducted, the obtained signal is given by [65]

$$S = \ln\left(\frac{N(E_H)}{N(E_L)}\right) = \sum_i \left(\frac{\Delta\mu}{\rho}\right)_i \rho_i t_i \approx \left(\frac{\Delta\mu}{\rho}\right)_C \rho_C t_C \quad (3.2)$$

where $\frac{\Delta\mu}{\rho}$ is the change in the mass attenuation coefficient between two different energies, $\left(\frac{\Delta\mu}{\rho}\right)_C$ is this value for the contrast agent, ρ_C is the density, and t_C is the transmitted path length of the contrast agent. Although a more accurate signal equation will be given later, this equation shows more clearly that the signal in the logarithmic subtraction image is determined by the change of the mass attenuation coefficient, mass density, and the thickness of the components of the object. The change of the mass attenuation coefficient for the contrast agent, such as iodine, can be as high as 12,300 times of that of the soft tissue and 560 times of that of bone when the incident beam energies cross the absorption edge. The resulting image is dominated by the contrast agent signal when the summation of the multiplications of the mass density and the thickness of the tissue and the bone is far from compensating the changes in the mass attenuation coefficient of iodine. In this way the subtraction in KES removes the structural noise or anatomical information and enhances the location with the contrast agent.

If the object is assumed to be composed of contrast (subscripted as C) and matrix material (subscripted as M) for rest of the object, the high energy image and low energy image can be described by the following equations according to equation (3.1).

$$N(E_H) = N_0(E_H) e^{-\left(\frac{\mu(E_H)}{\rho}\right)_M \rho_M t_M} e^{-\left(\frac{\mu(E_H)}{\rho}\right)_C \rho_C t_C} \quad (3.3)$$

$$N(E_L) = N_0(E_L) e^{-\left(\frac{\mu(E_L)}{\rho}\right)_M \rho_M t_M} e^{-\left(\frac{\mu(E_L)}{\rho}\right)_C \rho_C t_C} \quad (3.4)$$

If denote the variables for high energy with a subscription H and variables for low energy with a subscription L , the logarithm of the above two equations are:

$$\ln\left(\frac{N_H}{N_{0H}}\right) = r_H = -\left(\frac{\mu}{\rho}\right)_{MH} \rho_M t_M - \left(\frac{\mu}{\rho}\right)_{CH} \rho_C t_C \quad (3.5)$$

$$\ln\left(\frac{N_L}{N_{0L}}\right) = r_L = -\left(\frac{\mu}{\rho}\right)_{ML} \rho_M t_M - \left(\frac{\mu}{\rho}\right)_{CL} \rho_C t_C \quad (3.6)$$

Two projected images, contrast agent image ($\rho_C t_C$) and matrix material image ($\rho_M t_M$), can be exactly solved from Eq. 3.5 and 3.6.

$$A = \left(\frac{\mu}{\rho}\right)_{ML} \left(\frac{\mu}{\rho}\right)_{CH} - \left(\frac{\mu}{\rho}\right)_{CL} \left(\frac{\mu}{\rho}\right)_{MH} \quad (3.7)$$

$$\rho_C t_C = \frac{\left(\frac{\mu}{\rho}\right)_{MH} r_L - \left(\frac{\mu}{\rho}\right)_{ML} r_H}{A} \quad (3.8)$$

$$\rho_M t_M = \frac{\left(\frac{\mu}{\rho}\right)_{CL} r_H - \left(\frac{\mu}{\rho}\right)_{CH} r_L}{A} \quad (3.9)$$

The contrast agent image ideally only contains the projected amount of the contrast agent without any anatomy and structure information. The matrix material image sometimes is also called water image because normally water is selected to be the matrix material. The information of the water image is the equivalent absorption length of the water converted from all the materials in the object except contrast agent. Since the useful information of the contrast agent is distilled from two transmission images, one is taken below the absorption edge and one is above the absorption edge, these two images together are called one image set.

There are many factors that affect the SNR of the resulting images of the KES, such as the beam intensity variation in both temporal domain and spatial domain, the vibration caused by the motor motion, the movement of the object, and the statistics of the detector. Among these factors, only the statistics of the detector is considered in the following derivation of the theoretical SNR of the contrast agent image. So the theoretical SNR gives the upper limit of the achievable SNR of the imaging system which can be used to direct the improvement of the imaging system.

According to Eq. 3.5 – 3.8, the variance of the detected projected amount of the contrast agent $\sigma_{\rho_C t_C}^2$ can be expressed as

$$\sigma_{\rho_{ctc}}^2 = \left[\frac{\partial \rho_{ctc}}{\partial N_L} \right]^2 \sigma_{N_L}^2 + \left[\frac{\partial \rho_{ctc}}{\partial N_H} \right]^2 \sigma_{N_H}^2 + \left[\frac{\partial \rho_{ctc}}{\partial N_{0H}} \right]^2 \sigma_{N_{0H}}^2 + \left[\frac{\partial \rho_{ctc}}{\partial N_{0L}} \right]^2 \sigma_{N_{0L}}^2 \quad (3.10)$$

Assuming the detected N_L , N_H , N_{0L} , and N_{0H} are in Poisson distribution, the following equations hold. $\sigma_{N_L}^2 = N_L$, $\sigma_{N_H}^2 = N_H$, $\sigma_{N_{0L}}^2 = N_{0L}$ and $\sigma_{N_{0H}}^2 = N_{0H}$. So

$$\sigma_{\rho_{ctc}}^2 = \frac{1}{A^2} \left[\frac{\left(\frac{\mu}{\rho} \right)_{MH}^2}{N_L} + \frac{\left(\frac{\mu}{\rho} \right)_{ML}^2}{N_H} + \frac{\left(\frac{\mu}{\rho} \right)_{MH}^2}{N_{0L}} + \frac{\left(\frac{\mu}{\rho} \right)_{ML}^2}{N_{0H}} \right] \quad (3.11)$$

Since the changes in the mass attenuation coefficient of the matrix material between high and low energies are very small, they can be approximated equal to each other and both recorded as $\left(\frac{\mu}{\rho} \right)_M$. N_{0H} and N_{0L} can both be recorded as N_0 because the incident

beam intensity of high energy and low energy are typically close to each other. N_H and N_L can be approximated as $N_0 e^{-\left(\frac{\mu}{\rho} \right)_M \rho_M t_M}$ since the imaging method is only employed when the amount and the concentration of the contrast agent both are very low. If we denote $\left(\frac{\mu}{\rho} \right)_{CH} - \left(\frac{\mu}{\rho} \right)_{CL}$ as $\Delta \left(\frac{\mu}{\rho} \right)_C$,

$$\sigma_{\rho_{ctc}}^2 \cong \frac{1}{\left[\Delta \left(\frac{\mu}{\rho} \right)_C \right]^2} \left[\frac{2}{N_0 e^{-\left(\frac{\mu}{\rho} \right)_M \rho_M t_M}} + \frac{2}{N_0} \right] \quad (3.12)$$

So the SNR of the contrast agent image can be estimated by

$$SNR^2 = \left(\frac{\rho_{ctc}}{\sigma_{\rho_{ctc}}} \right)^2 = \frac{\left[\Delta \left(\frac{\mu}{\rho} \right)_C \rho_{ctc} \right]^2 N_0 e^{-\left(\frac{\mu}{\rho} \right)_M \rho_M t_M}}{2 \left(1 + e^{-\left(\frac{\mu}{\rho} \right)_M \rho_M t_M} \right)} \quad (3.13)$$

The SNR is proportional to the square root of the incident photon count and the projected amount of the contrast agent. In practice, to improve SNR, more than one

image set can be taken independently to increase the incident photon count because the incident photon count in one image set is limited by the saturation of the detector, practical imaging time, and the delivered flux of the beamline. If k image sets are taken, Eq. 3.5 and Eq. 3.6 become

$$\ln \left(\frac{\sum_{i=1}^k (N_H)_i}{\sum_{i=1}^k (N_{0H})_i} \right) = r_H = - \left(\frac{\mu}{\rho} \right)_{MH} \rho_M t_M - \left(\frac{\mu}{\rho} \right)_{CH} \rho_C t_C \quad (3.14)$$

$$\ln \left(\frac{\sum_{i=1}^k (N_L)_i}{\sum_{i=1}^k (N_{0L})_i} \right) = r_L = - \left(\frac{\mu}{\rho} \right)_{ML} \rho_M t_M - \left(\frac{\mu}{\rho} \right)_{CL} \rho_C t_C \quad (3.15)$$

According to the property of Poisson distribution, the sum of the independent Poisson distributed variables also follows a Poisson distribution whose parameter is the sum of the component parameters. It can be easily proved that SNR is improved to \sqrt{k} times of the original SNR as shown in Eq. 3.16 when the incident photon count are approximately equal to each other in each image taken.

$$SNR_k^2 = \left(\frac{\rho_C t_C}{\sigma_{\rho_C t_C}} \right)^2 = \frac{\left[\Delta \left(\frac{\mu}{\rho} \right)_C \rho_C t_C \right]^2 k N_0 e^{-\left(\frac{\mu}{\rho} \right)_M \rho_M t_M}}{2 \left(1 + e^{-\left(\frac{\mu}{\rho} \right)_M \rho_M t_M} \right)} \quad (3.16)$$

Normally, the incident photon count N_0 is measured by an ion chamber positioned before the object to be imaged.

$$N_0 = \frac{i}{q_e \frac{E_{ph}}{\varepsilon_{e-ion}} \frac{\mu_{ea}}{\mu_T} (1 - e^{-\mu_T L})}} \approx \frac{i}{q_e \frac{E_{ph}}{\varepsilon_{e-ion}} \mu_{ea} L} \quad (3.17)$$

where i is the measured current by the ion chamber, q_e is the electron charge which is equal to $1.602 \times 10^{-19} \text{C}$, E_{ph} is the incident photon energy, ε_{e-ion} is the average energy required to produce an electron-ion pair in the gas filled in the ion chamber, μ_{ea} and μ_T are the energy absorption coefficient and the total attenuation coefficient of the gas,

respectively. The approximation holds because normally there is little attenuation when x-ray goes through the ion chamber.

For biomedical x-ray imaging, radiation dose D is always a major issue which is defined as the energy deposited per object mass when x-rays go through the object.

$$D = \frac{N_0 E_{ph} \frac{\mu_{ea}}{\mu_T} (1 - e^{-\mu_T t})}{\rho A t} \quad (3.18)$$

where ρ is the mass density of the object, A is the area on the object for the incident photon count N_0 , and t is the thickness of the object. Obviously, the dose on the surface of the object which is called surface dose (D_s) reflects the maximum dose to the object where the thickness t goes to 0.

$$D_s = D_{t \rightarrow 0} = \frac{N_0 E_{ph} \frac{\mu_{ea}}{\mu_T} (1 - (1 - \mu_T t))}{\rho A t} = \frac{N_0 E_{ph} \mu_{ea}}{\rho A} \quad (3.19)$$

3.2.2 Fluorescence Subtraction Imaging

In this part, the basics of XRF and its extension FSI are introduced. Also, the properties of the energy dispersive fluorescence detector used in our experiments are discussed.

3.2.2.1 X-Ray Fluorescence Imaging

When an x-ray photon with enough energy expels an electron from the inner atomic shell of an element (Fig. 3.2(a)), the hole left by the electron can be filled by an electron from the outer shell and release a certain amount of energy which is equal to the difference in the binding energies of these two shells. The released energy can be used to emit a photon holding the same energy (Fig. 3.2(b)) and the emitted radiation is known as fluorescence [66]. Alternatively the energy can be used to expel another electron from one of the outer shells which is called auger electron (Fig. 3.2(c)). The relative numbers of the excited atoms that fluoresce are described by the fluorescence yield, which increases with the increasing of the atomic number [67].

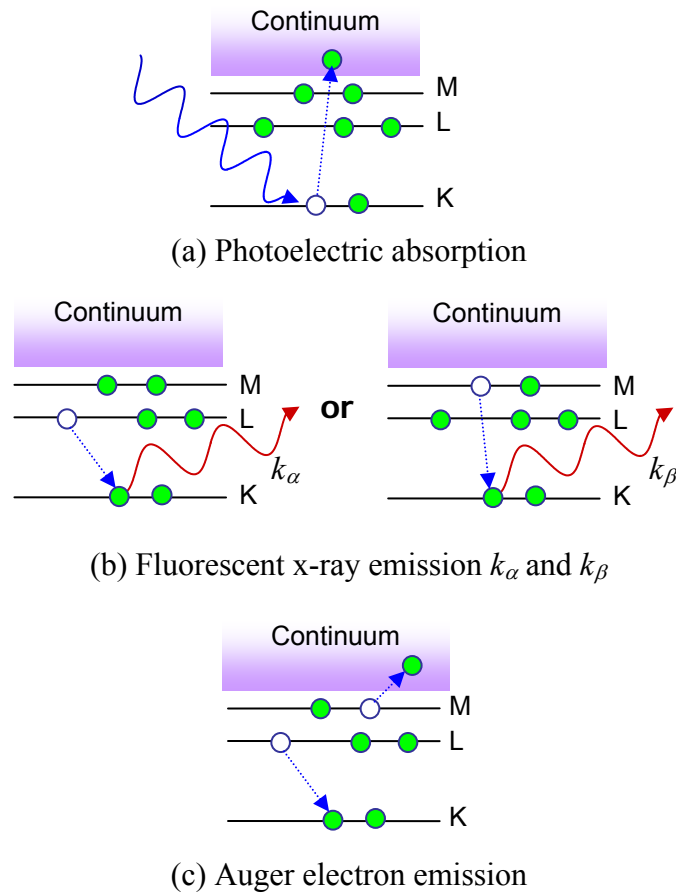


Figure 3.2 Illustration of fluorescent x-ray emission. The Auger electron emission is a complete process to the fluorescent x-ray emission.

When the object is hit by a pencil x-ray beam and raster scanned relative to it, the fluorescence signal can be collected by an energy dispersive detector with a preset energy window. This imaging method is the so called XRF.

3.2.2.2 Fluorescence Subtraction Imaging

In the normal fluorescence imaging, the energy of the incident beam is selected so that there is negligible Compton scatter at the fluorescence energy. An incident energy 1-2keV higher than the fluorescent emission line of the trace element is usually sufficient for the fluorescence imaging below 13keV which is where the vast majority of fluorescence imaging is done. For high energy fluorescence imaging, it needs to go much higher than this – perhaps 5keV or more above the edge – to minimize Compton scatter; such is the case for iodine K-edge fluorescence imaging.

However, XRF experiments at high x-ray energies (e.g. at the iodine K-edge) are more complicated than those at low x-ray energies. As shown in Fig. 3.3, the photoelectric absorption coefficient drops rapidly with energy increasing while there is almost no change in the Compton scatter coefficient. For example, an increase of beam energy from 33.27keV to 38.27keV (a 5keV change) reduces the mass photoelectric absorption coefficient from 0.53cm²/g to 0.37cm²/g while the mass Compton scatter coefficient keeps nearly constant at 0.18cm²/g. The Compton peak moves from 31.24keV to 35.60keV when the energy of the incident beam is increased from 33.27keV to 38.27keV. The drop of the Compton scatter at the iodine fluorescence emission line (28.612keV) is about 60% as estimated from a measured spectrum while the drop of the fluorescence signal is about 30% based on the change of the photoelectric coefficient. Although the drop of the Compton scatter is more than the drop of the fluorescence, the intensity of the Compton scatter from the soft tissue is still significant, which will cause a high noise background. At the same time, the photon count drop so that the statistics is reduced. Furthermore, higher energy limits the beamline availability where the experiment is conducted. For example, we were unable to move the Compton peak to a sufficient high energy to eliminate its interference with the iodine fluorescence because the upper limit of the beamline monochromator at *Hard X-ray Micro-Analysis (HXMA)* beamline at *Canadian Light Source (CLS)* was 40keV.

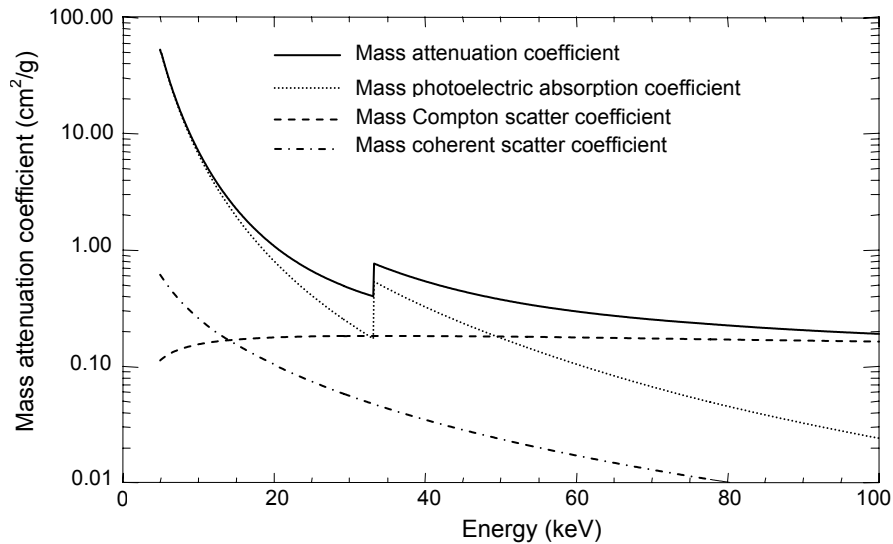


Figure 3.3 Mass attenuation coefficient and its components of 100mM iodine solution as a function of x-ray energy

Furthermore, there is interfering fluorescence from other elements. For example, the fluorescence from Sn serves as the interfering fluorescence when iodine is selected to be the contrast agent. The K-edge of Sn is at 29.200keV which is below the absorption edge of iodine (33.169keV), so Sn will emit fluorescence during imaging. The energy of the $K_{\beta 1}$ emission line of Sn is at 28.486keV which is hard to separate from iodine $K_{\alpha 1}$ (28.612keV) and $K_{\alpha 2}$ (28.317keV) using solid state energy dispersive detectors. The interfering fluorescence will appear as signals in fluorescence imaging.

When the energy of the incident beam is less than the absorption edge of the contrast element, there is no fluorescence radiation emitted at the corresponding energy. When the energy of the incident beam reaches the absorption edge of the contrast element, the photoelectric absorption jumps and the process yields fluorescent x-rays with high efficiency. For example, when the energy of the incident beam is slightly higher than the K-edge of iodine (33.169keV), the photoelectric absorption jumps from 5.812cm²/g (calculated at 33.069keV) to 34.828cm²/g (calculated at 33.269keV) and as high as 84% of the photoelectric absorption will yield fluorescence radiation [68]. At the same time the spectral changes in the Compton scatter and the fluorescence from other elements are not significant since the below-edge energy and above-edge energy are close to each other and the concentration of the contrast agent is sufficiently low to be in the dilute limit. Figure 3.4 shows the spectra obtained from a 5mm×5mm filter paper absorbed with dilute iodine solution at two different incident beam energies; 33.25keV, just above iodine K-edge, and 33.10keV, just below iodine K-edge.

FSI is a technique for fluorescence imaging using two incident beam energies just above and below the absorption edge of a contrast element. The low-energy or below-edge image can be assumed to be a “background” image which includes Compton scatter and fluorescence from other elements. The high energy or above-edge image will contain nearly identical spectral content as the below-edge image but will contain the additional fluorescence of the contrast element. The subtraction of the low energy image from the high energy image will lead to an image free from background (including interfering fluorescence), only containing the useful fluorescence signal. This imaging method is especially promising with thick objects with dilute contrast materials, significant Compton background, and/or competing fluorescence lines from other material.

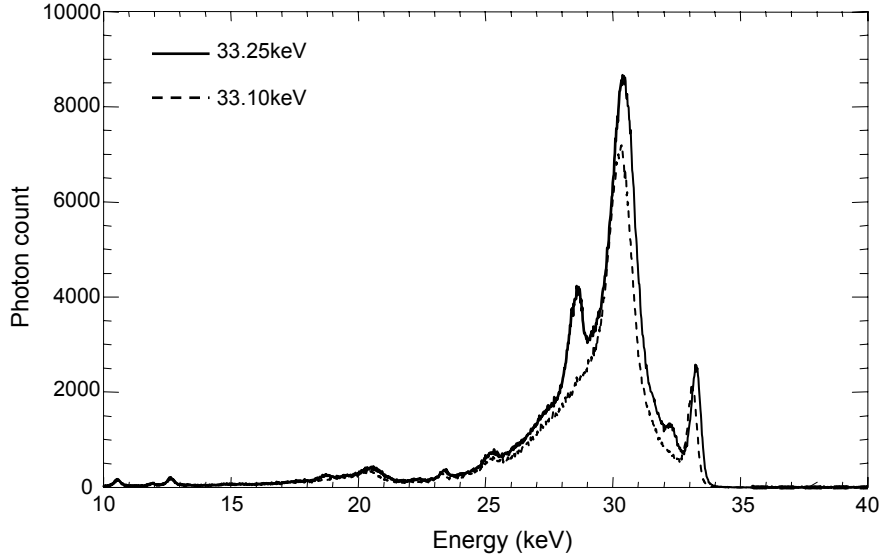


Figure 3.4 Fluorescence spectra obtained from a $5\text{mm} \times 5\text{mm}$ filter paper absorbed with dilute iodine solution at two different incident beam energies: 33.25keV and 33.10keV

There is no numerical interpretation from the signal in XRF image to the amount of the contrast agent because of the complicated geometry in imaging process. However, it is clear that the signal increases with the flux of the incident beam and the projected amount of the contrast element.

In FSI, the measured fluorescence signal N_F is equal to the subtraction of the low energy signal N_L from the high energy signal N_H as shown in Eq. 3.20.

$$N_F = N_H - N_L \quad (3.20)$$

The variance of the measured signal is shown in Eq. 3.21 if the detected photon count are in Poisson distribution.

$$\sigma_{N_F}^2 = \left(\frac{\partial N_F}{\partial N_H} \right)^2 \sigma_{N_H}^2 + \left(\frac{\partial N_F}{\partial N_L} \right)^2 \sigma_{N_L}^2 = N_H + N_L \quad (3.21)$$

The SNR for FSI can be estimated as

$$SNR^2 = \frac{N_F^2}{\sigma_{N_F}^2} = \frac{(N_H - N_L)^2}{N_H + N_L} \quad (3.22)$$

From Eq. 3.22, the SNR of the FSI is proportional to the square root of the incident photon count.

3.2.2.3 Fluorescence Detector

The properties and the geometries of the fluorescence detector are very important for the design and the alignment of the experiment. In this part, only the detector used in our experiments is introduced.

In our FSI experiment, a 32-channel germanium detector (Canberra GUL0055S, Canberra Corporate, USA) was used. The arrangement of the channels of the detector is in a rectangular pattern with 4 rows of 8 channels each as shown in Fig. 3.5. The active diameter of the channels is 8mm with a center to center spacing of 10mm. The 32 channels of the detector can collect signal simultaneously. The multi-channel detector improves solid angle collection efficiency while allowing high count rates due to the multiplicity of channels.

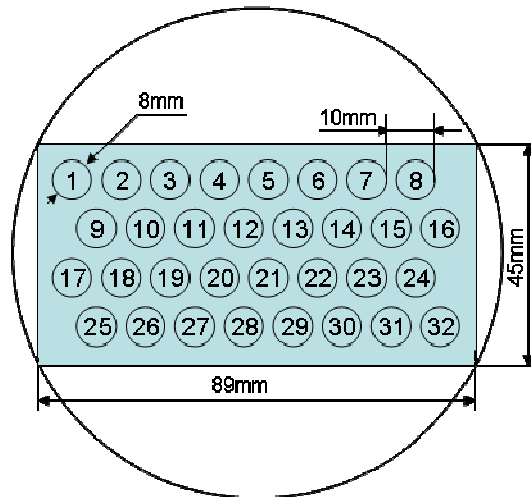


Figure 3.5 The arrangement of the channels of the fluorescence detector

The detector was positioned perpendicular to the incident beam direction in the electron orbital plane of the synchrotron so that the Compton scatter is minimal. The angular distribution of the incoherent scattered photons can be estimated by the Klein-Nishina formula (Eq. 3.23) when x-rays are incident upon a single electron. This formula can be used when the x-ray energy is significantly higher than the binding energies of most or all of the electrons in the subject. Since the object is composed of low Z elements (except for the dilute concentration of iodine), this is a very good approximation for us. The polarized, angular dependent Klein-Nishina cross section is

$$\frac{d\sigma}{d\Omega} = \frac{1}{2} r_e^2 \left[P(E_0, \theta) - P(E_0, \theta)^2 \sin^2 \theta + P(E_0, \theta)^3 \right] \kappa^2 \quad (3.23)$$

where $\frac{d\sigma}{d\Omega}$ is the differential cross section which describes the probability to observe a scattered photon per solid angle defined by $d\Omega = 2\pi \sin \theta d\theta$, r_e is the classical electron radius, E_0 is the incident photon energy, θ is the angle between the incident beam and the scattered photon as shown in Fig. 3.6, κ is the polarization term, and $P(E_0, \theta)$ is the ratio of the photon energy after and before the collision which can be calculated by Eq. 3.24.

$$P(E_0, \theta) = \frac{E'}{E_0} = \frac{1}{1 + \frac{E_0}{m_e c^2} (1 - \cos \theta)} \quad (3.24)$$

where E' is the energy of the scattered photon, m_e is the electron mass, c is the light speed, $m_e c^2$ is the rest energy of the electron which is equal to 511keV. Equation 3.24 also predicts the energy of the Compton peak in the spectrum.

The polarization term κ is defined as

$$\kappa^2 = \cos^2 \theta + \sin^2 \theta \sin^2 \phi \quad (3.25)$$

where ϕ is an azimuthal angle measured away from x in the x-y plane as shown in Fig. 3.6 where the incident beam is assumed to be horizontally polarized along the x-direction and propagates along the z-direction. The scattered beam is π polarized when ϕ is 0° or 180° and it is σ polarized when ϕ equals to 90° or 270° .

Figure 3.7 shows the differential cross section of Compton scattering changing with the scatter angle between the incident beam and the scattered radiation when the incident photon energy is at the K-edge of iodine, 33.169keV. The Compton scattering is minimal at an angle of 90° to the incident beam direction when the detector is positioned on the π polarized plane which is our case. However, since the sample is close to the detector, the channels of the detector expand a quite big solid angle around the sample.

The spectrum of a 5mm×5mm filter paper absorbed with 100mM sodium iodide solution was analyzed in the experiments. Figure 3.8 shows the spectrum from the channels of 1, 8, 25, and 32 excited by the incident beam with energy of 33.25keV.

There are two main differences in the spectrum: the shift of the Compton peak and the amplitudes of the peaks, including Compton peak, fluorescence peak, and the peak of the coherent scatter. The differences among the spectrum are caused by the locations of the channels of the detector and the paths the fluorescent signal and the scattered photons travel.

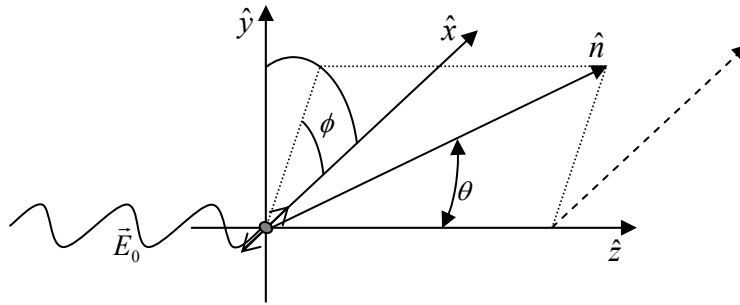


Figure 3.6 Scattering geometry. The incident photon propagates along the z -direction and is assumed to be horizontally polarized along the x -direction. The scattered ray propagates along \hat{n} with angle θ measured away from z . The azimuthal angle ϕ is measured away from x in the x - y plane.

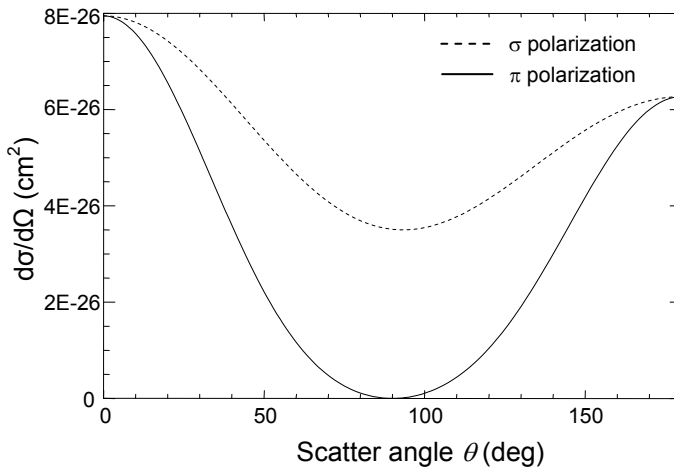


Figure 3.7 Differential cross section of Compton scattering as a function of the scatter angle θ . The energy of the incident photon is at the K-edge of iodine (33.169keV)

From Fig. 3.8, the fluorescence signal is sitting on the waist of the Compton scatter. It is obvious that the SNR of the FSI imaging is affected by the channel position of the detector which collects the signal. Calculations show that the weighted average based on each detector channel of the spectrum provides higher SNR than the equal weighted

average. The weight w_j of the spectrum collected by the j^{th} channel of the detector is selected by the ratio of the SNR of the spectrum in the j^{th} channel and the sum of the SNR of all 32 channels of the detector.

$$w_j = \frac{SNR_j^2}{\sum_{i=1}^{32} SNR_i^2} \quad (3.26)$$

where SNR_j is calculated by Eq. 3.22 for the j^{th} spectrum collected by the j^{th} channel of the detector.

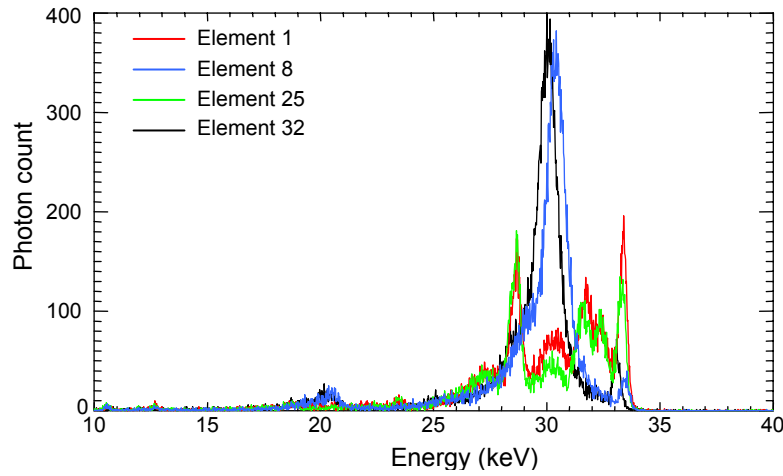


Figure 3.8 Spectrum collected by different elements of the detector with the filter paper absorbed with 100mM iodine solution.

Figure 3.9 shows the weighted and un-weighted average of the spectrum in (a) and the difference spectrum acquired from weighted and un-weighted average of the spectrum in (b). It is clear that the Compton scatter is suppressed while the fluorescence signal is strengthened. And the SNR was significantly improved from 30.6 to 42.2.

The position information of sample can be estimated since the amplitude of the Compton peak changes with the relative angle θ (Fig. 3.7) and the angle θ can be predicted by the energy shift of the Compton peak by Eq. 3.27 which is derived from Eq. 3.24.

$$\cos \theta = 1 - \left(\frac{1}{E'} - \frac{1}{E_0} \right) m_e c^2 \quad (3.27)$$

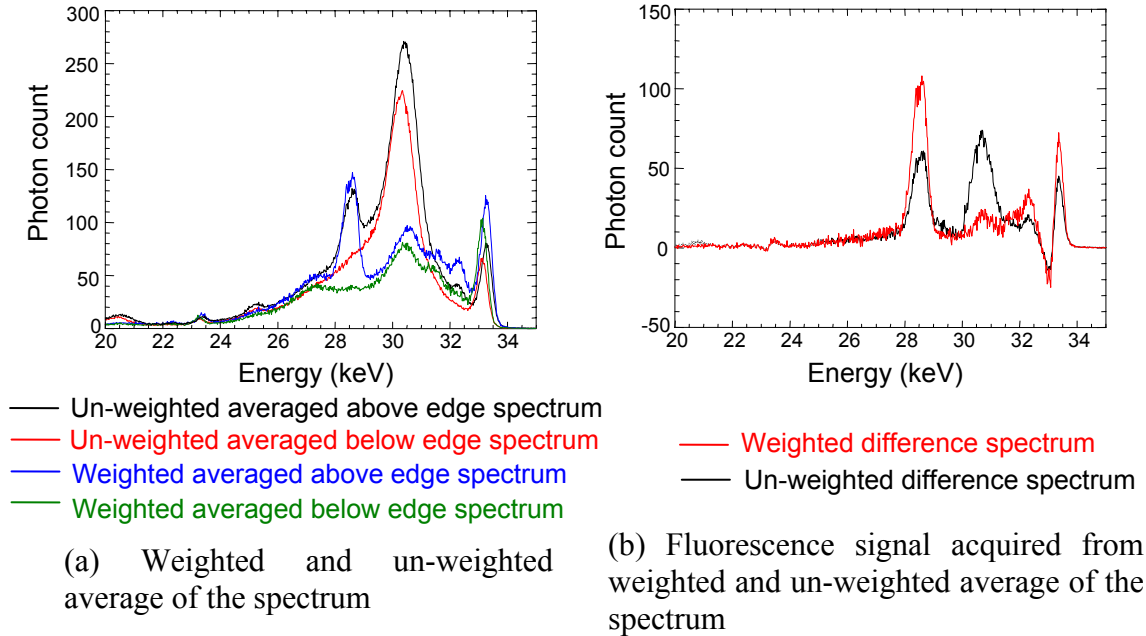
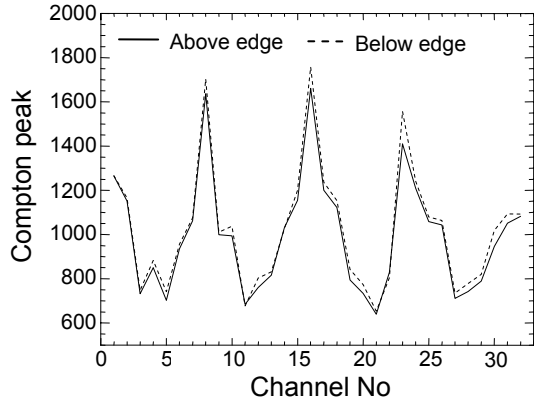
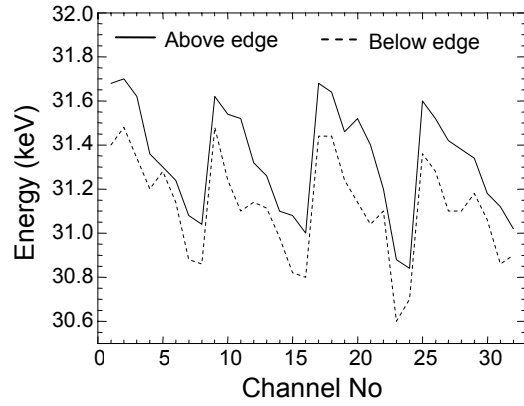


Figure 3.9 Weighted and un-weighted spectrum and their corresponding fluorescence signal

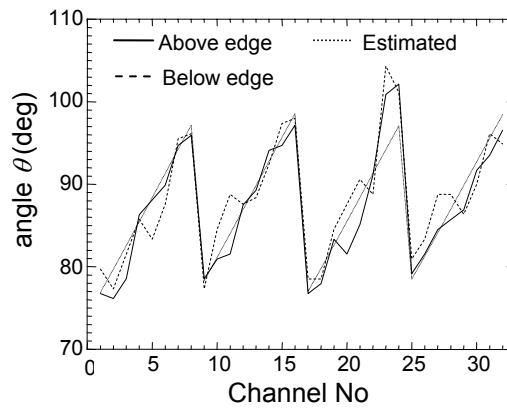
To display this effect, the spectrum of a 25mM iodine solution filled in 1mm thick container was taken. Figure 3.10 shows data from all 32 Compton peaks from this sample. The solid lines are for the incident beam energy above the K-edge (33.269keV) and dashed line below the edge (33.069keV). Figure 3.10(a) shows the amplitude of the peak as a function of channel number. Figure 3.10(b) shows the Compton peak energy for each detector channel while Fig. 3.10(c) shows the scattering angle θ derived from the Compton peak energy. The sample position can be estimated at 45.5mm on the right of the center of the 1st channel (X coordinate) and 189mm out of the detector channels plane (Z coordinate) (Fig. 3.11). The other position information (Y coordinate) is not sensitive to this angular change. The scattering angle θ changing with the channel number was plotted in Fig. 3.10(c) with a dotted line when the sample location was at the point (45.5, -15, 189)mm relative to the center of the first channel of the detector as shown in Fig. 3.11. The estimated position matched well with the real value in the experiment.



(a) Compton peak as a function of the channel No.



(b) Energy of the Compton peak as a function of the channel No.



(c) Angular locations of the sample as a function of the channel No.

Figure 3.10 Characteristics of the collected spectrum as functions of the relative locations of the sample and the channels of the detector

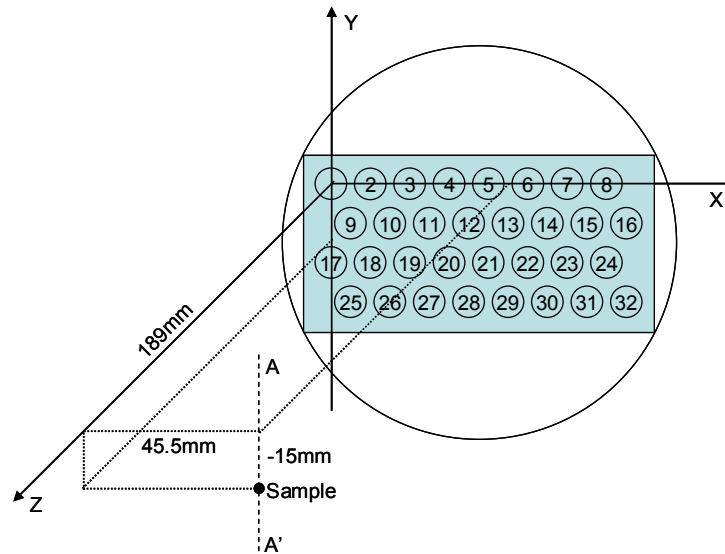


Figure 3.11 Estimated sample position. It was along A-A' since the angular change θ is not sensitive to the Y-coordinate.

3.2.3 Quality Factor

Leclair and Johns divided SNR by $\sqrt{K_c^{air}}$, the square root of the air collision kerma, to normalize the variations of x-ray tube output and measurement time and used this parameter to compare imaging systems with the scattered x-rays at different angles [69, 70]. For our case, a quality factor was developed by integrating the influence of SNR, radiation surface dose (D_s), and spatial resolution together to make the imaging systems comparable and evaluable irrespective of the imaging conditions. The quality factor is defined as

$$Q \equiv \frac{SNR^2}{D_s A_{pixel}} \quad (3.28)$$

where A_{pixel} is the area of the pixel. Considering the units for surface dose and spatial resolution are Gy and mm squared, the unit for quality factor is $mGy^{-1}mm^{-2}$.

Considering the theoretical value of SNR can be estimated by Eq. 3.16 as long as the detected photon count is in Poisson distribution for KES imaging and the surface dose can be calculated by Eq. 3.19, we can have theoretical value of the quality factor as shown in Eq. 3.29. It is obvious that theoretically the quality factor is a constant for a certain amount of the contrast agent with its matrix material at certain energy for KES imaging. Although taking more than one image set can improve the SNR of the contrast agent image, it can not improve the quality factor.

$$Q = \frac{\left(\Delta \left(\frac{\mu}{\rho} \right)_C \rho_C t_C \right)^2 e^{-\left(\frac{\mu}{\rho} \right)_M \rho_M t_M} \rho}{2 \left(1 + e^{-\left(\frac{\mu}{\rho} \right)_M \rho_M t_M} \right) E_{ph} \mu_{ea}} \quad (3.29)$$

The theoretical quality factor sets an upper achievable limit for the imaging techniques such as KES as long as the noise is Poisson distributed. The imaging method which obtains a quality factor close to the limit is optimal because it indicates the noise from other sources, such as the vibration of motor motion, in the imaging system is low. A low quality factor compared to the Poisson value indicates the presence of additional noise which may be improved by some methods, such as changing electrical equipment, trying another alignment, including more recording channels, etc.

3.2.4 Harmonics Analysis

At synchrotron facilities, the spectrum of the beam delivered by the monochromator to the experimental hutch is determined by some parameters of the facility. For example, in the CLS where our experiments were done, the electron beam energy E_R is 2.9GeV. The magnetic field strength B of the wiggler used on the HXMA beamline is 1.9T. So the critical energy of the beamline E_C is 10.63keV which is calculated by [71]

$$E_C = 0.665E_R^2B \quad (3.30)$$

The spectrum of the beam is shown in Fig. 3.12 when electron beam is at its normal operation current 200mA.

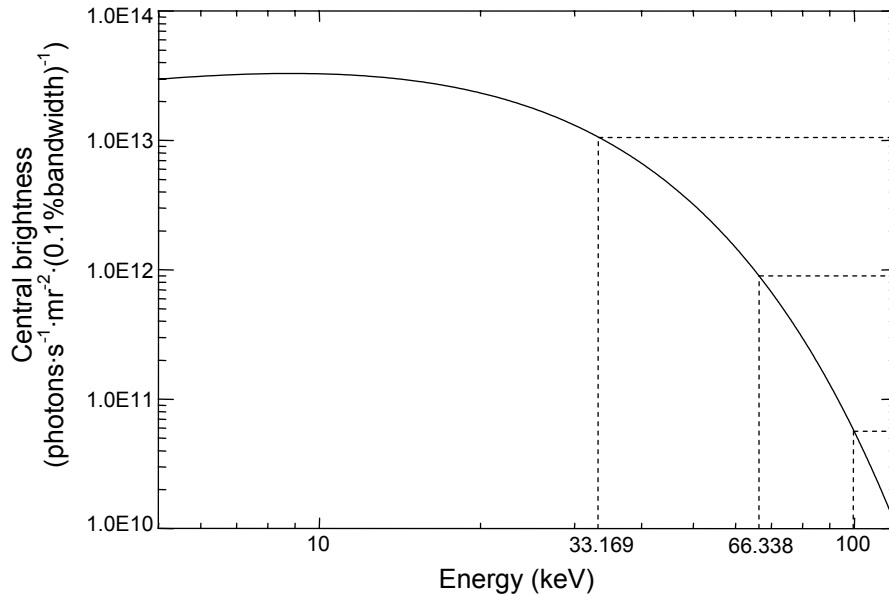


Figure 3.12 Spectrum of the beam delivered by the HXMA wiggler

According to the spectrum in Fig. 3.12, the central brightness for the beam at 33.169keV is 1.065×10^{13} photons/(s·m²·0.1%bandwidth) while the central brightness for the higher order harmonics at 66.338keV and 99.507keV are 8.987×10^{11} photons/(s·m²·0.1%bandwidth) and 5.845×10^{10} photons/(s·m²·0.1%bandwidth) respectively. This means the 2nd and 3rd higher harmonics are 8.44% and 0.55% of their fundamentals in the beam. So denote

$$R_s = [100\% \quad 8.44\% \quad 0.55\%]$$

where R_S is the composition ratio of the beam delivered from the HXMA wiggler at energy 33.169keV, 66.338keV, and 99.507keV respectively.

When double crystals are used in the beamline as monochromator which is the case in our experiments, not only the beam at the energy expected can survive but also its higher order harmonics can be reflected by the crystals to reach the object. The harmonics ruin the images since they are not at the expected energy.

Bragg's law shows that when a white beam is incident upon a Bragg crystal with an angle, only the rays at a certain energy can be reflected and the wavelength of the reflected rays λ , the incident angle θ , and the d-spacing of the crystal lattice plane d are in the following relationship:

$$\lambda = 2d \sin \theta \quad (3.31)$$

So for a certain kind of crystal, the incident angle corresponding to a certain wavelength or energy is called the Bragg angle for this energy.

It is obvious that when d-spacing of the crystal decreases to $1/n$ of the original d-spacing, the corresponding wavelength drops by $1/n$, thus allowing harmonics to be present.

The crystal used in the HXMA is Si(2,2,0). Figure 3.13 shows the reflectivity of the 2nd crystal when the 2nd crystal is rocked relative to the 1st one which is also called rocking curve. The solid line is for the beam at 33.169keV while the dashed line is for the beam at 66.338keV and the dotted line for 99.507keV.

When the 2nd crystal is in accurate alignment with the 1st one, the reflectivity is the same for the fundamental and its harmonics. Although detuning the 2nd crystal from the 1st one causes the drop of the reflectivity of the fundamental, the reflectivity drops much faster for the higher order harmonics. When the 2nd crystal is detuned to have 50% reflectivity of the in-tune fundamental reflectivity, the reflectivity of the 2nd and 3rd order harmonics decrease to 0.68% and 0.06% of their in-tune reflectivity respectively. So in the experiments, the 2nd crystal is detuned to 3.88 μ r or -3.88 μ r relative to the Bragg angle for the beam at 33.169keV to get 50% of its original reflectivity and reject its higher order harmonics which decreases to 0.68% and 0.06% of their original reflectivity for 2nd and 3rd order harmonics respectively. So

$$R_m = [50\% \quad 0.68\% \quad 0.06\%]$$

where R_m is the ratio of the reflectivity relative to the original reflectivity corresponding to the in-tune setting of the monochromator.

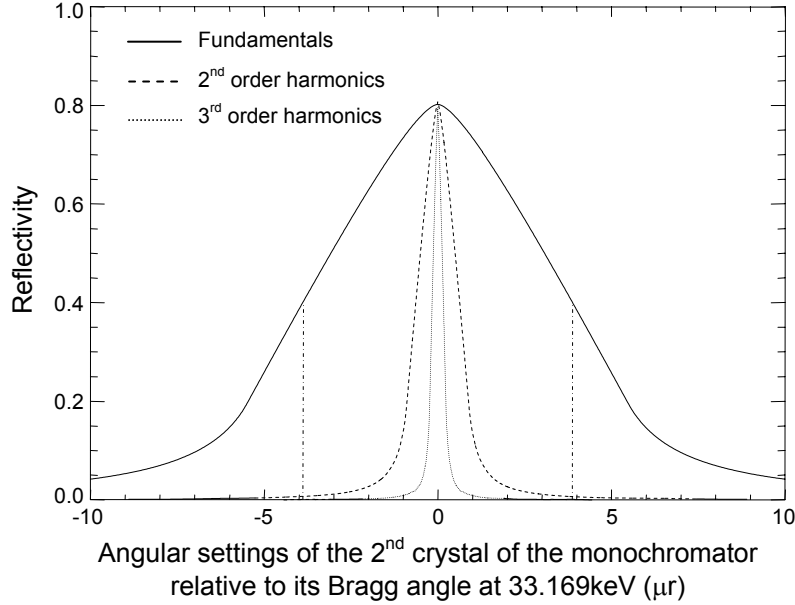


Figure 3.13 Reflectivity of the fundamentals (33.169keV) and its 2nd and 3rd order harmonics (66.338keV and 99.507keV) by Si(2, 2, 0) monochromator

Normally in KES imaging, the absorber is needed to control the surface dose for the object and prevent the detector from overflow. Since the beam with higher energy is attenuated less in the absorber and object, the higher order harmonics are more likely to reach the detector. The ratio of the fundamental and its harmonics after the absorber and the object R_o depends on the absorber and the object which will be discussed for each specific experiment.

The detector is collecting the number of photons which are stopped by the scintillator layer of the detector. The scintillator used in the transmission detector (Photonic Science X-ray FDI VHR 90mm) in the experiments is 7.5mg/cm² Terbium-doped gadolinium oxysulfide which can stop 6.27% of the fundamental, 4.23% of the 2nd order harmonics, and 3.25% of the 3rd order harmonics. So

$$R_D = [6.27\% \quad 4.23\% \quad 3.25\%]$$

where R_D is the ratio of the photons at those three energies stopped by the scintillator of the detector when the incident photon numbers are the same for all three energies.

So the detected photon composition at different energies can be calculated by

$$R = R_S R_m R_O R_D / \sum R_S R_m R_O R_D \quad (3.32)$$

3.3 Experiments and Results

All the experiments were conducted on the HXMA beamline at the CLS. The energy range on this beamline is 5-40keV. The beam was monochromated by a Si (2, 2, 0) double crystal monochromator and was unfocused. The high energy was selected as 33.269keV while the low energy was 33.069keV. The total energy bandwidth was 3.78eV which includes the intrinsic energy bandwidth (1.66eV) caused by the Darwin width of the crystal and the divergent energy bandwidth (2.12eV) caused by the divergence of the incident beam (6.4 μ m for HXMA). The flux of the beam was about 2.0×10^9 photons $\text{mm}^{-2} \text{s}^{-1}$ at normal ring operating conditions of 130mA.

3.3.1 The 1st Experiments and Results

The first experiment was done in July, 2005. The experiment was to verify that the KES method is possible using film detectors. In the experiment, the images were collected by mammography film and digitalized afterward by scanning with an EPSON Perfection 2480/2580. The test object in the experiments as illustrated in Fig. 3.14 was a cubic Lucite cup full of water with 3 identical Lucite cuvettes filled with sodium iodide water solution in different concentrations: 2mM, 10mM and 50mM. The inner dimension of the Lucite cuvette is 10mm \times 5mm. In this thesis, the unit of the concentration of the solution employs mM other than mg/cm³. The conversion from mM to mg/cm³ is as

$$1\text{mM} = 0.127\text{mg}/\text{cm}^3$$

Figure 3.15 shows the high energy image, low energy image, and the calculated iodine image, equivalent water image of the test object according to Eq. 3.8 and Eq. 3.9. The iodine image shows the interpreted projected iodine amount in mM-cm. Only the most concentrated iodine solution is visible with a SNR of 0.5 due to significant of noise involved during the scan.

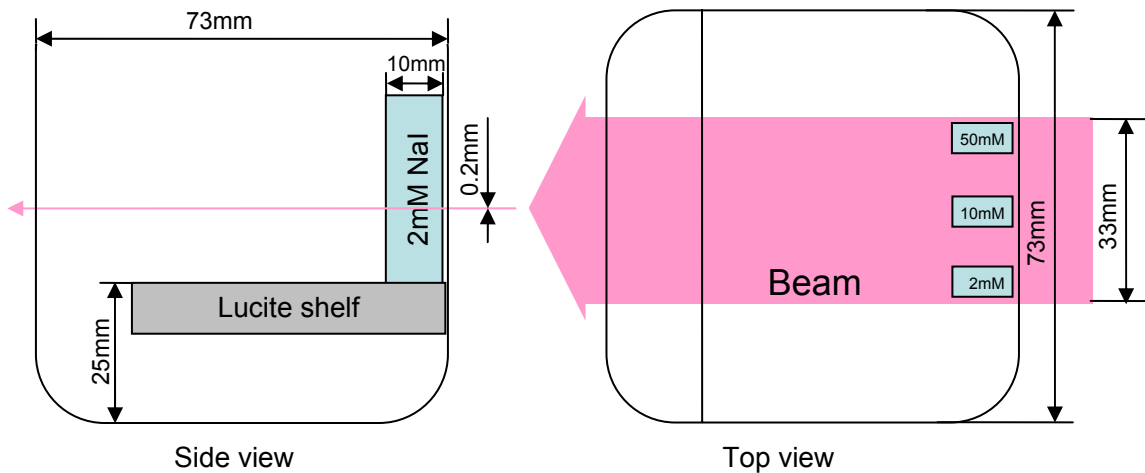


Figure 3.14 Illustration of the test object in the 1st experiment and the incident beam

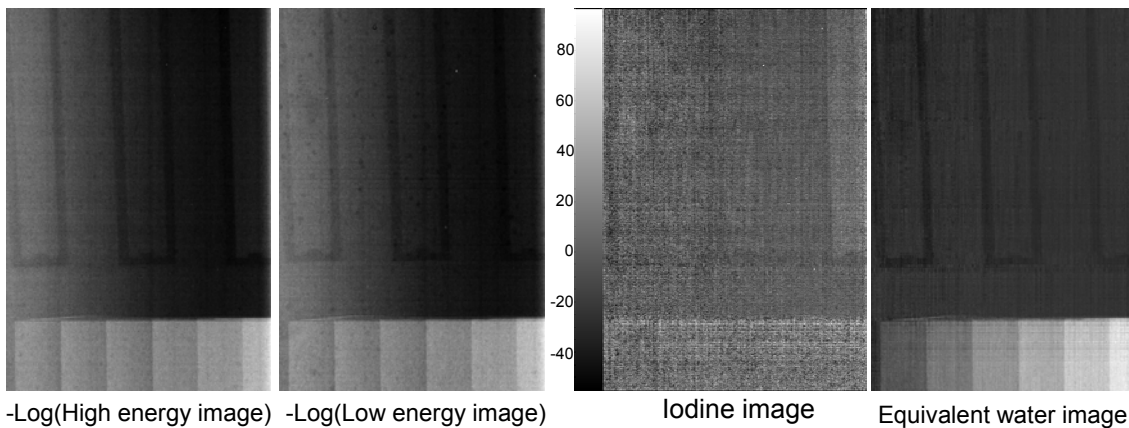


Figure 3.15 Result images of the test object in the 1st experiments

3.3.2 The 2nd Experiments and Results

The second experiment was done in Sep., 2005. A photo-stimulable phosphor (image plate) detector was used with a read-out pixel size of $50\mu\text{m}^2$ instead of the mammography film. The test object was improved as shown in Fig. 3.16. More cuvettes with iodide solutions in different concentrations, 1mM, 2mM, 10mM, 50mM, and 100mM, were delicately aligned in the same cup to get full usage of the beam width (The outer dimension of the cuvette is $13\text{mm}\times 13\text{mm}$).

The incident beam size was 35mm in width and 0.2mm in height limited by a horizontal slit. The object was scanned through the beam cross section at a speed of

3.175mm/s. In the resulting images shown in Fig. 3.17, the 100mM and 50mM iodide solution are very clear with SNRs of 10 and 5 respectively. The 10mM iodide solution can just be discerned with a SNR of 1.2. The improvement of the image was due to the change of the detector.

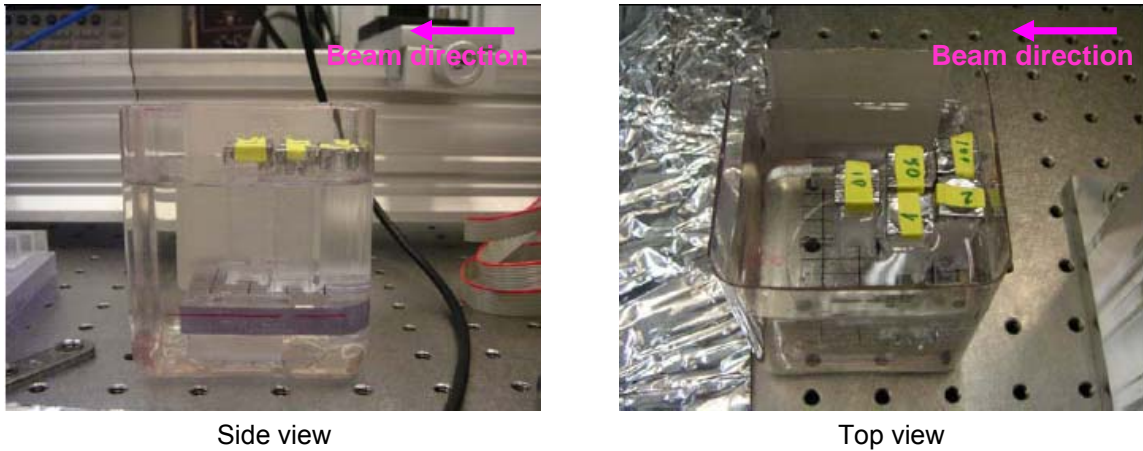


Figure 3.16 Test object in 2nd experiment

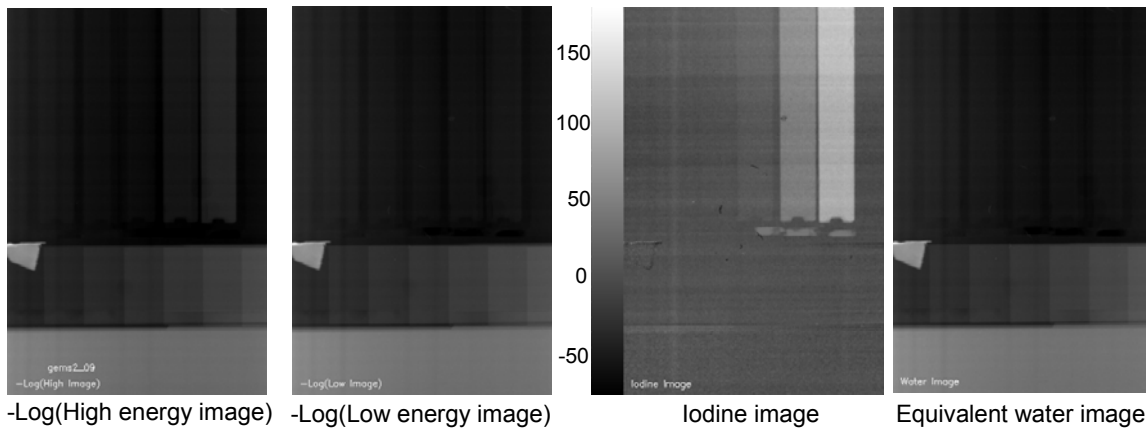


Figure 3.17 Result images of the test object in the 2nd experiments

3.3.3 The 3rd Experiments and Results

The KES imaging and FSI were both involved in the 3rd experiments. Test objects were designed to measure the detection limit and to simulate the real condition of a tumor in the rat head. To improve the SNR in the KES imaging, multiple image sets were taken and the quality factor was used to evaluate the imaging system.

Also, a rat head restraint was designed and fabricated to eliminate head movements [72] and a field flattener [73] to decrease the anatomy structure in the image so that the statistics of the detected signal can be pushed as high as possible within the limitation of the detector. Both devices are to improve the detection limit and the SNR of the imaging methods.

3.3.3.1 Rat Head Restraint

Figure 3.18 shows the rat head restraint fabricated by the 3-D printer in Engineering Machine Shop of the University of Saskatchewan. The restraint is to hold the rat head motionless during the imaging period. Furthermore, once the restraint is aligned in the imaging system, the accurate position of the rat head is given so that the imaging is repeatable. And this kind of restraint does not apply excessive pressure on the animal head to avoid morbidity and mortality.

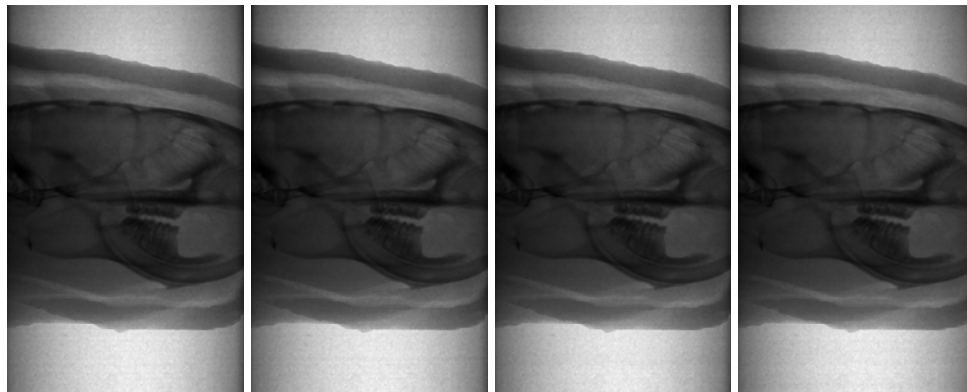


Figure 3.18 Rat head restraint fabricated by a rapid prototyper

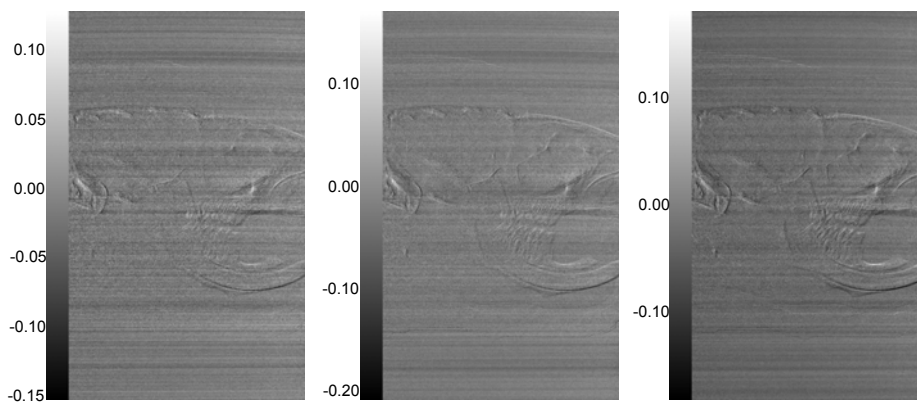
The procedures to fabricate the restraint are described as follows: At first, a living rat in the weight range of the rats used in the experiments was euthanized and frozen with its head horizontally positioned. Secondly, a CT scan was taken for the rat with an axial slice thickness of 0.625mm and a transverse plane spacing of 0.352mm and the slices from nose to the shoulder with a total length of 63.125mm were used to fabricate the restraint. An appropriate grey level threshold was set to reflect the radio-opacity level of the skin so that the contour of the rat head could be found. The contour was expanded

into a solid head mold with a thickness of 3mm. Finally the frame was added and the data was converted into *Standard Tessellation Language (STL)* format which can be read by the 3-D printer.

Figure 3.19 shows the experimental results on the test of the restraint. A demised rat head was held by the restraint. The four images shown in Fig 3.19(a) were taken at four minutes intervals. No movement or blur can be detected indicating no obvious movement of the rat head during each imaging period. However, when the difference images (image taken at 0min was subtracted from the images taken at 4min, 8min, and 12min) were calculated, some anatomy structure were shown. The images shown in Fig 3.19(b) were the difference images normalized by the image taken at 0min. An average standard deviation of 1.76% exists in the normalized difference images.



(a) Lateral view images of a rat head in the restraint taken at four minutes intervals



(b) Difference images of the first image and the others in (a) normalized by the first image

Figure 3.19 Experimental results on the restraint

This kind of restraint is easy to build and use. It is also friendly to the imaged animal; less excessive pressure on the animal and less respiratory distress compared to other type of restraints, such as bite bar, ear pin, etc. This type of restraint holds great promise in improving the quality and repeatability of images while reducing stress on experimental animals.

3.3.3.2 Field Flattener

Figure 3.20 shows a dorsal-ventral view field flattener of a rat head. The field flattener was designed to push the statistics of the detected signal to the upper limit of the detector by compensating the beam attenuation variation of the object. It is a device to make the transmitted beam equally attenuated so that a flattened image is created which does not contain any structural information of the object. The original thought of the flattener was to make each x-ray hit something in its path to prevent the detector from saturation and keep the dynamic range of the signal as small as possible in the KES experiments where the structure of the object is not interesting.

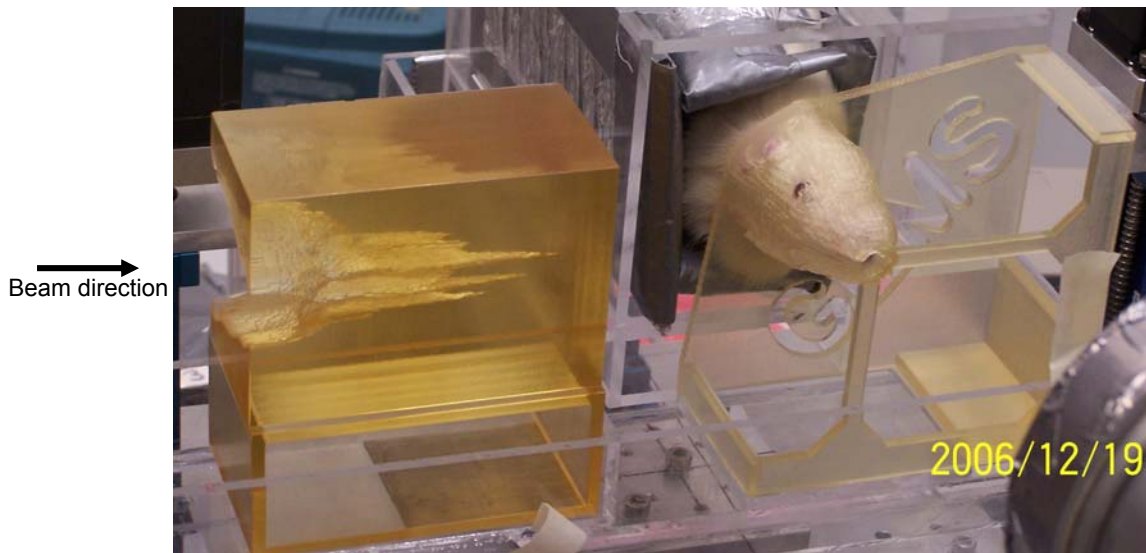


Figure 3.20 A dorsal-ventral view flattener and the rat head in its restraint in the experiment

The needed information for building the flattener is the projected attenuation of the object along the imaging direction at the imaging beam energy. For our case, the imaging direction is the lateral view and the dorsal-ventral view of the rat head. The imaging beam energies are just above and below the K-edge of the iodine, 33.169keV.

The simplest and also the best way to obtain this information is to image the object in the required view at the required energy of the beam. However, it is not practical because the synchrotron beam time is expensive and is not always available. In our case, the needed information was extracted from the CT scan data which was used to build the rat head restraint.

Facilitated by the same CT scan of a phantom whose exact composition was known, the equivalent energy of the CT scan and the detector gain can be determined. With the volume information of the object, the projected absorption lengths of the object along any direction including the imaging direction at the required imaging energy can be calculated and they can be converted into the equivalent thicknesses of the material used to fabricate the flattener. Once the thickness of the flattener is determined, the equivalent thickness should be deleted from the whole thickness of the flattener to determine the thickness of the flattener at this point (pixel). A support frame was added and the whole flattener information was converted into the STL format which can be read by the 3-D printer.

3.3.3.3 K-Edge Subtraction Imaging Experiments and the Results

Two test objects were designed to do the KES imaging. The first one was for the detection limit of the imaging system and so a simple geometry was employed. The second test object was a demised rat with 3 micropipettes inserted in the head. This sample is a model of a live animal system which was being investigated for gene expression studies.

3.3.3.3.1 K-Edge Subtraction Imaging Experiments with the First Test Object

The first object shown in Fig. 3.21 was designed for measurement of the detection limit of the KES system. The iodine concentration in the object was in a logarithmic distribution from 100mM to 0.01mM. The projected thickness for all solutions was 1cm.

During KES imaging, both the sample and the detector were scanned at a constant vertical speed of 2mm/s (line scan mode). The data was collected at one energy first and then at the other energy. To improve the detection limit and to investigate the SNR as a function of the incident photon count, 32 images were obtained at each energy for the test

object, of which 16 images were with the sample and 16 images were without the sample (I_0 image). On average, it took 1min for one image in dimensions of 75mm×50mm which is determined by the transmission detector.

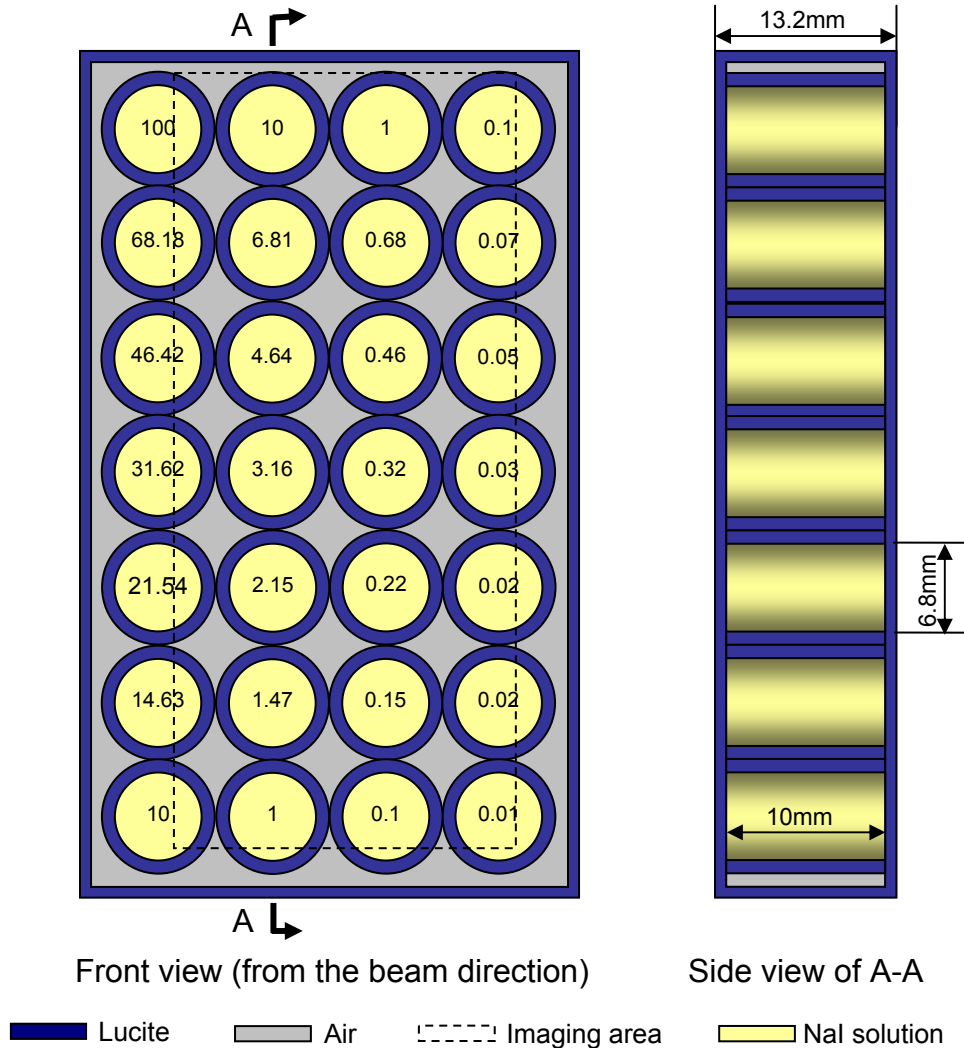


Figure 3.21 Test object in the 3rd experiments. The numbers in the iodine solution circles are the concentrations of the iodine solution in that circle in mM.

Figure 3.22 shows the experimental setup. The removable horizontal aperture (a) made the horizontal size of the beam adjustable from 30mm (for KES imaging) to 0.25mm (for FSI imaging). The slit (b) determined the vertical beam size of 0.25mm which was both for KES and FSI; The ion chamber (c) right after the slit measured the incident photon count delivered by the beamline in the restricted dimension by the aperture and the slit. The 80mm Lucite absorber (d) controlled the surface dose of the

object at 0.7mGy/image with 2mm/s scan speed for KES imaging. The Lucite absorber was taken out during FSI imaging to get more incident photon count and so the fluorescence signal. The lead walls (e) keep the scatter away from the object and the detectors. The object (f) in Fig. 3.22 was the 1st test object. It was changed to the 2nd test object and real animals afterwards. The fluorescence detector (g) had been introduced in detail in Section 3.2.2.3. It was positioned perpendicular to the incident beam at a distance around 150mm to collect fluorescence signal. The transmission detector (h) was a cooled *Charge-Coupled Device (CCD)* detector (Photonic Science X-ray FDI VHR 90mm, Photonic Science Limited, UK) with a pixel size of 18.7 μm^2 .

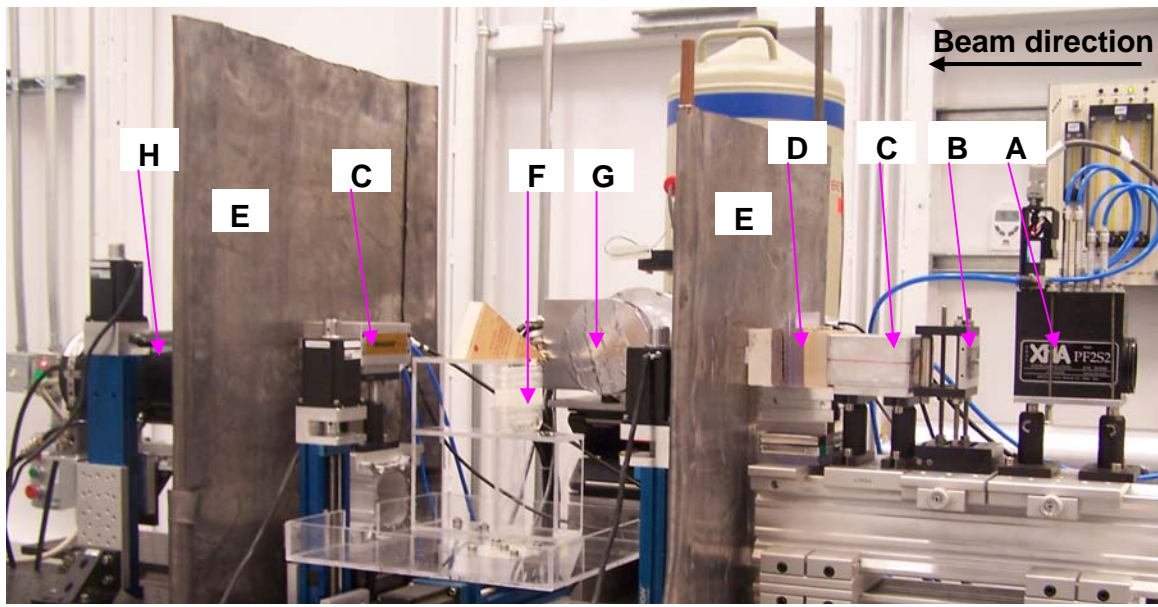


Figure 3.22 Experimental setup in the 3rd experiments: (A) Horizontal aperture; (B) Slit; (C) Ion chamber; (D) Lucite absorber; (E) Lead wall; (F) Object; (G) Fluorescence detector; (H) Transmission detector

The transmission ratio R_o of the Lucite absorber and the object (estimated as 1cm water) for the beam at 33.169keV, 66.338keV, and 99.507keV is [5.57%, 14.03%, 17.62%]. So 99.98% of the detected signal is at the expected energy, 33.169keV, according to Eq. 3.32.

Figure 3.23 is the high energy image, low energy image, iodine image and the equivalent water image of the test object. In the iodine image, the iodine in the circle down to 4.64mM-cm projected iodine amount is clearly visible. Some air bubbles can be seen in the images which indicate the imperfection of the object. The contrast in the

image is driven by the circle with 100mM-cm projected iodine amount. To eliminate this effect, the high energy image and low energy image were partitioned by the circles and processed separately. The iodine images for each circle of the left two columns of the object are shown in Table 3.1. The circle with a projected iodine amount of 3.16mM-cm can be clearly discerned and even the circle with a projected iodine amount of 2.15mM-cm is visible when 4 and more image sets were used in the calculation. Since each image set was taken independently, more image sets involved in the calculation can be considered as more incident photon illuminated the object if the image sets were added together.

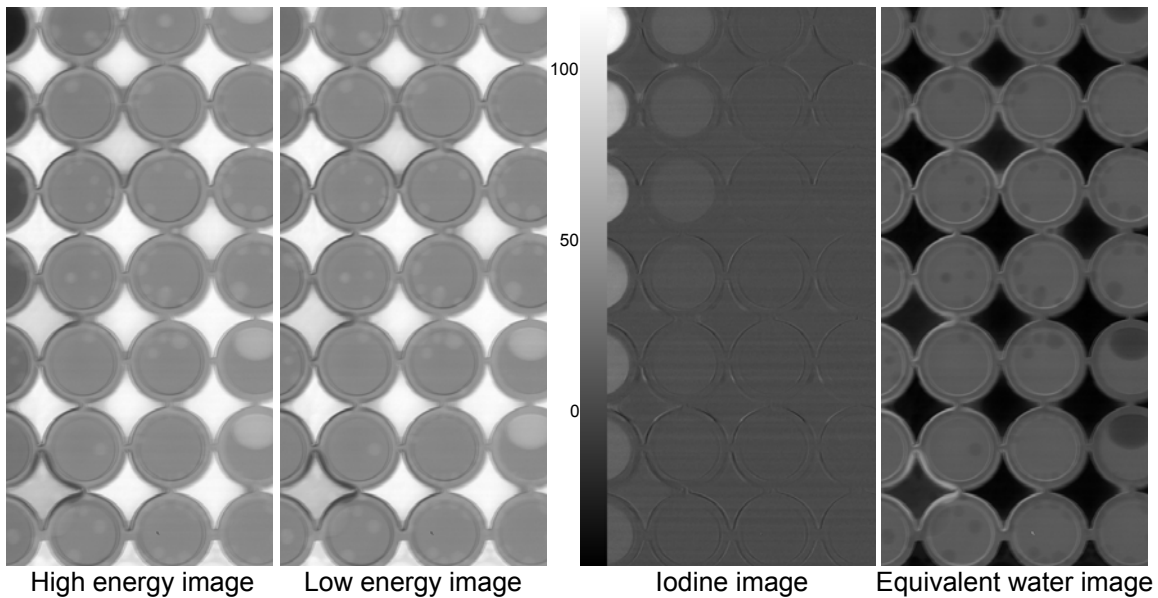


Figure 3.23 Resulting images of the test object

Table 3.2 shows the x-ray measured signals compared to the expected or theoretical values based on the concentration and the thickness of the contrast material. The measured signal is the average of the pixel value in the signal area. As predicted in Eq. 3.16, the higher SNR was acquired with more image sets. The measured signals obtained from 8 image sets and the corresponding errors are listed in Table 3.3. The estimated errors were the median of the values bigger than the measured signal and the median of the values smaller than the measured signal.

Table 3.1 Iodine images obtained with different image sets and different projected iodine amount

Iodine amount	Measured value changes with the number of the image sets							
	1	2	3	4	5	6	7	8
1.47								
2.15								
3.16								
4.64								
6.81								
10.0								
14.68								
21.54								
31.62								
46.42								
68.13								
100.0								

Table 3.2 Theoretical and measured value of the projected iodine amount in mM-cm

Theoretical value	Measured value changes with the number of the image sets							
	1	2	3	4	5	6	7	8
1.47	1.58	1.07	1.30	1.39	1.42	1.58	1.54	1.50
2.15	2.22	2.23	2.18	2.23	2.15	2.38	2.47	2.44
3.16	4.26	4.28	4.26	4.20	3.97	3.94	3.94	3.70
4.64	5.65	5.52	5.13	5.35	5.49	5.60	5.56	5.48
6.81	8.27	7.80	7.56	7.52	7.56	7.66	7.65	7.68
10.0	11.61	11.31	11.18	11.33	11.58	11.70	11.82	11.75
14.68	14.72	14.22	14.60	14.85	14.79	14.88	14.90	14.81
21.54	22.72	22.30	22.53	22.76	22.70	22.71	22.87	22.73
31.62	35.80	35.67	35.99	36.01	35.81	35.64	35.67	35.50
46.42	55.01	54.67	54.60	54.93	55.04	55.05	55.03	54.88
68.13	71.71	70.31	70.60	70.67	70.71	70.69	70.72	70.60
100.0	108.76	108.34	108.61	108.82	108.99	109.07	109.23	108.98

Table 3.3 Measured signals from 8 image sets and their corresponding errors (mM-cm)

Signal	1.50	2.44	3.70	5.48	7.68	11.75	14.81	22.73	35.50	54.88	70.60	108.98
Error(+)	1.54	1.60	1.52	1.53	1.47	1.48	1.88	1.97	2.03	2.12	2.11	2.46
Error(-)	1.52	1.59	1.53	1.57	1.48	1.51	1.91	1.96	2.05	2.14	2.12	2.51

Since the iodine concentration in the object was designed in a logarithmic distribution, the logarithmic plots of the theoretical and measured projected iodine amounts and a linear fitting of the measured values are shown in Fig. 3.24. The

horizontal coordinate is selected as the theoretical iodine concentration in the logarithmic plot to make the slope of the theoretical line 1 and the intercept 0. The error bars were not plotted in the figure because of the logarithmic plot which expands small errors while compressing big errors. The slope of the fitted line is 0.994 and the intercept is 0.05. Since the projected iodine amount is the multiplication of its concentration and thickness in the beam direction, the systematic error in the measured projected iodine amount shows as a translation from the theoretical signal line in Fig. 3.24.

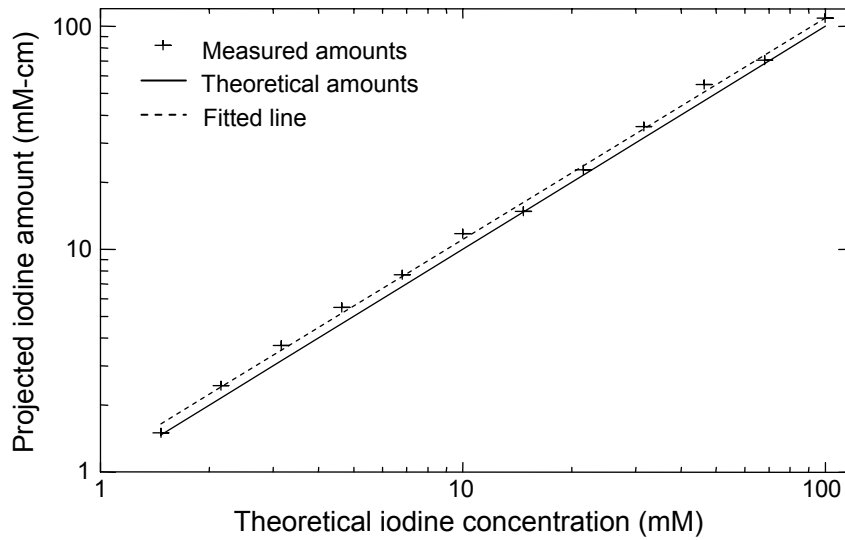


Figure 3.24 Logarithmic plots of the theoretical and measured projected iodine amounts and a linear fitting of the measured values. The error bars didn't show because of the logarithmic plot which expands small errors while compress big errors. The measured and theoretical values in the plots can refer to Table 3.3 and Table 3.2 respectively.

Table 3.4 lists the measured SNR changes with the projected iodine amount and the number of image sets used to obtain the iodine image. SNRs were measured by the iodine images shown in Tab. 3.1. Table 3.5 lists the theoretical SNRs of the test object with the incident photon count of 8.6×10^4 /pixel for one image set. The photon count were calculated by Eq. 3.17 with the measured current of the ion chamber of 48.13nA. The objects other than iodine in the beam were 9.362cm thick Lucite, 1cm thick water, and the same projected amount of sodium as that of iodine. The theoretical SNRs were estimated by Eq. 3.13.

Table 3.4 Measured SNRs of the projected iodine amount of the iodine image obtained with different number of image sets for 1st object in the 3rd experiment

Iodine amount	The number of the image sets to obtain the iodine image							
	1	2	3	4	5	6	7	8
1.47	0.25	0.24	0.35	0.42	0.50	0.60	0.65	0.66
2.15	0.34	0.48	0.58	0.68	0.72	0.86	0.98	1.03
3.16	0.64	0.96	1.14	1.29	1.38	1.49	1.64	1.63
4.64	0.85	1.21	1.40	1.70	1.98	2.18	2.37	2.37
6.81	1.32	1.79	2.17	2.51	2.81	3.06	3.31	3.49
10.0	1.86	2.52	3.11	3.59	4.14	4.57	4.97	5.29
14.68	1.86	2.60	3.21	3.73	4.22	4.57	4.95	5.26
21.54	2.79	3.83	4.77	5.43	6.10	6.53	7.34	7.73
31.62	4.33	6.26	7.44	8.32	9.32	9.98	10.66	11.41
46.42	6.45	9.35	11.43	13.27	14.60	15.60	16.55	17.17
68.13	8.76	12.26	14.79	16.71	18.54	19.80	20.83	22.10
100.0	11.80	16.60	19.75	22.57	24.65	26.81	28.44	29.18

Figure 3.25 plots curves of the SNRs changing with the number of the images sets used to obtain the iodine image. Only the curves for 100mM projected iodine amount were shown. The measured value is below the theoretical value as expected and indicates that there was noise beyond that considered in the theoretical derivation of SNR. This noise could arise from the beam variation, object vibration with the motor motion. The SNR increases with the number of image sets which is proportional to the incident photon count. However, the measured SNR does not gain as much as the theoretical SNR because of the intensity variation of the beam between the acquisition of the images. The

intensity variation of the beam can systematically increase or decrease the detected projected iodine amount since the flat field image (I_{0H} or I_{0L}) and the object image (I_H or I_L) were taken at different times. However, this error can be compensated by the detected amount of iodine of the background where no iodine is present. In the calculation, an iodine concentration of 2.43mM-cm was found in the background and had been deleted from the measured iodine signals. One source of the intensity variation of the beam is the vibration of the double-crystal monochromator which can dramatically change the intensity of the beam.

Table 3.5 Theoretical SNRs with different projected iodine amount and the number of image sets for the 1st object in the 3rd experiment

Iodine amount	Theoretical SNR changes with the number of the image sets							
	1	2	3	4	5	6	7	8
1.47	0.21	0.30	0.36	0.42	0.47	0.51	0.55	0.59
2.15	0.31	0.43	0.53	0.61	0.69	0.75	0.81	0.87
3.16	0.45	0.64	0.78	0.90	1.01	1.10	1.19	1.27
4.64	0.66	0.94	1.15	1.32	1.48	1.62	1.75	1.87
6.81	0.97	1.37	1.68	1.94	2.17	2.38	2.57	2.75
10.0	1.43	2.02	2.47	2.85	3.19	3.49	3.77	4.03
14.68	2.09	2.96	3.62	4.19	4.68	5.13	5.54	5.92
21.54	3.07	4.34	5.32	6.14	6.86	7.52	8.12	8.68
31.62	4.51	6.37	7.80	9.01	10.07	11.04	11.92	12.74
46.42	6.61	9.35	11.45	13.22	14.78	16.19	17.49	18.70
68.13	9.69	13.71	16.79	19.39	21.68	23.75	25.65	27.42
100.0	14.21	20.10	24.62	28.43	31.78	34.82	37.61	40.20

The detection limit can be defined as the projected iodine amount which has a SNR no less than 1. In this experiment, the detection limits are 2.15mM-cm with 8 image sets

(a radiation dose of 11.2mGy), 3.16mM-cm with 3 image sets (a radiation dose of 4.2mGy), 4.64mM-cm with 2 image sets (2.8mGy), and 6.81mM-cm (1.4mGy).

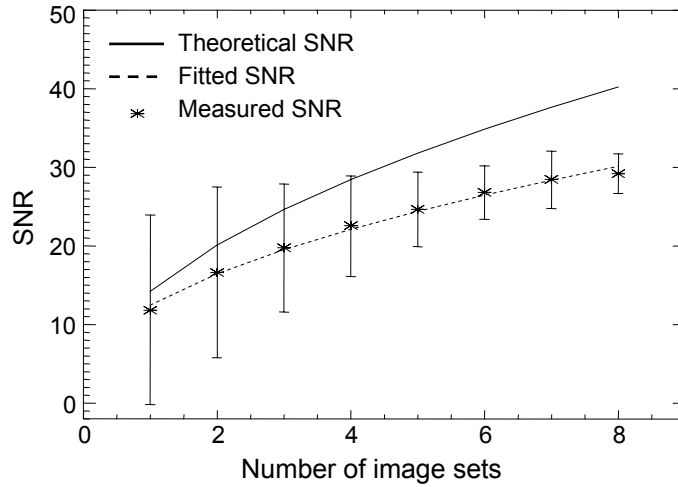


Figure 3.25 The theoretical and measured SNRs for 100mM projected iodine amount as a function of the number of the image sets used to obtain the iodine

The quality factor is calculated based on one image set to ignore the temporal variation of the beam intensity. The image system achieved a quality factor of $284/\mu\text{Gy}/\text{mm}^2$ which was 69% of the upper limit of $412 \mu\text{Gy}^{-1}\text{mm}^{-2}$ at a location where the projected iodine amount was 100mM-cm in spite of the beam intensity variation and the vibration caused by the motor motion. It is noticeable that the measured SNRs are bigger than the theoretical ones when the theoretical projected iodine amounts are equal or less than 10mM-cm. This might be raised by the systematic error in the theoretical values of $\rho_C t_C$ and $\rho_M t_M$ which is also indicated in Fig. 3.24.

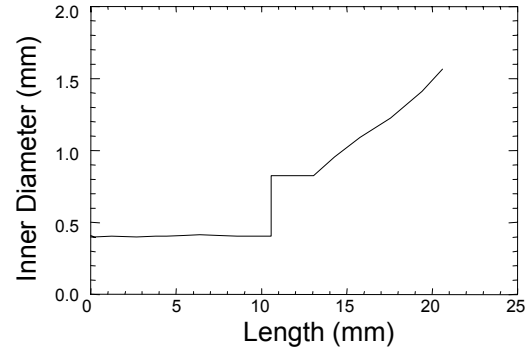
3.3.3.3.2 K-Edge Subtraction Imaging Experiments with the Second Test Object

Also, to model a live animal system which was investigated in gene expression studies, a demised rat with 3 micropipettes inserted in the head was imaged in the experiments to simulate the accumulated iodine by the transgenic cancer cells in living rat head. One of the micropipettes is shown in Fig. 3.26(a) and the inner diameters changing with the length of the micropipette is shown in Fig. 3.26(b). In the experiments the three exact same micropipettes were full of solutions of sodium iodide in water in

different concentrations, 50mM, 10mM, and 1mM. The rat's head was held by the previous introduced restraint.



(a) Picture of a micropipette



(b) Inner diameter of the micropipette

Figure 3.26 The micropipette used in the experiments

Figure 3.27 and 3.28 shows the resulting high energy image, low energy image, iodine image, and the equivalent water image of the lateral view and the dorsal-ventral view of the rat respectively. In the iodine images of both views, the micropipette filled with the iodine solution in the concentration of 50mM can be clearly discerned. The micropipette with 10mM iodine solution is also visible in the lateral view image. Also in the iodine images, the beam variation and the anatomy structure of the rat head are clear because the original images (high and low energy images w/o object) were taken at different times and the intensity of the beam changes with time. The vibration of the motor motion makes the problem worse.

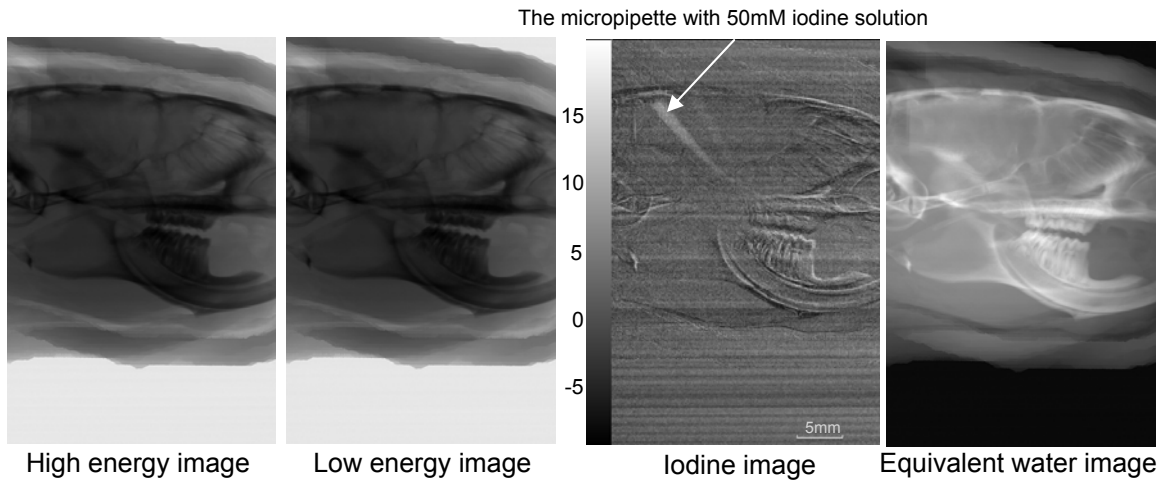


Figure 3.27 KES resulting images of the lateral view of the demised rat head

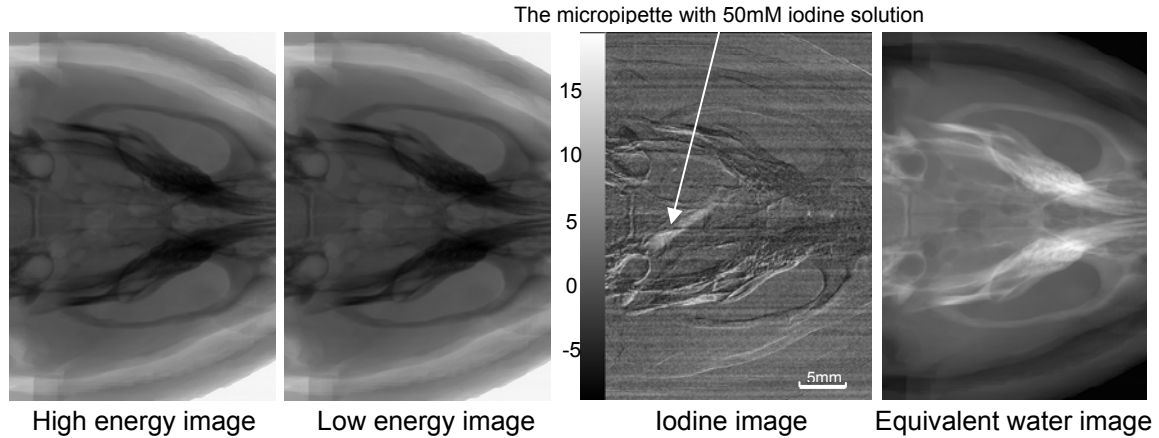


Figure 3.28 KES resulting images of the dorsal ventral view of the demised rat head

To investigate the SNR dependence on the incident photon count, different number of the image sets were used to extract the iodine images. Figure 3.29 shows the local iodine images with the micropipette filled with the 50mM iodine solution extracted from the different number of the image sets. The SNR was measured at the location of A-A cross section (Fig. 3.29) of the image which corresponds to a projected iodine amount of 10mM-cm. The inner diameter of the micropipette at this location was 1.4mm and the micropipette was inserted in a 45° with the beam direction so that the total length of the iodine solution in the beam was 2mm. The stripes in the images have been smoothed away using a median filter algorithm. The measured SNRs were plotted in Fig. 3.30. The errors were estimated by the signal variances of the cross sections above A-A and

below A-A. The theoretical SNRs were not shown together because of the difficulties in estimation the anatomy composition of the rat head.

The image system with the 2nd test object achieved a quality factor of $5.43/\mu\text{Gy}/\text{mm}^2$ at the same location as where the measured SNR was conducted with 1 image set. It is smaller than the quality factor achieved by the imaging system with the 1st test object at the same projected amount of iodine, which is $7.1 \mu\text{Gy}^{-1}\text{mm}^{-2}$, because of the complicated matrix material in which the micropipette was imbedded and the $\rho_{M}t_M$ is more than that of the 1st test object, which decreases the upper limit of the achievable quality factor.

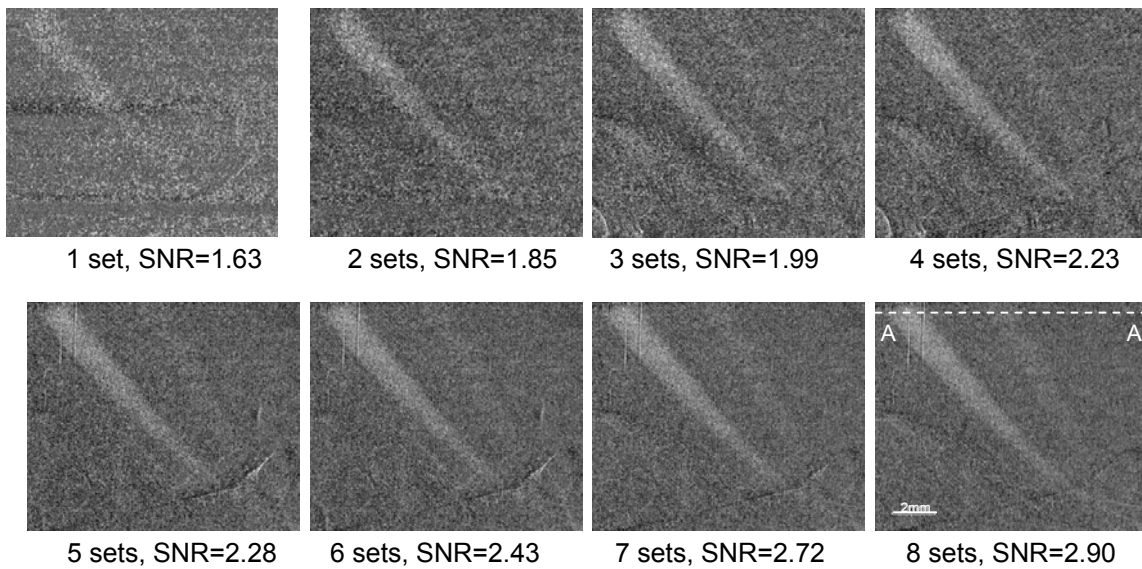


Figure 3.29 Local iodine images obtained from different image sets. The SNR shown for each iodine image was measured at A-A cross section which corresponds to a projected iodine amount of 10mM-cm. The radiation dose for one image sets was 1.4mGy.

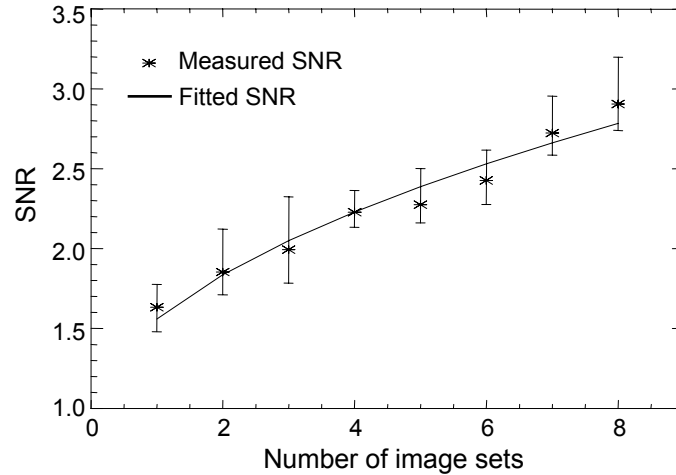


Figure 3.30 The measured SNRs as a function of the number of the image sets used to obtain the iodine images. The SNR was measured along A-A cross-section shown in Fig. 3.21 which corresponds to a projected iodine amount of 10mM-cm. The errors were estimated by the signal variances of the cross

Figure 3.31 shows the resulting images from 8 image sets when the flatteners of the lateral view and the dorsal-ventral view were used in the imaging system. Compared to Fig. 3.27 and Fig. 3.28 which were obtained without the flattener, the anatomy structures of the rat head in Fig. 3.31(a) and (b) were blurred and the SNRs of the iodine images were improved from 2.90 to 3.24 in the lateral view and from 2.35 to 3.26 in the dorsal-ventral view. The SNRs were measured along the dotted line in the iodine images. The improvement of SNR in the dorsal-ventral view is significant.

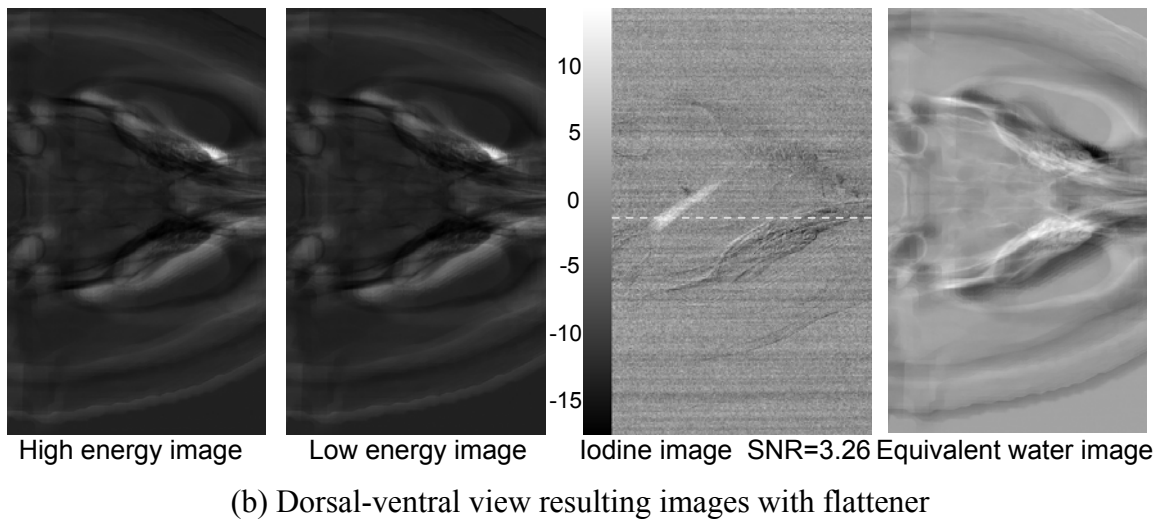
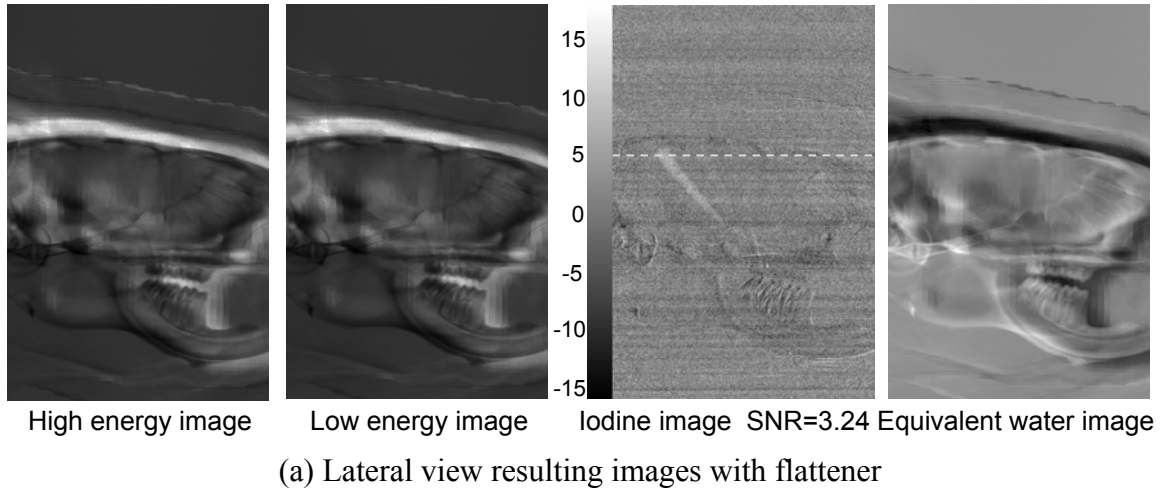


Figure 3.31 The Resulting images from 8 image sets with flatteners. The SNR was measured along the line drawn in the corresponding image.

An interesting fact for a ‘perfect built and perfect aligned’ flattener is that it should completely remove all anatomical structure from the image. Thus it is possible, in principle, to obtain an iodine image directly due to the increased absorption that is not compensated by the flattener. Also, the exposure to the object is not uniform as is usually the case in imaging; the dose spatially varies across the entrance surface leading to a constant exposure at the detector. This leads to a unique situation where the subject exit dose is uniform, rather than the entrance dose. This also makes the calculation of the quality factor impossible.

3.3.3.4 Fluorescence Subtraction Imaging Experiments and the Results

FSI experiments were done with the 2nd object, a demised rat head with 3 identical micropipettes inserted in which were full of iodine solution in different concentrations: 50mM, 10mM, and 1mM using the experimental setup shown in Fig. 3.22. In FSI experiments, the spatial resolution was 0.25mm×0.25mm determined by the pencil beam size with the considerations of beam flux, iodine concentration, feasible imaging time, and the sensitivity of the fluorescence detector. The sample was raster scanned at 0.25mm/s. The scan area was 20mm×18mm around the iodine micropipettes region. It took about 90min for one image set with a surface dose of 272mGy. To control the experiment time, only the first column of 4 channels of the detector (channel 1, 9, 17, 25) were used in the experiments to collect signal. An energy window was set at the iodine fluorescence line (28.600keV) with a window of 100eV. A Soller slit [74] was used to reduce the Compton scatter.

Figure 3.32 shows the original fluorescence images at high and low energy, and the iodine image obtained by subtracting the low energy image from the high energy image. The images from 4 channels of the detector were simply added because the channels are all arranged at approximately the same scattering angle. In the iodine image, two (filled with 50mM and 25mM iodine solution respectively) of the micropipettes are clearly visible. The other one (filled with 10mM iodine solution) can not be discerned because of the low projected amount of iodine. The Compton scatter which carries the information of the anatomy structure is obvious in the original high and low energy images and is completely removed by the subtraction.

The highest SNR (12.8 ± 2.1) in the fluorescence iodine image is achieved at the location where the inner diameter of the micropipette with 50mM iodine solution is 1.23mm (the path length is approximated as $1.414\times$ inner diameter since the micropipette was inserted 45° to the beam incident direction). At the same place or the same projected iodine amount, the SNR of the KES iodine image is 2.3 ± 0.3 obtained by 8 image sets. Along the micropipette full of 50mM iodine solution, SNR in both imaging systems are decreased as the beam path in iodine solution is shortened. The FSI system can detect as small an amount as 2.83mM-cm iodine with a high SNR 6.5 ± 3.0 while KES system can not. The SNR of the FSI system can be further improved with more channels involved.

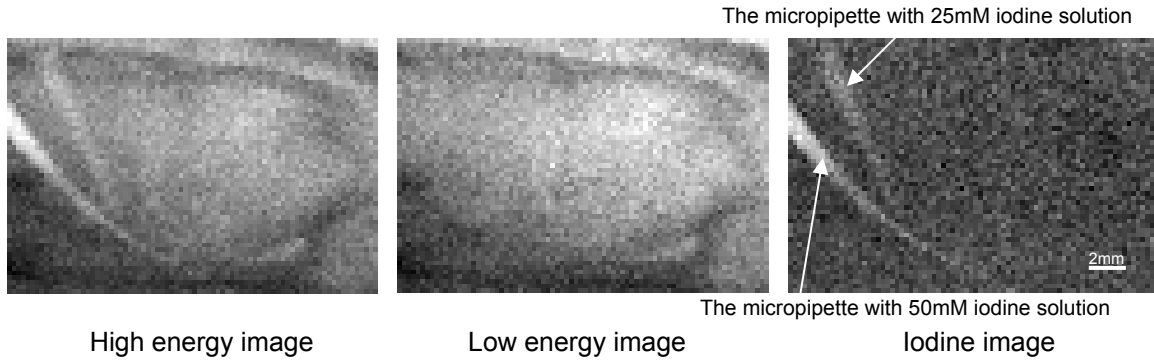


Figure 3.32 FSI experimental resulting images of the interested area from the lateral view

However, the quality factor of the fluorescence imaging system is as small as $0.01\mu\text{Gy}^{-1}\text{mm}^{-2}$ because of its huge radiation dose and poor spatial resolution.

3.3.4 The 4th Experiments and Results

The projected iodine amount is not easy to exactly measure in the micropipette because of the shape of the micropipette and the difficulties in the measurement of its insertion in the rat head. So a new sample is designed to model this living rat system. Both the restraint and the flatteners were smoothed to reduce image structure from them.

3.3.4.1 Smoothing of the Flatteners

A ‘Perfect built and perfect aligned’ flattener does not exist in the real world. Mismatch of the flattener and the imaging object can not be avoided in the experiments mainly because of the difference between the imaging object and the object used to build the flattener. In addition, the precision of the fabrication of the flattener, misalignment of the flattener and the object, and vibration during motor scan make the situation worse. The bright area in the high and low energy images shown in Fig. 3.31 were the results of the improper compensation of x-ray absorption by the field flattener. The steps in the equivalent water images indicate that a smoothed flattener may make it suitable for a ‘generic’ object.

The flattener can be looked at as a 2-D x-ray transmission image of the object in which each pixel value is the equivalent length of the material of the flattener which would have the same absorption property as the object in the projection direction. In this

way, a 3-D smoothing problem is converted to a 2-D smooth problem which can be fulfilled easily. The smoothing algorithm used was a local averaging filter applied to each pixel with the average being derived from a rectangular window centered on the pixel. The rectangular window was necessary since the spatial dimensions of the data were anamorphic.

However, rat's teeth make sharp stripes in the flattener and they are difficult to get rid of with the same smooth width which keeps the other parts of the rat reasonably smoothed. Since each slice along the axial direction of the rat head is projected onto a 1-D curve, a threshold can be set to identify the teeth in the curve and the sharp stripes over the threshold were replaced by a preset parabola function before the 2-D smoothing. The replacement keeps the maximum value of the original curve and the replaced curve at the same pixel. Figure 3.33 shows the original projected curve of a slice with the teeth and the teeth-cut curve when the threshold was set as 63.28mm (180 pixels).

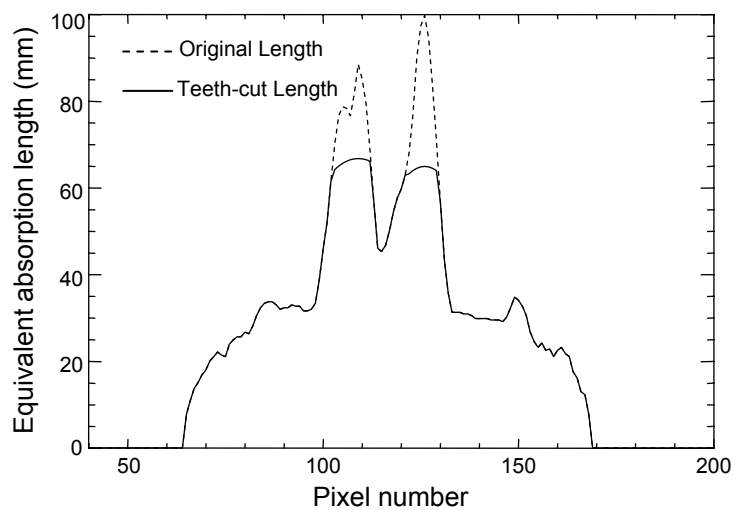
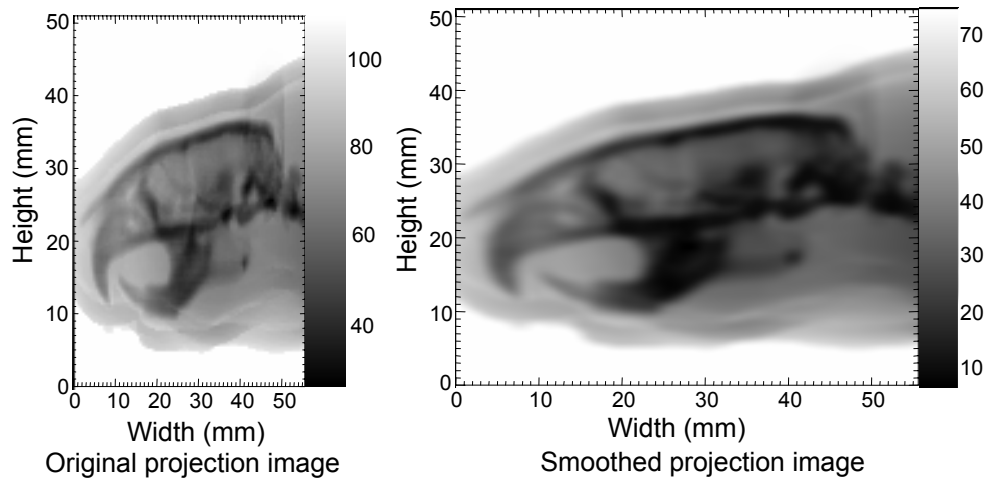


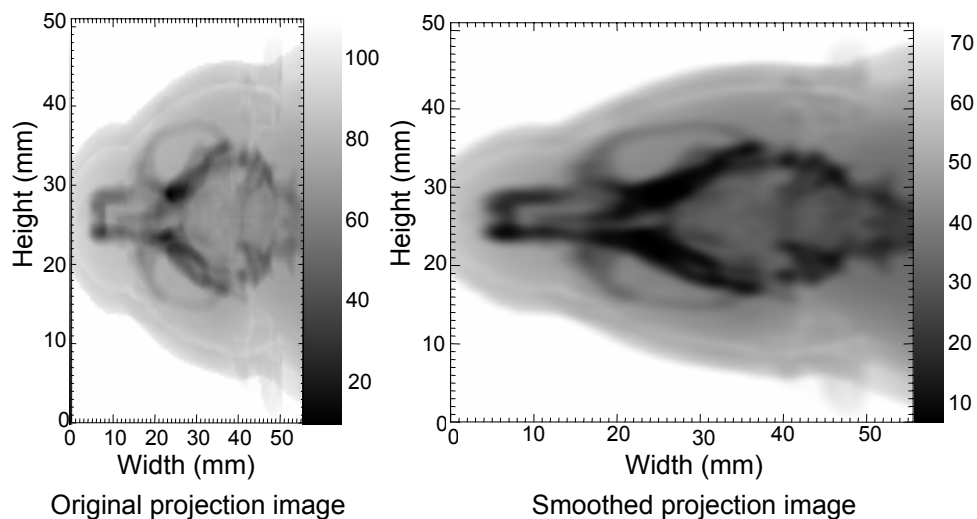
Figure 3.33 The original projected curve of a slice with the teeth and the teeth-cut curve

Figure 3.34 shows the original 2-D image and the smoothed one with the teeth cut. The grey level in the images is the thickness of the flattener at the corresponding pixel location. The pixel size for the original projection images is 0.625mm(W) × 0.352mm(H) while the pixel size for the smoothed ones is 0.03125mm(W) × 0.0352mm(H). The original images are obviously anamorphic because of the big asymmetry in pixel size (the width of the pixel is almost 2 times of the height of the pixel), while the smoothed image

is much less anamorphic because the width and the height of the pixel were selected close to each other.



(a) Original and smoothed projection images of the lateral view



(b) Original and smoothed projection images of the dorsal ventral view

Figure 3.34 The original and the smoothed projection images. The grey level in the images is the thickness of the flatteners at that pixel location (mm). The original images are anamorphic because of the asymmetry in pixel size, while the smoothed image is much less anamorphic.

3.3.4.2 Smoothing of the Restraint

The 3-D restraint is converted to 2-D axial images so that 3-D smoothing can be avoided. The inner contour of each axial slice of the restraint can be found and a point which is always in the inner of each slice's contour is defined as the origin of a polar coordinate system. The contour is converted to a curve defined in Cartesian coordinate

system on which the radial coordinate of the points on the curve changes with their angular coordinate. In this way, all the 2-D contours of the restraint can be converted to 1-D curves and the smooth of the 3-D restraint is converted to a 2-D smooth problem. The curve was calculated with the left (0°) and right (360°) end points wrapped so that the smoothed curve would be continuous over the 360° range. The origin of the polar coordinate system was selected so that it would be inside of all the contours of the slices. The center of the contour of the first slice was selected since it has the smallest contour.

Figure 3.35 shows a 2-D contour was converted to 1-D curve by using the polar coordinates of each point on the contour as its Cartesian coordinates.

When the contours of all the slices are converted to the curves, a 2-D image can be constructed by putting the curves one by one. This image can be easily smoothed as shown in Fig. 3.36. The pixel size in the original converted image is $0.625\text{mm} \times 0.45^\circ$ while the smoothed one is $0.0625\text{mm} \times 0.09^\circ$. When the 1-D curve from the smoothed image is recovered to the corresponding contour as shown in Fig. 3.37, the 3-D restraint is successfully smoothed.

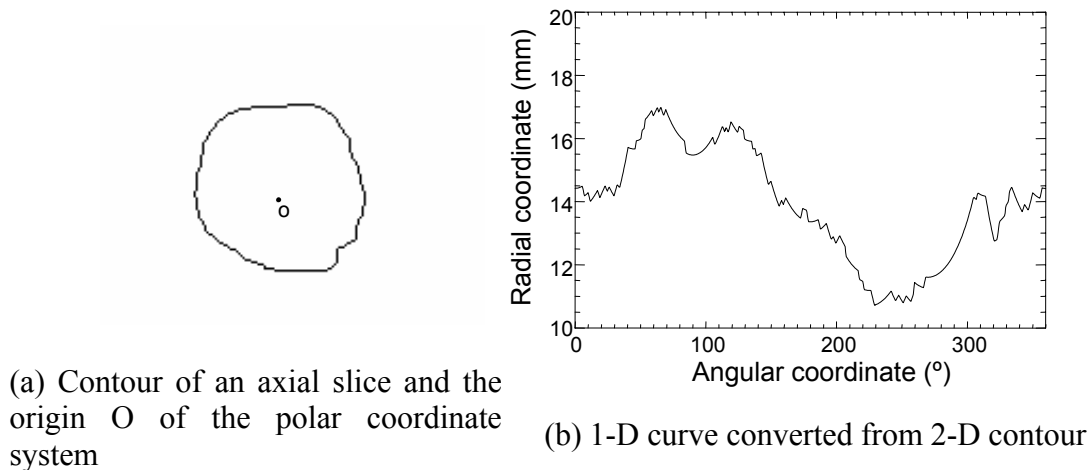


Figure 3.35 Conversion of a 2-D contour to 1-D curve with the polar coordinates of each point as its Cartesian coordinates

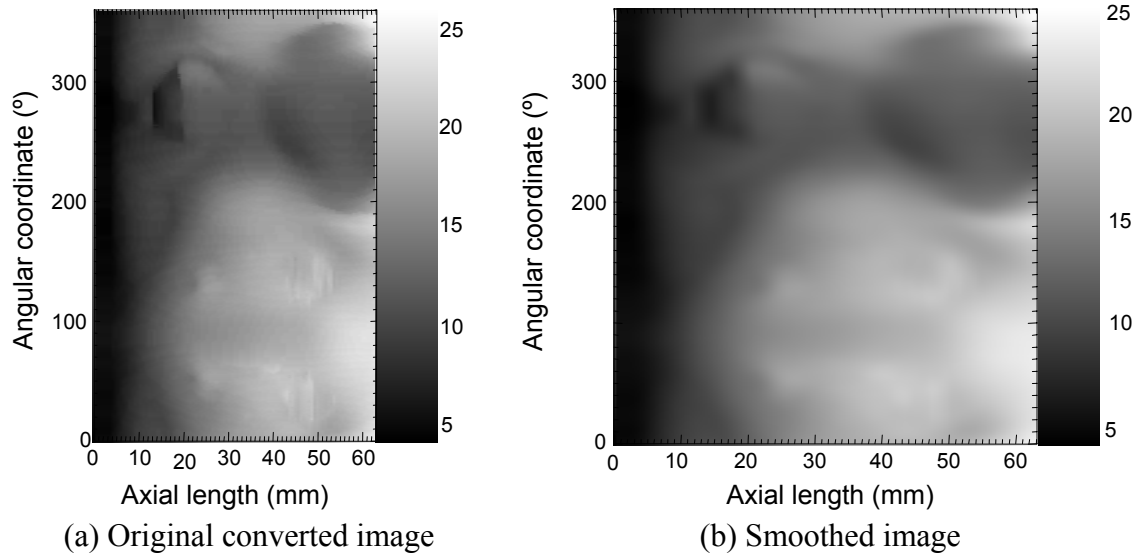


Figure 3.36 The original converted image and the smoothed one. The grey level in the image is the radial coordinate of the corresponding point in mm. The original images are anamorphic because of the asymmetry in pixel size, while the smoothed image is much less anamorphic.

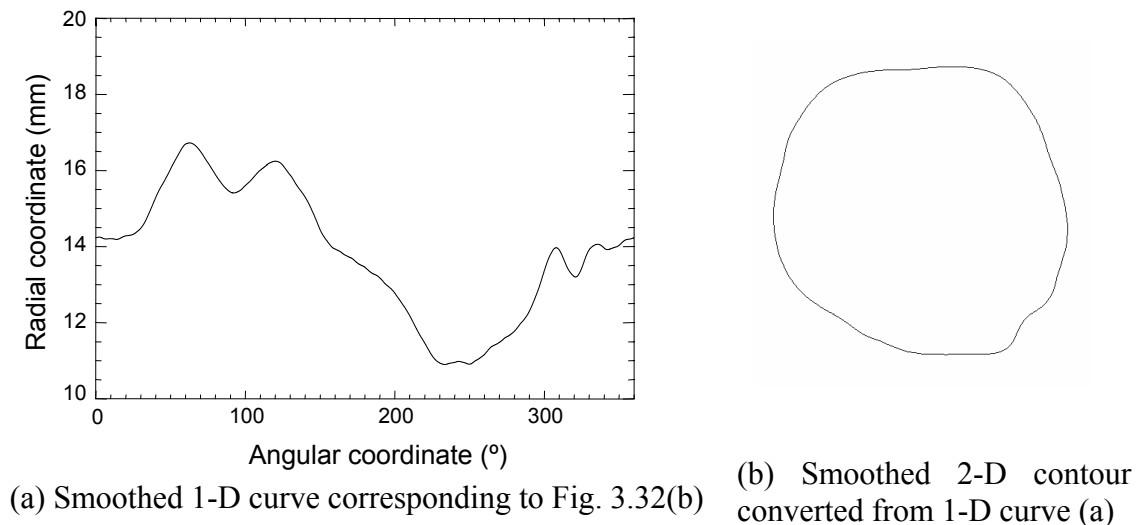


Figure 3.37 Conversion of a 1-D smoothed curve to 2-D contour

This smooth method can be used for any 3-D volume as long as the angular coordinate of each point in each slice has a singular value corresponding to the radial coordinate.

3.3.4.3 The Sample Used in the Experiments

The sample used in the 4th experiment as shown in Fig. 3.38(a) was designed to measure the detection limit of iodine in the rat head in both imaging methods. It employed the rat head holder in the 3rd experiment. The holder was sealed and filled with water. A cuvette with a step wedge inside was imbedded in the center of the holder. The inner cross section of the cuvette is 10mm×10mm and the length is 40mm. The step wedge (Fig. 3.38(b)) has 10 steps and the width for each step is 0.1cm to provide 0-0.9cm space for contrast agent as shown in Fig. 3.38(c). In the experiments the cuvette was full of a sodium iodide (NaI) water solution with a concentration of 25mM. The step wedge provided a projected iodine amount from 0 to 22.5mM-cm in 2.5mM-cm increments. In the future, this sample will be refined by adding channels filled with calcium carbonate solution to simulate bones.

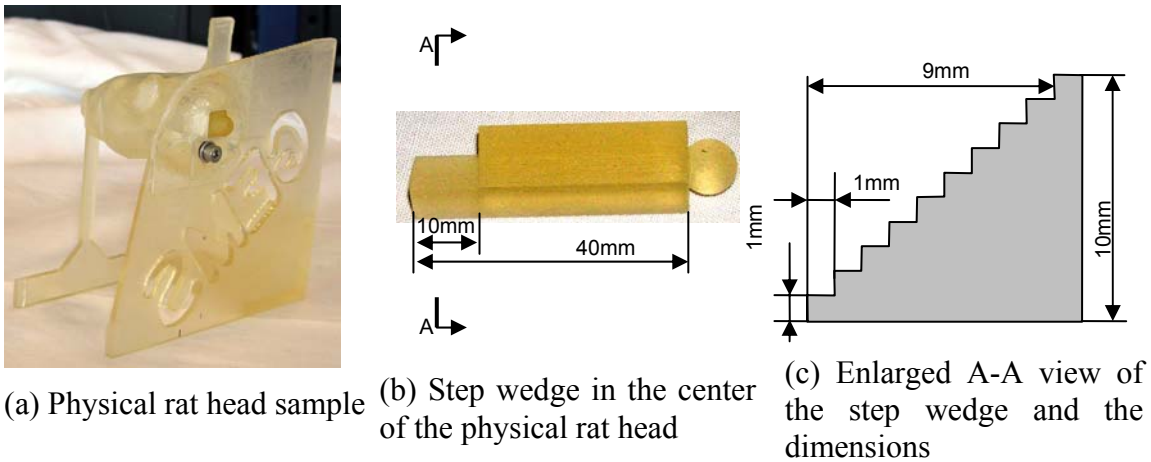
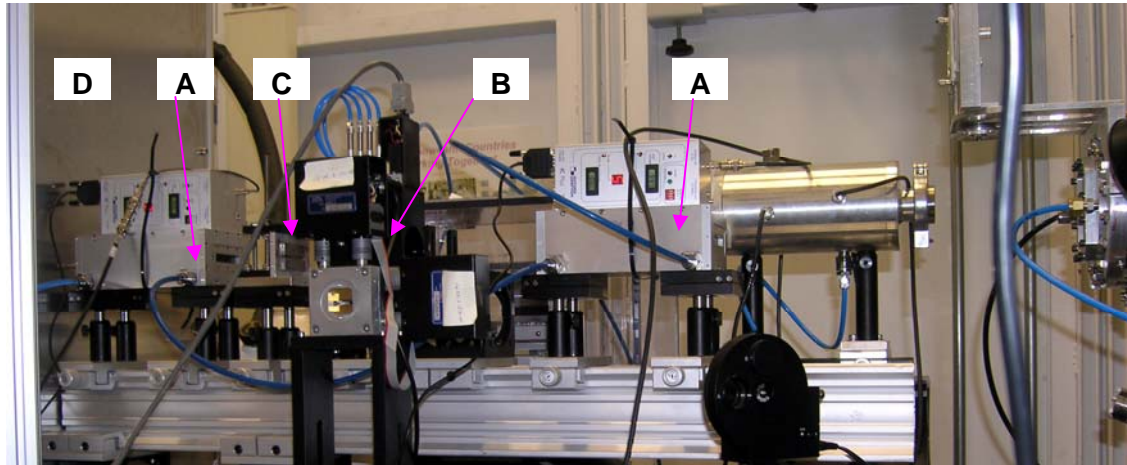


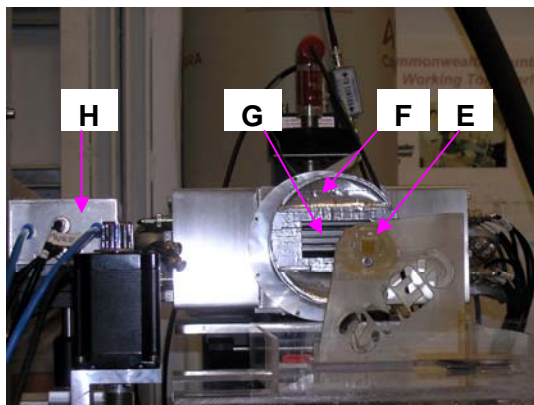
Figure 3.38 Sample in the 4th experiment. When the shown step wedge is put into a cuvette with an inner dimension of 10mm square which is full of iodine solution, an iodine step wedge is formed with the projected iodine amount from 0 to 22.5mM-cm in 2.5mM-cm increments.

3.3.4.4 Experimental Setup

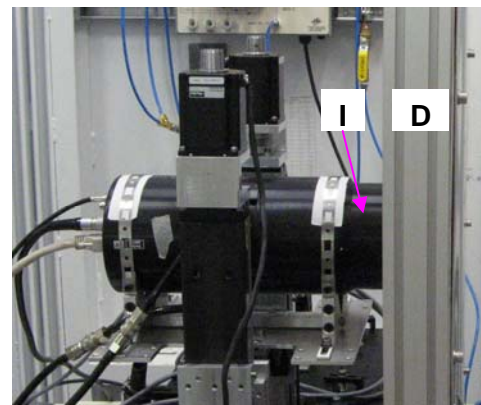
The experimental setup is shown in Fig. 3.39. It was divided into 3 parts along the beam transmission direction by two lead walls; the upstream setup (Fig. 3.39(a)), the object and fluorescence detector setup (Fig. 3.39(b)), and the downstream setup or the transmission detector setup (Fig. 3.39(c)).



(a) Upstream setup



(b) Object and fluorescence detector setup



(c) Downstream setup

Figure 3.39 Experimental setup for the 4th experiment. (A) Ion chamber filled with Ar (15cm plate length); (B) Aperture; (C) Slit; (D) Lead wall; (E) Object (Physical rat head); (F) Fluorescence detector; (G) Soller slit; (H) Ion chamber filled with Ar (5cm plate length); (I) Transmission detector

The upstream setup included one ion chamber with 15cm active plate length filled with Ar to measure the beam flux coming into the hutch, one removable horizontal aperture to change the beam width from 29.8mm to 0.25mm, one slit to control the vertical size of the beam at 0.25mm, and another identical ion chamber just before the object to measure the surface dose rate delivered to the object. The object and the fluorescence detector setup was the same as that of the 3rd experiment. The fluorescence detector was positioned perpendicular to the incident beam at a distance of 150mm to collect the fluorescence signal. An energy window for the fluorescence detector was set at the iodine fluorescence line (28.6keV) with a window width of 100eV. A Soller slit

was positioned just before the fluorescence detector to prevent Compton scatter from arriving the detector. An ion chamber with 5cm active plate length filled with Ar measured the beam flux after the object (detector dose). The downstream setup only contained the transmission detector.

3.3.4.5 K-Edge Subtraction Imaging Experiments and Results

For KES transmission experiments, the size of the beam was 0.25mm (V) \times 29.8mm (H). During imaging, both the sample and the detector were scanned at a constant vertical speed of 3mm/s (line scan mode). On average, it took 2min for one image set composed of one above-edge image and one below-edge image. With a 0.55mm thick Copper absorber in the incident beam to avoid the saturation of the detector, the surface dose was controlled at 0.33mGy/image set. The data was collected at one energy first and then at the other energy. To investigate the SNR as a function of detected signal, 16 images were obtained at each energy, of which 8 images were with the sample and 8 images were without the sample (I_0 image).

As shown in Section 3.2.4 on harmonics analysis, 96.7% of the detected signal is at fundamental energy for this experiment. The harmonics can be neglected in this case. The ratio R_o included the attenuation of the absorber and object of this experiment. There was 1.8% of the beam at the imaging energy (33.169keV) left after the transmission of the absorber (0.55mm copper) while 55.1% and 79.7% were left of the second and third harmonics at 66.338keV and 99.507keV respectively. If assume the object was 3.0cm water, 37.9%, 55.4%, and 59.8% of the beam at 33.169keV, 66.338keV, and 99.507keV transmitted the object. So R_o in this experiment was

$$R_o = [0.68\% \quad 30.5\% \quad 47.7\%]$$

Figure 3.40 shows the experimental result of KES with one image set, the above-edge image (high energy image) I_H , the below-edge image (low energy image) I_L , the iodine image (contrast agent image) ρ_{CTC} obtained by the logarithm subtraction of I_H and I_L as shown in Eq. 3.8, and the equivalent water image calculated by Eq. 3.9.

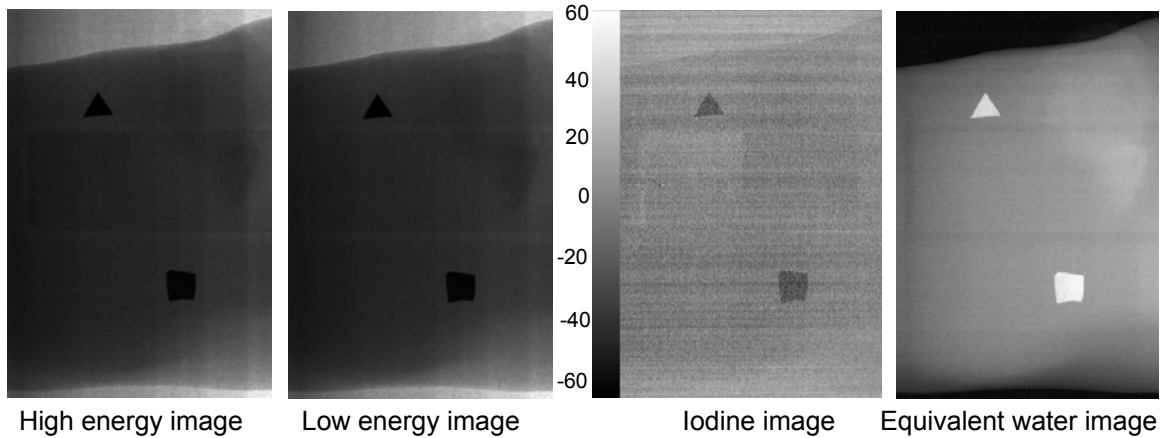


Figure 3.40 Experimental results of KES with one image set. The iodine step wedge can be discerned just below the triangular marker lead.

In the iodine image of Fig. 3.40, the iodine step wedge can be discerned just below the triangular marker lead. The triangular and square marker leads shown as dark patches in the iodine image were pasted on the shell of the restraint for the alignment of the images. Figure 3.41 shows the iodine images obtained from 1 to 8 image sets. Correspondingly, the surface doses are from 0.33mGy to 2.64mGy. With the increasing of the number of the image sets, the SNR of the iodine step wedge increases. In each image of Fig. 3.41, the highest SNR corresponds to the maximum projected iodine contrast amount of 22.5mM-cm (25mM \times 0.9cm) which is quantified in the figure.

All the measured SNRs of each projected iodine amount of each iodine image are listed in Table 3.6. The detection limit can be estimated as 17.5mM-cm projected iodine amount with 8 image sets.

The SNR can be estimated theoretically by Eq. 3.13 with the assumption that the noise arises from a Poisson distribution of photon count. With the estimation of the projected matrix material absorption length at each projected iodine amount, the theoretical SNRs are listed in Table 3.7 for each projected iodine amount of each iodine image.

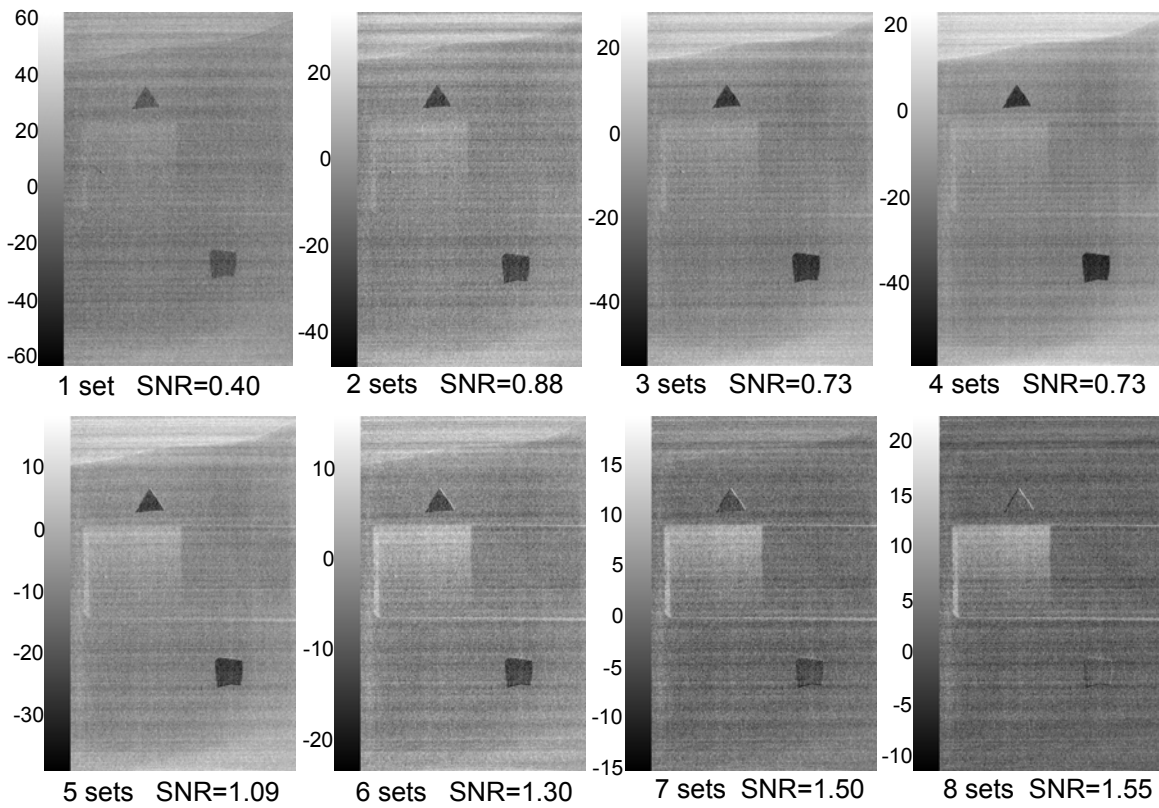


Figure 3.41 Iodine images obtained from 1-8 image sets in KES. The SNR shown for each iodine image is for a theoretical projected iodine amount of 22.5mM-cm.

Table 3.6 Measured SNRs of each projected iodine amount of each iodine image for the simulated rat head with iodine step wedge

Projected iodine amount (mM-cm)	Number of image sets used to obtain the iodine image							
	1	2	3	4	5	6	7	8
0.0	-0.03	0.05	-0.00	0.03	0.03	0.07	0.06	0.08
2.5	0.11	0.10	0.10	0.05	0.04	0.21	0.16	0.14
5.0	0.07	0.18	0.15	0.12	0.23	0.26	0.33	0.30
7.5	0.08	0.17	0.25	0.14	0.20	0.27	0.29	0.27
10.0	0.23	0.27	0.16	0.17	0.28	0.44	0.49	0.55
12.5	-0.01	0.49	0.37	0.27	0.44	0.57	0.75	0.79
15.0	0.35	0.50	0.37	0.32	0.59	0.79	0.95	0.97
17.5	0.31	0.53	0.48	0.41	0.67	0.91	1.13	1.14
20.0	0.33	0.52	0.55	0.59	0.81	1.15	1.28	1.32
22.5	0.40	0.88	0.73	0.73	1.09	1.30	1.50	1.55

Table 3.7 Theoretical SNRs of each projected iodine amount of each iodine image for the simulated rat head with iodine step wedge

Projected iodine amount (mM-cm)	Number of image sets used to obtain the iodine image							
	1	2	3	4	5	6	7	8
0.0	0.00	0.00	0.00	0.00	0.00	0.00	0.00	0.00
2.5	0.06	0.08	0.10	0.11	0.13	0.14	0.15	0.16
5.0	0.12	0.16	0.20	0.23	0.26	0.28	0.31	0.33
7.5	0.18	0.26	0.32	0.36	0.41	0.45	0.48	0.52
10.0	0.25	0.35	0.43	0.50	0.55	0.61	0.66	0.70
12.5	0.32	0.46	0.56	0.65	0.72	0.79	0.85	0.91
15.0	0.41	0.58	0.71	0.82	0.92	1.01	1.09	1.17
17.5	0.51	0.72	0.88	1.02	1.14	1.25	1.35	1.44
20.0	0.61	0.86	1.05	1.21	1.36	1.49	1.61	1.72
22.5	0.72	1.02	1.25	1.44	1.61	1.77	1.91	2.04

The relationship of SNR, the amount of the contrast agent ($\rho_C t_C$), and the photon count per pixel before hitting the object (I_0) can be proved by the experimental results.

In Fig. 3.42, the SNR has been compensated by a factor of $\sqrt{1 + e^{\left(\frac{\mu}{\rho}\right)_M \rho_M t_M}}$ to get rid of the effect of the matrix material. The stars are the measured values from the resulting images, the solid lines are calculated by Eq. 3.13, and the dashed lines are the linear fitting results of the measured values. Fig. 3.42(a) shows the SNR is proportional to the projected amount of the contrast agent. The curves were calculated or measured from the iodine image obtained from 8 image sets. Fig. 3.42(b) shows that the SNR is proportional to the square root of the number of image sets since the number of image sets is proportional to the total number of photons. The curves were calculated or measured from the area in each iodine image where the projected iodine amount was 22.5mM-cm. The errors in the

measured values are calculated from the data variance and arise primarily from the measurement of I_0 , the variation of the beam intensity during the imaging period, and the vibration of motor motion.

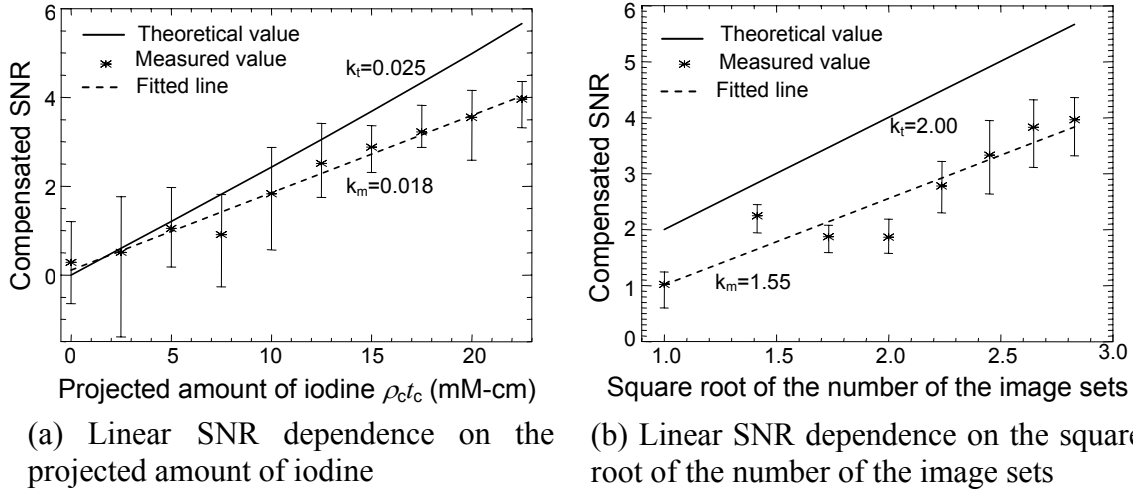


Figure 3.42 SNR as a function of the projected amount of the contrast agent and the square root of the number of the image sets. The slope of the theoretical line is denoted as k_t and that of the fitted line is denoted as k_m .

The quality factor of the imaging system is $0.46 \mu\text{Gy}^{-1}\text{mm}^{-2}$ which is 87% of its upper limit of $0.53\mu\text{Gy}^{-1}\text{mm}^{-2}$ at the location where the projected iodine amount is 10mM-cm.

3.3.4.6 Fluorescence Subtraction Imaging Experiments and Results

In FSI experiments, the pixel size was $0.25\text{mm}\times 0.25\text{mm}$ as determined by the pencil beam size, raster scan speed and integration time for each data point in the image. Other considerations were the beam flux, iodine concentration, feasible imaging time, and the collection efficiency of the fluorescence detector. The sample was raster scanned at 5mm/s which was limited by the read-out time of the fluorescence detector. The scan area was $15\text{mm}\times 15\text{mm}$ around the step wedge region. It took about 15min for one image set with a surface dose of 24mGy. The radiation dose and the imaging time were set to make FSI possible for *in vivo* imaging. In the FSI experiments, only one set of images (one above-edge image and one below-edge image) was taken.

The resulting images are shown in Fig. 3.43, including the original fluorescence images at high and low energies, and the iodine image obtained by the subtraction of the high energy fluorescence image and the low energy one. The measured SNRs are listed in Table 3.8 for each projected iodine amount of the iodine image obtained with different number of channels of the fluorescence detector. There is no analytical equation for the calculation of SNR in FSI because the FSI signal is not only related to the quantity of the contrast agent but also the geometrical relationship of the sample and the detector. The structure of the sample, such as a living rat, makes the problem more complicated. Figure 3.44 shows the linear SNR dependence on the projected iodine content (Fig. 3.44(a)) and the square root of the number of the channels used of the detector (Fig. 3.44(b)). In the figure, the measured values are indicated by stars and they are linearly fit by the dashed lines. The error bars plotted in the figure were measured by the minimum and maximum signal in the corresponding projected iodine amount area.

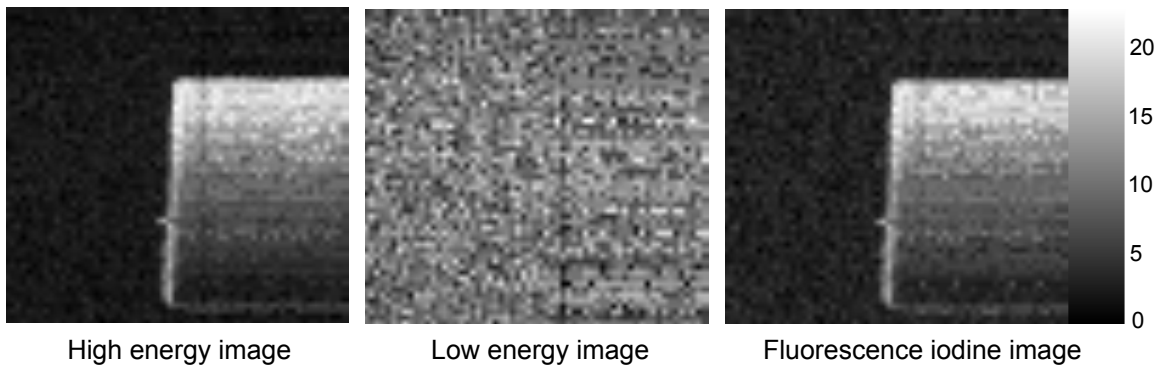


Figure 3.43 Resulting images of the fluorescence experiment

Table 3.8 clearly shows that the detection limit for the imaging system was a projected iodine amount of 2.5mM-cm with 4 channels collecting signal.

The imaging system acquired a quality factor of $0.02\mu\text{Gy}^{-1}\text{mm}^{-2}$.

Table 3.8 Measured SNRs of each projected iodine amount of the iodine image obtained with different number of channels of the fluorescence detector for the simulated rat head with iodine step wedge

No. of channels	Projected iodine amount (mM-cm)									
	0	2.5	5.0	7.5	10.0	12.5	15.0	17.5	20.0	22.5
1	0.22	1.02	0.88	2.40	2.67	2.54	4.29	6.97	7.66	8.19
2	0.43	0.73	2.46	3.50	4.31	4.31	6.81	9.54	11.30	12.41
3	0.55	0.99	2.86	4.87	4.97	5.75	8.35	11.57	13.85	15.01
4	0.28	1.00	3.29	5.73	5.66	7.17	9.69	13.64	16.01	18.12

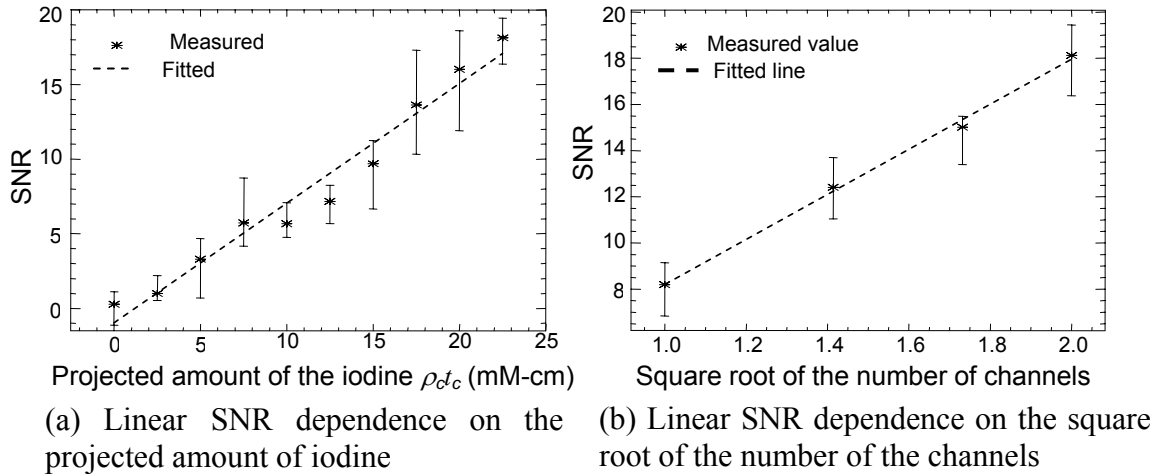


Figure 3.44 Linear dependence of SNR on the projected amount of the contrast agent and the square root of the incident photon count

3.4 Comparison of K-Edge Subtraction Imaging and Fluorescence Subtraction Imaging

The comparison of KES and FSI is based on the 4th experimental result.

The highest SNR (18.1) was achieved by the FSI at the location where the projected iodine amount was 22.5mM-cm. For the same projected iodine amount, the SNR in KES with 8 image sets is 1.6. However, KES provides a much better image resolution (18.7microns×18.7microns) compared to FSI (250microns×250microns), with smaller

radiation surface dose (0.33mGy/image set) than that of FSI (24mGy/image set), as well as taking less time for imaging (2min/image set) compared to FSI (15min/image set).

To more closely compare KES and FSI, the iodine image from the KES with 8 image sets was recast into an image whose pixel size is 13 times that of the original pixel size ($243\mu\text{m}\times 243\mu\text{m}$) which is close to the pixel size of FSI ($250\mu\text{m}\times 250\mu\text{m}$). Since the pixel size is proportional to the collected photon count, the SNR is predicted to improve by 13 times the original SNR which is 20.8 (1.6×13) for the location where the iodine amount is 22.5mM-cm. However, the SNR in the resultant iodine image (Fig. 3.45) only increased from 1.6 to 9.1 at this location because of the intensity variation in the beam and the different imaging times. With the similar pixel size and the imaging time (8 image sets in KES took 16min while 1 image set in FSI took 15min), KES still has the advantage of less surface dose (2.65mGy) and bigger imaging area which can be 75mm*50mm without changing any other imaging parameter while the expansion of the imaging area of FSI increases imaging time. FSI offers the highest SNR obtained in our experiments which the KES method can not compete. Figure 3.46 shows how the SNR changes with the projected iodine amount with the two imaging techniques, KES as a dashed line, and FSI as a solid line. The advantage of FSI on SNR became obvious when the iodine thickness went greater than 0.2cm. The SNR of FSI can be further improved by including more channels of the fluorescence detector to increase the collected signal. However, this takes more time for read-out.

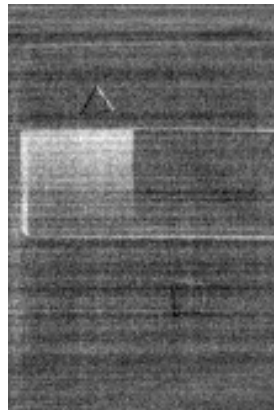


Figure 3.45 Recast iodine image of KES

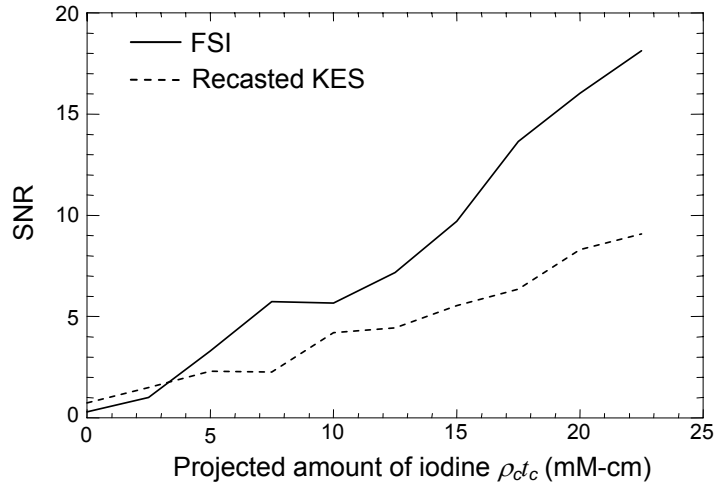


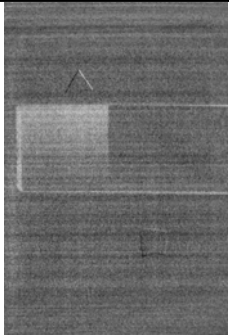
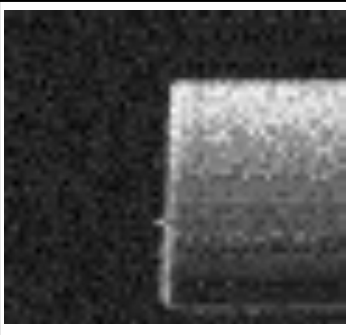
Figure 3.46 Comparison of SNR in recast KES iodine image and the FSI iodine image

In the above comparisons, the FSI method achieves a high SNR at the cost of a high dose and a low spatial resolution, while the KES technique has a good spatial resolution, a large imaging area, and a tolerable imaging dose with a moderate SNR. The Quality factor introduced in Eq. 3.28 makes the two imaging methods comparable irrespective of the geometric dependent factors.

For our object, at the location where the iodine amount is 22.5mM-cm, the theoretical quality factor is $5.31/\mu\text{Gy mm}^2$. At the same location, the measured quality factor for the KES experiment is $2.59/\mu\text{Gy mm}^2$, and for the FSI, it is $0.22/\mu\text{Gy mm}^2$. The above comparison on quality factors along with the resulting images, imaging time and area, spatial resolution, and surface dose is listed in Tab. 3.9.

A quick comparison of the quality factor would lead one to believe the KES is better compared to FSI under our experimental conditions. However, one should realize that for KES to have the same SNR as FSI under similar spatial resolution in our experiments we would need to acquire in excess of 24 image sets theoretically and even more in practice. Then the imaging time increases to 64min. It is not practical for living animals. On the other hand, the exposure dose, the resolution, and the imaging time of FSI can not be on the same level as those of KES to get perceivable signal even with the compensation of its high SNR.

Table 3.9 Comparison of KES and FSI

	KES (8 image sets)	FSI
Result Image		
Dose (mGy)	2.65	24.08
Imaging Time (min)	16	15
Pixel Size (mm×mm)	0.0187×0.0187	0.25×0.25
Imaging Area (mm×mm)	26.9×40.4	15×15
Quality Factor ($\mu\text{Gy}^{-1}\text{mm}^{-2}$)	2.59	0.22

3.5 Conclusions

In this chapter, the major motivation was to improve and quantify the detection limit and the quality factor of two imaging systems: KES and FSI.

For KES imaging, the detector was changed from a mammography film in 1st experiment, an image plate in the 2nd experiment, to a CCD detector in the 3rd and 4th experiments. The pixel size improved from 50 μm square to 18.7 μm square. A restraint was developed and smoothed to hold the animal nearly motionless. To have more photons hit the detector while preventing the detector from saturation, flatteners for both lateral and dorsal-ventral views were designed and smoothed to keep the dynamic range of the photons arriving at the detector as small as possible. To improve the SNR, multiple image sets were taken as long as the radiation dose and the imaging time were acceptable for in vivo imaging. The improvement of SNR was significant. A projected iodine amount of 10mM-cm was invisible in the 1st experiment while its SNR was 1.2 in the 2nd experiment. In the 3rd experiments, multiple image sets (8 image sets with a total radiation dose of 11.2mGy) improved the SNR of 10mM-cm projected iodine amount

from 1.86 to 5.29 for the 1st object, 1.63 to 2.90 for the lateral view of the 2nd object without the flattener. The flattener made contributions to improve the SNR for the same projected iodine amount from 2.90 to 3.24 for lateral view and from 2.35 to 3.26 for the dorsal-ventral view. The detection limit is found where the SNR is just over 1. The upper detection limit was found by a ‘pure’ object (approximated by the 1st object in the 3rd experiment which does not have many structures) for the KES imaging system was 3.16mM-cm with a total radiation dose of 4.2mGy (3 image sets) and 4.64mM-cm with a radiation dose of 2.8mGy (2 image sets). The upper detection limit for the rat head was found by a simulated one (no bone inside) in the 4th experiment which was 17.5mM-cm with a total radiation dose of 2.65mGy (8 image sets). So with the similar radiation dose (2.8mGy for 2 image sets in the 3rd experiment and 2.65mGy for 8 image sets in the 4th experiment), the big difference (12.86mM-cm) in the detection limits is caused by the material matrix that the iodine solution was embedded in. With the similar radiation dose and a projected iodine amount of 10mM-cm, a quality factor of approximately 100% was achieved in the 3rd while it was 87% in the 4th experiment. The result from the 4th experiment is closer to what we would expect in a live animal system.

Based on the calculated results which is close to the measured values, to detect a 0.1mM-cm iodated object in the head of a rat we would need an exposure of approximately 2.7kGy to achieve a SNR of 10 with a square pixel size of 18.7 microns. This large exposure will certainly be fatal. This dose drops to a value of 0.15Gy if we expand the pixel size to 0.25mm and loosen the SNR requirement to 1. This indicates that using KES for dilute iodine detection is possible when the size of features that can be detected is large (millimeter size). This marginally meets our objective for visualizing gene expression in a small animal such as a rat. Experimental proof was not possible at this time due to limitations in beam time at the Canadian Light Source.

For FSI imaging, a radiation dose of 272mGy and imaging time of 90min was used in the 3rd experiment. A small projected iodine amount (2.83mM-cm) was detected with a high SNR of 6.5. However, the quality factor for the imaging system is low at $0.01\mu\text{Gy}^{-1}\text{mm}^{-2}$ because of the large radiation dose and poor spatial resolution (250 μm square). The scan speed was improved from 0.25mm/s to 5mm/s to decrease the radiation dose in the 4th experiment. With the moderate radiation dose (24mGy) and

imaging time (15min), a projected iodine amount of 2.5mM-cm was detected with a SNR of 1.0. The quality factor was improved to $0.02\mu\text{Gy}^{-1}\text{mm}^{-2}$. The detection limit measured in the 4th experiment for the FSI indicates that FSI might be a candidate imaging method for GEMS experiments.

Thus for FSI to achieve a SNR of 1 with a 0.1mM-cm feature in the rat head would require an exposure of approximately 0.6Gy which is marginally acceptable. An improvement in solid angle can easily be had by including all 32 channels in the fluorescence detector. This would drop the exposure to approximately 0.2Gy which is similar to that obtained with KES. Therefore, FSI also marginally meets our objective for visualizing gene expression in a small animal such as a rat.

However, the imaging area of the FSI has to be small because of the limit of the imaging time and there is no reference anatomy structure image created by the FSI to locate the exact position of the cancer cells. Compared to the KES, an imaging plan is proposed. Since the results show these two imaging techniques have their own advantages and disadvantages they can be used complementarily. Due to the short imaging time and large imaging area, KES can be used first to locate the area of interest with low radiation dose, do the preliminary diagnosis and decide whether the further FSI is necessary. Due to its high SNR for the dilute sample without the concern about the saturation of the detector, FSI can be used when the area of interest is known. The combination of these two imaging techniques will be very promising and powerful.

The similar detection capability of KES and FSI also indicate that an imaging system should detect iodine using both methods and is how the present imaging system is being developed at the Canadian Light Source Biomedical Imaging and Therapy beamline. A pencil beam KES imaging system which can be done at the same time as the FSI has been done [75] and still need further improvement. In that combined KES and FSI system, these two imaging methods will be more comparable with the same radiation dose and spatial resolution. And the KES imaging will provide the local anatomy reference.

To further improve the performance of KES, a bent Laue monochromator was designed to do the simultaneous KES imaging [76]. Since the high energy image and the low energy image are taken at the same time in this imaging method, the temporal noise

caused by the beam variance, the animal movements, and the vibration of the motor scan can be avoided. The SNR will be further improved with the KES imaging. This part of the work will be discussed in detail in the next chapter.

To implement an optimal FSI system, the optical geometry including the position and orientation of the fluorescence detector can be studied by the simulation of the Compton scatter and the fluorescence signal with Monte Carlo method. The 3D reconstruction of the rat head which we already have can be used to conduct this study.

Chapter 4

A Design Study of a Bent Laue Monochromator for Simultaneous K-Edge Subtraction Imaging

Simultaneous KES can overcome the artifacts in the resulting image caused by the movement especially when the object is a living animal. To further improve the performance of the KES imaging, a bent Laue KES monochromator was designed. Bent Laue KES monochromators have been previously implemented. However, they do not meet the resolution requirements for small animal imaging. A high resolution device will be developed in this study. During the design of the bent Laue monochromator, the property of the polychromatic focus is firstly defined when the incident beam is in a lower incident case. In this chapter, the position of the polychromatic focus is calculated by a simulation method and firstly realized that high spatial resolution and good energy resolution can be achieved at the same time.

4.1 Introduction

As we have seen, KES imaging in which the high and low energy images are taken at different times, significant noise from animal motion, mechanical vibration, and intensity variation occurs. The iodine images in Figures 3.27 and 3.28 showed this phenomenon clearly. Figure 4.1 shows a typical simultaneous KES imaging setup which can overcome the temporal difference in imaging to further improve the quality factor by taking the high and low energy image at the same time. A bent Laue monochromator can provide two beams at just below and above the K-edge of the contrast agent in the object. The object is positioned at the focus point of the two beams and vertically scanned during imaging. A dual-line detector is employed to collect both high and low images. It is clear that the spatial resolution of the imaging method is determined by the focus size of the two beams.

Bent Laue monochromators have been widely used at synchrotron radiation facilities to provide sufficient beam flux for simultaneous KES imaging since the successful implementation of the coronary angiography project at the NSLS during 1988-1993 [77-

79]. A Si(1,1,1) with an asymmetry angle of 26.22° was employed and a focus size of 0.6mm at the patient position was achieved. The focus size does not match our study since our imaging object is a small animal, i.e. rat. Micro-focusing can be achieved by the coincidence of geometrical and polychromatic foci through a small angle asymmetrical cut of the crystal [80-82]. In this case, the resulting focus size is only limited by the source size. In this part of the thesis, a preliminary design of a bent Laue monochromator is given which is based on the simulation of the photon going through the crystal. Also, the beam reflectivity is calculated. The design parameters match the theoretical prediction. The energy resolution of the monochromator is also predicted which indicates that this kind of monochromator can also be used for energy *Dispersive X-ray Absorption Spectroscopy (DXAS)*.

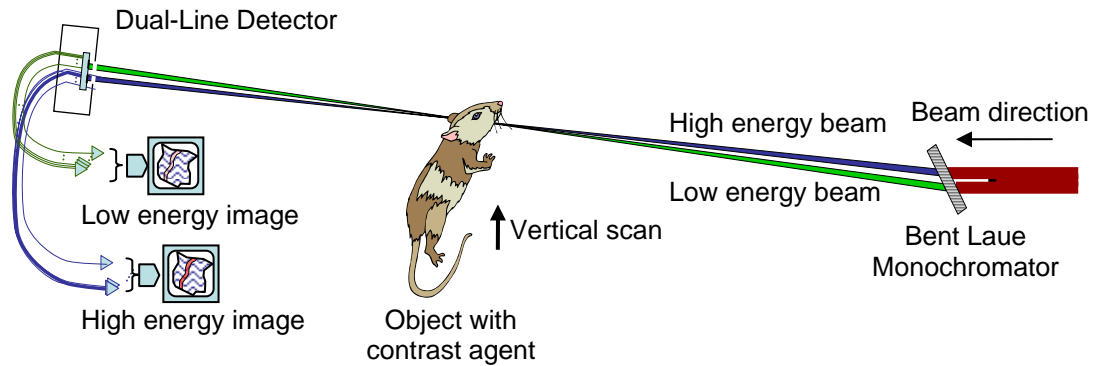


Figure 4.1 Typical simultaneous KES imaging experimental setup. The high and low energy beam is provided by a bent Laue monochromator at the same time. The object with contrast agent is positioned at the focus point of the beam and vertically scanned to have a 2-D image. The high and low energy images are collected by a dual-line detector.

4.2 Cylindrically Bent Laue Crystal Optics

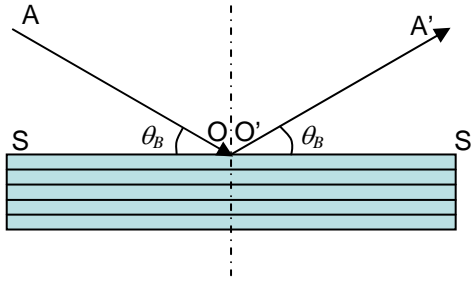
A Laue crystal when bent produces a number of effects; the diffracted beam may be geometrically focused (or defocused), a single incident ray will result in a spatially dispersed diffracted beam which may be focused (or defocused), and the range of lattice planes which the crystal bending presents to the incident beam will enhance the angular acceptance or energy bandwidth of the beam. Finally the intensity of the diffraction will depend strongly on the bending as well as the crystal plane type, the crystal thickness, and other factors.

In this section, some basic definitions in crystal x-ray optics are introduced. The geometrical focus and the polychromatic focus of a bent Laue crystal are analyzed and quantified. The quantification of the polychromatic focus is based on a lamellae simulation model of the crystal. The focus size and the reflectivity of the bent Laue crystal are also discussed.

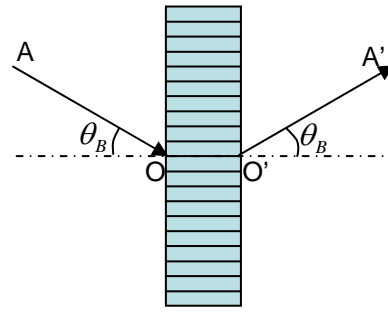
4.2.1 Some Definitions

X-ray diffraction from single crystals is broken into two types; Bragg (reflection) geometry and Laue (transmission) geometry. If the incident beam and the reflected beam both are on the same side of the crystal, as shown in Fig. 4.2(a) and (c), it is called Bragg type. If the incident beam impinges on one surface and the reflected beam emerges from another surface as shown in Fig. 4.2(b) and (d), it is known as a Laue type. The crystal can be cut symmetrically (Fig. 4.2(a) and (b)) or asymmetrically at an asymmetry angle χ (Fig. 4.2(c) and (d)). The asymmetry angle is defined in relation to the angle between the lattice planes and the crystal surface. The asymmetry angle is defined as the angle between the current cut surface plane and the symmetrical one. The asymmetry angle is positive if the surface plane is rotated counterclockwise from its symmetrical position [83]. So the asymmetry angle of a Bragg crystal is the angle between the lattice plane and the surface plane of the crystal or the angle between the normals of the lattice plane and the surface plane (Fig. 4.2(c)). The asymmetry angle of a Laue crystal is the angle between the lattice plane and the surface normal (Fig. 4.2(d)). Both asymmetry angles in Fig. 4.2 are positive. Since the sign of the asymmetry angle does not affect any analysis result, its absolute value is used in the following analysis and simulation.

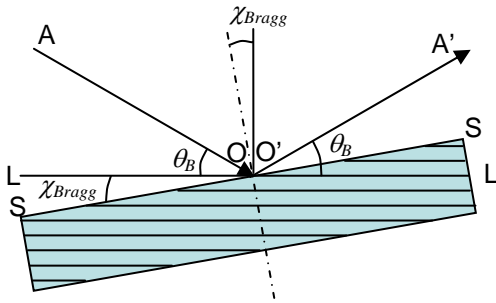
When an x-ray is incident upon a Laue crystal, it can be either in a lower condition or an upper condition according to the angular relationship of the incident ray, the lattice plane and also the surface plane of the crystal. As shown in Fig. 4.3, the incident ray can be on the either side of the lattice plane at its Bragg angle θ_B to be reflected. If the incident ray has an angle of $\chi + \theta_B$ with the surface normal of the crystal, it is called upper incident condition. Otherwise, if the angle of the incident ray and the surface normal of the crystal is $\chi - \theta_B$, it is called lower incident condition.



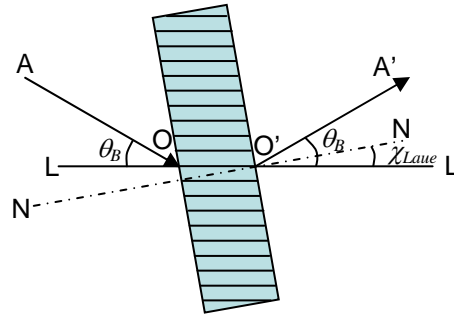
(a) Optics of symmetrical Bragg crystal



(b) Optics of symmetrical Laue crystal

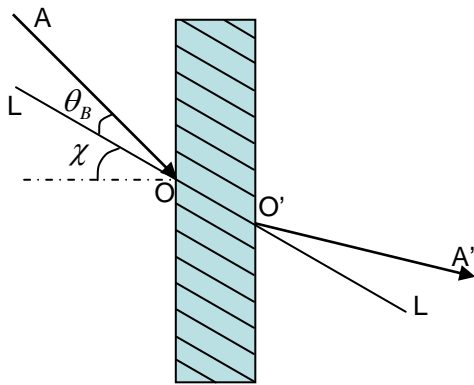


(c) Optics of asymmetrical Bragg crystal

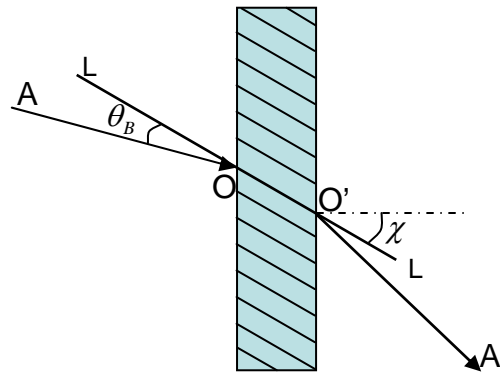


(d) Optics of asymmetrical Laue crystal

Figure 4.2 Optics of Bragg type and Laue type crystals. In the figure, AO is the incident ray, O'A' is the reflected ray. S-S is the crystal surface plane, L-L is the lattice plane, N-N is the surface normal, θ_B is the Bragg angle, χ_{Bragg} is the asymmetry angle of Bragg crystal, and χ_{Laue} is the asymmetry angle of Laue crystal. Both the asymmetry angles are positive.



(a) Upper condition



(b) Lower condition

Figure 4.3 Definition of upper and lower incident conditions. In the figure, AO is the incident beam, O'A' is the reflected ray, LL is the lattice plane, θ_B is the Bragg angle, and χ is the asymmetry angle.

4.2.2 Geometrical Focusing

When the Laue crystal is cylindrically bent, if the x-ray source is located at the concave side of the crystal, the whole beam is diverged on the other side of the crystal and forms a virtual focus point at the same side as the source (Fig. 4.4(a)). If the x-ray source is located on the convex side of the crystal, the whole beam is converged on the other side of the crystal and forms a real focus (Fig. 4.4(b)). The convergent geometry is discussed in detail. It is also called focusing geometry.

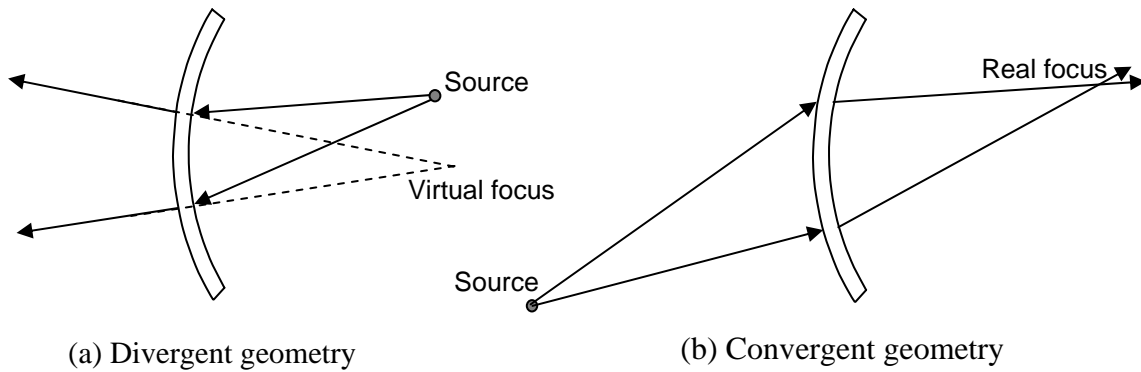


Figure 4.4 Definition of divergent and convergent geometry

Figure 4.5 shows the geometrical focusing of the bent Laue crystal. The crystal is positioned so that the central ray of the x-ray beam is incident upon the center of the crystal lattice plane (along thickness) at its Bragg angle. The relationship between the distance from the source to the crystal f_1 , the distance from the crystal to the beam focus point f_2 , and the bending radius of the crystal ρ is given by [76]

$$\frac{\cos(\chi \mp \theta_B)}{f_2} - \frac{\cos(\chi \pm \theta_B)}{f_1} = \frac{2}{\rho} \quad (4.1)$$

Upper and lower signs in the equation correspond to the upper and lower conditions of the incident beam.

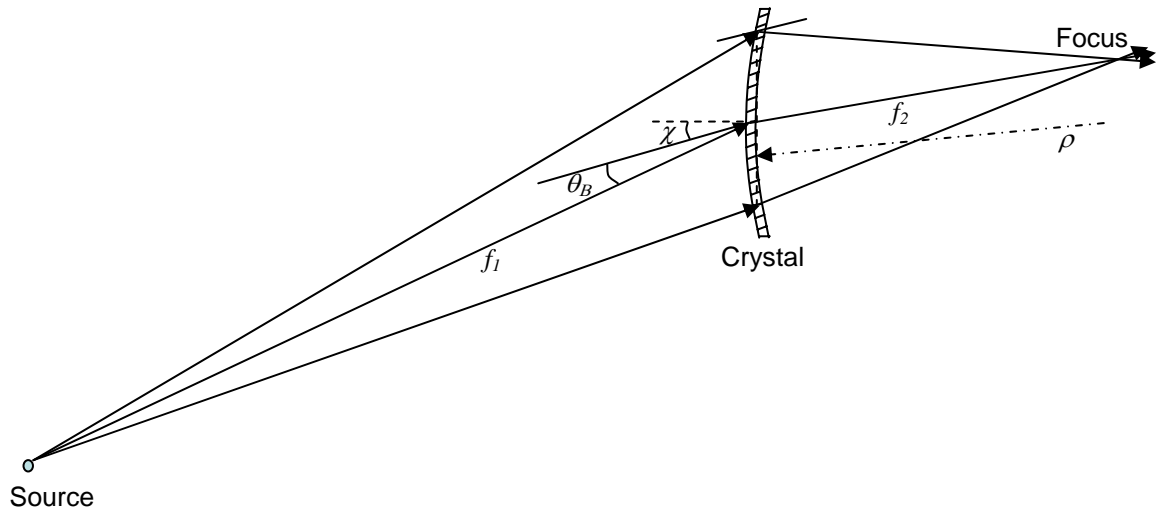
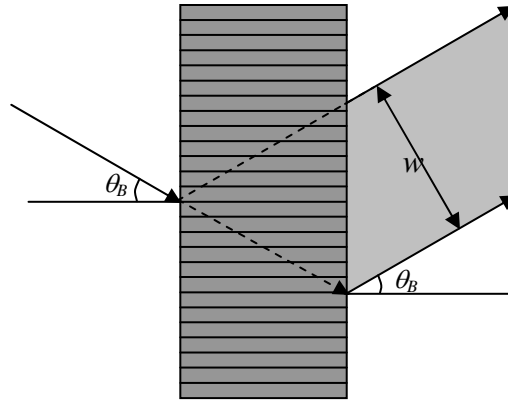


Figure 4.5 Geometrical focusing of the bent Laue crystal. In the figure, f_1 is the source-crystal distance, f_2 is the crystal-focus distance, ρ is the bending radius, χ is the asymmetry angle, and θ_B is the Bragg angle of the crystal.

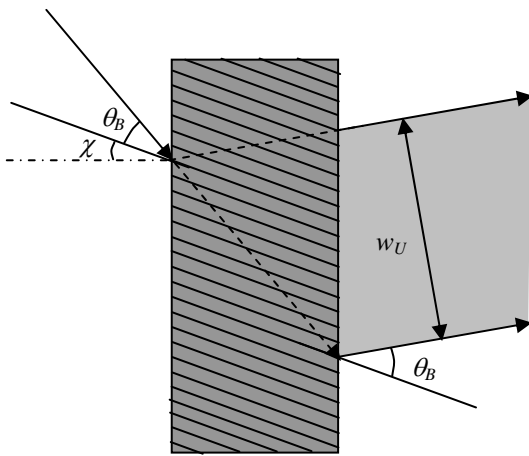
4.2.3 Polychromatic Focusing

When a single ray is incident to a crystal, the crystal can be looked as a stack of lattice planes and the ray is partly reflected by each plane, and partly transmitted through to the next plane. So the ray is broadened along its path. Figure 4.6(a) shows that single ray is broadened by the symmetrical Laue crystal. The broadening depends on the thickness of the crystal and the Bragg angle of the incident ray. The broadening also depends on the asymmetry cut angle of the crystal and the incident condition. When an asymmetry angle presents, the ray in upper incident condition has longer path in the crystal and interacts with more lattice planes, so the broadening is bigger as shown in Fig. 4.6(b). And vice versa, the ray in lower incident condition is broadened less because it has shorter path in the crystal and interacts with less lattice planes as shown in Fig. 4.6(c).

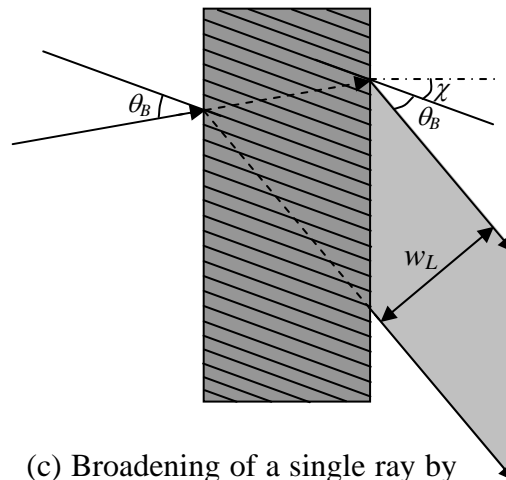
The examples in Fig. 4.6 show the maximum extent of the exit beam. The intensity distribution across the exit beam is set by the details of the diffraction process and the geometrical path that the rays follow. In our case, the diffraction probability is uniform along the incident beam path leading to an exit beam spatial distribution determined only by absorption along the incident beam and exit beam paths.



(a) Broadening of a single ray by a symmetrical Laue crystal



(b) Broadening of a single ray by an asymmetrical Laue crystal in upper incident condition



(c) Broadening of a single ray by an asymmetrical Laue crystal in lower incident condition

Figure 4.6 Single ray broadening by Laue crystal. The upper incident condition broadens the ray more than the lower condition ($w_U > w_L$). The dark grey area is the crystal and the light grey area is the diffracted broadened x-ray beam.

When the crystal is bent, the orientation of the lattice plane changes not only for the different lattice planes but also along the same lattice plane according to the deformation of the crystal. The reflected rays are broadened not only spatially but also spectrally and they are no longer parallel to each other in most cases. This gives rise to a focus (real or virtual). This effect is referred to as single ray focus or polychromatic focus. Figure 4.7 shows a bent Laue crystal with an asymmetry angle. When the incident ray is in the upper incident condition, the broadened reflected rays have a real focus on the other side of the crystal, as shown in Fig. 4.7(a). When the incident ray is in the lower incident

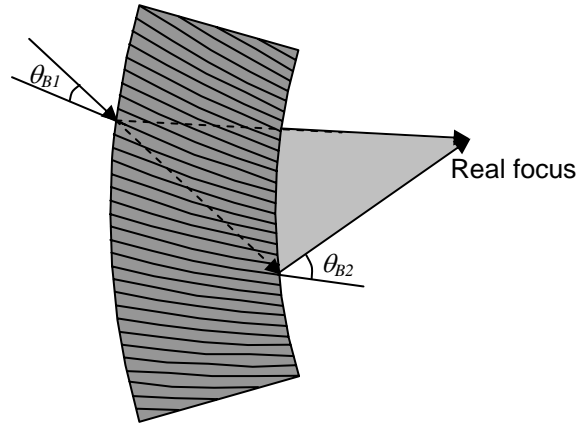
condition, the broadened reflected rays may have a real or virtual focus, as shown in Fig. 4.7(b) and (c). When the incident angle is big enough (the reflected rays are in relative low energy), there is a real focus (Fig. 4.7(b)). However, the reflected rays may have a virtual focus as shown in Fig. 4.7(c) when the incident angle is small enough, which means the reflected rays are in relative high energy. There is an incident angle at which the reflected rays are parallel to each other. The real focus is obtained when the incident angle to the entrance lattice plane θ_{B1} is smaller than the incident angle to the exit lattice plane θ_{B2} . To do the quantity analysis of the focus property, a lamellar model of the crystal is introduced to simulate the deformation of the crystal.

Since the real distance between two lattice planes of the crystal is very small (less than 3.14\AA for Si; Si(1,1,1) achieves this minimum.), the thickness of the lamellar plane in the lamellar model can be selected as long as it is small enough relative to the thickness of the crystal to satisfy the requirement of the calculation precision. Figure 4.8(a) shows the lamellar model of an un-bent Laue crystal. The lattice points are connected by lattice planes (dashed lines), lamellar planes (vertically dotted lines), and horizontally dash dotted lines. If the distance between two lamellar planes is t and the asymmetry angle of the crystal is χ , the lattice points distribute equally vertically with a distance of $t \tan \chi$. When the crystal is cylindrically bent as shown in Fig. 4.8(b), the lattice points keep equally distributed on the lamellar planes which have the same bending center. The horizontal dash dotted lines in un-bent crystal keep normal to the bent lamellar planes and so they converge to the bending center.

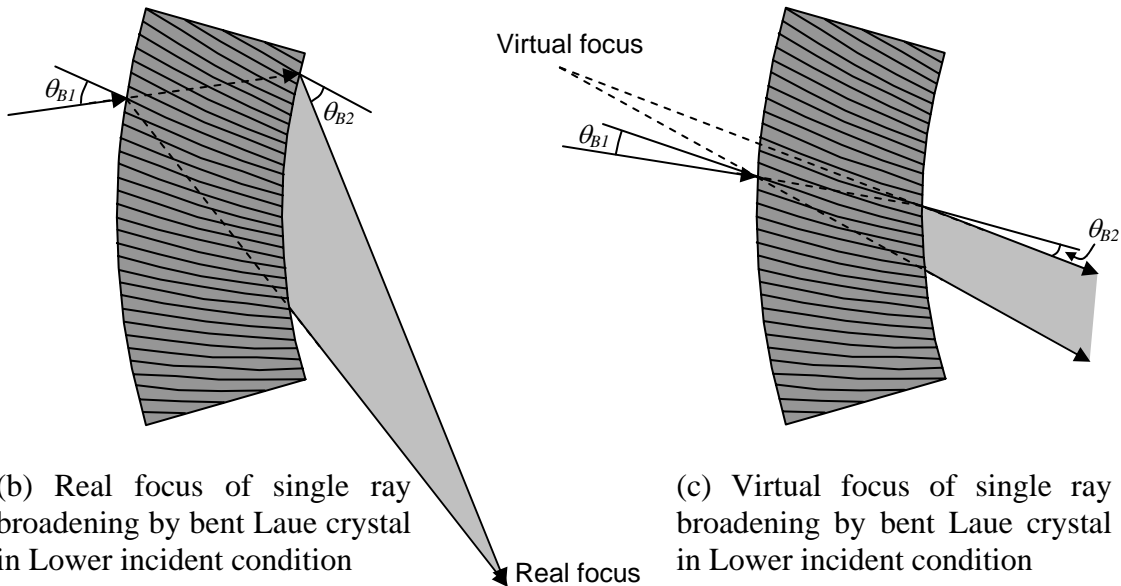
The location of the polychromatic focus is determined by the angle between two reflected rays which comes from the changes of the orientation of the lattice plane, the incident angle and the crystal thickness. The angle between two reflected rays $\Delta\theta_R$ ($\Delta\theta_R = 2(\theta_2 - \theta_1)$) is two times of the angle between the corresponding two lattice planes $\Delta\theta_L$ ($\Delta\theta_L = \theta_2 - \theta_1$) as shown in Fig. 4.8(b). Suppose the ray is incident upon the crystal at point A and leaves the crystal at point C as shown in Fig. 4.8(b), $\Delta\theta_L$ is composed from two parts; $\Delta\theta_{AB}$ and $\Delta\theta_{BC}$. $\Delta\theta_{AB}$ is the angular change along the same lattice plane on different lamellar planes from AA' to B'B (Point B is on the same lamellar plane as

point C). $\Delta\theta_{BC}$ is the angular change across multiple lattice planes at the same lamellar plane from B'B to C'C.

A coordinate system XOY is built as shown in Fig. 4.8(b) with the origin O at the center of the crystal along its thickness and on the same lattice plane as the point A which the x-ray is incident upon. The X-axis is along the tangent of the lamellar plane at the origin, and Y-axis along the normal to the lamellar plane.



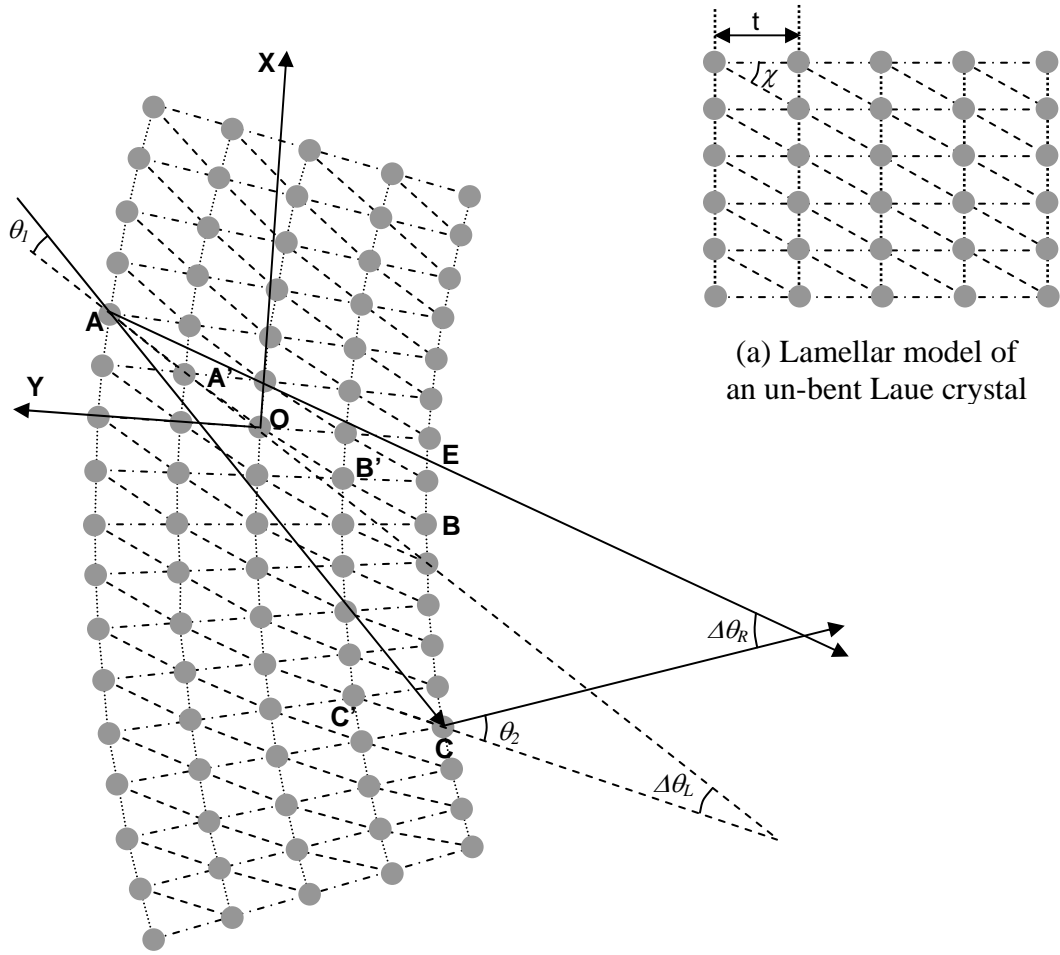
(a) Real focus of single ray broadening by bent Laue



(b) Real focus of single ray broadening by bent Laue crystal in Lower incident condition

(c) Virtual focus of single ray broadening by bent Laue crystal in Lower incident condition

Figure 4.7 Real and virtual polychromatic foci after the broadening of the single ray by the bent Laue crystal. When the incident angle θ_{B1} is smaller than the exit angle θ_{B2} , a real focus exists. Otherwise, no focus or a virtual focus forms.



(a) Lamellar model of an un-bent Laue crystal

(b) Lamellar model of a bent Laue crystal and its optics

- Lattice point - - - - - Lattice plane Lamellar plane
- Coordinate system, incident ray and the reflected rays

Figure 4.8 Lamellar model for calculation of the single ray focus.

Without losing the generality, the number of the lamellar planes can be an odd number n . If the lamellar planes are counted from the concave side to the convex side of the crystal, A is at the n th lamellar plane, A' is at the $(n-1)$ th lamellar plane, B' is at the second lamellar plane, and B is at the first lamellar plane. Accordingly, the origin O is at $((n+1)/2)$ th lamellar plane.

The X-Y coordinates for the points A , A' , B' , and B are

$$\begin{aligned}
 A &: (-\rho_A \sin \alpha_A, \rho_A \cos \alpha_A - \rho) & A' &: (-\rho_{A'} \sin \alpha_{A'}, \rho_{A'} \cos \alpha_{A'} - \rho) \\
 B' &: (\rho_{B'} \sin \alpha_{B'}, \rho_{B'} \cos \alpha_{B'} - \rho) & B &: (\rho_B \sin \alpha_B, \rho_B \cos \alpha_B - \rho)
 \end{aligned}$$

where $\rho_A, \rho_{A'}, \rho_{B'}, \rho_B$, and ρ are the bending radius of the lamellar planes on which the points A, A', B', B , and O exist. $\rho_A, \rho_{A'}, \rho_{B'}$, and ρ_B can be calculated as $\rho_n, \rho_{n-1}, \rho_2$, and ρ_1 by the following recursive equations respectively.

$$\begin{cases} \rho_i = \rho, & i = \frac{n+1}{2} \\ \rho_i = \rho_{i+1} - t_i, t_i = \frac{\rho t - \nu t(\rho_{i+1} - \rho)}{\rho - \nu t}, & i = \frac{n+1}{2} - 1, \dots, 1 \\ \rho_i = \rho_{i-1} + t_i, t_i = \frac{\rho t - \nu t(\rho_{i-1} - \rho)}{\rho + \nu t}, & i = \frac{n+1}{2} + 1, \dots, n \end{cases} \quad (4.2)$$

where ν is the Poisson ratio of the crystal and t is the distance between two adjacent lamellar planes when the crystal is not bent.

The angles $\alpha_A, \alpha_{A'}, \alpha_{B'}$, and α_B in the coordinates of the points $A, A', B',$ and B are the central angles for these points away from Y-axis respectively. They can be calculated by

$$\alpha_A = \alpha_B = \frac{n-1}{2} \cdot \frac{t \tan \chi}{\rho} = \frac{T \tan \chi}{2\rho} \quad (4.3)$$

$$\alpha_{A'} = \alpha_{B'} = \left(\frac{n-1}{2} - 1 \right) \cdot \frac{t \tan \chi}{\rho} = \frac{T \tan \chi}{2\rho} - \frac{t \tan \chi}{\rho} \quad (4.4)$$

where T is the thickness of the crystal.

So the angle between lattice planes AA' and B'B is

$$\Delta\theta_{AB} = \arccos \frac{\vec{AA'} \cdot \vec{B'B}}{|\vec{AA'}| |\vec{B'B}|} \quad (4.5)$$

The curve in Fig. 4.9 shows that when the number of the lamellar planes used in the calculation is big enough, the calculated angular change along one lattice plane by bending is almost constant. This verifies that using the lamellar model of the crystal to calculate this angular change is appropriate. The calculation is for a crystal with 3.33° asymmetry angle, 0.5mm thick, 2.2m bending radius, and the Poisson ratio is 0.28.

The angular change between lattice plane B'B and C'C can be simply calculated by

$$\Delta\theta_{BC} = T [\tan(\chi \pm \theta_B) - \tan \chi] / \rho \quad (4.6)$$

This angular change does not include the effect of lamellar bending which affects the result less than 1% obtained by calculation.

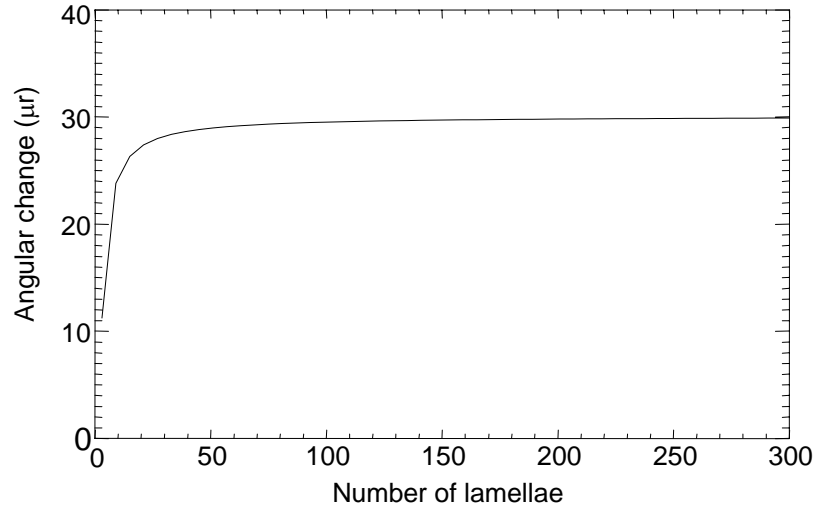


Figure 4.9 Relationship between the number of lamellar plane used in the calculation and the calculated angular change along one lattice plane by bending

The angular change $\Delta\theta_{BC}$ is negative when the lower sign is used in lower incident condition. The total angular difference of the lattice planes for one single ray is

$$\Delta\theta_L = \pm(\Delta\theta_{AB} + \Delta\theta_{BC}) \quad (4.7)$$

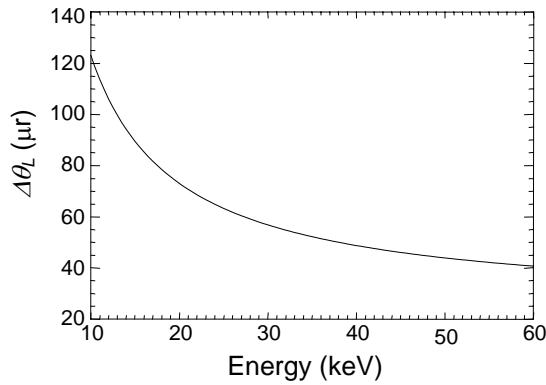
The distance from the crystal to the single ray focus L can be calculated by

$$L = \frac{T \sin 2\theta_B}{2\Delta\theta_L \cos(\chi \pm \theta_B)} \quad (4.8)$$

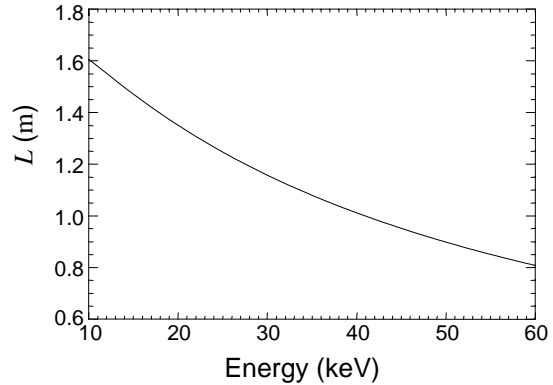
From the Eq. 4.6-4.8, the distance from the crystal to the single ray focus is smaller in the upper condition than that of the lower condition. This distance can be negative corresponding to a virtual focus shown in Fig. 4.7(c). Figure 4.10(a) and (c) show the angular change of the lattice plane from the x-ray incident point to the x-ray exit point decreases when the energy of the incident x-ray increases both for upper and lower incident condition. However, the angular change crosses 0 in the lower incident condition which indicates that the angle of the lattice plane relative to the incident ray changes from increasing to decreasing along the transmission of the ray. Figure 4.10(b) shows the distance of the single ray focus to the crystal decreasing with the increase of the energy of the ray in the upper incident condition. Fig 4.10(d) shows this distance increases with the increase of the energy and the real focus turns to a virtual one at a ray energy of 38.9keV which is also the energy for the angular change of the lattice plane

crossing 0. The curves in Fig. 4.10 were calculated for a Si(1, 1, 1) crystal with an asymmetry angle of 1.28° , and a bending radius of 2.05m. The Poisson ratio is 0.28.

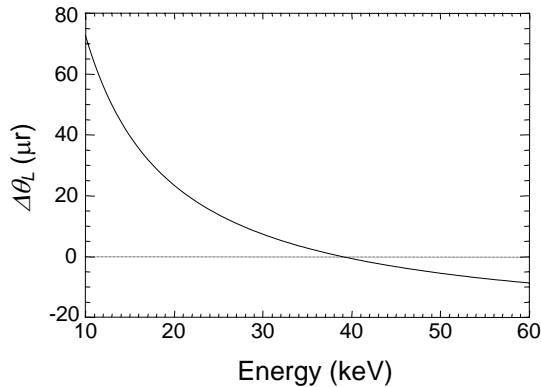
It is also easy to tell from Eq. 4.8 that the single ray focus distance increases with the increase of the asymmetry angle.



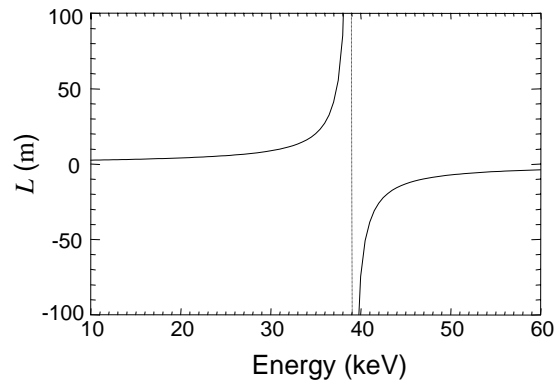
(a) Angular change of the lattice plane as a function of energy in upper incident condition



(b) Distance of single ray focus to crystal as a function of energy in upper incident condition



(c) Angular change of the lattice plane as a function of energy in lower incident condition



(d) Distance of single ray focus to crystal as a function of energy in lower incident condition

Figure 4.10 Angular change of the lattice planes and the single ray focus distance as functions of energy. Negative angular change indicates the x-ray exit angle from the lattice plane is smaller than the x-ray incident angle to the lattice plane. When the single ray focus is virtual, the single ray focus distance is negative.

4.2.4 Focus Size

The focus size refers to the vertical size of the beam at the geometrical focus of the bent Laue crystal. It directly affects the spatial resolution of the KES imaging since the object is positioned at this point.

The locations of the polychromatic focus and the geometric focus affect the focus size. As shown in Fig. 4.11, as long as the polychromatic focus is not at the same position as the geometric focus (Fig. 4.11(a) and (b)), the broadening of the single ray at the geometric focus will enlarge the focus size. When both the geometric focus and the polychromatic focus are at the same point ($f_2 = L$) as shown in Fig. 4.11(c), the focus size is minimal and it is only limited by the size of the source.

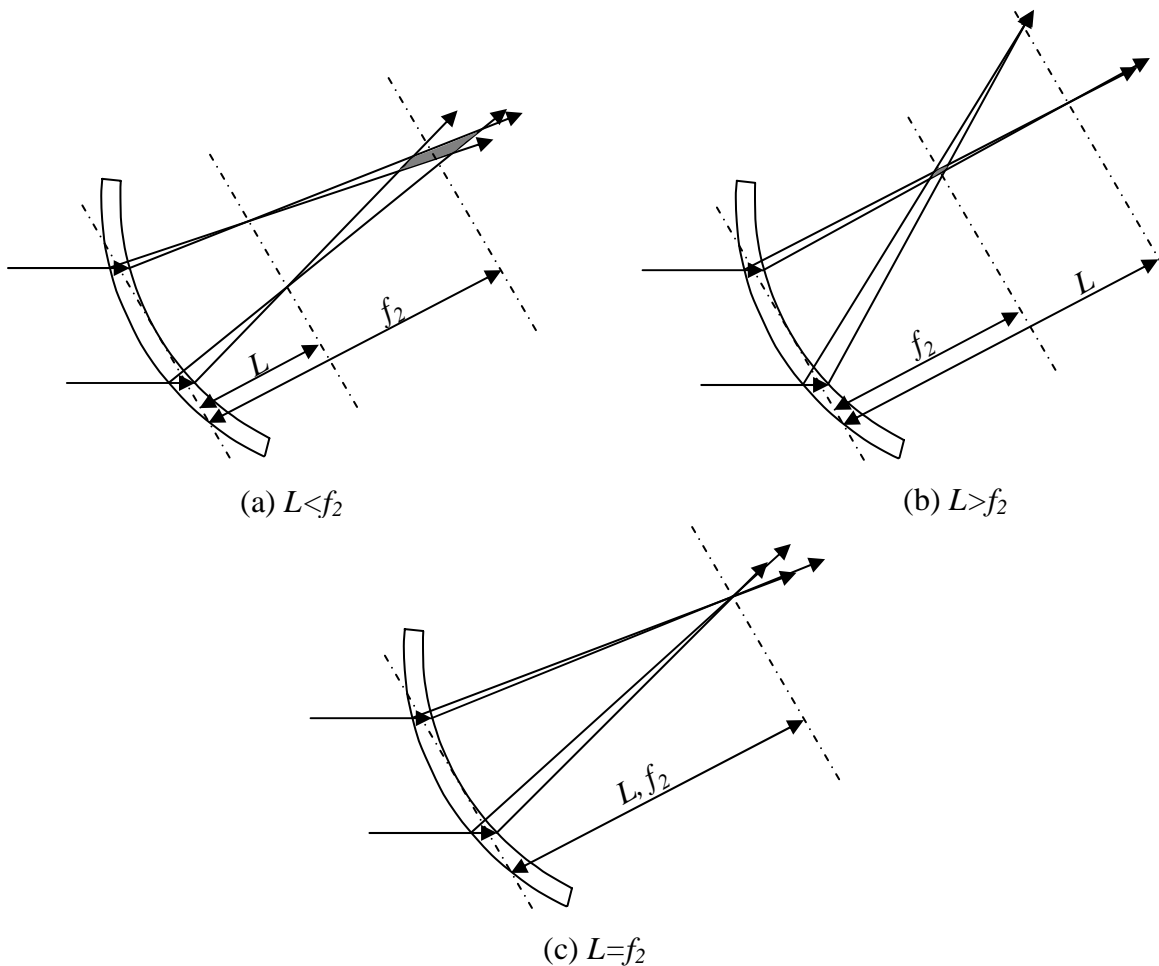


Figure 4.11 Three relative locations of the geometric focus and the polychromatic focus. The focus size is minimal when these two foci are at the same point.

The parameters used in the calculation of the distances of the geometric focus and the polychromatic focus are:

- (1) The distance of the source to the crystal f_1 which is determined by the experimental hutch size and position;
- (2) The Bragg angle θ_B which depends on the energy of the beam E ;
- (3) The type of the crystal (i.e. element and the orientation of the lattice plane) which is considered as unchangeable in this design phase. It is selected at the beginning of the design.
- (4) The crystal thickness T which does not affect the geometric focus. It has very little effect on the polychromatic focus because normally the thickness of the crystal can be ignored when it is compared to the bending radius, in a ratio from 1 over 10^3 to 10^4 . Fig. 4.12 shows a quantitative evaluation of the effect of the crystal thickness on the polychromatic focus length. Note that in this figure the change in the polychromatic focus length is approximately $5\mu\text{m}$ per 1mm of change in crystal thickness. This calculation is for Si(1,1,1) with an asymmetry angle of 20° , the energy of the incident beam is 33.169keV, the source to the crystal distance is 22m, the bending radius is 5.1m, and the Poisson ratio is 0.28.

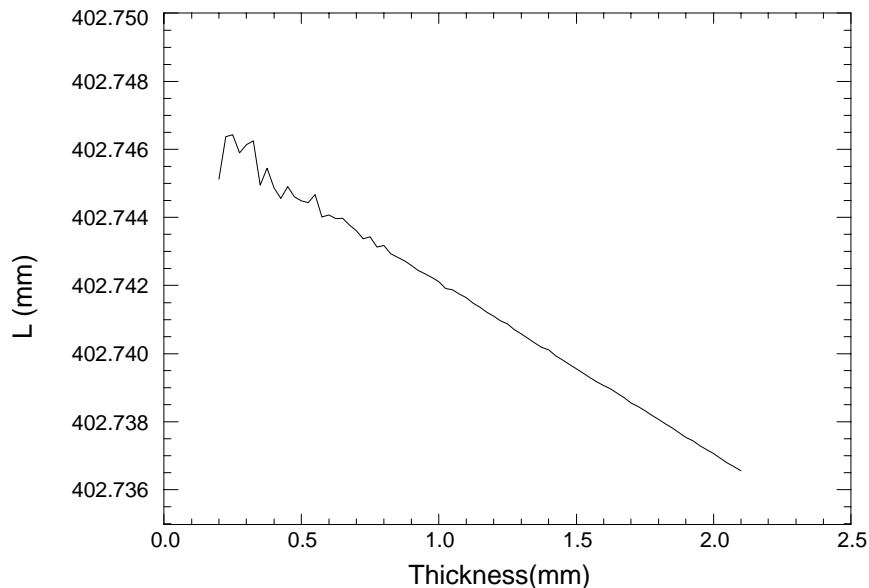
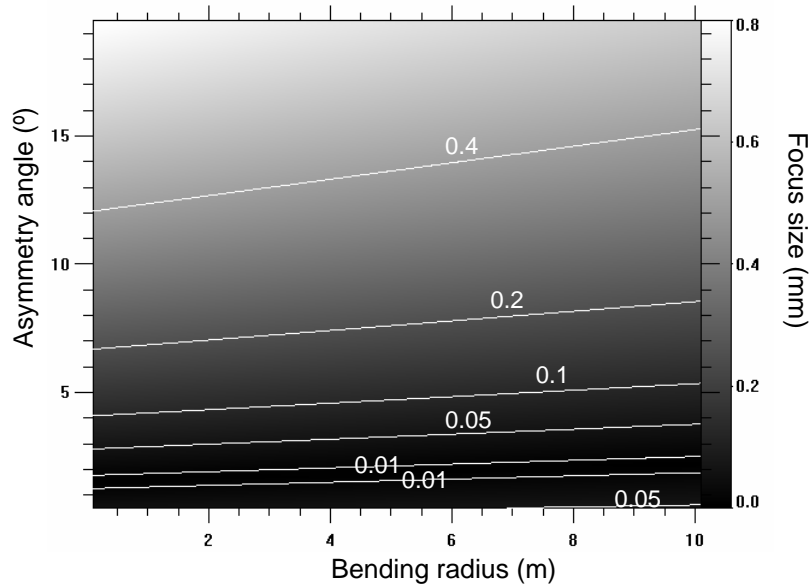


Figure 4.12 The distance from the crystal to the polychromatic focus as a function of crystal thickness

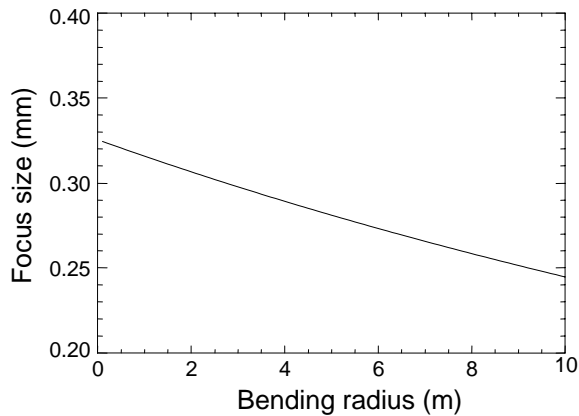
- (5) The incident condition. According to Eq. 4.7, $\Delta\theta_L$ of the upper incident condition is always bigger than that of the lower incident condition. So even in a case that the single ray with the lower incident condition has a real focus, the distance to this focus is bigger than that of the single ray with the upper incident condition. Furthermore, there is a possibility that no real focus exists for the single ray with the lower incident condition when the required beam energy is high.
- (6) The bending radius of the crystal. According to Eq. 4.1, the geometric focus increases with the increase of the bending radius. The bending radius changes the polychromatic focus in the same way.
- (7) The asymmetry angle of the crystal, which needs further investigation.

Of the above parameters, the two most important parameters of the geometrical focus and the polychromatic focus are the bending radius and the asymmetry angle. The effect of the bending radius and the asymmetry angle on the focus size can be evaluated by changing the bending radius and the asymmetry angle in the calculation while keeping the other parameters constant. Figure 4.13(a) shows the focus size as a function of the bending radius and the asymmetry angle. The focus size is indicated by the grayscale value in the image with the mapping between grayscale and focus size shown in the bar on the right hand side. Small focus size can be achieved by a small asymmetry angle while the effect of the bending radius on the focus size is not so significant. Figure 4.13(b) shows that the focus size decreases with the increase of the bending radius when the asymmetry angle keeps constant at 20° . The effect of the asymmetry angle on the focus size is dramatic as shown in Fig. 4.13(c) when the bending radius is a constant of 2m. The curve also shows that a minimum focus size $1.44\mu\text{m}$ is obtained at an asymmetry angle of 1.72 degree which is limited by the calculation precision. So the asymmetry angle χ is very important for achieving small focus size and it is used to obtain the coincidence of f_2 and L within the constraints set by f_1 and θ_B .

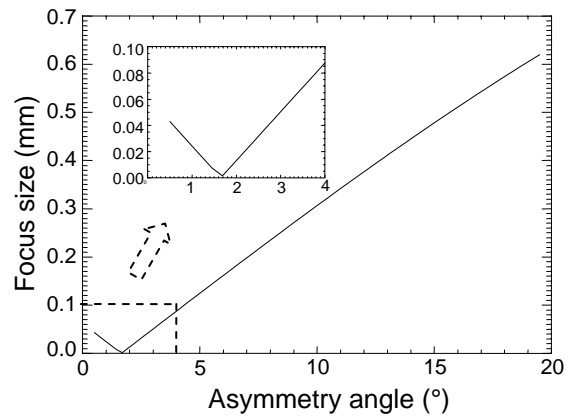
When f_2 and L perfectly overlap, the focus size is only limited by the source size.



(a) Focus size as a function of bending radius and asymmetry angle. The focus size is indicated by the grayscale value in the image with a mapping bar on the right.



(b) Focus size as a function of bending radius when the asymmetry angle is 10°



(c) The focus size changes with the asymmetry angle when the bending radius is 2m

Figure 4.13 Effects of bending radius and asymmetry angle on focus size. The calculation is for Si(1,1,1) with a thickness of 1mm. The distance from the source to the crystal is 22m and the beam incident direction is at the Bragg angle of 33.169keV.

4.2.5 Reflectivity

The calculation of the reflectivity of the crystal is based on the same lamellar model of the crystal as shown in Fig. 4.8. The Lamellar model has been previously developed for a curved crystal by White in 1950 [84]. The model has been applied in both Bragg

and Laue geometries and the agreement is quite good with rigorous dynamical calculations [85].

As an x-ray transverses the crystal, it is incident upon a stack of perfect crystal lamellae which have a gradually changing orientation caused by bending. The incident beam for the current lamella (the j^{th} lamella) is the transmitted beam from the last lamella (the $(j-1)^{\text{th}}$ lamella). The reflected beam by the j^{th} lamella is corrected for the absorption when it goes out the crystal lamella. The reflectivity of the crystal R is the summation of the reflections in each lamella.

$$R = \sum_{j=1}^n \left(r_j e^{-\mu_0 S_j} \prod_{k=0}^{j-1} t_k \right) \quad (4.9)$$

where r_j and t_j are the reflection and transmission ratios of the j^{th} lamella, S_j is the absorption path length of the reflected beam at the j^{th} lamella, and μ_0 is the linear absorption coefficient of the crystal. The thickness of the lamella can be determined so that the angular change of the lattice plane between two successive lamellae is equal to the Darwin width of the reflection.

Although the lamellar models are similar to each other in the calculation of the polychromatic focus and the reflectivity, the thickness of one lamella is quite different. To accurately estimate the location of the polychromatic focus, the number of lamellae normally is selected more than 100. In the calculation of the reflectivity, the thickness of one lamella has to be big enough so that the dynamical diffraction theory (Appendix A.3) can be applied to each lamella. As a result, only a few lamellae contribute to the reflection for each incident ray.

4.3 Conceptual Design

As introduced in Chapter 3, the bent Laue monochromator is for simultaneous KES imaging and the object being imaged is a small animal, i.e. rat. The imaging system will be implemented at *BioMedical Imaging and Therapy Bending Magnet (BMIT-BM)* beamline. Some constraints of the design are listed as follows:

- (1) The distance from the source to the crystal is 22m.
- (2) The energies of the imaging beam are $33.169\text{keV} \pm 100\text{eV}$.

- (3) The distance from the crystal to the geometric focus should be less than 3m which is limited by the size of the experimental hutch.
- (4) The focus size has the priority in the design to achieve good spatial resolution since the imaging target is a small animal (i.e. rat or mouse).

4.3.1 Selection of the Crystal

To reduce the cost of the crystal, several commercially available wafers were considered; Si(2, 2, 0), Si(5, 1, 1), Si(4, 0, 0), Si(2, 1, 1), and Si(1, 1, 1). The stereographic projections of the silicon crystal (Appendix A.4) in the above directions are plotted in Fig. 4.14. Stereographic projection graphically shows the accurate angular relationship between lattice planes and directions of a crystal. In the projections, the farther the point (normal direction of the lattice plane) to the center of the circle (normal direction of the wafer), the smaller the asymmetry angle. The minimum asymmetry angles and the corresponding lattice direction of the silicon crystal are listed in Table 4.1. And the lattice directions are also marked in bold italic in the stereographic projections in Fig. 4.14. The asymmetry angle is calculated by

$$\chi_{HKL}(hkl) = 90^\circ - \arccos \frac{(h,k,l) \cdot (H,K,L)}{\|(h,k,l)\| \|(H,K,L)\|} \quad (4.10)$$

where (H, K, L) is the wafer direction and (h, k, l) is the direction of the lattice plane.

The minimum asymmetry angle is achieved by lattice plane directions of (1, -1, -3) and (1, -3, -1) cut from the wafer with a direction of (5, 1, 1).

Thus we will chose the Si(5, 5, 1) wafer in which the Si(1, -1, -3) or Si(1, -3, -1) lattice planes will be used for diffraction. This combination has a small asymmetry which we need for good spatial resolution. Since the properties of the Si(1, -1, -3) and Si(1, -3, -1) are same to each other, Si(1, -1, -3) is selected to do the following discussion.

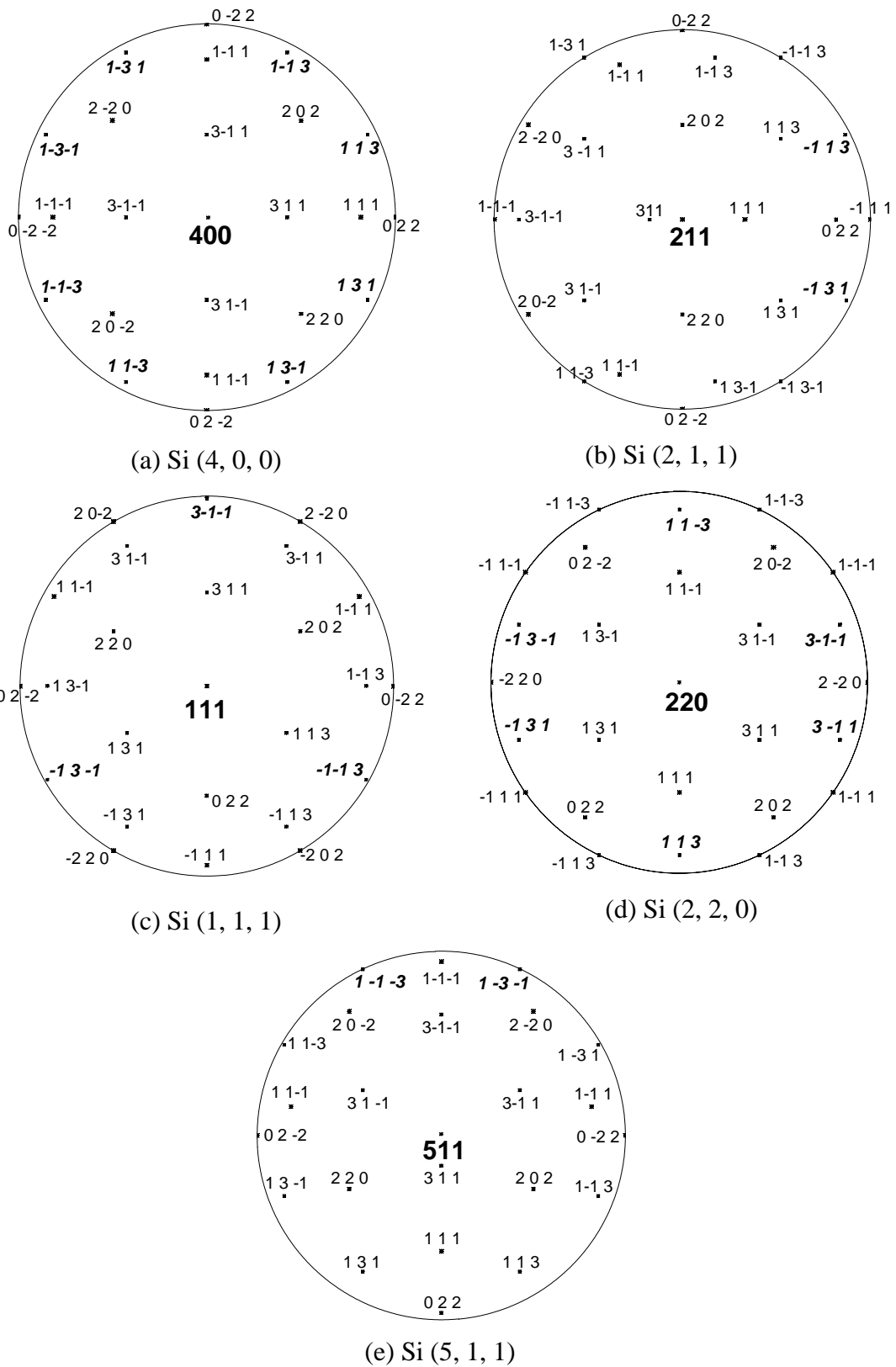


Figure 4.14 Stereographic projection of silicon wafer Si(4, 0, 0), Si(2, 1, 1), Si(1, 1, 1), Si(2, 2, 0), and Si(5, 1, 1)

Table 4.1 Minimum asymmetry angles achieved in widely available silicon wafers and their corresponding lattice plane directions

Wafer	Asymmetry angle	Lattice direction
Si(4, 0, 0)	17.5484°	(1, 1, -3), (1, -1, -3), (1, -3, -1), (1, -3, 1), (1, -1, 3), (1, 1, 3), (1, 3, 1), (1, 3, -1)
Si(2, 1, 1)	14.2518°	(-1, 3, 1), (-1, 1, 3)
Si(1, 1, 1)	10.025°	(-1, -1, 3), (-1, 3, -1), (3, -1, -1)
Si(2, 2, 0)	25.2394°	(1, 1, -3), (-1, 3, -1), (-1, 3, 1), (1, 1, 3), (3, -1, 1), (3, -1, -1)
Si(5, 1, 1)	3.32651°	(1, -1, -3), (1, -3, -1)

4.3.2 Design of the Bending Radius and the Focus Size

Figure 4.15 shows that an optimum focus size can always be achieved by a reasonable bending radius when the asymmetry angle of the crystal is small. So the bending radius is designed to make the focus size optimum based on the known parameters; 1) the source-crystal distance $f_1 = 22m$, 2) the lattice plane direction of the crystal which is (1, -1, -3), 3) the asymmetry angle $\chi = 3.32651^\circ$, 4) the thickness of the crystal $t = 0.5mm$, and, 5) the beam energy required in the experiment $E = 33.169keV \pm 100eV$. Figure 4.16(a) shows the calculated polychromatic focus L and the geometric focus f_2 dependence on the bending radius with the upper incident condition. The two foci are almost at the same point when the bending radius is smaller than 4m. Figure 4.16(b) gives a clearer view which shows the focus size as a function of the bending radius. The flat bottom of the curve was caused by the precision of the computation. According to the calculation, the focus size is minimal at $0.55\mu m$ when the bending radius is 3.4m. The geometric focus and the polychromatic focus of the beam are coincident at the point which is 1.58m from the concave side of the crystal.

Note that the focus size is limited by the source size. The source size is defined by Gaussian distribution with standard deviations, σ_x of $173\mu m$ horizontally and σ_y of $30.8\mu m$ vertically at the CLS. The focus size will be affected by the vertical source size

whose FWHM is $72.53\mu\text{m}$. This size is de-magnified by the crystal by the ratio of f_2/f_1 which is 0.0718. Thus the focus size due to the source is $5.21\mu\text{m}$. This number set the upper limit of the focus size which can be achieved by the design of the crystal at the CLS.

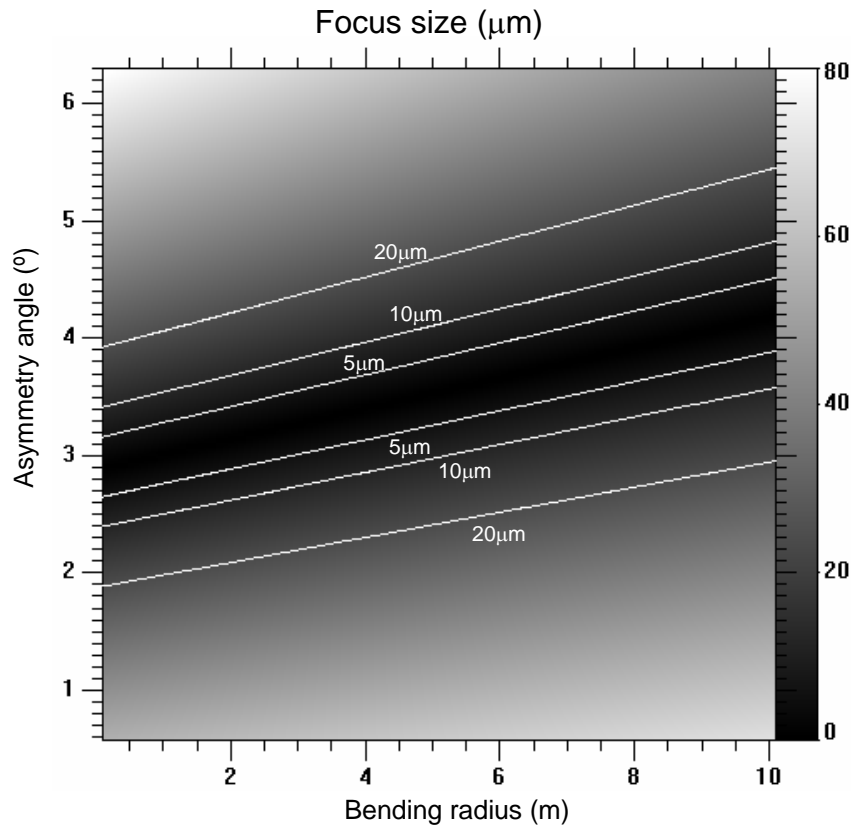


Figure 4.15 Focus size as a function of bending radius and asymmetry angle of the crystal. The focus size is indicated by the grayscale value in the image with the mapping between grayscale and focus size shown in the bar on the right hand side. Contours are plotted for the focus size equal to $5\mu\text{m}$, $10\mu\text{m}$, and $20\mu\text{m}$.

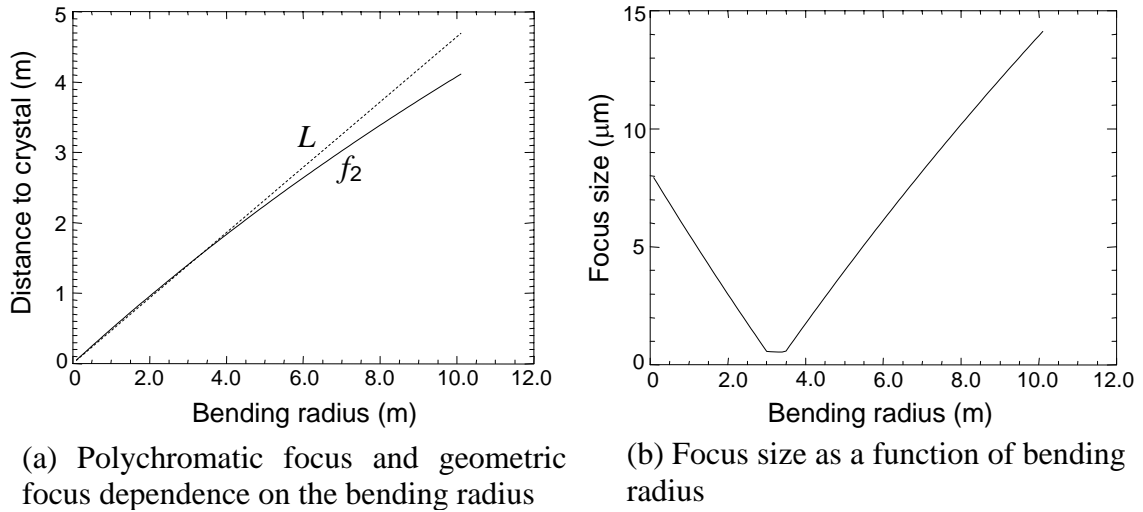


Figure 4.16 The dependence of polychromatic focus, geometric focus, and focus size on the bending radius

4.3.3 Requirement of the Beam Vertical Size of the Design

The vertical size of the beam on to the crystal is determined to satisfy the requirement of the energy bandwidth of the experiment ($\pm 100eV$). Figure 4.17 shows that the required vertical beam size also changes with the bending radius. At the designed bending radius (3.4m), the required vertical beam size is 2mm which can be satisfied by the beamline.

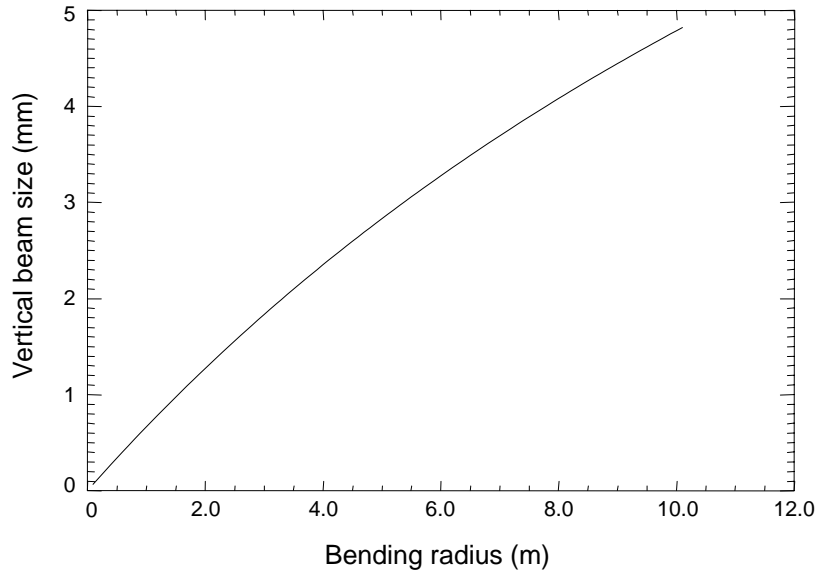


Figure 4.17 Vertical beam size as a function of bending radius. The vertical beam size is determined to satisfy the energy requirement.

4.3.4 Reflectivity of the Design

The calculated reflectivity of this design is shown in Fig. 4.18 as a solid curve. The dashed line in the figure is the reflectivity of the design for the coronary angiography project implemented in the NSLS. In that project, the crystal was selected as Si(1, 1, 1) with an asymmetry angle of 26.22° , a thickness of 0.7mm, a bending radius of 13.81m. The saw-tooth shape of the curves is due to the lamellar model used to approximate the bent crystal.

The integrated reflectivity of our design is approximately $10.93\mu\text{r}$. The FWHM of the reflectivity curve is $15.91\mu\text{r}$ which corresponds to an energy width of 4.59eV at 33.169keV. The integrated reflectivity of the design for the coronary angiography project is 29.72 with an angular bandwidth of $34.48\mu\text{r}$ (FWHM) which corresponds to an energy width of 19.15eV at 33.169keV.

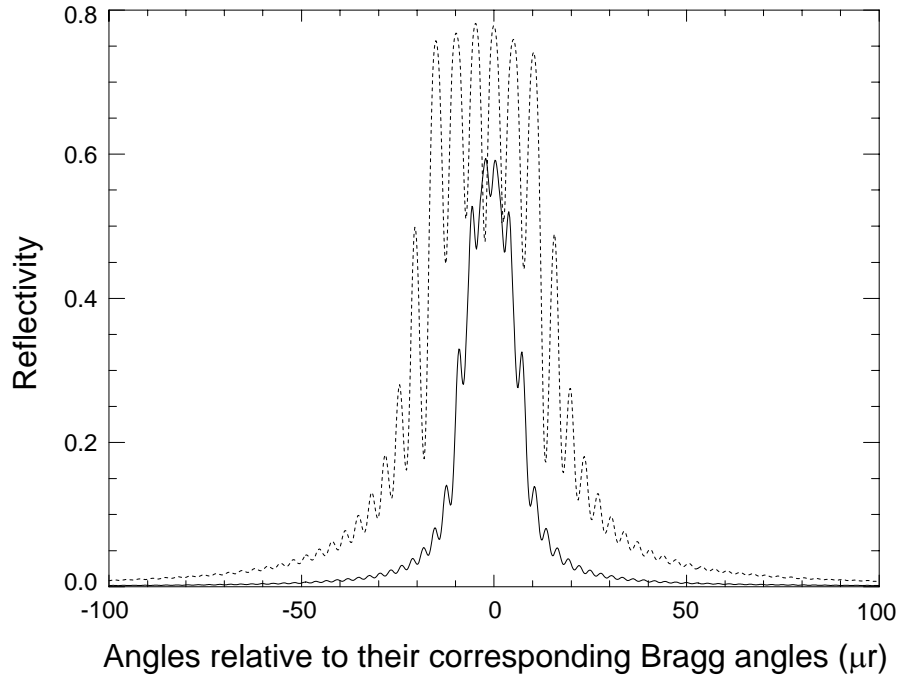


Figure 4.18 Reflectivity of the design (solid line) and a comparison to the design of the coronary angiography project in the NSLS (dashed line)

4.3.5 Energy Resolution of the Design

The energy resolution depends on the single ray bandwidth of the design and the pixel size of the detector. The energy resolution can be understood by a phase space representation [86]. Figure 4.19(a) shows the phase space of the diffracted beam of our design in the plane of diffraction with the coordinate transverse to the center ray. The position of a ray is measured relative to the center ray and the slope is calculated as the change in position per change in propagation distance along the center ray. Since the energy of the ray is directly related to the transmission angle of the ray, the phase space can be interpreted to energy space as shown in Fig. 4.19(b). Compared to the phase space (Fig. 4.19(a)) and energy space (Fig. 4.19(b)) of our design, Fig. 4.19(c) and (d) show the phase space and energy space of the design in NSLS coronary project. In our design, since the beam converges to one point at the geometric focus or polychromatic focus, the area of the phase space at this point is 0 which indicates the area of the phase space at any intersection of the beam is 0 according to Liouville's theorem [87] – the distribution function is constant along any trajectory in phase space. This means along the trajectory of the beam, one ray is at one energy if the rocking curve width of the

reflection is ignored. So the energy resolution can be as good as 1eV estimated by the Darwin width of the crystal Si(1, -1, -3) which is $3.42\mu\text{r}$. Compared to our design, there is an energy width for any point in the beam in NSLS design. Figure 4.20 shows this energy width of the center ray as a function of the distance to the crystal when the distance is longer than the geometric focus of the beam. This energy width set the upper limit of the energy resolution. At a distance of 10m from the crystal, the energy width of the center ray is 53.87eV which does not include the energy width caused by the Darwin width and the pixel size of the detector.

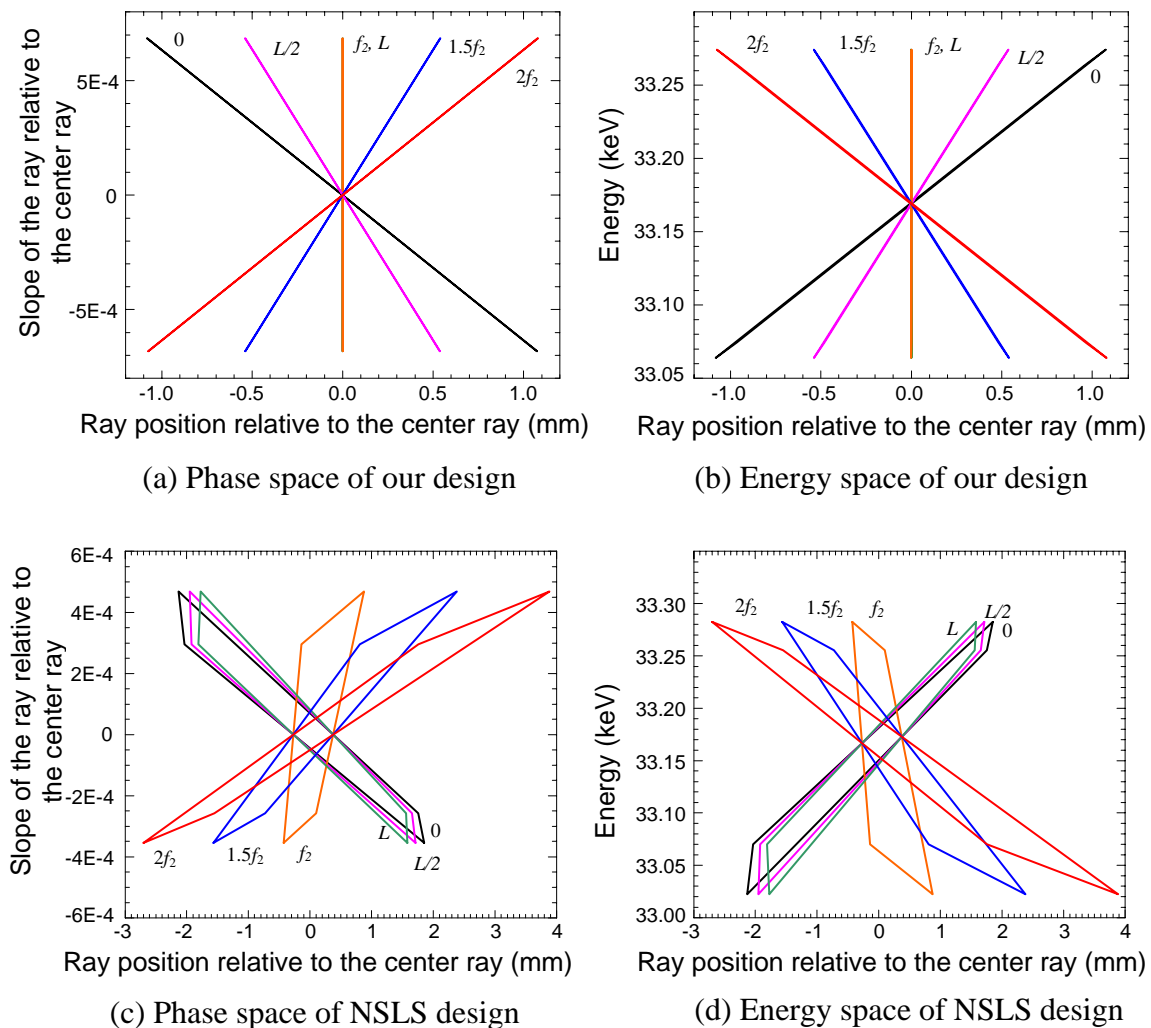


Figure 4.19 Phase space and energy space of the beam of our design compared to the phase space and energy space of the beam transmission in NSLS design

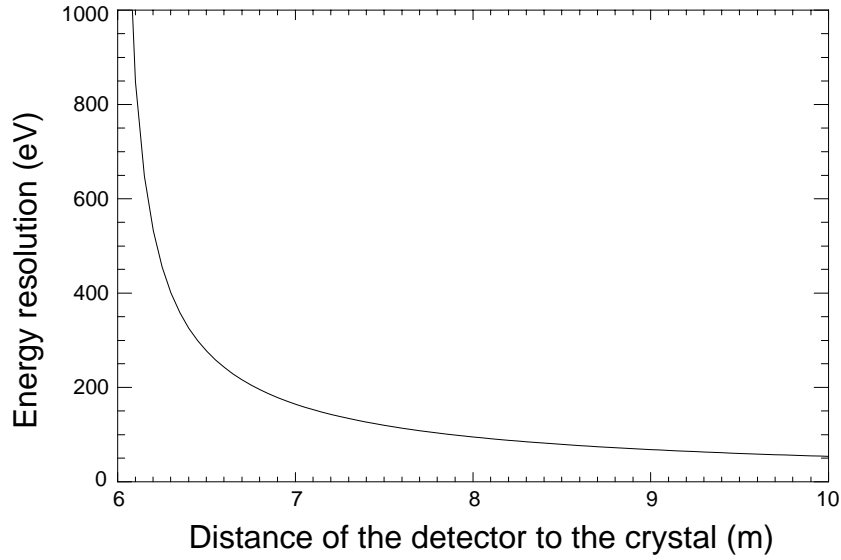


Figure 4.20 Energy resolution of the center ray that the NSLS design can achieved as a function of the distance from the detector to the crvstal

The energy resolution is also affected both by the distance of the detector to the focus point and the pixel size of the detector. For our case, the distance of the detector to the crystal can be as far as 5m which is limited by the BMIT-BM hutch size. Figure 4.21 shows the energy resolution changes with the detector position when the pixel size of the detector is $20\mu\text{m}$. The minimum energy resolution of 7.5eV can be achieved including the energy bandwidth caused by the Darwin width of the reflection.

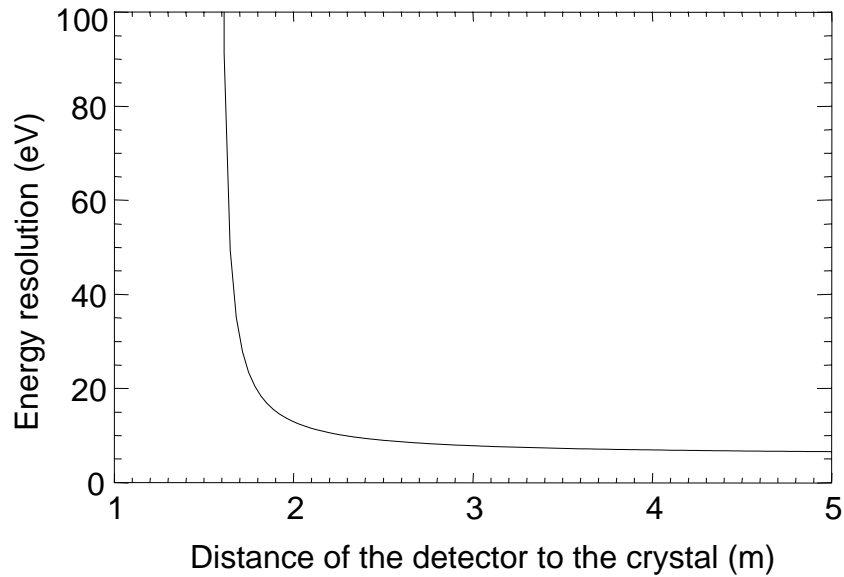


Figure 4.21 Energy resolution as a function of the distance from the detector to the crystal

4.4 Conclusions

A bent Laue monochromator was designed for KES imaging with small animals at the BMIT-BM beamline at the CLS where the source to the crystal distance is 22m. In the design, the crystal was selected as Si(1, -1, -3) with an asymmetry cut of 3.33° from a widely commercial available wafer Si(5, 1, 1). The thickness of the crystal was 0.5mm. With a bending radius of 3.4m and upper incident condition of the x-ray beam, the coincidence of the polychromatic focus and the geometric focus was achieved at 1.58m from the crystal so that the focus size can be only limited by the source size. Currently, a focus size of $0.55\mu\text{m}$ was obtained which was limited by the calculation precision of the computer if the source size was ignored. A beam height of 2mm is required to fulfill an energy bandwidth of $\pm 100\text{eV}$ at the iodine K-edge 33.169keV which can be easily satisfied by the beamline (4.4mm at 22m vertically). An energy resolution of 7.5eV was achieved when the detector was positioned 5m from the crystal which indicates that this monochromator can be also used for DXAS.

To implement the design in the beamline, a bender need be designed which is flexible for different bending radius and different crystal thickness. Also, the correct

alignment of the orientation of the crystal need be easily achieved when the crystal is put into the bender. Local stress should be avoided which will break the crystal.

Normally, a dual-line detector is employed in the simultaneous KES imaging. In our case, the total beam height is around 7mm at the position which is 5m from the crystal. This beam size limits the size of the detector.

Chapter 5

Conclusions and Further Research

Using synchrotron light, two non-invasive imaging techniques, KES and FSI, were used to image dilute contrast materials in small animals, such as a rat. In this chapter, the main achievements are summarized and the further research is discussed.

5.1 Summary and Achievements

Both KES and FSI need monochromatic beams. At the synchrotron facility, the monochromatic beam typically is prepared by a double-crystal monochromator. The wide horizontal beam acceptance of the crystals requires high precision alignment of the crystals in both the Bragg angle and the azimuthal tilt angle (tilt error) to keep the beam intensity consistent along the beam width. Although the normalization by a blank image can get rid of the effect of the visible tilt error in KES images, the SNR of the resulted image varies because of the variation of the incident photon number. In Chapter 2, we studied the effects of the tilt error through DEI and MIR which employ an analyzer crystal to transfer the small angular variation in the transmitted beam into huge intensity change. The relationship of the tilt errors of the three crystals in the DEI imaging system was firstly derived and verified by the experiments; the experiments showed that although the tilt of the monochromator can be compensated by the tilt of the analyzer, the induced intensity variation of the beam can not be compensated; an algorithm was developed to correct the images taken with the tilt error and the suggestions were provided on the experimental parameter settings to achieve the DEI and MIR analysis methods.

With double crystal monochromator, KES and FSI imaging techniques were studied and improved by a series of experiments in Chapter 3. The energies were switched by changing the Bragg angle of the crystals. A rat head restraint and a field flattener were designed and smoothed to improve the SNR of the contrast agent image. A quality factor was developed to evaluate the imaging systems and facilitate the comparison of KES and FSI. Through the quality factor, the achievable upper limit of an imaging system was

defined. Both the quality factor and the detection limit were quantified in a series of experiments. For KES imaging, the detection limits were measured with pure dilute contrast material (almost no significant structure in the object) and simulated physical rat head. Although the detection limit of FSI was only measured with simulated physical rat head, FSI showed great potential in detecting dilute contrast material with high SNR. After the comparison of these two imaging techniques, we concluded that KES and FSI could be used complementarily. KES should be used first to locate the area of interests due to its fast imaging time and large imaging area. FSI should focus on the area of interests due to its high SNR for dilute samples with no concern about the saturation of the detector.

To further improve the performance of KES and overcome the temporal difference during imaging at above edge energy and below edge energy, a bent Laue monochromator was designed to realize simultaneous KES in Chapter 4. The monochromatic focus was studied by simulation method and the coincidence of the geometrical focus and the monochromatic focus was achieved by small asymmetrical cut (several degrees) of the crystal. In this way, good spatial resolution (several microns) can be obtained which is only limited by the source size. High energy resolution (several eV) was also achieved at the same time which can compete that of the double crystal monochromator.

In summary, the contributions of this thesis are listed as follows:

- (i) The effect of tilt error was studied and the relationship of the tilt errors of the three crystals in the DEI imaging system was firstly derived and verified by the experiments.
- (ii) An algorithm was developed to correct the images taken with the tilt error and the suggestions were provided on the experimental parameter settings to achieve the DEI and MIR analysis methods while the tilt error exists.
- (iii) A quality factor was developed for the contrast agent image. The achievable upper limit of an imaging system was defined.
- (iv) The imaging systems, KES and FSI, were critically compared with references to the radiation dose, imaging time and area, spatial resolution, SNR, and the newly developed quality factor.

- (v) Based on the comparison of KES and FSI, a conclusion has been made that these two imaging techniques can be used complementarily for viewing dilute contrast materials; KES can be used first to locate the area of interests due to its fast imaging time and large imaging area, FSI should focus on the area of interests due to its high SNR for dilute samples.
- (vi) An algorithm was developed to convert a 3D smoothing problem into a 2D one and it was applied to smoothing the rat head restraint.
- (vii) Bent Laue crystal was studied and the properties of the monochromatic focus (real or virtual) were defined.
- (viii) A bent Laue monochromator was designed. Both good spatial resolution and high energy resolution were achieved by the coincidence of the geometrical focus and the monochromatic focus of the crystal.

5.2 Challenges for Further Research

In KES imaging, the high and/or low energy images and the blank image for the normalization were taken at the different time which caused the significant noise in the contrast agent image. To further improve the detection limit of the KES, it is required to simultaneously record the photon numbers before they hit the object and after the transmission of the object. Also, the saturation of the detector limits the radiation dose to the animal for one imaging. The similar detection capability of KES and FSI (similar dose to detect 0.1mM-cm iodine solution in physical rat head estimated in Chapter 3) also indicate that an imaging system should detect iodine using both methods. A combined KES and FSI imaging system is being implemented at the Canadian Light Source Biomedical Imaging and Therapy beamline. However, the precision of the currently used ion chamber is not good enough and the recording time frame need be deliberately scheduled.

To implement an optimal FSI system, the optical geometry including the position and orientation of the fluorescence detector can be studied by the simulation of the Compton scatter and the fluorescence signal with Monte Carlo method. The 3D reconstruction of the rat head can be used to conduct this study.

The geometry of the fluorescence detector (multiple channels at multiple positions) gives us a chance to further investigate the distribution of the contrast material in the object.

A more complicated physical rat head needs to be designed and constructed to facilitate the study of the imaging systems. The bone in the rat head should be simulated which will definitely affect the detection limit and the quality factor of the imaging system.

The design of the bent Laue monochromator needs to be verified in the synchrotron facility. To implement the design in the beamline, a bender needs to be designed adaptive to different bending radius and different crystal thickness. Also, the correct alignment of the orientation of the crystal need be easily achieved. The photon flux, the spatial resolution, and the energy resolution need to be measured. The obtained simultaneous KES images can be compared to those taken with temporal difference with reference to the quality factor.

Appendix A

Basic physics concepts

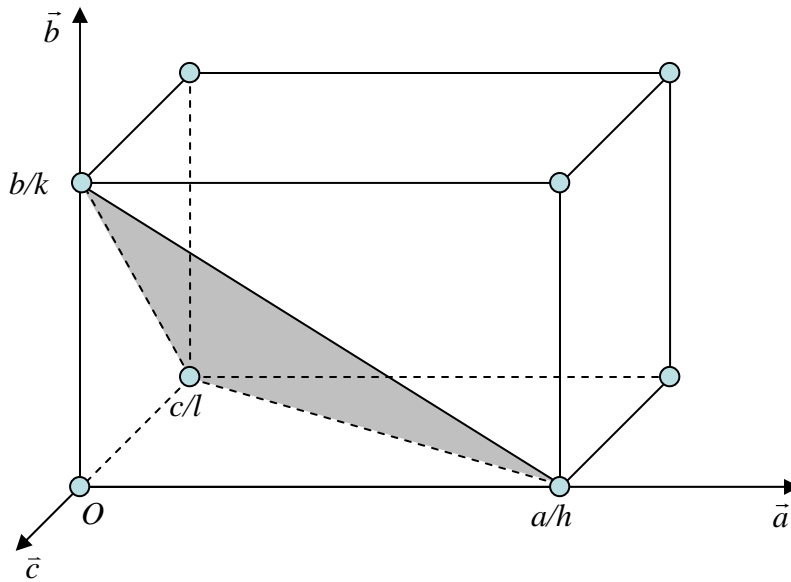
A.1 Miller indices and d-spacing

Miller indices [88] are used to describe the orientation of a family of parallel equidistant planes in the lattices of a crystal. They are defined as the reciprocals of the fractional intercepts which the plane closest to the origin (but not including the origin) makes with the crystallographic axes. As shown in Fig. A.1(a), a plane with Miller indices of (h, k, l) makes fractional intercepts of a/h , b/k , c/l with the axes \vec{a} , \vec{b} , and \vec{c} , where a , b , and c are the unit axial lengths. Figure A.1(b) shows several different orientations of the lattice planes exist in the same lattice points of crystal by a two-dimensional lattice.

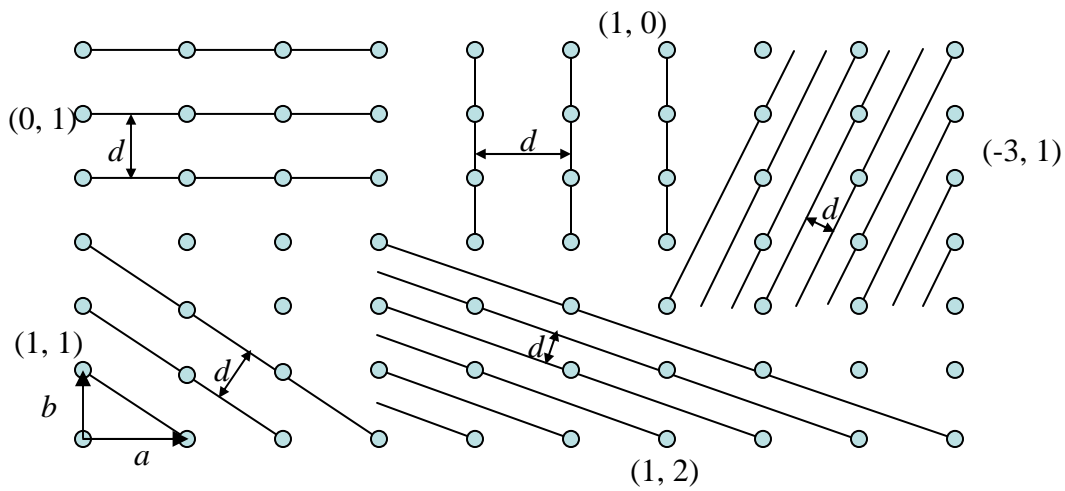
Figure A.1(b) also shows the interplanar spacing d , also denoted as d_{hkl} and called as d-spacing, for different lattice planes. D-spacing is defined as the distance between the lattice planes with the same orientation. For cubic crystal system, d-spacing can be simply calculated by

$$d_{hkl} = \frac{a}{\sqrt{h^2 + k^2 + l^2}}$$

where a is the lattice parameter which is 5.43\AA for silicon crystal.



(a) A plane with Miller indices of (h, k, l)



(b) Lattice planes and their Miller indices, d-spacings in a two dimensional illustration

Figure A.1 Miller indices and d-spacing of crystal lattice plane. (Courtesy B.D. Cullity, Elements of X-ray Diffraction, Addison-Wesley Publishing Company Inc.,USA, 1956)

A.2 Reciprocal lattice

Reciprocal lattice [88] is constructed corresponding to any crystal lattice to make many of its properties are reciprocal to those of the crystal lattice. The unit cell of the reciprocal lattice is defined by the vectors b_1 , b_2 , and b_3 .

$$b_1 = \frac{1}{V}(a_2 \times a_3)$$

$$b_2 = \frac{1}{V}(a_3 \times a_1)$$

$$b_3 = \frac{1}{V}(a_1 \times a_2)$$

where a_1 , a_2 , and a_3 are the unit cell vectors of the crystal lattice, and V is the volume of the crystal unit cell.

Reciprocal lattice vector is defined by the vector H_{hkl} drawn from the origin of the reciprocal lattice vector to the point having coordinates h , k , and l .

$$H_{hkl} = hb_1 + kb_2 + lb_3$$

This vector is perpendicular to the crystal lattice plane with Miller indices (h, k, l) and its length is equal to the reciprocal of the d spacing of those lattice planes.

$$|H_{hkl}| = \frac{1}{d_{hkl}}$$

In the reciprocal lattice, each reciprocal lattice point is related to a set of planes in the crystal and represents the orientation and spacing of that set of planes.

Figure A.2 shows a crystal lattice and reciprocal lattice of a cubic crystal.

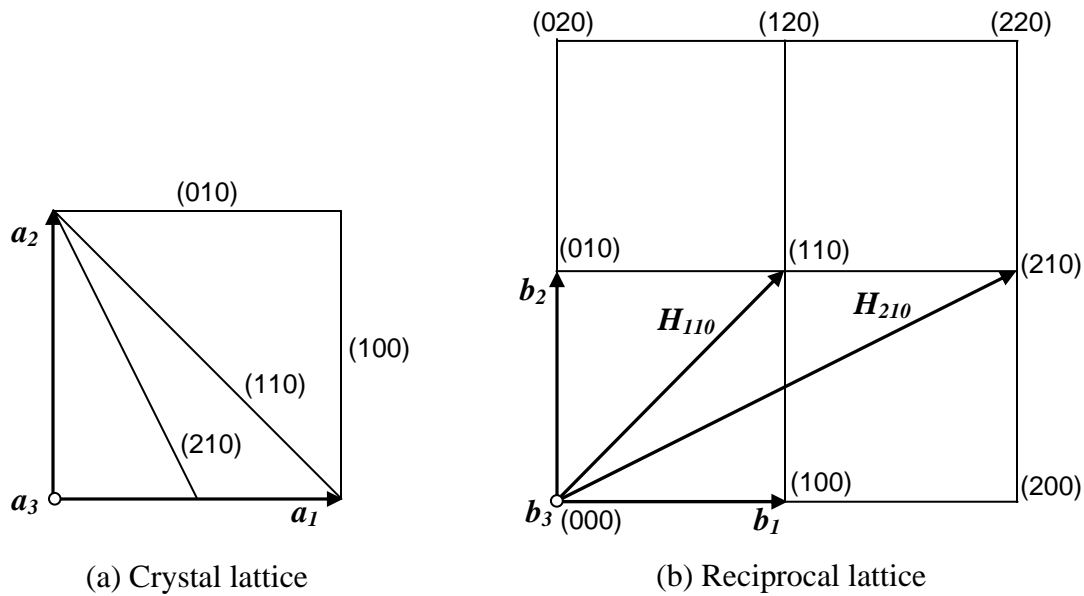


Figure A.2 Crystal lattice and the reciprocal lattice of a cubic crystal. (Courtesy B.D. Cullity, Elements of X-ray Diffraction, Addison-Wesley Publishing Company Inc.,USA, 1956)

A.3 Dynamical Diffraction Theory, Crystal Reflectivity and Darwin width

There are two theories to describe x-ray diffraction, kinematical theory and dynamical theory [64]. The kinematical theory is applied to imperfect crystals, formed from microscopic mosaic blocks whose size is small enough that the magnitude of the x-ray wavefield does not change appreciably over the depth of the block. The scattering amplitude can be evaluated by summing together the amplitude of the scattered waves. This is not the case of crystals in the thesis. The crystals used in my research are macroscopic perfect, essentially free from any defects or dislocations. The amplitude of x-rays diminishes as they propagate down into the crystal and a small fraction is reflected into the exit beam at each atomic plane. Furthermore, the reflected beam can be re-scattered into the direction of the incident beam. The theory that allows for these multiple scattering effects is known as dynamical diffraction theory.

As introduced in Chapter 2.2 of the thesis, the direction of the reflected beam is given by Bragg's law when x-rays are diffracted in the perfect crystal. The reflectivity of the crystal is given by the dynamical diffraction theory and the angular width of the reflectivity is given by Darwin width.

The equations given here were firstly developed by C. G. Darwin in 1914 [64]. The crystal was treated as an infinite stack of atomic planes, each of which gives rise to a small reflected wave which may subsequently be re-scattered into the direction of the incident beam.

The explicit formulae for the Darwin reflectivity curve are as follows.

$$R(x) = \begin{cases} \left| x_c - \sqrt{x_c^2 - 1} \right|^2 & \text{Re}(x_c) \geq 1 \\ \left| x_c - i\sqrt{1 - x_c^2} \right|^2 & |\text{Re}(x_c)| \leq 1 \\ \left| x_c + \sqrt{x_c^2 - 1} \right|^2 & \text{Re}(x_c) \leq -1 \end{cases}$$

where x_c is given by $x_c = m\pi \frac{\zeta}{g} - \frac{g_0}{g}$ with g_0 and g complex. The subscription c is just to remind that x_c is a complex number. In the equation, m is the order of the reflection, i.e. $m=1$ is the fundamental, $m=2$ is the 2nd order, etc; ζ is the relative wavelength band, defined by $\zeta = \Delta\lambda/\lambda$, λ is the wavelength of the reflected beam; g is defined by $g = \frac{1}{m} \left(\frac{2d^2 r_0}{v_c} \right) F$ and so g_0 is given by $g_0 = \frac{1}{m} \left(\frac{2d^2 r_0}{v_c} \right) F_0$, where d is the d-spacing of the crystal, $r_0 = 2.818 \times 10^{-15} m$ is the classical electron radius, v_c is the volume of the unit cell ($v_c = a^3$ for cubic unit cell, a is the lattice parameter), F is the structure factor of the unit cell to describe how the crystal scatters the incident radiation which is determined by the element of the crystal, the structure of the unit cell, the lattice plane orientation, and the energy of the reflected beam. F_0 is this parameter in the forward direction (for $[0, 0, 0]$).

The reflectivity curve of the perfect crystal can be plotted as a function of the relative angular change to its Bragg angle as shown in Fig. A.3 by introducing the differential form of Bragg's equation.

$$\frac{\Delta\lambda}{\lambda} = \frac{\Delta\theta}{\tan\theta}$$

The relative angular change to the corresponding Bragg angle can be understood in two ways; white beam is incident to the crystal at the right Bragg angle of a known

energy, the reflected beam extends to be in an energy range defined by the reflectivity curve; monochromatic x-rays are incident to the crystal at different angles, the reflected x-rays extends to the defined angular range by the reflected curve.

The full width half maximum of the reflected curve is called angular Darwin width. It can be estimated approximately by

$$\omega_D = \frac{2r_0\lambda d}{\pi v_c \cos\theta_B} |F|$$

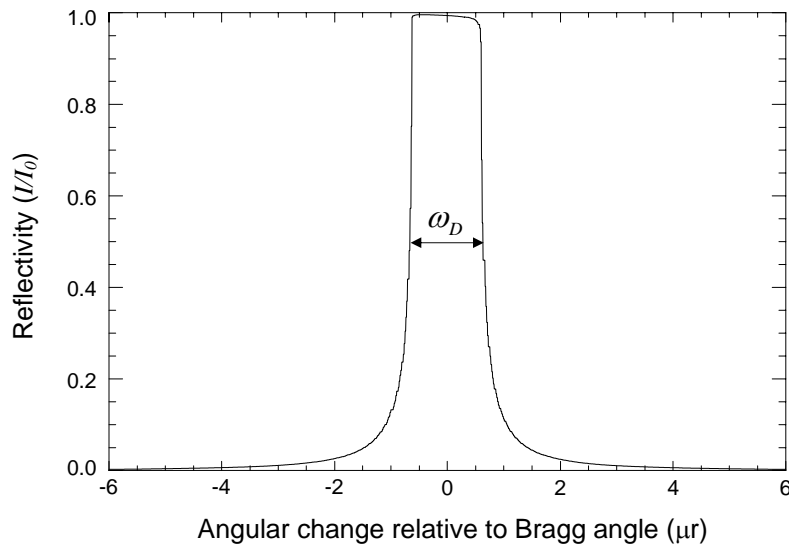


Figure A.3 Reflectivity of Si(3,3,3) at 40keV and the definition of Darwin width

A.4 Stereographic projection

Stereographic projection graphically shows the accurate angular relationship between lattice planes and directions of a crystal [88]. If the normal of the lattice plane is used to represent that plane, all the planes in a crystal can be represented by a set of plane normals radiating from one point within the crystal. The angular relationship of planes is thus converted to the angular relationship of plane normals. If a reference sphere is drawn around this point, the plane normals will intersect the sphere surface in a set of points which is called poles. A circle can be created which passes any two poles and has the same center as the sphere. Thus the angular relationship of plane normals is transferred to the circular distances of poles which are on the sphere surface. To measure these circular distances on a plane rather than on the sphere surface, an equiangular

stereographic projection is used to preserve the angular relationships. As shown in Fig. A.3, the crystal is at the sphere center and the projection plane is put perpendicularly at one end A of a chosen diameter AB. The other end of the diameter B can be used as the point of projection. If a plane has its pole at P, the stereographic projection of P is at P' which is obtained by connecting BP and extending it to have an intersect P' with the projection plane. The plane NWSE passes through the sphere center C and is perpendicular to the diameter AB. It intersects the sphere with a circle and the projection of this circle is also a circle N'W'S'E'. All the poles on the left side of the plane NWSE are projected inside of the circle N'W'S'E'.

For the projections of poles on the left hand side of the sphere, the projection point B can be switched to A and the projection plane can be put perpendicularly at B. Note that the projection plane in fact can be moved along the chosen diameter which only changes the magnification of the projection.

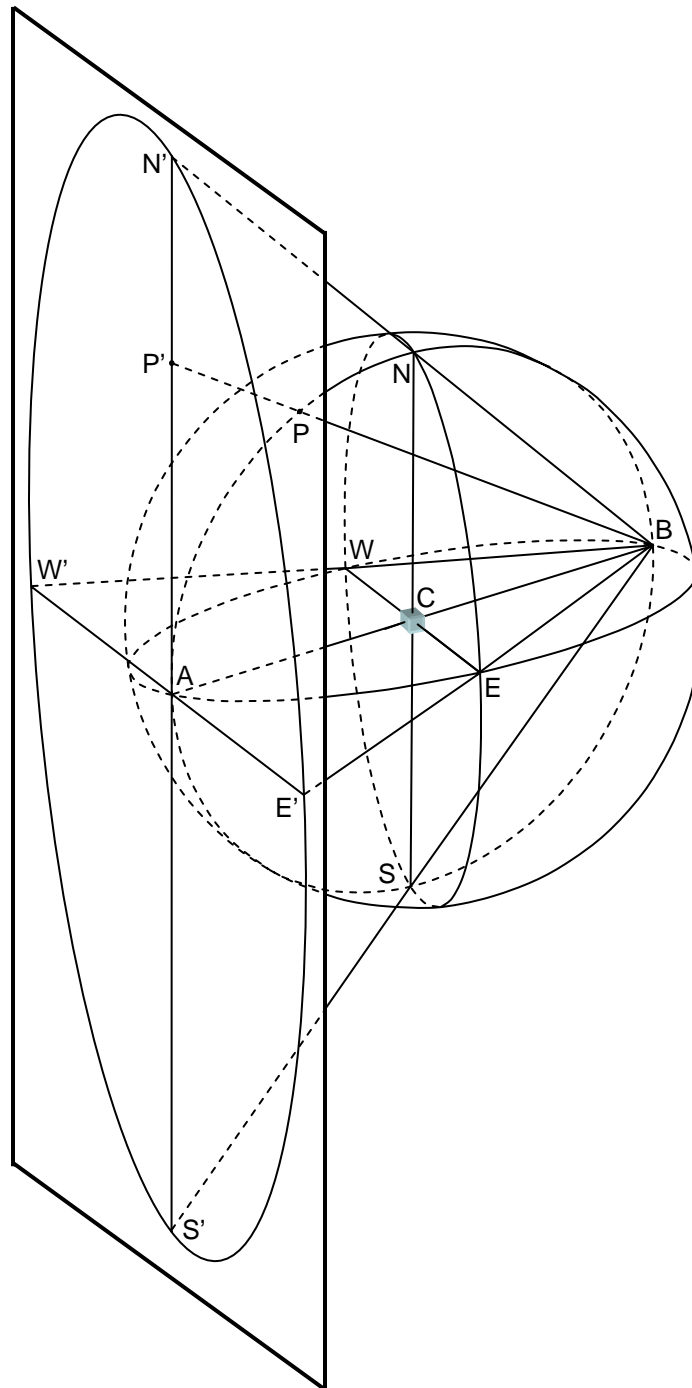
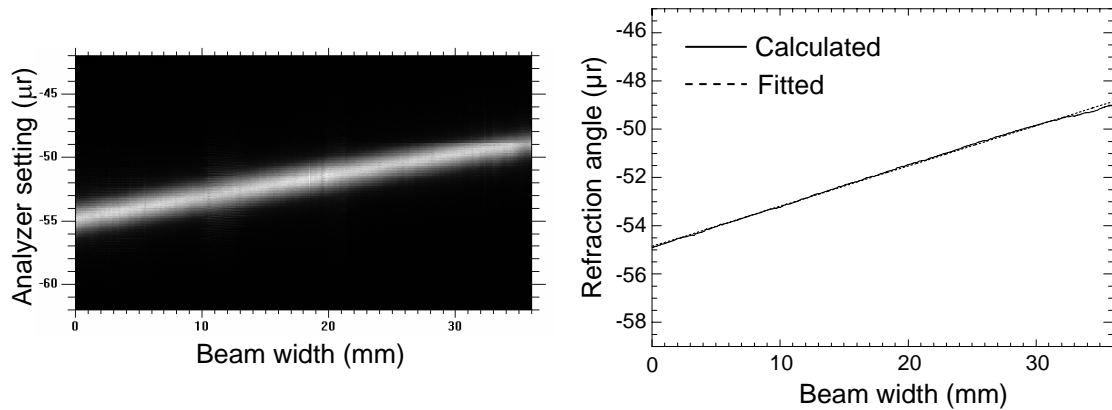


Figure A.4 The stereographic projection (Courtesy B.D. Cullity, Elements of X-ray Diffraction, Addison-Wesley Publishing Company Inc., USA, 1956)

Appendix B

Analysis of tilt errors

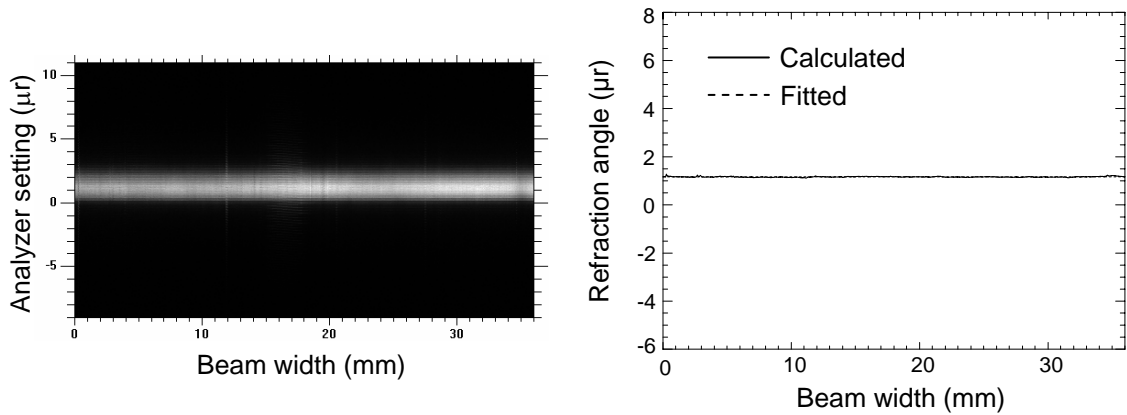
When the double crystal of the monochromator is aligned, the data collected with analyzer tilt errors of 3.03mr, 0.0mr, -3.03mr, and -6.06mr can be analyzed. Figure B.1(a) – B.4(a) show the images created by the extraction of the useful information from each original beam image using the method described in Chapter 2. Figure B.1(b) – B.4(b) show the calculated refracted angle together with its linear fitting and the listed slope of the fitted line corresponding to $-k_{\Delta\theta}$.



(a) Image of the beam at different analyzer settings

(b) Refraction angle as a function of the beam width and its linear fitting. The slope of the fitted line is $0.167\mu\text{r}/\text{mm}$

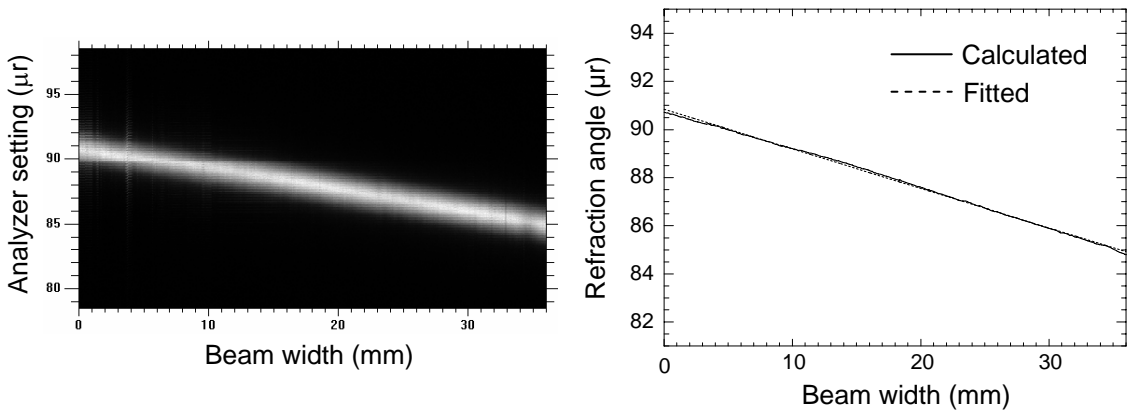
Figure B.1 Image of the beam at different analyzer settings and the accordingly calculated refraction angle as a function of the beam width and its linear fitting when the tilt of the analyzer was set at 3.03mr.



(a) Image of the beam at different analyzer settings

(b) Refraction angle as a function of the beam width and its linear fitting. The slope of the fitted line is $0.000\mu\text{r}/\text{mm}$

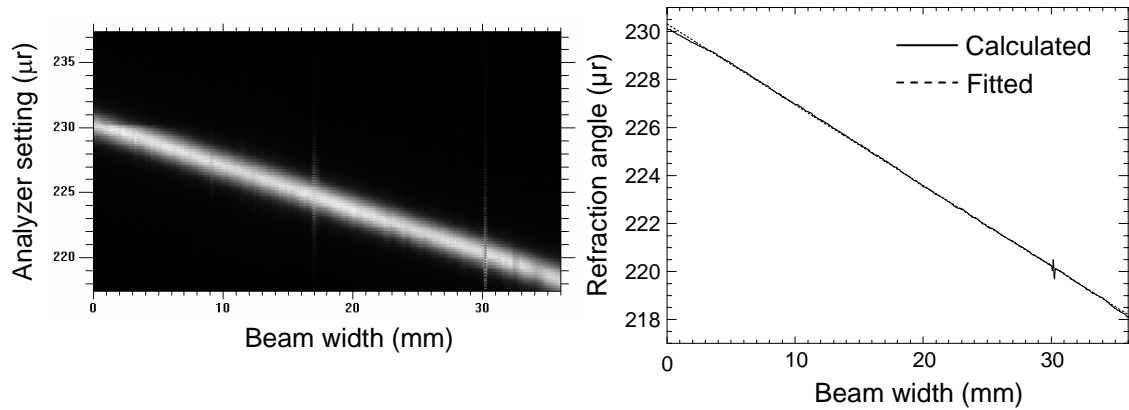
Figure B.2 Image of the beam at different analyzer settings and the accordingly calculated refraction angle as a function of the beam width and its linear fitting when there was no tilt of the analyzer



(a) Image of the beam at different analyzer settings

(b) Refraction angle as a function of the beam width and its linear fitting. The slope of the fitted line is $-0.164\mu\text{r}/\text{mm}$

Figure B.3 Image of the beam at different analyzer settings and the accordingly calculated refraction angle as a function of the beam width and its linear fitting when the tilt of the analyzer was set at -3.03mr .

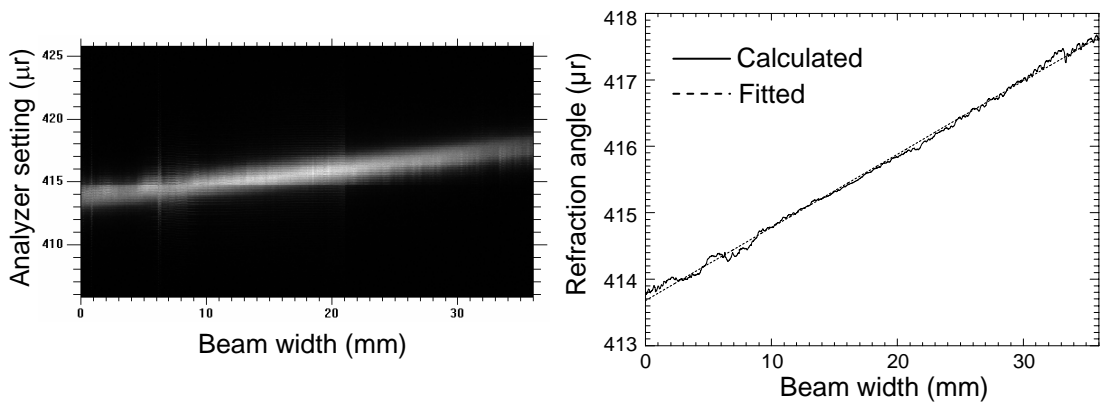


(a) Image of the beam at different analyzer settings

(b) Refraction angle as a function of the beam width and its linear fitting. The slope of the fitted line is $-0.336\mu\text{r}/\text{mm}$

Figure B.4 Image of the beam at different analyzer settings and the accordingly calculated refraction angle as a function of the beam width and its linear fitting when the tilt of the analyzer was set at -6.06mr

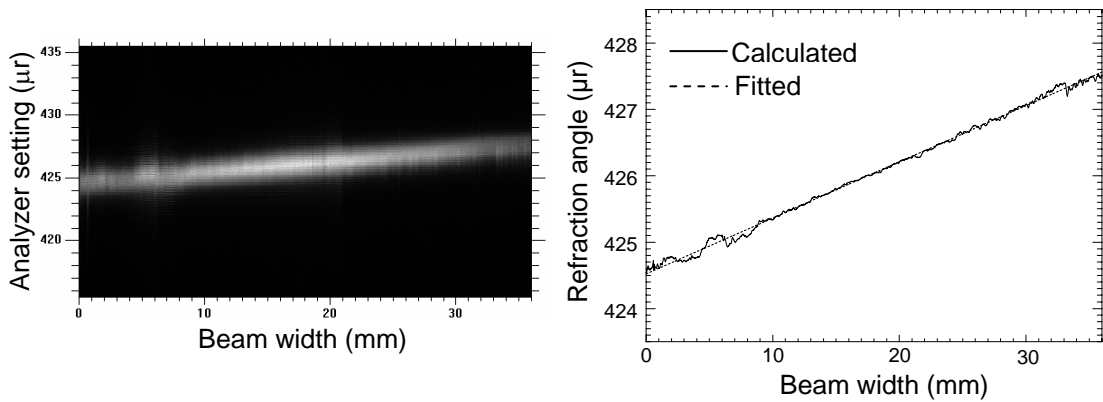
When the 2nd crystal of the monochromator was set at the 1st tilt, analyzer tilts of 0.606mr , 0mr , -0.606mr , -1.212mr , -1.818mr were applied. Figure B.5(a) – B.9(a) shown the track of the bright spot of the beam for different analyzer tilts. Figure B.5(b) – B.9(b) show the refraction angles along the beam width, together with their slopes corresponding to $-k_{\Delta\theta}$.



(a) Image of the beam at different analyzer settings

(b) Refraction angle as a function of the beam width and its linear fitting. The slope of the fitted line is $0.110\mu\text{r}/\text{mm}$

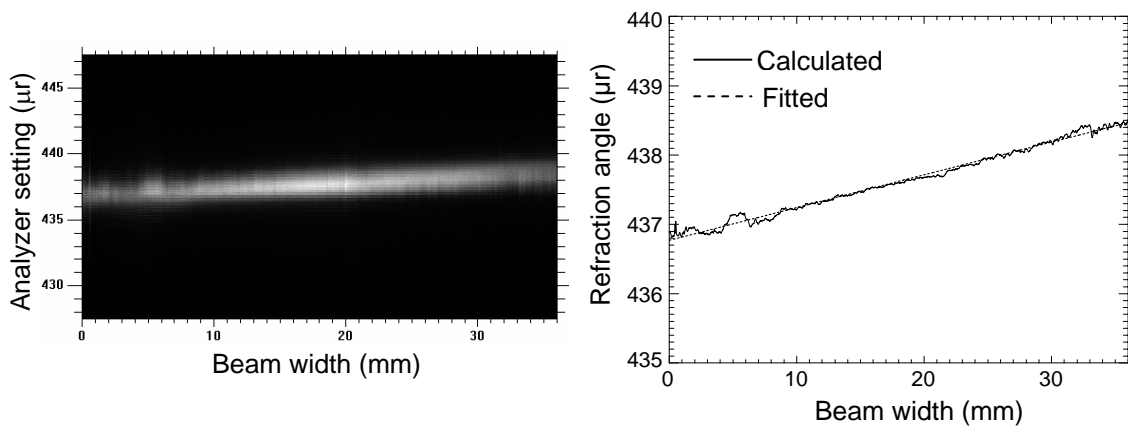
Figure B.5 Image of the beam at different analyzer settings and the accordingly calculated refraction angle as a function of the beam width and its linear fitting when the tilt of the analyzer was set at 0.606mr and the tilt of the 2nd crystal of the monochromator was set at the 1st tilt value.



(a) Image of the beam at different analyzer settings

(b) Refraction angle as a function of the beam width and its linear fitting. The slope of the fitted line is $0.084\mu\text{r}/\text{mm}$

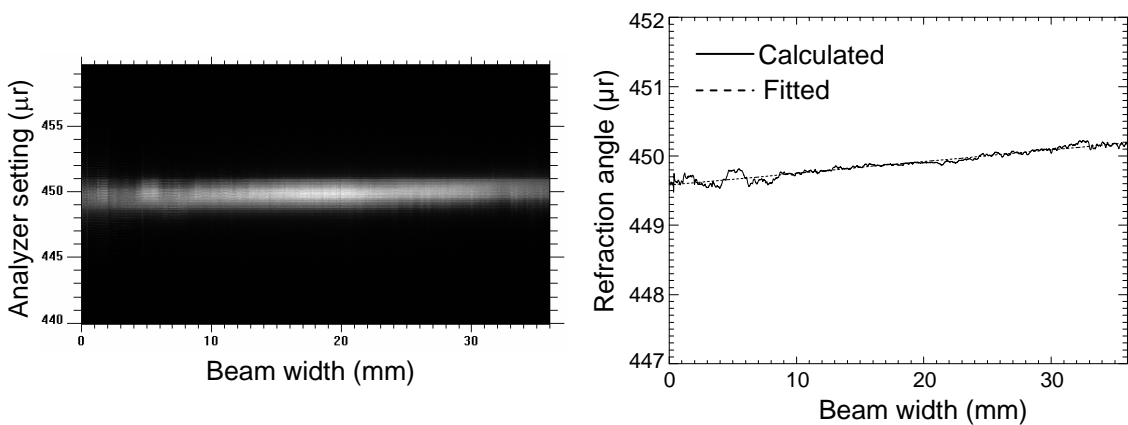
Figure B.6 Image of the beam at different analyzer settings and the accordingly calculated refraction angle as a function of the beam width and its linear fitting when the tilt of the analyzer was set at 0mr and the tilt of the 2nd crystal of the monochromator was set at the 1st tilt value.



(a) Image of the beam at different analyzer settings

(b) Refraction angle as a function of the beam width and its linear fitting. The slope of the fitted line is $0.047\mu\text{r}/\text{mm}$

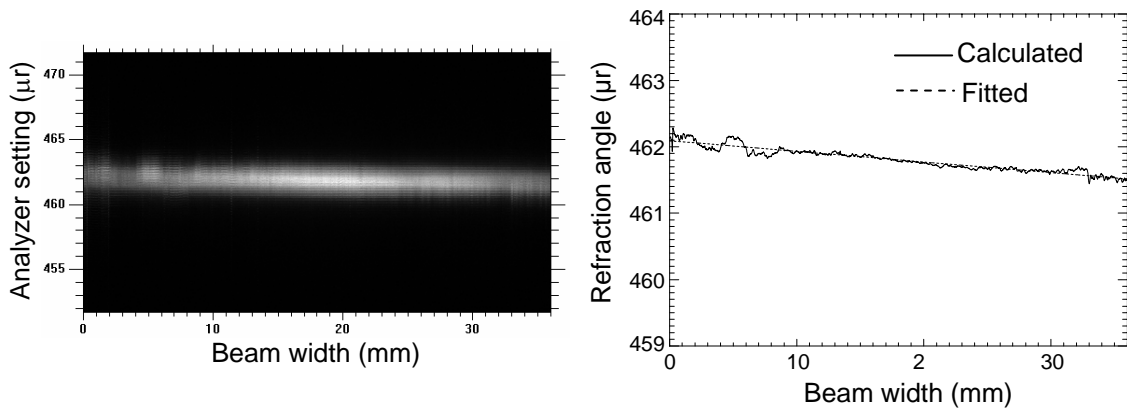
Figure B.7 Image of the beam at different analyzer settings and the accordingly calculated refraction angle as a function of the beam width and its linear fitting when the tilt of the analyzer was set at -0.606mr and the tilt of the 2nd crystal of the monochromator was set at the 1st tilt value.



(a) Image of the beam at different analyzer settings

(b) Refraction angle as a function of the beam width and its linear fitting. The slope of the fitted line is $0.017\mu\text{r}/\text{mm}$

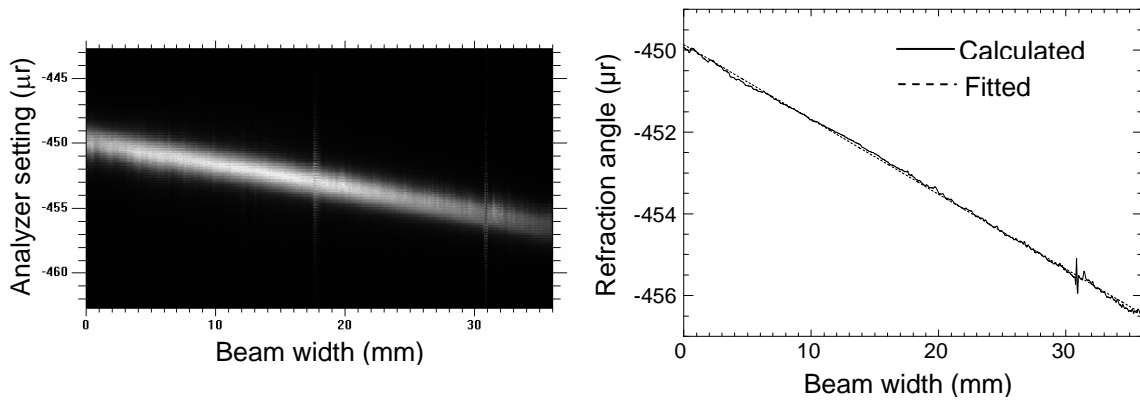
Figure B.8 Image of the beam at different analyzer settings and the accordingly calculated refraction angle as a function of the beam width and its linear fitting when the tilt of the analyzer was set at -1.212mr and the tilt of the 2nd crystal of the monochromator was set at the 1st tilt value.



(a) Image of the beam at different analyzer settings (b) Refraction angle as a function of the beam width and its linear fitting. The slope of the fitted line is $-0.016\mu\text{r}/\text{mm}$

Figure B.9 Image of the beam at different analyzer settings and the accordingly calculated refraction angle as a function of the beam width and its linear fitting when the tilt of the analyzer was set at -1.818mr and the tilt of the 2nd crystal of the monochromator was set at the 1st tilt value.

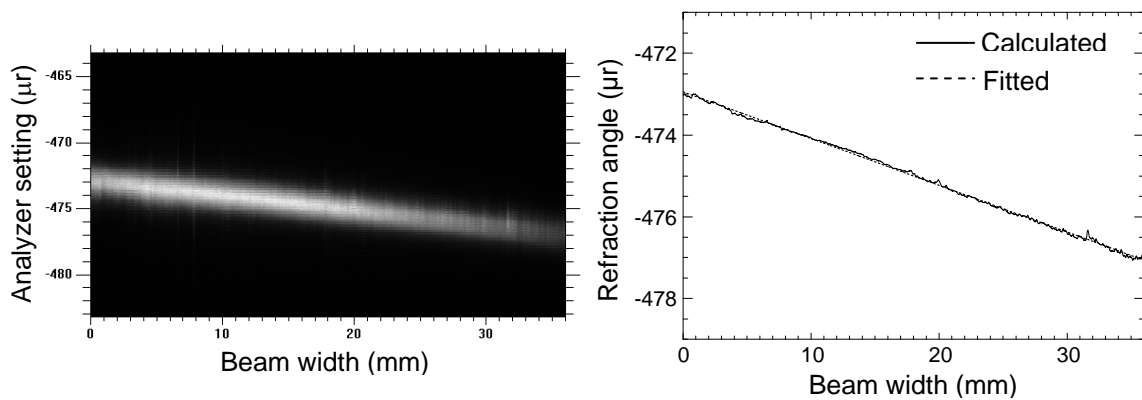
When the 2nd crystal of the monochromator was set at its 2nd tilt value (approximately the same value as the 1st tilt value but with opposite sign), analyzer tilts of -1.818mr , -0.606mr , 0mr , 0.606mr , 1.212mr , 1.828mr , 2.424mr were applied. Similarly, Figure B.10 – B.16 show the position of the bright spot of the beam at different analyzer settings and the calculated refraction angle as a function of the beam width.



(a) Image of the beam at different analyzer settings

(b) Refraction angle as a function of the beam width and its linear fitting. The slope of the fitted line is $-0.183\mu\text{r}/\text{mm}$

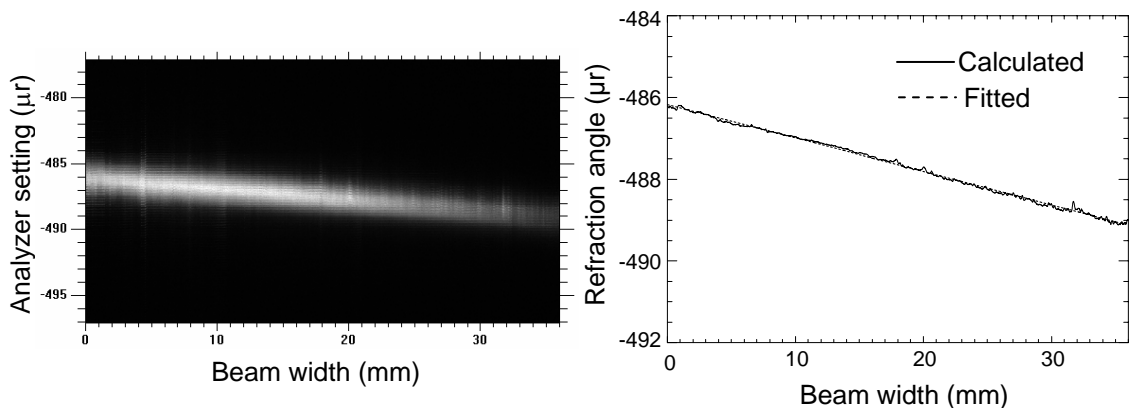
Figure B.10 Image of the beam at different analyzer settings and the accordingly calculated refraction angle as a function of the beam width and its linear fitting when the tilt of the analyzer was set at -1.818mr and the tilt of the 2nd crystal of the monochromator was set at the 2nd tilt value.



(a) Image of the beam at different analyzer settings

(b) Refraction angle as a function of the beam width and its linear fitting. The slope of the fitted line is $-0.114\mu\text{r}/\text{mm}$

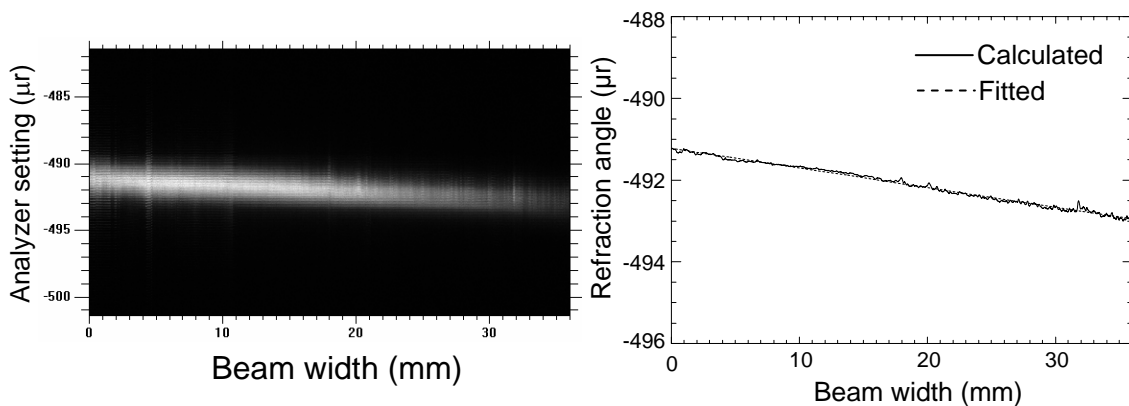
Figure B.11 Image of the beam at different analyzer settings and the accordingly calculated refraction angle as a function of the beam width and its linear fitting when the tilt of the analyzer was set at -0.606mr and the tilt of the 2nd crystal of the monochromator was set at the 2nd tilt value.



(a) Image of the beam at different analyzer settings

(b) Refraction angle as a function of the beam width and its linear fitting. The slope of the fitted line is $-0.082\mu\text{r}/\text{mm}$

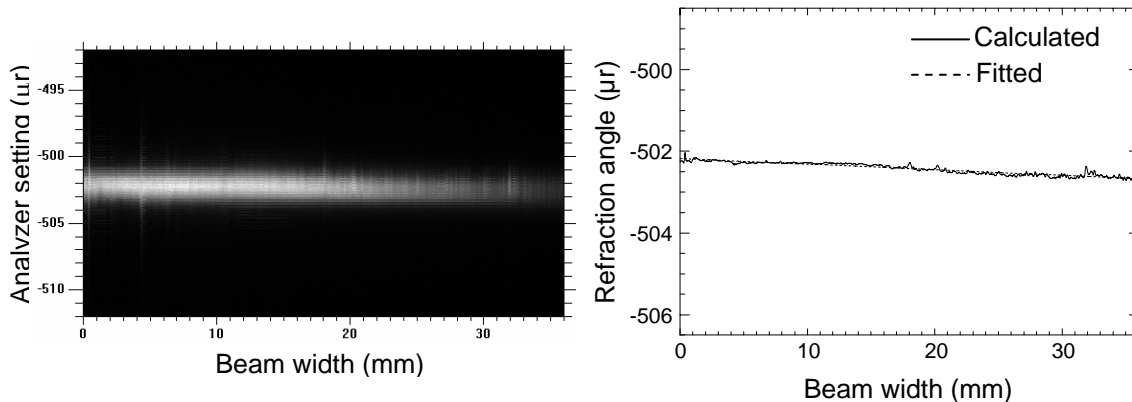
Figure B.12 Image of the beam at different analyzer settings and the accordingly calculated refraction angle as a function of the beam width and its linear fitting when the tilt of the analyzer was set at 0mr and the tilt of the 2nd crystal of the monochromator was set at the 2nd tilt value.



(a) Image of the beam at different analyzer settings

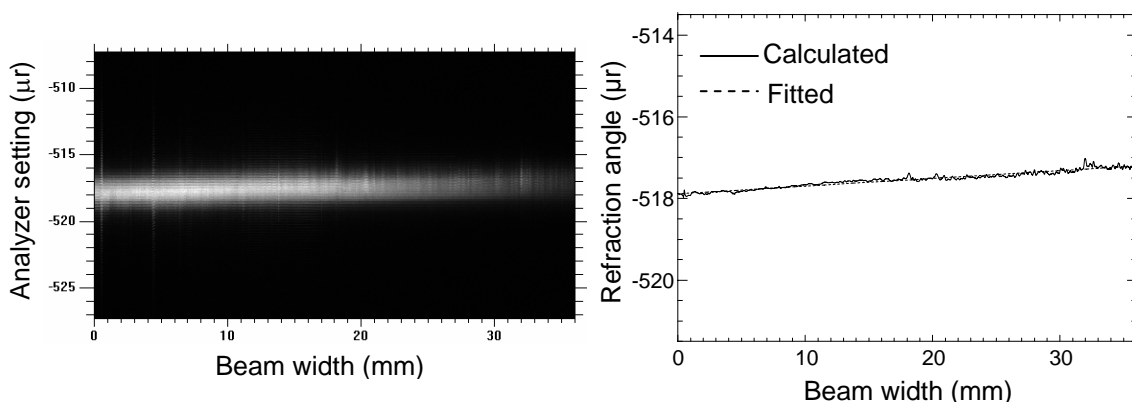
(b) Refraction angle as a function of the beam width and its linear fitting. The slope of the fitted line is $-0.048\mu\text{r}/\text{mm}$

Figure B.13 Image of the beam at different analyzer settings and the accordingly calculated refraction angle as a function of the beam width and its linear fitting when the tilt of the analyzer was set at 0.606mr and the tilt of the 2nd crystal of the monochromator was set at the 2nd tilt value.



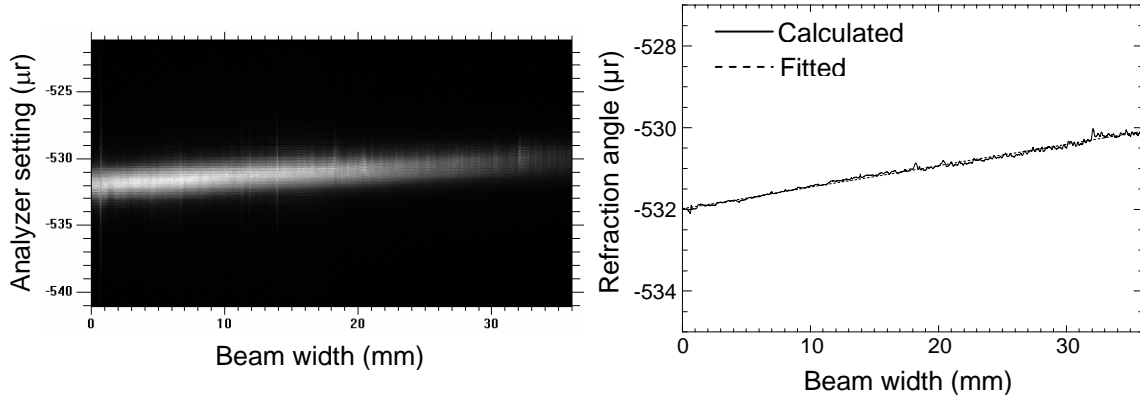
(a) Image of the beam at different analyzer settings (b) Refraction angle as a function of the beam width and its linear fitting. The slope of the fitted line is $-0.013\mu\text{r}/\text{mm}$

Figure B.14 Image of the beam at different analyzer settings and the accordingly calculated refraction angle as a function of the beam width and its linear fitting when the tilt of the analyzer was set at 1.212mr and the tilt of the 2nd crystal of the monochromator was set at the 2nd tilt value.



(a) Image of the beam at different analyzer settings (b) Refraction angle as a function of the beam width and its linear fitting. The slope of the fitted line is $0.019\mu\text{r}/\text{mm}$

Figure B.15 Image of the beam at different analyzer settings and the accordingly calculated refraction angle as a function of the beam width and its linear fitting when the tilt of the analyzer was set at 1.818mr and the tilt of the 2nd crystal of the monochromator was set at the 2nd tilt value.



(a) Image of the beam at different analyzer settings (b) Refraction angle as a function of the beam width and its linear fitting. The slope of the fitted line is $0.053\mu\text{r}/\text{mm}$

Figure B.16 Image of the beam at different analyzer settings and the accordingly calculated refraction angle as a function of the beam width and its linear fitting when the tilt of the analyzer was set at 2.424mr and the tilt of the 2nd crystal of the monochromator was set at the 2nd tilt value.

References

- [1] D Chapman, X-ray optics for emission line X-ray source diffraction enhanced systems, Nuclear Instruments Methods in Physics Research Section A: Accelerators, Spectrometers, Detectors and Associated Equipment, 562 (2006) 461.
- [2] D Chapman, W Thomlinson, RE Johnston, D Washburn, E Pisano, N Gmur, et al. Diffraction enhanced X-ray imaging, Physics in Medicine and Biology, 42 (1997) 2015-25.
- [3] MN Wernick, O Wirjadi, D Chapman, O Oltulu, Z Zhong, Y Yang, Preliminary investigation of a multiple-image radiography method, Proceedings of the International Symposium on Biomedical Imaging, (2002) 129-32.
- [4] MN Wernick, O Wirjadi, D Chapman, Z Zhong, NP Galatsanos, Y Yang, et al. Multiple-image radiography, Physics in Medicine and Biology, 48 (2003) 3875-95.
- [5] Z Zhong, W Thomlinson, D Chapman, D Sayers. Implementation of diffraction-enhanced imaging experiments: at the NSLS and APS, Nuclear Instruments Methods in Physics Research Section A: Accelerators, Spectrometers, Detectors and Associated Equipment, 450 (2000) 556-67.
- [6] CJ Hall, M Ibison, KC Cheung, K Siu, RA Lewis, A Hufton, et al. Diffraction-enhanced imaging at the UK synchrotron radiation source, Nuclear Instruments Methods in Physics Research Section A: Accelerators, Spectrometers, Detectors and Associated Equipment, 548 (2005) 181-6.
- [7] RH Menk, L Rigon, F Arfelli. Diffraction-enhanced X-ray medical imaging at the ELETTRA synchrotron light source, Nuclear Instruments Methods in Physics Research Section A: Accelerators, Spectrometers, Detectors and Associated Equipment, 548 (2005) 213-20.

- [8] F Arfelli, Recent development of diffraction enhanced imaging, AIP Conference Proceedings, (2002) 1-10.
- [9] RA Lewis, CJ Hall, AP Hufton, S Evans, RH Menk, F Arfelli, et al. X-ray refraction effects: application to the imaging of biological tissues, The British Journal of Radiology, 76 (2003) 301-308.
- [10] S Fiedler, A Bravin, J Keyrilainen, M Fernandez, P Suortti, W Thomlinson, et al. Imaging lobular breast carcinoma: comparison of synchrotron radiation DEI-CT technique with clinical CT, mammography and histology, Physics in Medicine and Biology, 49 (2004) 175-88.
- [11] J Keyrilainen, Visualization of calcifications and thin collagen strands in human breast tumor specimens by the diffraction-enhanced imaging technique: a comparison with conventional mammography and histology, European Journal of Radiology, 53 (2005) 226.
- [12] ED Pisano, Human breast cancer specimens: diffraction-enhanced imaging with histologic correlation — improved conspicuity of lesion detail compared with digital radiography, Radiology, 214 (2000) 895.
- [13] MZ Kiss, Improved image contrast of calcifications in breast tissue specimens using diffraction enhanced imaging, Physics in Medicine and Biology, 49 (2004) 3427.
- [14] C Liu, Evaluation of x-ray diffraction enhanced imaging in the diagnosis of breast cancer, Physics in Medicine and Biology, 52 (2007) 419.
- [15] J Mollenhauer, Diffraction-enhanced X-ray imaging of articular cartilage, Osteoarthritis and Cartilage. 10 (2002) 163.
- [16] C Muehleman, Radiography of rabbit articular cartilage with diffraction-enhanced imaging. The Anatomical Record Part A: Discoveries in Molecular, Cellular, and Evolutionary Biology, 272 (2003) 392.

- [17] S Majumdar, Diffraction enhanced imaging of articular cartilage and comparison with micro-computed tomography of the underlying bone structure, *European Radiology*, 14 (2004) 1440.
- [18] J Li, Reliability of diffraction enhanced imaging for assessment of cartilage lesions, *ex vivo*, *Osteoarthritis and Cartilage*, 13 (2005) 187.
- [19] S Crittell, Diffraction enhanced imaging of normal and arthritic mice feet, *Nuclear Instruments Methods in Physics Research Section A: Accelerators, Spectrometers, Detectors and Associated Equipment*, 573 (2007) 126.
- [20] ME Kelly, Diffraction-enhanced imaging of the rat spine, *Canadian Association of Radiologists Journal*, 57 (2006) 204.
- [21] ME Kelly, Diffraction-enhanced imaging of a porcine eye, *Canadian Journal of Ophthalmology*, 42 (2007) 731.
- [22] J Li, Radiography of soft tissue of the foot and ankle with diffraction enhanced imaging, *Journal of Anatomy*, 202 (2003) 463.
- [23] B Jacobson, Dichromatic absorption radiography: dichromography, *Acta Radiologica*, 39 (1953) 437-452.
- [24] R Lewis, Medical applications of synchrotron radiation X-rays, *Physics in Medicine and Biology*, 42 (1997) 1213-43.
- [25] W Thomlinson, N Gmur, D Chapman, R Garrett, N Lazarz, H Houlin, et al., First operation of the medical research facility at the NSLS for coronary angiography, *Review of Scientific Instruments*, 63 (1992) 625-8.
- [26] T Dill, W Dix, CW Hamm, M Jung, W Kupper, M Lohmann, et al. Intravenous coronary angiography with synchrotron radiation, *European Journal of Physics*, 19 (1998) 499-511.

- [27] H Elleaume, S Fiedler, F Esteve, B Bertrand, AM Charvet, P Berkvens, et al. First human transvenous coronary angiography at the European Synchrotron Radiation Facility, *Physics in Medicine and Biology*, 45 (2000) 39-43.
- [28] ME Kelly, E Schultke, S Fiedler, C Nemoz, R Guzman, S Corde, et al. Synchrotron-based intravenous cerebral angiography in a small animal model, *Physics in Medicine and Biology*, 52 (2007) 1001-1012.
- [29] E Schultke, S Fiedler, M Kelly, R Griebel, B Juurlink, G Leduc, et al., The potential for neurovascular intravenous angiography using K-edge digital subtraction angiography, *Nuclear Instruments Methods in Physics Research Section A: Accelerators, Spectrometers, Detectors and Associated Equipment*, 548 (2005) 84-87.
- [30] E Rubenstein, JC Giacomini, HJ Gordon, Rubenstein, J. A. L., G Brown. Xenon K-edge dichromographic bronchography: synchrotron radiation based medical imaging, *Nuclear Instruments Methods in Physics Research Section A: Accelerators, Spectrometers, Detectors and Associated Equipment*, 364 (1995) 360-1.
- [31] S Bayat, G Le Duc, L Porra, G Berruyer, C Nemoz, S Monfraix, et al. Quantitative functional lung imaging with synchrotron radiation using inhaled xenon as contrast agent, *Physics in Medicine and Biology*, 46 (2001) 3287-3299.
- [32] S Monfraix, S Bayat, L Porra, G Berruyer, C Nemoz, W Thomlinson, et al. Quantitative measurement of regional lung gas volume by synchrotron radiation computed tomography, *Physics in Medicine and Biology*, 50 (2005) 1-11.
- [33] H Bornefalk, JM Lewin, M Danielsson, M Lundqvist. Single-shot dual-energy subtraction mammography with electronic spectrum splitting: Feasibility, *European Journal of Radiology*, 60 (2006) 275-278.
- [34] KA Kolesnikov, GN Kulipanov, MV Kuzin, NA Mezentsev, SI Nesterov, VF Pindyurin, et al. Preliminary results of an animal's lymphatic system study at the angiography station of the VEPP-3 storage ring, *Nuclear Instruments Methods in Physics*

Research Section A: Accelerators, Spectrometers, Detectors and Associated Equipment, 359 (1995) 364-369.

[35] S Rigley, L Rigon, K Ataelmannan, D Chapman, R Doucette, R Griebel, et al., Absorption edge subtraction imaging for volumetric measurement in an animal model of malignant brain tumor, Nuclear Instruments Methods in Physics Research Section A: Accelerators, Spectrometers, Detectors and Associated Equipment, 548 (2005) 88-93.

[36] WR Dix, W Kupper, T Dill, CW Hamm, H Job, M Lohmann, et al. Comparison of intravenous coronary angiography using synchrotron radiation with selective coronary angiography, Journal of Synchrotron Radiation, 10 (2003) 219-227.

[37] AC Thompson, J Llacer, L Campbell Finman, EB Hughes, JN Otis, S Wilson, et al. Computed tomography using synchrotron radiation, Nuclear Instruments Methods in Physics Research Section A: Accelerators, Spectrometers, Detectors and Associated Equipment, 222 (1984) 319-323.

[38] H Elleaume, AM Charvet, S Corde, F Esteve, JF Le Bas. Performance of computed tomography for contrast agent concentration measurements with monochromatic x-ray beams: Comparison of K-edge versus temporal subtraction, Physics in Medicine and Biology, 47 (2002) 3369-3385.

[39] T Takeda, Y Itai, H Yoshioka, K Umetani, K Ueda, M Akisada. Synchrotron radiation cine K-edge energy subtraction coronary arteriography using an iodine filter method, Medical and Biological Engineering and Computing, 32 (1994) 462-467.

[40] B Beckhoff, Handbook of practical X-ray fluorescence analysis, 1st ed. ed., Springer, Berlin, 2006.

[41] S Ebashi, M Koch, E Rubenstein, Handbook on synchrotron radiation, North Holland, Amsterdam, 1991.

[42] F Pfeiffer, C David, M Burghammer, C Riekkel, T Salditt. Two-dimensional x-ray waveguides and point sources, Science, 297 (2002) 230-234.

- [43] CG Schroer, O Kurapova, J Patommel, P Boye, J Feldkamp, B Lengeler, et al. Hard x-ray nanoprobe based on refractive x-ray lenses, *Applied Physics Letters*, 87 (2005) 124103-1.
- [44] B De Samber, G Silversmit, R Evens, K De Schampelaere, C Janssen, B Masschaele, et al. Three-dimensional elemental imaging by means of synchrotron radiation micro-XRF: Developments and applications in environmental chemistry, *Analytical and Bioanalytical Chemistry*, 390 (2008) 267-271.
- [45] JV Gilfrich, EF Skelton, SB Qadri, JP Kirkland, DJ Nagel, Synchrotron radiation X-ray fluorescence analysis, *Analytical Chemistry*, 55 (1983) 187.
- [46] LM Miller, RJ Smith, ME Ruppel, CH Ott, A Lanzarotti. Development and applications of an epifluorescence module for synchrotron x-ray fluorescence microprobe imaging, *Review of Scientific Instruments*, 76 (2005) 066107.
- [47] C Reiners, X-ray fluorescence analysis (XFA) of thyroidal iodine content (TIC) with an improved measuring system, *Experimental and Clinical Endocrinology Diabetes*, 106 Suppl 3 (1998).
- [48] M Hansson, M Isaksson, A Monte Carlo (MC) based individual calibration method for in vivo x-ray fluorescence analysis (XRF), *Physics in Medicine and Biology*, 52 (2007) 2009.
- [49] JM O'Meara, DR Chettle, FE McNeill, CE Webber. In vivo X-ray fluorescence (XRF) measurement of uranium in bone, *Applied Radiation and Isotopes*, 49 (1998) 713-715.
- [50] A Pejović-Milić, Quantification of bone strontium levels in humans by in vivo x-ray fluorescence, *Medical Physics*, 31 (2004) 528.
- [51] M Zamburlini, In vivo study of an x-ray fluorescence system to detect bone strontium non-invasively, *Physics in Medicine and Biology*, 52 (2007) 2107.

- [52] AC Aro, Improvements in the calibration of ^{109}Cd K x-ray fluorescence systems for measuring bone lead in vivo, *Physics in Medicine and Biology*, 39 (1994) 2263.
- [53] DEB Fleming, A 4 x 500 mm² cloverleaf detector system for in vivo bone lead measurement, *Medical physics*, 34 (2007) 945.
- [54] L Ahlgren, Cadmium in man measured in vivo by x-ray fluorescence analysis, *Physics in Medicine and Biology*, 26 (1981) 19.
- [55] JO Christoffersson, Cadmium concentration in the kidney cortex of occupationally exposed workers measured in vivo using X-ray fluorescence analysis, *Environmental Research*, 42 (1987) 489.
- [56] J Börjesson, In vivo XRF analysis of mercury: the relation between concentrations in the kidney and the urine, *Physics in Medicine and Biology*, 40 (1995) 413.
- [57] A Khuder, MA Bakir, R Hasan, A Mohammad, Determination of nickel, copper, zinc and lead in human scalp hair in Syrian occupationally exposed workers by total reflection X-ray fluorescence, *Environmental Monitoring and Assessment*, (2007).
- [58] RCN Studinski, FE McNeill, DR Chettle, JM O'Meara, Estimation of a method detection limit for an in vivo XRF arsenic detection system, *Physics in Medicine and Biology*, 50 (2005) 521.
- [59] E Pagot, P Cloetens, S Fiedler, A Bravin, P Coan, J Baruchel, et al, A method to extract quantitative information in analyzer-based x-ray phase contrast imaging, *Applied Physics Letters*, 82 (2003) 3421-3.
- [60] O Oltulu, Z Zhong, M Hasnah, MN Wernick, D Chapman. Extraction of extinction, refraction and absorption properties in diffraction enhanced imaging, *Journal of Applied Physics*, 36 (2003) 2152-2156.
- [61] CA Parham, System parameters and performance specifications for the application of diffraction enhanced imaging and multiple image radiography to breast imaging, Ph.D. thesis, (2006).

- [62] DHY Shen, RT Kloos, EL Mazzaferri, SM Jhiang, Sodium iodide symporter in health and disease, *Thyroid*, 11 (2001) 415.
- [63] D Kotyzová, V Eybl, M Mihaljevič, E Glattre. Effect of long-term administration of Arsenic(III) and Bromine with and without Selenium and Iodine supplementation on the element level in the thyroid of rat, *Biomedical Papers of the Medical Faculty of the University Palacký, Olomouc, Czechoslovakia*, 149 (2005) 329-333.
- [64] CT Badea, M Drangova, DW Holdsworth, and GA Johnson, In vivo small-animal imaging using micro-CT and digital subtraction angiography, *Physics in Medicine and Biology*, 53 (2008) 319
- [65] D Chapman, C Schulze, Arterial Cross-Section Measurements from Dual Energy Transvenous Coronary Angiography Images, *Proceedings of IEEE Nuclear Science Symposium & Medical Imaging Conference*, (1994) 1528-1532.
- [66] J Als-Nielsen, *Elements of modern X-ray physics*, Wiley, New York, c2001.
- [67] R Jenkins, *X-ray fluorescence spectrometry*, J. Wiley, New York, c1988.
- [68] A Brunetti, Sanchez Del Rio, M., B Golosio, A Simionovici, A Somogyi, A library for X-ray-matter interaction cross sections for X-ray fluorescence applications, *Proceedings of 17th International Congress on X-Ray Optics and Microanalysis*, 59 (2004) 1725-1731.
- [69] RJ Leclair, PC Johns, X-ray forward-scatter imaging: Experimental validation of model, *Proceedings of 22nd Annual International Conference of the IEEE Engineering in Medicine and Biology Society*, 4 (2000) 3074-3077.
- [70] RJ Leclair, PC Johns, Optimum momentum transfer arguments for x-ray forward scatter imaging, *Medical Physics*, 29 (2002) 2881-90.
- [71] A Thompson, D Attwood, E Gullikson, M Howells, K Kim, J Kirz, et al., *X-ray data booklet*, Lawrence Berkeley National Laboratory, university of California, Berkeley, CA, USA, 2001.

- [72] Y Zhu, H Zhang, R McCrea, B Bewer, S Wiebe, H Nichol, et al. Fabrication of a small animal restraint for synchrotron biomedical imaging using a rapid prototyper, Nuclear Instruments Methods in Physics Research Section A: Accelerators, Spectrometers, Detectors and Associated Equipment, 582 (2007) 229-232.
- [73] Y Zhu, H Zhang, B Bewer, BFG Popescu, H Nichol, D Chapman. Field flatteners fabricated with a rapid prototyper for K-edge subtraction imaging of small animals, Nuclear Instruments and Methods in Physics Research Section A: Accelerators, Spectrometers, Detectors and Associated Equipment, 588 (2008) 442-7.
- [74] W Soller, A new precision X-ray spectrometer, Physical Review, 24 (1924) 158-167.
- [75] B Bewer, H Zhang, Y Zhu, L Zhang, G George, IJ Pickering, et al. Development of a combined K-edge subtraction and fluorescence subtraction imaging system for small animals, Review of Scientific Instruments, 79 (2008) 085102.
- [76] H Zhang, D Chapman, A design study of a bent Laue K-edge subtraction monochromator for small animal imaging, Proceedings of the Fifteenth Pan-American Synchrotron Radiation Instrumentation, (2008).
- [77] P Suortti, W Thomlinson. Bent Laue crystal monochromator for angiography at the NSLS, Nuclear Instruments Methods in Physics Research Section A: Accelerators, Spectrometers, Detectors and Associated Equipment, A269 (1988) 639-648.
- [78] P Suortti, W Thomlinson, D Chapman, N Gmuer, R Greene, N Lazarz. Performance evaluation of a bent Laue monochromator, Nuclear Instruments Methods in Physics Research Section A: Accelerators, Spectrometers, Detectors and Associated Equipment, A297 (1990) 268.
- [79] P Suortti, W Thomlinson, D Chapman, N Gmur, DP Siddons, C Schulze. Single crystal bent Laue monochromator for coronary angiography, Nuclear Instruments Methods in Physics Research Section A: Accelerators, Spectrometers, Detectors and Associated Equipment, 336 (1993) 304-309.

- [80] P Suortti, U Lienert, C Schulze, Bent crystal optics for high energy synchrotron radiation, AIP Conference Proceedings, (1997) 175-92.
- [81] C Schulze, U Lienert, M Hanfland, M Lorenzen, F Zontone. Microfocusing of hard X-rays with cylindrically bent crystal monochromators, Journal of Synchrotron Radiation, 5 (1998) 77-81.
- [82] YI Nesterets, SW Wilkins, A flexible configuration for a high-energy phase-contrast imaging beamline involving in-line focusing crystal optics, Radiation Physics and Chemistry, 75 (2006) 1981-1985.
- [83] FN Chuckhovskii, M Krisch, Lens equation for Bragg diffraction optics: the general case of asymmetrical reflection, Journal of Applied Crystallography, 25 (1992) 211-213.
- [84] JE White, X-ray diffraction by elastically deformed crystals, Journal of Applied Physics, 21 (1950) 855-859.
- [85] E Erola, V Etelaniemi, P Suortti, P Pattison, W Thomlinson, X-ray reflectivity of bent perfect crystals in Bragg and Laue geometry, Journal of Applied Crystallography, 23 (1990) 35-42.
- [86] W Greiner, Classical Mechanics: Systems of Particles and Hamiltonian Dynamics, Springer 2001.
- [87] WFG Swann, Application of Liouville's theorem to electron orbits in the earth's magnetic field, Physical Review, 44 (1933) 224-227.
- [88] BD Cullity, Elements of X-ray diffraction., Addison-Wesley Pub. Co., 1956.